PETROLOGY, TECTONIC SETTING, AND REGIONAL IMPLICATIONS OF THE OPHIOLITIC LIUYUAN COMPLEX, NW CHINA

by

Gabriel Sombini dos Santos

A thesis
presented to the University of Waterloo
in fulfillment of the
thesis requirement for the degree of
Doctor in Philosophy
in
Earth Sciences

Waterloo, Ontario, Canada, 2022

Author's Declaration

I hereby declare that I am the sole author of this thesis. This is a true copy of the thesis, including any required final revisions, as accepted by my examiners.

I understand that my thesis may be made electronically available to the public.

Abstract

Located along the southern margin of the Central Asian Orogenic Belt (CAOB), the mafic 290-280 Ma Liuyuan Complex stratigraphy and tectonic setting have been controversial for decades. Here, the results of a detailed field and petrological study are presented, where the Liuyuan Complex is subdivided into troctolite, melatroctolite, layered gabbro, olivine gabbro, podiform olivine gabbro, podiform hornblende gabbro, intrusive hornblende gabbro, plagiogranite, sheeted dyke, and mafic tectonite in addition to previously identified and studied basalt and chert. All contacts between the igneous facies are intrusive, with gabbroic rocks separated from the overlying basalt by a newly discovered, well-developed and laterally continuous sheeted dyke complex. Based on their trace element signature and thermodynamic modeling, the basalts of the Liuyuan Complex formed by 10-17% partial melting of a spinel lherzolite mantle source in a back-arc basin setting. The parental melt of the suite followed a typical tholeiitic liquid line of descent, fractionating olivine, plagioclase, clinopyroxene, and ilmenite. Stratigraphic relations, mineral chemistry, and trace element inversions further indicate that the gabbroic rocks in the Liuyuan Complex are comagmatic with the overlying basalts. The formation of the Liuyuan Complex as a back-arc basin ophiolite is inconsistent with previously proposed tectonic models for the southern CAOB, which required the Liuyuan Complex to have formed as a continental rift or a fore-arc ophiolite. Based on recent field investigations in the Liuyuan area, a tectonic model where the Liuyuan Complex formed as a back-arc to the recently identified Ganquan Arc is proposed. The back-arc basin was then consumed by a north-dipping subduction zone beneath the active margin of Composite Siberia starting ca. 281 Ma. The magmatic center of this arc migrated southwards, likely caused by slab roll-back, with the Liuyuan Complex becoming the basement of this arc. Exhumation of the Liuyuan Complex took place by 267 Ma, marking the closure of the southernmost and youngest known tract of the Paleo-Asian Ocean.

Acknowledgements

I would like to first acknowledge my supervisors, Shoufa Lin and Cees van Staal, for conceiving this PhD project, and for all the support and encouragement, in and out of the field. The past four years have been quite an adventure, and I couldn’t have wished for better mentors and guides. I would also like to thank Jean Bédard for the guidance and generosity. You have all taught me a lot. I also thank Sandra Barr for the friendship, advice, and for importing me in the first place. No longer such a stranger in a strange land after all. Many many thanks to my dear friends and borderline family members Tong Hong, Quinn Worthington, and Ludovico Scorsolini, from being by my side from day one. Well, almost day one, but Italians do tend to be late to the party. I also extend my endless appreciation to Mary Ann Kavanagh, Erik Matthew, Crystal Smith, and Jonathan Shute, for showing me the way. Many thanks to Thiago Benega, the very best of the Brazilian diaspora in Waterloo. Much love and a heartfelt thank you to all of you for everything. On the field end of things, I must also acknowledge the Chinese Geological Survey for their invaluable support. The field work conducted during the PhD project would not have been possible without them. To Song Yueting, the greatest field assistant one could possibly have, my brother from a different mother. On the home front, many thanks to Toca, Xerxes, and Ganso, for the decades (!) of friendship. Finally, I would like to thank my mother, Vera Lucia Sombini, and my father, Edson dos Santos, for being the greatest parents one could ever hope for. All the love in the world, and thank you for absolutely everything.

Table of Contents

List of Figures

List of Tables

Chapter 1: Introduction

1.1 Introduction

The Early Permian Liuyuan Complex, located at the southern edge of the Beishan Orogen, along the southern tip of the Central Asia Orogenic Belt, is mainly composed of pillow basalts, with subordinate gabbroic rocks, trondhjemite, and associated turbidites, carbonates and cherts. Although the area has been investigated in recent years (e.g. Mao et al. 2012, Wang et al. 2017), there is still considerable debate about whether the Liuyuan Complex formed in a continental rift (Zuo et al. 1991, Qin et al. 2011, Su et al. 2011, Wang et al. 2017) or in an oceanic setting (Mao et al. 2010, Xiao et al. 2010, Mao et al. 2012, Tian and Xiao 2020). The internal structure and stratigraphy of the Complex are poorly known and are controversial. The importance of the Liuyuan Complex for understanding the Beishan Orogen and hence, the terminal stages of the Paleo-Asian Ocean justifies a more detailed petrological and structural analysis. The goal of this project is to discriminate between these models by providing a new geological map and a robust petrographic, geochemical and geochronological dataset that will facilitate development of new petrologic and tectonic models for the formation of the Complex and the terminal collision of the Central Asian Orogenic Belt.

1.2 The Central Asian Orogenic Belt

The Central Asian Orogenic Belt (CAOB) (Fig. 1.1) is bounded by the Siberian and Baltic cratons to the north and by the Tarim and North China cratons to the south. With a geologic history extending from 1 Ga to 250 Ma, the CAOB is one of the largest and longest - lived accretionary orogens in the geological record (Windley et al. 2007, Wilhem et al. 2012, Xiao et al. 2015, Xiao et. al. 2018), recording Neoproterozoic-Phanerozoic crustal growth (Jahn et al. 2004, Zhou et al. 2011), and being a major site of mineral exploration (Yakubchuk et al. 2004).

Several models have been proposed to explain the evolution and architecture of the CAOB, and the major ones are briefly described here. Sengör et al. (1993) proposed a model for where the Altaids (the younger part of the CAOB developed between 600 Ma to 250 Ma) was formed by oroclinal bending and tectonic duplication of a single, approximately 7000 km long Kiochack-Tuva-Mongol arc. This arc would have been formed along the combined margin of the Siberian and Baltic Cratons. In this model slab roll-back led to the formation of back-arc basins and subordinate arcs, and rotation of the Baltic and Siberian cratons was responsible for the Mongolia-Okhotsk and Kazakhstan orocline. However, several lines of evidence, particularly the Gondwana affinity identified for several terranes in the orogen (Masago et al. 2010, Bazhenov et al. 2012), and paleomagnetic data indicating Siberian and Baltic cratons were not adjacent in the Neoproterozoic (Pisarevsky et al. 2003), are not consistent with the single arc model.

In contrast to the single-arc model of Sengör et al. (1993), many (e.g. Zonenshain et al. 1990, Kheraskova et al. 2003, Windley et al. 2007, Xiao et al. 2015, Xiao et al. 2018) have interpreted the geology of the CAOB as the result of convergence and accretion of multiple terranes, in an architecture analogous to the present day western-Pacific Ocean, and the North American Cordillera. The litho-stratigraphic units that compose the CAOB have been grouped by Xiao et al. (2015) based on faunal similarities into three major units: the Southern Mongolia collage in the north, the Kazakhstan collage in the west, and the Tarim-North China collage in the south. Overall, the CAOB evolved by the progressive accretion of terranes, with igneous and metamorphic ages systematically decreasing from north to south (i.e. Windley et al. 2007, Wilhem et al. 2012, Xiao et al. 2015, Xiao et al. 2018) (present day coordinates) at the margin of the Siberian and Baltic Cratons, terminating in the Solonker Suture, located in northern China (Sengor et al. 1993, Windley et al. 2007, Xiao et al. 2015, Xiao et al. 2018) during the Early Permian. A major question regarding the tectonic evolution of the orogen is whether the final accretion event occurred during the Carboniferous (e.g. Sengor et al. 1993) or the Permian (e.g. Xiao et al. 2009).

Formed by rocks ranging in age from Neoproterozoic to Triassic, the Beishan Orogen (Fig. 1.2) is located in the North China collage system, between the Solonker suture to the northeast and the Southern Tien Shan suture to the southwest and connects the Chinese Tianshan Orogen and the Inner Mongolia Orogen (Xiao et al. 2010, Song et al. 2013). It developed during the accretion of the Tarim and North China Cratons to the northern Mongolia Collage and is therefore a key area to investigate the final stages of the evolution of the CAOB. Xiao et al. (2010) provides an excellent review of the Beishan Orogen, describing several East-West trending lithotectonic units, bounded by transcurrent faults that commonly contain ophiolitic mélanges. From North to South, these units are: the Queershan arc, the Hongshishan mélange, the Heiyingshan-Hansan arc, the Xingxingxia-Shibanjing mélange, the Mazongshan arc, the Hongliuhe-Xichangjing mélange, the Shiuangyingshan-Huaniushan arc, the Liuyuan Complex, the Shibanshan arc, and the Dunhuang Block. These units are organized in E-W trending belts, with distinct arc terranes commonly separated by sutures marked by dismembered ophiolitic assemblages distributed along fault zones (Fig. 1.2).

According to Xiao et al. (2010), the Beishan Orogen developed through the accretion of a series of arcs formed in the large Paleo-Asian Ocean. The northernmost Queershan continental arc developed during the Ordovician to Early Silurian, along the southern margin of the Siberian craton, above a north-dipping subduction zone. The Paleo-Asian Ocean separated the Queershan continental arc and the Dunhuang block in the south. To the south, the Hanshan, Shuangyingshan, and Mazongshan intra-oceanic arcs developed coevally on the closing Paleo-Asian Ocean, the first two above north-dipping subduction zones, and the last above a south-dipping subduction zone (Xiao et al. 2010). The Hanshan and Mazongshan arcs amalgamated in the Middle Silurian, and the Shibanjing mélange obducted onto the Hanshan arc during this collision. The combination of these two sutured arcs and the intervening ophiolitic mélange has been called the Gongpoquan arc-accretionary system (Xiao et al. 2010). Subsequently, the Heiyingshan intraoceanic arc likely developed above a north-dipping subduction zone between the Queershan continental arc and the Gonponquan arc-accretionary system. The Heyingshan arc and the Gonponquan arc-accretionary system collided during the Carboniferous.

By this stage in the development of the Beishan orogen, two subduction zones remained active beneath the Gonponquan system in the south and the Queershan arc in the north. In Xiao et al. (2010) model, the final accretionary events took place in the late Carboniferous to Early Permian, when these two subduction zones consumed the Paleo-Asian Ocean. According to Xiao et al. (2010) and Mao et al. (2012), the Liuyuan Complex formed as a suprasubduction zone ophiolite during the final closure of the Paleo-Asian Ocean. Several Permian mafic and ultramafic complexes (e.g. Han et al. 2006, Xue et al. 2018) are present along the southernmost suture zone of the Beishan Orogen. They were interpreted by Xiao et al. (2010) as late products of subduction related to the final closure of the Paleo Asian Ocean. In this model, the Liuyuan Complex is an ophiolite, and its emplacement records the final accretionary event in the evolution of the Beishan Orogen, and by extension of the CAOB.

In the most recent published review on the tectonics of the Beishan Orogen, He et al. (2018) analyzed a large dataset of 88 U-Pb ages and Hf isotopes and proposed a new tectonic history for the orogen. They reported T_{DM} Hf ages peaks between 2.0-1.8 Ga and 1.0-0.8 Ga and interpreted these data as an indication that all units in the orogen were built on a Precambrian basement. He et al. (2018) proposes a model where all the units that accreted to form the Beishan orogen originally were part of a single Mesoproterozoic continental terrane with affinity to the Baltic craton, which they named the Liuyuan continental terrane (LCU). According to this model, evolution of the Beishan Orogen would have started in the Paleozoic.

According to this model (Fig. 1.3), all the major tectonostratigraphic terranes in the Beishan orogen, except the ophiolitic mélanges, initially formed as part of the LCU, with a Precambrian basement. Subduction along the northern and southern edges of the LCU started between 500-470 Ma. The main oceanic tract between the LCU and the southern Dunhuang block closed by 430 Ma. He et al. (2018) interpret the 465 Ma Gobaoquan eclogite, the presence of 440-424 Ma adakites and 436-433 Ma post tectonic plutonism in both the Dunhuang block and the southern Beishan orogens as evidence for this closure of a major oceanic basin. This closure was followed in the Carboniferous and Permian by major crustal extension within the LCU caused by slab roll-back on a south-dipping subduction zone to the north of the LCU. Therefore, in the model proposed by He et al. (2018), the major ophiolitic mélanges that separate the tectonostratigraphic terranes in the Beishan orogen are vestiges of fore-arc, inter-arc, or back-arc basins (Fig. 1.4). The authors accept the interpretation of Wang et al. (2017) that the Liuyuan Complex formed as an intracontinental rift. This rifting took place after the closure of the main tract of the Paleo-Asian Ocean, which in their model took place before 430 Ma. The hypothesis the Beishan orogen was a “retreating” orogen during the Permian is supported by the isotopic data presented by He et al. (2018), where the εHf(t) values of Permian granitoids are higher than early Paleozoic granitoids, suggesting a depleted astenospheric contribution which the authors interpreted as evidence for a rift setting.

1.3 The Liuyuan Complex

Located along the southern edge of the Beishan Orogen, the Liuyuan Complex occurs at the contact between the Cambrian-Silurian Shuangyingshan-Huaniushan arc and the Devonian-Permian Shibanshan arc, the southernmost tectonostratigraphic units in this Orogen (Mao et al. 2010). With an exposed length of approximately 90 Km, and a maximum exposed width of 9 Km, the Liuyuan Complex consists mainly of basalts, typically showing pillow structures, intercalated with pelagic sediments, together with subordinate plutonic facies. However, the overall distribution of rock facies in the Liuyuan Complex and their genetic relationships are poorly constrained, as is their inferred tectonic setting.

In the context of the regional-scale interpretations of the CAOB, the Liuyuan Complex plays an important role. Many authors have worked on the Liuyuan Complex in the past three decades, with several competing models being proposed. Most of that work is published in Chinese, typically only with an English abstract (e.g. Jiang et al. 2007). A summary of the work available in English is presented here. Zuo et al. (1991), Jian et al. (2007), Su et al. (2011), and Wang et al. (2017) proposed the Liuyuan Complex formed as a continental rift complex, likely related with the impingement of the Tarim Plume or with slab roll-back (He et al. 2018). Meanwhile, Mao et al. (2010), Xiao et al. (2010), and Mao et al. (2012) proposed the Complex is a suprasubduction zone (SSZ) ophiolite. The most recent studies focused on the Liuyuan Complex were published by Mao et al. (2012) and Wang et al. (2017), and they defended the SSZ ophiolite and rift models, respectively.

The distribution and significance of lithologies in the Liuyuan Complex remain debated and poorly understood. Jiang at al. (2007) describes the Liuyuan Complex as a belt of alkaline to transitional trachybasalts with MORB affinity. These trachybasalts are LREE-depleted, and have εNd values between 10.14 and 10.89, and are interpreted to have formed as product of decompression melting of asthenospheric mantle in the stability field of spinel peridotite during an episode of continental rifting. In contrast, Xiao et al. (2010) interpret the Liuyuan Complex as an ophiolitic mélange belt, incorporating tectonic slices of ophiolitic and active continental margin rocks, whose geochemistry shows a MORB and island arc tholeiite (IAT) affinity. Given along-strike correlations with other ophiolitic mélanges, they interpreted the Liuyuan Complex as a suture zone that might have been connected to the Solonker Suture.

Mao et al. (2012) focused on the Liuyuan Complex, with most of their data collected along highway sections near the town of Liuyuan. They describe the Liuyuan Complex as being composed of ultramafic rocks, olivine gabbro, massive gabbro, massive basalt, pillow basalt, volcaniclastic breccias, chert, tuff, and late hornblende gabbro dykes (Mao et al. 2012). Several instances of gabbro and hornblende gabbro intrusions in the basalts were also described, but the presence of a sheeted dyke complex was not reported. Mao et al. (2012) inferred a suprasubduction setting for the Liuyuan basalts based on the high TiO_2 values, high Th, low Nb-Ta, and their flat REE patterns. Mao et al. (2012) also present radiogenic isotopic data, showing a zircon U-Pb age of 280 Ma for a gabbro, positive εNd(t) values between +6.6 and +9, and a range in initial $^{87}Sr/^{86}Sr$ between 0.7037 and 0.7093. Both the εNd(t) and the initial $^{87}Sr/^{86}Sr$ were calculated for a 280 Ma age. Based on their observation that the Liuyuan Complex is imbricated against Permian tuffaceous sediments and limestone, these authors proposed it formed as an ophiolite in a fore-arc setting.

Most recently, Wang et al. (2017) provided a stratigraphic and geochemical data for several traverses across the Liuyuan Complex and surrounding units, with particular focus on the eastern end of the Complex, where sedimentary rocks are proportionally more abundant. The contact relations between these strata and the igneous rocks of the Liuyuan Complex are disputed. The strata at the eastern region of the Complex were interpreted by Wang et al. (2017) as lacustrine deposits, and detrital zircon ages of 291-285 Ma were reported for these rocks. Wang et al also reported U-Pb ages of 280-277 Ma for dacites and rhyolites associated with the basalts in the Liuyuan Complex. The igneous ages reported by Wang et al. (2017) for the felsic volcanic are consistent with the gabbro age reported by Mao et al. (2012). However, Wang et al. (2017) interprets a plume origin for the basalts, in contrast with the fore-arc interpretation of Mao et al. (2012). Wang et al. (2017) considered the Liuyuan Complex to be a typical example of a rift sequence based on the following observations: a) the lack of any oceanic sedimentary rocks or marine fossils; b) a resemblance between the sedimentary facies on the northern and southern flanks of the Liuyuan Complex; c) the absence of a tectonic contact between the basalts and gabbros within the Liuyuan Complex; and d) the observation that the basaltic dikes from the Complex intrude the granites and gneisses of the Cambrian-Silurian rocks of the Shuangyingshan-Huaniushan arc.

To summarize, the question of whether the Liuyuan Complex formed in rift or a suprasubduction zone is controversial and the answer is of critical importance regarding reconstructions of the tectonic history of the CAOB. This PhD project is an attempt to contribute to this debate.

1.4 Thesis Objectives

Given the importance and poorly understood nature of the Liuyuan Complex for the reconstruction of the final stages of the tectonic evolution of the CAOB, the main goals of this thesis are:

I. identify and map in detail the units that comprise the Liuyuan Complex, with emphasis on the plutonic rocks and their relationship with the dominant overlying basalt;
II. characterize the petrogenesis of the basalts, including mantle source, melting, fractionation conditions, and tectonic environment;
III. characterize the petrogenesis of the plutonic rocks of the Liuyuan Complex, including their cumulate assemblage, trapped melt fraction, and tectonic setting;
IV. provide a new framework for the Permian evolution of the southern CAOB based on the tectonic setting of the Liuyuan Complex and the geology of the surrounding units.

To fulfill these objectives, the work presented in this thesis is heavily based on detailed geological mapping and sampling of the Liuyuan Complex and surrounding units, major and trace element lithogeochemistry, in situ mineral chemistry, and U-Pb zircon geochronology (Sensitive High-Resolution Ion MicroProbe, SHRIMP) of igneous rocks. In addition to the collected data, the conclusions presented here also build on the data available in the literature.

1.5 Thesis Organization

This thesis consists of three journal articles. The first two chapters provide a comprehensive description of the geology and petrology of the basalts and gabbroic rocks of the Liuyuan Complex, with the fourth chapter proposing a new tectonic framework for the southern CAOB. Chapter two consists of a detailed description of the geology of the Liuyuan Complex and petrology of the basalts. The results indicated the Liuyuan Complex represents an ophiolite formed in a fast-spreading back-arc basin. The third chapter is focused on the petrology of the plutonic rocks at the base of the Liuyuan Complex. It concludes the plutonic rocks are comagmatic with the basalts. Based on the conclusions reached in chapters two and three, and on new published results in the units that surround the Liuyuan Complex, a new tectonic framework for the Permian tectonic of the southern edge of the CAOB is presented in chapter four. Given the nature of the publications, some repetition in the introduction, regional geology, and local geology sections is unavoidable. A few modifications were made from the original submitted manuscripts to make the reading of the thesis more fluid and less repetitive. References and supplementary materials for all chapters are presented at the end of the thesis.

1.6 Publication of Chapters and Statement of Contributions

Chapter 4 has been published by Geological Journal. Chapter 2 is in press at the Geological Society of America Bulletin. Chapter 3 is being prepared for publication and will be submitted to the Journal of Petrology. Below is a statement of contributions for the published chapter:

Chapter 2: Santos, G.S., Bédard, J., van Staal, C., Lin, S., Hong, T., Wang, K., 2022. Geology of the Liuyuan Complex, NW China: A Permian back-ac basin ophiolite at the southern edge of the Central Asian orogenic belt. GSA Bulletin, *in press*, DOI:10.1130/B36736.1 Gabriel S. Santos: Investigation, Writing–Original Draft, Writing–Review and Editing. Jean Bédard: Supervision, Investigation, Writing–Review and Editing. Cees R. van Staal: Supervision, Investigation, Writing–Review and Editing. Shoufa Lin: Supervision, Conceptualization, Writing–Review and Editing, Project Administration, Funding Acquisition. Tong Hong: Investigation. Kai Wang: Project Administration, Funding Acquisition.

Chapter 4: Santos, G.S., Hong, T., van Staal, C., Bédard, J., Lin, S., Wang, K., 2022. Permian back-arc basin formation and arc migration in the southern Central Asian Orogenic Belt, Northwest China. Geological Journal, DOI: 10.1002/gj.4609. Gabriel S. Santos: Investigation, Writing–Original Draft, Writing–Review and Editing. Tong Hong: Investigation. Cees R. van Staal: Supervision, Investigation, Writing–Review and Editing. Jean Bédard: Supervision, Investigation, Writing–Review and Editing. Shoufa Lin: Supervision, Conceptualization, Writing–Review & Editing, Project Administration, Funding Acquisition. Kai Wang: Project Administration, Funding Acquisition.

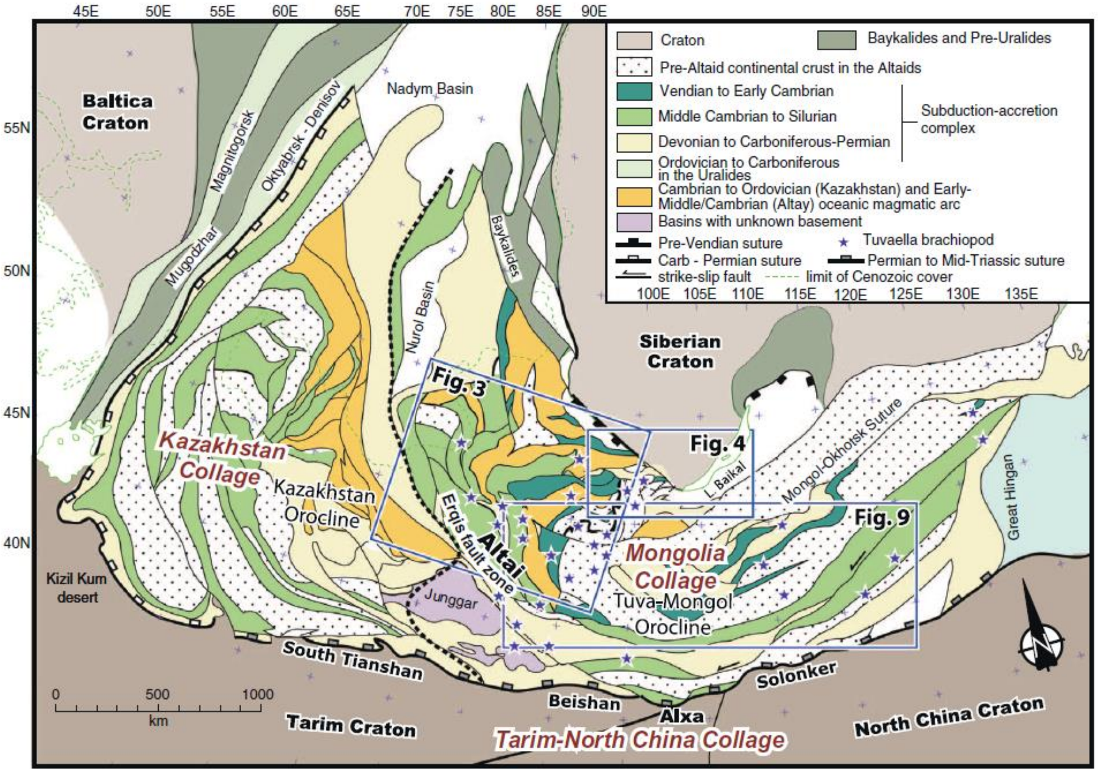

Figure 1.1: General geology of the Central Asian Orogenic Belt (Xiao et al. 2018).

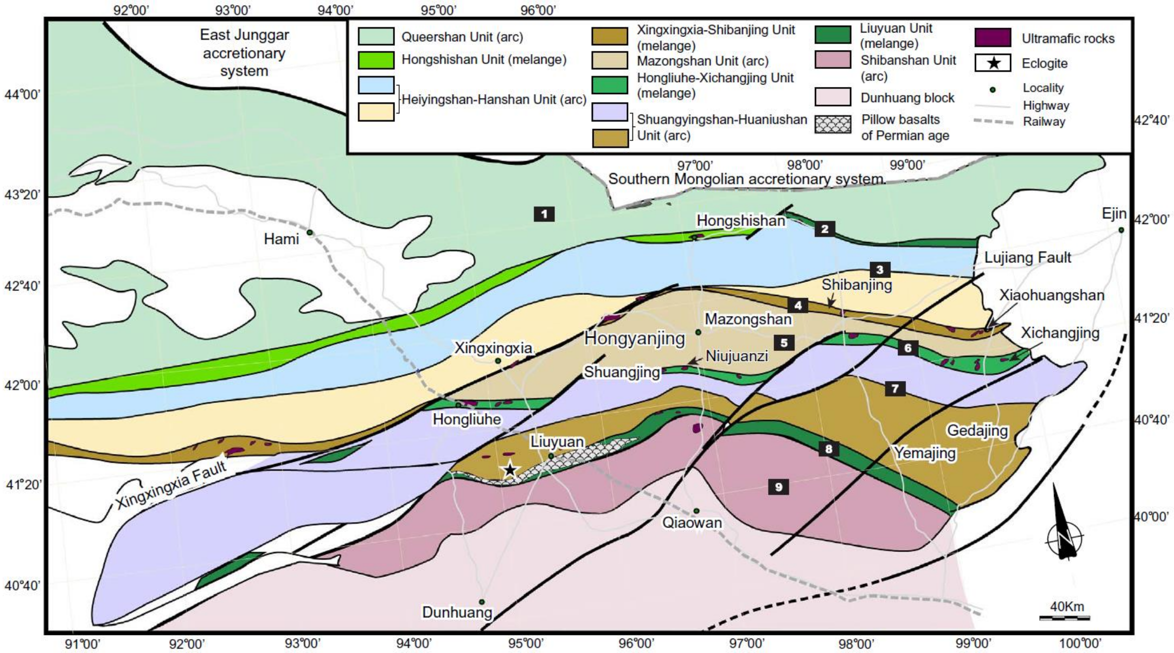

Figure 1.2: Geological context of the Liuyuan Complex in the southern CAOB (Xiao et al. 2018).

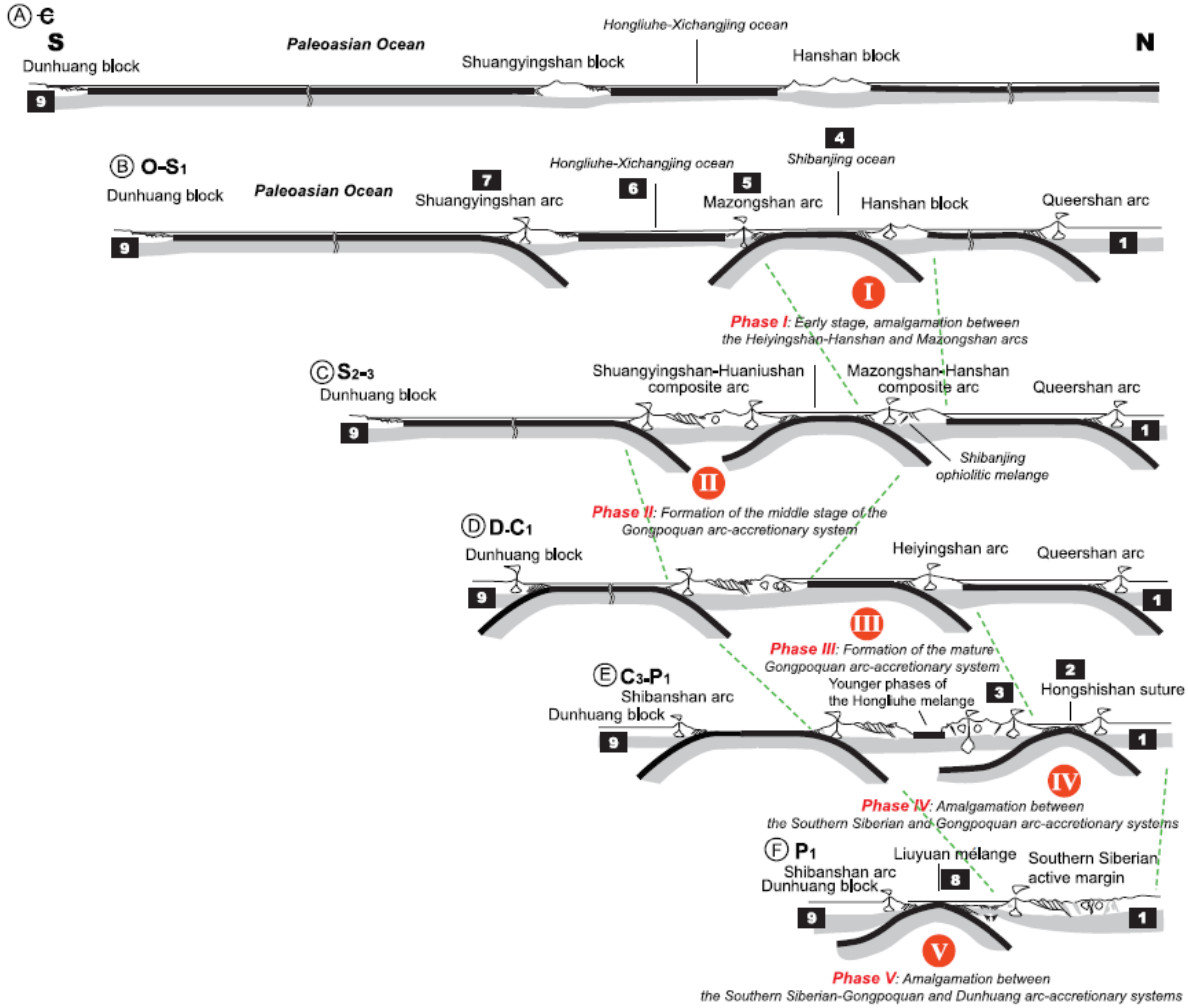

Figure 1.3: Tectonic model proposed by Xiao et al. (2010) for the evolution of the Beishan orogen and the formation of the Liuyuan Complex.

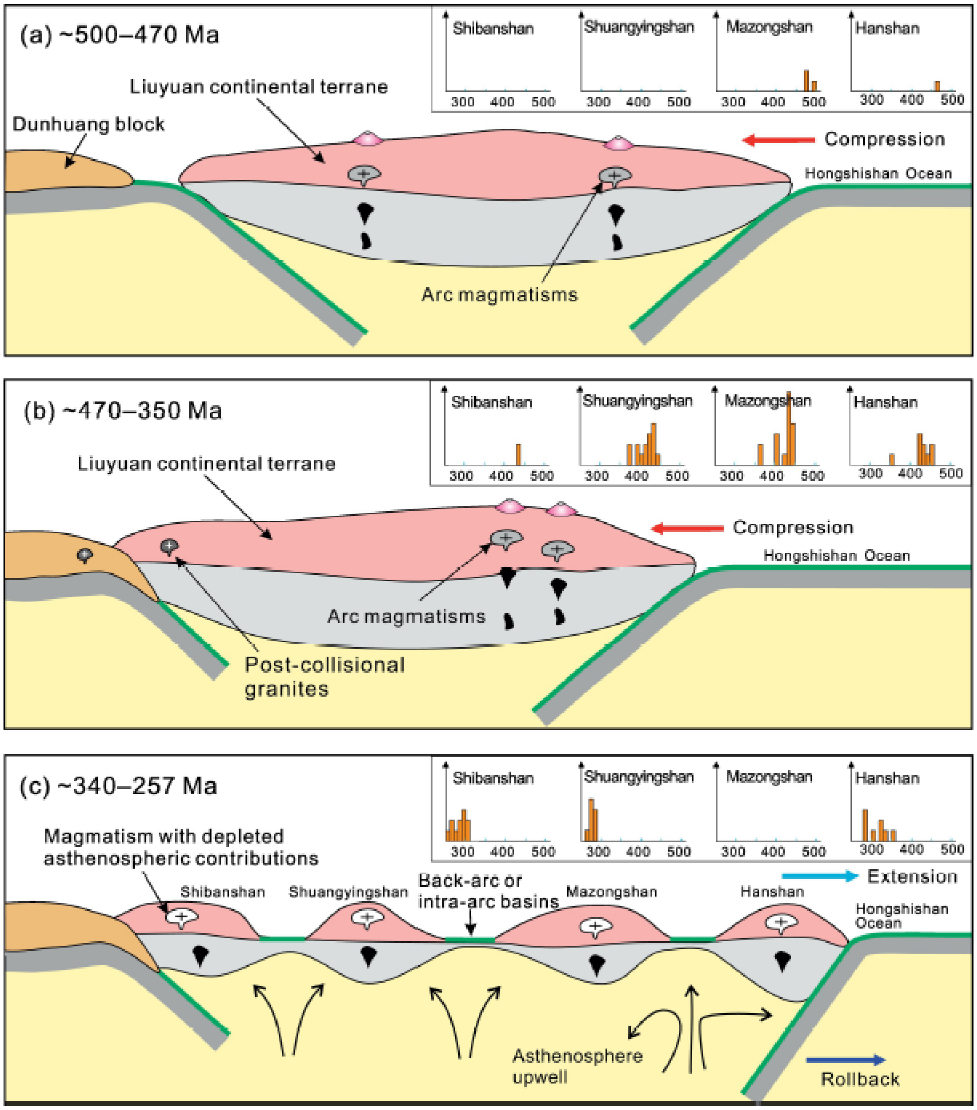

Figure 1.4: Tectonic model proposed by He et al. (2018) for the evolution of the Beishan orogen and the formation of the Liuyuan Complex.

Chapter 2: Geology of the Liuyuan Complex, NW China: a Permian back-arc basin ophiolite at the southern edge of the Central Asian Orogenic Belt

2.1 Introduction

The Central Asian Orogenic Belt (CAOB) is one of the largest and longest-lived accretionary orogens in the geological record (Jahn et al. 2000, Jahn et al. 2004, Yakubchuk et al. 2004, Windley et al. 2007, Zhu et al. 2011, Wilhem et al. 2012, Xiao et al. 2015, Xiao et. al. 2018). It is bounded by the Siberian and Baltic cratons to the north and the Tarim and North China cratons to the south. At the northern margin of the Tarim Craton, the Dunhuang terrane (Xiao et al. 2010, Gan et al. 2021, Shi et al. 2021) is an important and controversial piece in the orogenic architecture of NW China. The relationship between the Tarim Craton, the Dunhuang terrane and the North China Craton remains poorly understood. The Early Permian Liuyuan Complex, located at the southern edge of the CAOB, was involved in the terminal tectonic events during the formation of the CAOB. It is mainly composed of pillow basalts and associated minor chert and dacite beds; but there are locally prominent plutonic cumulate facies (Mao et al. 2012, Wang et al. 2017).

Xiao et al. (2010) proposed a model where the Silurian-Carboniferous CAOB consisted of several intra-oceanic arcs that separated the Siberian Craton to the north and the Dunhuang terrane to the south, with the final collisional event in the orogen taking place in the Permian, when the Paleo-Asian Ocean was finally consumed by a double-vergent subduction zone beneath the southern margin of Composite Siberia and the northern margin of the Dunhuang terrane.

According to Xiao et al. (2010) and Mao et al. (2010, 2012), the Liuyuan Complex is a fore-arc ophiolite that formed during the early stages of this final collisional event, which sutured Composite Siberia and the Dunhuang terrane, completing the assembly of the CAOB. In contrast, Wang et al. (2017) and He et al. (2018) proposed that the different terranes of the southern CAOB were already assembled by the Silurian and interpret the Liuyuan Complex as a layered intrusion with an extrusive cap that formed in an intracontinental rift setting (Zuo et al. 1991, Qin et al. 2011, Su et al. 2011, Wang et al. 2017) that postdated the CAOB assembly by ca. 140 My. Based on an extensive geochronology dataset, Tian and Xiao (2020) proposed the Liuyuan Complex formed as a back-arc basin when slab roll-back on a south dipping subduction zone under the Shibanshan arc of Xiao et al. (2010), causing it to rift and drift away from its Dunhuang Block basement. Resolution of these contrasting hypotheses for the nature of the Liuyuan Complex have major implications for how the Permian evolution of the CAOB is interpreted, especially regarding when and how the Paleo-Asian Ocean closed.

Despite its critical importance for our understanding of the terminal stages of the CAOB assembly, the internal structure and stratigraphy of the Liuyuan Complex remains poorly known. In this paper we present results of detailed new mapping (covering an area of 95 x 30 Km), petrography, geochemistry, and geochronology of the Liuyuan Complex and its bounding terranes with the objective of establishing whether it formed as an ophiolite or in a rift environment. We then propose a revised interpretation of the region’s geological history and the final tectonic events in the accretion of the CAOB.

2.2 Regional Geology

The Liuyuan Complex is located between the Shuangyingshan and Shibanshan continental arcs of Xiao et al. (2010) and He et al. (2018) (Fig 2.1). North of the Liuyuan

Complex, the Shuanyingshan arc terrane comprises Paleozoic clastic rocks and carbonates (Xiao et al. 2010, Li 2019), associated with Ordovician to Devonian volcanic rocks (He et al. 2018). Granitoids range in age from Neoproterozoic to Mesozoic (Xiao et al. 2010). Mesoproterozoic to Neoproterozoic metamorphic basement in the region west of the town of Liuyuan has been identified and mapped in detail by de Vries (2022). To the south of the Liuyuan complex are rocks assigned to the Shibanshan continental arc suite (e.g. Xiao et al. 2010 and He et al. 2018). The arc was supposedly built on the northern margin of the Dunhuang terrane during southward subduction between the Carboniferous and the Permian, which was followed by southward imbrication and telescoping of parautochtonous units during the final CAOB collision, as the Liuyuan complex was thrust onto the Dunhuang terrane margin. However, recent detailed geological investigations by our group (Li 2019, van Staal et al., 2021, Hong et al. 2022, Chapter 2-5) indicate a more complex tectonic history than previously proposed, and the main results of these parallel studies are summarized here.

On the northern side of the Liuyuan Complex, west of the town of Liuyuan, Li (2019) identified two distinct fault-bounded chaotic sedimentary units unconformably overlain by an imbricated and folded turbidite unit (Fig. 2.1). Li (2019) interpreted the chaotic units as syn-tectonic deposits formed in a forearc basin (the Liuyuan forearc basin) developed on the upper plate during the final accretion events associated with the CAOB. The chaotic sedimentary units comprise graded, poorly sorted arenite, conglomerate and shale, which locally are transformed into a mélange with exotic clasts and knockers of basalt in the structurally lower chaotic unit. The upper chaotic unit also contains boulders of porphyritic rhyolite, which are absent in the structurally lower unit. The basalt knockers are interpreted to be derived from the adjacent Liuyuan Complex, which structurally underlies both chaotic sedimentary units. Minor porphyritic rhyolite and ash beds are interlayered in the turbiditic sedimentary rocks, and yielded U-Pb zircon ages (SHRIMP) between 282 and 279 Ma (Li, 2019).

To the south of the Liuyuan Complex, referred to by previous authors as the Shibanshan arc (e.g. Xiao et al. 2010 and He et al. 2018), van Staal et al. (2021) identified two major litho-tectonic units: the Ganquan and the Baidunzi Complexes (Fig. 2.1). The Ganquan Complex comprises at least two major units (lower Ganquan Complex and the upper Ganquan Complex), which are everywhere in tectonic contact with each other. The lower Ganquan Complex mainly comprises felsic rhyolite and rhyodacite crystal and lithic tuff, locally intruded by porphyritic intrusions, which yielded Samarkian to Artinskian SHRIMP U-Pb zircon ages between 297 and 285 Ma. The lower Ganquan Complex is locally unconformably overlain by fluvial red arenite, conglomerate, shale, and interlayered minor white and light green tuff. The tuff and ash beds in this unconformable subaerial cover yielded Kungurian SHRIMP U-Pb zircon ages between 283 and 281 Ma (van Staal et al. 2021). The upper Ganquan Complex comprises marine dark grey shale and arenite interlayered with voluminous Kungurian felsic ash beds and rhyolite tuff. The felsic ash beds and the rhyolite tuff yielded Kungarian SHRIMP U-Pb age of ca. 282 Ma (van Staal et al. 2021). These pyroclastic felsic rocks correlate both in geochemistry and in age with the tuff beds interlayered with the subaerial cover sequence that unconformably overlies the lower Ganquan Complex. The Ganquan Complex was interpreted by van Staal et al. (2021) as a juvenile oceanic volcanic arc.

The Baidunzi Complex to the south is a large, syn-tectonic mafic to felsic intrusive suite ranging from diorite to granite, which commonly displays intense deformation, interlayered with marble, quartzite and wacke (van Staal et al. 2021). Lithologies in the Baidunzi Complex include hornblende gabbro, diorite, tonalite, granodiorite and granite. SHRIMP U-Pb ages for these plutonic rocks range between 295 Ma and 291 Ma (van Staal et al. 2021), with younger cross-cutting intrusions generally being more felsic than the older phases. These deformed plutonic rocks were previously interpreted (e.g. Xiao et al. 2010 and He et al. 2018) to comprise the basement of the Shibanshan arc. A large extensive and linear sheet of 285-281 Ma hornblende gabbro stitches the structural contact between the Kungurian lower Ganquan and the Baidunzi Complexes. This hornblende gabbro is absent in the Samarkian to Artinskian upper Ganquan Complex (van Staal et al. 2021), consistent with the two related units of the Ganquan Complex forming adjacent, rather than above each other.

South of the Baidunzi Complex, the Dunhuang terrane mainly consists of TTG and TTG-like orthogneisses, mainly formed between 2.7-2.5 Ga (Zhao et al. 2016, Zhao et al. 2019). Subordinate proportions of supracrustal rocks include mica schists, marbles, quartzites, paragneisses and metavolcanics (Zhao et al. 2016). The supracrustal rocks were mainly formed between 2.0 -1.83 Ga as a passive margin sequence (Zhao et al. 2019) and were affected by 1.83 – 1.80 Ga and 440-315 Ma metamorphic events (Zhao et al. 2019). Granitoids with arc-like geochemical signature are widespread in the Dunhuang terrane, with ages between 440-410 Ma and 375-360 Ma. The Dunhuang terrane may have acted as the backstop in the final closure of the Paleo-Asian Ocean, although the geology, timing, and significance of specific tectonic and magmatic events remain controversial (e.g. Xiao et al. 2021, Zhao et al. 2016, He et al. 2018, Zhao et al. 2019).

2.3 Geology of the Liuyuan Complex

The Liuyuan Complex has a preserved length of approximately 90 km, with a structural thickness of up to 9 km. Previous maps of the Liuyuan Complex show a voluminous basalt unit, but mapping identified bodies of mafic and ultramafic cumulate rocks that were investigated for their Ni potential and tentatively interpreted as a continental layered intrusion. Mao et al. (2012) identified gabbroic rocks, but their outcrops were widely dispersed. The studies of Mao et al. (2012) and Wang et al. (2017) were mainly restricted to road-accessible outcrops, and lacked the level of details required for stratigraphic and tectonic interpretations. We mapped the Liuyuan Complex in detail during the summers of 2018 and 2019 (Fig. 2.2). Our mapping has identified a variety of plutonic (troctolite, melatroctolite, layered gabbro, olivine gabbro, varitextured olivine gabbro, hornblende gabbro, plagiogranites, and sheeted dyke) and mafic tectonite (southern thrust-related mylonite complex) facies in addition to the previously studied basalts and cherts. The lower gabbroic plutonic rocks in the Liuyuan Complex are separated from the volumetrically dominant upper basalts by a well-developed sheeted dyke complex. All identified contacts between igneous facies are intrusive, with the southern thrust-mylonite complex solely formed within the upper basalts.

2.3.1 Lower Gabbroic Rocks

The thickness of the entire exposed lower gabbroic sequence ranges between 1.5 and 2.5 km. The lowermost unit of the Liuyuan Complex is a fine- to medium-grained troctolite (Fig. 2.3a, 2.3b) containing euhedral (cumulate) plagioclase and olivine (both commonly fresh), with minor amounts of interstitial clinopyroxene. The troctolite typically displays a weak magmatic foliation defined by aligned euhedral plagioclase grains. Clinopyroxene grains locally form oikocrysts reaching up to 5 cm in diameter, with predominantly olivine and rare plagioclase chadacrysts. The lower troctolite cumulate contains isolated layers of a dark, medium- to coarse-grained massive melatroctolite (Fig. 2.3c). The contact between the melatroctolite and the surrounding troctolite is gradational. Individual melatroctolite layers are approximately 5 m wide and laterally discontinuous, with maximum observed length in the order of tens of meters.

Centimeter-scale clinopyroxene oikocrysts (Fig. 2.3d) are locally abundant in this unit, changing the melatroctolite to an olivine melanogabbro. Plagioclase and olivine show intense saussurite alteration and serpentinization respectively, with fresh grains only preserved as chadacrysts. Interstitial hornblende, displaying well developed magmatic zoning locally reaches up to 5 modal % of these melanocratic intrusions. Hornblende was not observed in the underlying troctolite or in the overlying varitextured olivine gabbro. In these lower gabbroic rocks, groundmass olivine is only locally replaced by serpentine and chlorite. Alteration generally increases upwards in this sequence. Olivine chadacrysts are pristine (Fig. 2.3d), showing little to no alteration. In the lower troctolites, the dihedral angle between plagioclase and olivine grains in the groundmass typically approximates 60 degrees (Fig. 2.3b), suggesting that high temperature grain boundary migration and adjustments were widespread, although these textural metamorphic effects were not related to a regional high temperature metamorphism, which is instead characterized by heterogeneous greenschist facies conditions preferentially preserved in tectonised rocks.

The contact between the lower cumulate and the varitextured olivine gabbro is gradational, marked by a progressive increase in modal clinopyroxene (reaching up to 35% of the varitextured olivine gabbro) and a change from cumulate to non-cumulate textures. At the eastern edge of this contact, the troctolite and varitextured olivine gabbro are separated by an approximately 50 m thick sequence of rhythmically layered cumulates (Fig. 2.3e). Individual layers are graded, and range between 2 and 10 cm in thickness. The composition of individual layers ranges from anorthosite to olivine melanogabbro, becoming more olivine-poor and clinopyroxene-rich towards the top of the layered sequence. The layered rocks have euhedral plagioclase and olivine, and interstitial clinopyroxene, locally forming subophitic textures.

The varitextured olivine gabbro (Fig. 2.3f) is predominantly medium-grained, and textures include equigranular, interstitial, ophitic, and subophitic. Clinopyroxene and rare orthopyroxene are interstitial minerals (Fig. 2.3g). Locally gabbroic pegmatites are present (Fig. 2.3h). The upper part of the varitextured gabbro is intruded by several medium- to fine-grained hornblende gabbro (Fig. 2.4a) dykes. These dykes are subvertical, with strikes between 110-140^{o}. The hornblende gabbro is typically fine grained, showing a cumulate plagioclase framework with interstitial hornblende and clinopyroxene. The contact between these intrusions and the host gabbro is typically irregular. The varitextured olivine gabbro (and to a smaller extent the underlying troctolite) is intruded by leucotonalite and plagiogranite and diabase dykes, locally forming meter-scale composite dyke swarms (Fig. 2.4b, 2.4c) and net-vein complexes, commonly with hornblende-rich selvedges. Within individual composite dykes, the order of intrusion is variable, with both diabase intruding plagiogranite and vice-versa, suggesting they are coeval. Locally, plagiogranite intrusions form the matrix of magmatic breccias (Fig. 2.4d) that contain rounded diabase clasts up to half a meter in diameter, and a few angular medium-grained varitextured gabbro and hornblende gabbro clasts. Diabase and plagiogranite commonly have serrated, lobate contacts suggestive of liquid-liquid interfaces (e.g. Wiebe 1987, Wiebe 1994, Wiebe et al. 2004). This morphology suggests plagiogranite intrusion took place while the mafic lithologies were not fully solidified. Serpentinization of olivine in the varitextured gabbro is widespread.

Epidote veins are widespread in the lower gabbroic rocks, and the described greenschist facies metamorphism is more intense along or near faults, which were conduits of fluids. This suggests metamorphism in these gabbros was controlled by percolation of hydrothermal fluids along these faults into the lower oceanic crust. The petrology of the gabbroic rocks and plagiogranite are beyond the scope of this chapter and will be the subject of separate publications.

2.3.2 Sheeted Dyke Complex

The upper section of the Liuyuan Complex comprises well preserved exposures of sheeted dykes (Fig. 2.4e, 2.4f) and basalt. The sheeted dyke complex was mapped over the entire contact between the lower gabbroic rocks and the overlying basalts, and ranges in thickness from a few to more than 100 meters. The sheeted dykes are offset by NNE striking faults with sinistral kinematics. These faults offset the sheeted dykes by up to 500 meters and typically have a length between 1500-2000 meters. Displacement along these faults is restricted to the upper section of the gabbroic rocks and the lower section of the basalts. They do not produce major offsets in the stratigraphy of the Liuyuan Complex nor form any contact between different magmatic facies. The sheeted dyke complex is thicker where these faults form negative flower structures, implying they acted as conduits for magma transport. In most places, individual dykes are 0.5 to 2 m thick, with chilled margins ranging from sharp to slightly irregular (Fig. 2.4g). Locally, intrusive contacts are reworked by small-scale fault brecciation coeval with subseafloor hydrothermal circulation, as indicated by the presence of epidote in the breccia matrix and as cm-thick veins. Rocks in the sheeted dyke complex range from aphyric diabase to porphyritic diabase with up to 15% of 2 mm-long euhedral plagioclase phenocrysts. Minor olivine is also present in the porphyritic diabase. Diabase dykes commonly coarsen inward to microgabbro. The porphyritic diabase provides an excellent field marker for the sheeted dykes in the Liuyuan Complex. Metamorphism in the sheeted dyke complex ranges from sub-greenschist to amphibolite facies, with grade systematically increasing with depth, peaking at the contact between the sheeted dykes and the lower gabbro. The resulting metadiabase is composed of hornblende and plagioclase (Fig. 2.4h), locally displaying granoblastic textures. This is the highest-grade metamorphic rock observed in the Liuyuan Complex.

2.3.3 Basalt and Associated Chert and Dacites

Basaltic pillow lavas (Fig. 2.5a, 2.5b), lava tubes, massive flows and hyaloclastite dominate the stratigraphy above the sheeted dykes. The southward-younging directions deduced from pillows and lava tubes are consistent throughout the Liuyuan Complex. Locally, jasper (Fig. 2.5c) and grey-to-white chert fill inter-pillow interstices. The basalts form approximately 90% of the outcrop of the Liuyuan Complex. The basalts typically show a hypohaline to porphyritic texture. Vesicles and amygdales are widespread. Spherulitic texture is ubiquitous along the edge of individual basalt pillows (Fig. 2.5d). Euhedral olivine (up to 10%) (Fig. 2.5d) and plagioclase (up to 15%) phenocrysts (locally glomerocrysts), typically displaying belt-buckle and swallowtail (Fig. 2.5e) morphology, are present in the basalts. Rare clinopyroxene glomerocrysts (Fig. 2.5f) were also observed. Ilmenite is present as an accessory phase, but in a small proportion of collected samples can form up to 5% of the basalts (Fig. 2.5g). Chlorite typically forms olivine pseudomorphs, and the groundmass of the basalt is replaced by chlorite, epidote, fine-grained phyllosilicates, and locally tremolite, indicating greenschist facies metamorphism (Fig. 2.5h). A few E-W striking gabbro dikes, approximately 1 m wide, intruded the basalts. The basalts are also intruded by an approximately 800 x 250 m large fine-grained leucotonalite, emplaced along a fault. Higher in the stratigraphy, centimeter- to decimeter-scale beds of dacite, dark shale, and chert (Fig. 2.6a) (5-40 cm thick) appear. The chert beds locally contain small, euhedral plagioclase phenoclasts (Fig. 2.6b), suggesting deposition took place near active volcanism.

The upper sequence of basalt, chert and dacites of the Liuyuan Complex is unconformably overlain by decimeter- to meter-thick bodies of dacites and dacitic banded crystal tuffs (Fig. 2.6c). The banded crystal tuffs were formed subaerially, indicating their deposition took place over an already obducted and exhumed Liuyuan Complex. van Staal et al. (2021) reported SHRUIMP U-Pb ages of 276 Ma and 267 Ma for these rocks. The contact between these dacites and the underlying volcanic sequence is defined by an oligomictic pebble orthoconglomerate (Fig. 2.6d), with both basalt and chert clasts.

2.3.4 Lower Thrust Mylonite

An approximately 1 km thick E-W striking thrust, defined by a phyllonite complex, is present within the basalts of the Liuyuan Complex. The mafic phyllonite in the thrust zone (Fig. 2.6e) is very fine- to fine-grained and shows a strong continuous foliation defined by nematoblastic actinolite and chlorite. The metamorphic assemblage indicates deformation occurred under greenschist facies conditions. Remnants of sheared basalt pillows in this shear zone suggests deformation was preferentially partitioned into the softer interpillow material (Fig. 2.6f), creating anastomosing zones of enhanced strain. In areas of higher strain, the basalt pillows are completely overprinted by the mylonitic foliation. This shear zone also contains a pronounced NW plunging mineral stretching lineation, defined by actinolite and chlorite aggregates. Combined with the presence of asymmetric basalt pillows and S-C fabrics, a top to SE sense of movement is deduced. This sense of movement is consistent with the overall southward thrusting identified in the regional geology of the Liuyuan Complex (Li 2019, van Staal et al. 2021), suggesting this mylonite formed during and/or after obduction, and not by shearing along the seafloor. The stratigraphy of the Liuyuan Complex is summarized in Fig. 2.7.

2.4 Geochemistry

A total of 68 samples of basalts and diabase dykes from the sheeted dyke complex and 6 cherts were analyzed. Thin sections were made at the Heibei Geology and Mineral Resources Bureau's Langfang Laboratory. For analysis, about 1 kg of material was crushed until ≥ 70% would pass a 2 mm sieve. Then, 250 g of the crushed material was pulverized until ≥ 85% would pass a 75 µm sieve. Pulverized samples were analyzed for major and trace elements, including rare earth elements (REE), by inductively coupled plasma – atomic emission spectroscopy (ICP-AES) and inductively coupled plasma – mass spectrometry (ICP-MS) at ALS Chemex in Vancouver, Canada. The pulverized samples were mixed with a lithium borate flux and heated to 1000 ^{o}C in an inert crucible. The resulting homogeneous fusion product was digested in an aqua regia solution prior to ICP analysis. For quality assurance and control, several samples ran as pulp duplicates and international standards were analyzed. Blanks were also prepared. No problems were detected with the analytical results. The blanks were good, and the largest variation in observed in the analyzed sample duplicates and in the measured standards was 5%. All chemical data and sample coordinates are provided in the Appendix A1.

For data presentation and analysis, major element oxides were recalculated using FeO-total instead of Fe_2O_3. The lavas from the Liuyuan Complex plot between the fields of basalt and basaltic andesite on the Pearce (1996) discrimination diagram (Fig. 2.8a), and for brevity will be referred to as basalts. Based on their major element geochemistry, the basalts and diabase dykes from the sheeted dyke complex were divided into Group I (low-TiO_2) and Group II (high-TiO_2). Group I is the largest in the dataset, containing 63 of the 68 samples, followed by Group II, with 5 of the 68 samples. All samples from the sheeted dyke diabase fall in Group I, and will be discussed together. Most of the basalts of the Liuyuan Complex are calc-alkaline, with only 19 of the 68 collected samples plotting as tholeiites.

2.4.1 Major Elements

The major element trends of both Group I and II broadly overlap, with the largest difference observed in TiO_2 concentrations. These trends tend to be scattered, likely an effect of greenschist facies metamorphism and widespread hydrothermal alteration observed in the basalts of the Liuyuan Complex. For this reason, a lager focus was placed in immobile elements in the following descriptions and discussions. MgO and SiO_2 values for both groups overlap, respectively ranging between 45.75-52.76 wt% and 9.82-2.82 wt%. Two samples with high silica show unusually high alteration, characterized by quartz and calcite veins. Another highly altered sample has a lower (0.94 wt%) MgO concentration. FeO (Fig. 2.8b) concentration in both Groups inversely correlates with MgO, peaking at approximately 12.5 wt% at 4 wt% MgO. Group II basalts on average have the lowest MgO and the highest FeO concentrations measured in the Liuyuan Complex samples.

Group II basalts have the highest TiO_2 in the dataset (Fig. 2.8c), between 3.37-3.65 wt%, compared to the 1.41-2.44 wt% range observed in Group I samples with similar MgO contents. They also have consistently lower Al_2O_3 (Fig. 2.8d) than Group I. A higher concentration of ilmenite was observed in thin sections from Group II samples (Fig. 2.5g), consistent with the higher TiO_2 measured in these rocks. Groups I and II show an overlap in CaO and Na_2O, with oxides showing considerable scatter when plotted against MgO. CaO is the most scattered oxide when plotted against MgO, with a difference of up to 8 wt% at similar MgO values. CaO values in the dataset range between 3.35 and 12.96 wt%.

All the samples collected from the sheeted dyke complex fall within Group I. These samples span the entire range in major elements displayed by this group, but with one exception skew towards higher MgO values. Overall, the major element variations in the basalt and the diabase of the Liuyuan Complex suggest fractionation of olivine, plagioclase, and clinopyroxene. This is consistent with field and petrographic observations, where these three minerals were observed as phenocrysts in the basalts, with Group II samples possibly having the accumulation of ilmenite as an additional component.

2.4.2 Trace Elements

All samples from the Liuyuan Complex show broadly similar trace element patterns when normalized to the NMORB of Sun and McDonough (1989). They are enriched in the LILE, consistently displaying positive Ba, Cs and Rb anomalies and negative K anomalies. A prominent feature of the samples is the positive Th and negative Nb anomalies. Group I basalts (Fig. 2.9a) typically show a moderate enrichment to slight depletion in the light-REE (LREE) (La/Sm of 0.88-1.48), slight negative Eu anomalies (Eu/Eu^* of 1.00-0.82) and enriched medium-REE (MREE) relative to heavy-REE (Sm/Yb 1.38-1.99). Group I diabases (Fig. 2.9b), in contrast, have a flat to depleted LREE profile (La/Sm of 1.05-0.77) and larger Eu anomalies (Eu/Eu^* of 1.29-0.61), with a HREE profile similar to the basalts. The samples with higher total REE within this group show LREE to MREE pattern becoming progressively flatter to slightly enriched, with increasingly larger negative Eu anomalies. This systematic variation present in Group I is not present in Group II (Fig. 2.9c). Group II samples display a tighter REE pattern, with small range in LREE enrichment (La/Sm of 0.92-1.24), slight negative Eu anomalies (Eu/Eu^* of 0.78-0.90), a slightly enriched to flat MREE to HREE pattern (Sm/Yb of 1.18-1.55).

The characteristic high Ti of Group II lavas is also evident in the NMORB-normalized plot (Sun and McDonough, 1989).

2.4.5 Cherts

On the discrimination diagrams of Murray (1994), the cherts from the Liuyuan Complex consistently plot in the field of continental margin cherts (Fig 2.10a). On the ternary classification diagram of Adachi (1986), they plot in the non-hydrothermal field (Fig. 2.10b). Silica in these cherts range between 74.84 wt% to 89.15 wt%, with an average of 80.15 wt%. When normalized to Post-Archean Australian Shale (PAAS) (McLennan 1989), these cherts show an enrichment of the MREE and HREE when compared to the LREE (average Pr_{SN}/Yb_{SN} of 0.74). The MREE and HREE show a flat pattern (average Sm_{SN}/Yb_{SN} of 0.98) (Fig. 2.10c).

The cherts display slightly negative cerium anomalies, with Ce/Ce^{*} (SN) ranging between 0.89 and 1, averaging 0.95. Europium anomalies range from weakly positive to strongly negative, with Eu/Eu^{*} (SN) ranging from 1.09 to 0.53. Y/Ho values show a very narrow range (25.45 to 28.73) with an average of 27.50, very close to the chondritic value of 26 (McDonough and Sun 1995). All REE anomalies were calculated following Planavsky et al. (2010) and Garcia-Solsona et al. (2014).

2.5 Mineral Chemistry

Mineral chemistry data was obtained via a JEOL JXA-830F electron microprobe at the Earth and Planetary Materials Analysis Laboratory at the University of Western Ontario, London, ON, Canada. A beam current of 20 nA at 15 kV was used during the analytical run, with counting times varying between 20 and 40 seconds on peak and background positions. Analytical results are provided in the Appendix A2. Analysis was obtained from plagioclase and clinopyroxene from both Group I basalt and sheeted dyke diabase. Clinopyroxene analysis from the basalts were obtained in glomerocrysts from a single sample, as no other non-altered candidates were available. No fresh olivine grains were observed in thin section.

2.5.1 Plagioclase

Plagioclase compositions range between An_{83-58} in the basalts and An_{67-59} in the sheeted dyke diabase with complete overlap between basalts and diabase analysis. There is no correlation between the MgO (Fig. 2.11a), FeO, K_2O contents with An-content in the samples. Cr_2O_3 content is below detection limit for most samples.

2.5.2 Clinopyroxene

Analyzed clinopyroxene mg# varies between 63-79, with complete overlap between measurements in the basalt and diabase. Clinopyroxene shows a wide variation in incompatible element concentration at similar mg#, with TiO_2 ranging between 0.813-1.656 wt% (Fig. 2.11b) and Na_2O between 0.279-0.405 wt% (Fig. 2.11c). Diabase clinopyroxene has higher TiO_2 concentrations than basalt clinopyroxene, with a broader overlap in Na_2O concentration. Cr_2O3 ranges between 0.053 and 0.432 (Fig 2.11d), with no discernible correlation with grain mg#.

2.6 Discussion

2.6.1 Liuyuan Complex: Ophiolite or Layered Intrusion

The geology of the Liuyuan Complex is contentious. Proposed hypotheses include formation as a forearc ophiolite (e.g. Xiao et al. 2010; Mao et al. 2012); formation as an intrusive-extrusive complex in a continental rift (Wang et al. 2017; He et al. 2018); and formation as a back-arc basin ophiolite (Tian and Xiao, 2020). Our work has revealed igneous facies and an internal stratigraphy which are clearly ophiolitic, with lower cumulate troctolite grading up into varitextured gabbro and then to a well-developed and laterally continuous sheeted dyke complex capped by geochemically similar extrusive volcanic rocks associated with oceanic cherts. The Liuyuan complex preserves a near-complete ophiolite crustal sequence, associated with development of robust, fault guided sub-seafloor hydrothermal systems in its upper part. Taken together, the field relations are much more consistent with an ophiolitic interpretation, than a continental rift sequence. The rare dacites may correspond to the late plagiogranite suite (ca. 275 Ma) that forms dykes within the mafic cumulates, rather than a bimodal volcanic package (Chapter 4).

The sheeted dyke complex is laterally continuous and is present along the entire contact between the underlying gabbro and the overlying basalts. Such continuity suggests that the magma supply along the ridge was near continuous during oceanic spreading (e.g. Robinson 2008). At lower magma budgets more typical of slow spreading ridges, formation of core complexes and deep-rooted normal faults systems are expected (e.g. MacLeod et al. 2009, Tremblay et al. 2009, Manatschal et al. 2011, Tucholke 2008). Although greenschist facies conditions locally prevailed in the shear zones formed during accretion and subsequent tectonic events, most of the metamorphism observed in the Liuyuan Complex represents static mineral replacement, with intensity increasing with proximity to hydrothermal vein systems and associated brittle faults. The fault control of metamorphism in the lower gabbro and the progressive increase in metamorphic grade from greenschist in the basalt peaking at amphibolite at the base of the sheeted dyke complex suggests metamorphism was controlled by the circulation of ocean water at an oceanic spreading center, and not due to tectonically-induced dynamic metamorphism.

2.6.2 Chert Depositional Environment

The geochemistry of marine sediments can be used as a proxy for seawater conditions (e.g. Pufahl and Hiatt 2012). Their major and trace element compositions indicate the cherts of the Liuyuan Complex are not hydrothermal (Adaki 1986) and formed in a distal continental margin setting (Murray 1994). The local presence of angular plagioclase phenoclasts in the cherts further suggests they were deposited coevally with volcanic activity.

Overall, the petrography and geochemistry of the cherts are consistent with their formation in an oceanic basin wide and deep enough to allow the deposition of pelagic sediments, but close enough to active volcanism to contain volcanic phenoclasts. The negative Pr_{SN}/Yb_{SN} values and Sm_{SN}/Yb_{SN}, close to unity are consistent with their origin as oceanic sediments, and not hydrothermal alteration (e.g. Bolhar et al. 2004). The presence of flat to slightly negative Ce anomalies suggests these cherts were deposited in suboxic or anoxic waters (German and Elderfield 1990, German et al. 1991, Byrne and Sholkovitz 1996). In oxic waters, negative Ce anomalies are caused by the oxidation of Ce^{3+}, which reduces its solubility and results in the scavenging of Ce by Mn-Fe hydroxides and clay particles. This Ce shuttle does not operate in anoxic to suboxic waters. The strong continental influence is corroborated by their chondritic Y/Ho ratio and negative Eu anomalies, likely inherited from continental sources.

2.6.3 Magmatic Evolution as Recorded by Basalts and Sheeted Dyke Complex

The geology and stratigraphy of the Liuyuan Complex suggests it formed as an ophiolite. If so, the evolution of the basalts should have taken place in conditions similar to an oceanic spreading center. To test this hypothesis, a model liquid line of descent (LLD) was calculated for the basaltic suite of the Liuyuan Complex using the thermodynamic modelling software MELTS 1.2.0 (Gualda et al. 2012 and Ghiorso and Gualda 2015). The chosen parental melt for the model was sample 19LYS-7182B, with SiO_2 of 46.78 wt%, MgO of 9.58 wt%, mg# of 67.72, CaO of 12.96 wt%, 176 ppm of Ni, and 33 ppm of Sc. The variolitic texture and lack of phenocrysts observed in thin section combined with the relatively high mg#, and low CaO, Ni, and Sc suggests this sample is close to a primitive quenched liquid, minimally affected by crystal fractionation. FeO and Fe_2O_3 were redistributed and the liquidus temperature were calculated assuming $_fO_2$ was set at the QFM buffer.

Melt fractionation started with 0.5 wt% of H_2O at a liquidus temperature of 1206 ^{o}C, with pressure held at 1 kbar, corresponding to plausible differentiation depths for an ocean ridge-related melt (e.g. White and Klein, 2014). Olivine (Fo_{85}) and plagioclase (An_{87}) saturates at 1201 ^{o}C at a melt fraction (F) of 0.97 and liquid MgO of 9.5 wt%. Clinopyroxene saturates at lower temperatures (1186 ^{o}C, MgO = 9 wt%, An_{85}, $Fo_{84,}$ F of 0.82) and ilmenite at 1090 ^{o}C (MgO = 5 wt%, Fo_{68}, An_{76}, F of 0.35). The corresponding cumulate starts as leucocratic troctolite, evolving into troctolite and olivine gabbro when clinopyroxene reaches the solidus. The olivine gabbro consists of 50-57% plagioclase, 20-25% clinopyroxene and 19-23% olivine. These proportions are consistent with the gabbroic lithologies observed at the base of the Liuyuan Complex. On the Harker plot shown in Fig 8e, Ni concentrations show a positive correlation with MgO, consistent with the early fractionation of olivine predicted by the MELTS model. In Fig. 8f, Sc shows an early increase as MgO decreases, peaking at approximately 8.75 wt% MgO, and decreasing thereafter with lower MgO, the peak identifying the onset of clinopyroxene crystallization at similar MgO concentration in the liquid predicted by the model LLD. The Fe/Mg (molar) values of the liquids in equilibrium with the analyzed clinopyroxene grains was calculated using Eq. 11 from Bédard (2010). The recorded ratio ranges between 1.42 and 4.04, well within the 0.42-4.19 value for the sampled basalts and the 0.40 – 4.37 values of the model melt. The large variation in the concentration of incompatible elements in clinopyroxene at constant mg# suggests crystal-melt reactions played an important role in the crystal mush these rocks formed from. The sampling of such a mush is also consistent with the presence of clinopyroxene glomerocrysts in the basalt (Fig. 2.5f). The initial fractionation of olivine and plagioclase followed by clinopyroxene is consistent with the mineralogy observed in gabbroic rocks of the Liuyuan Complex and would be typical of an oceanic ridge (e.g. Coogan 2014, White and Klein, 2014).

Molar element ratio (MER) diagrams (Stanley 2017) were used to further evaluate and illustrate the differentiation of these basalts. On (Ca+Na)/(Si+Al) (molar) vs. (Fe+Mg)/(Si+Al) (molar) diagram (Fig. 2.12a), the lavas from the Liuyuan Complex form a coherent array that plots in a polygon defined by plagioclase, clinopyroxene, and olivine, closer to the plagioclase node. Addition or subtraction of any mineral component would displace whole rock compositions towards and away from the mineral node, respectively. Except for the three most differentiated samples, all lavas plot within the polygon defined by plagioclase, olivine, and clinopyroxene, suggesting negligible influence of orthopyroxene in the differentiation of the suite. Note that the sample differentiation trend clusters closer to the plagioclase than the olivine node, suggesting that plagioclase was the dominant fractionating mineral. This interpretation is consistent with petrographic observations and thermodynamic model results. The Ca/Si (molar) vs. Mg/Si (molar) diagram (Fig. 2.12b) allows us to compare the mineralogy predicted by the calculated LLD with the whole rock data. Olivine compositions plot along the abscissa and plagioclase compositions along the ordinate, with clinopyroxene showing mode complex behavior depending on composition. Plotted are the range in olivine, plagioclase, and clinopyroxene predicted by the thermodynamic model and the plagioclase and clinopyroxene compositions measured by microprobe. There is a good agreement between predicted and measured compositions. Given the extensive serpentinization of olivine in the basalts, Fe/Mg (molar) values of olivine compositions in equilibrium with each sampled basalt was calculated using the 0.3 Fe/Mg partition coefficient between olivine and basalt (Roeder and Emslie, 1970).

The calculated olivine Fe/Mg (molar) ranges between 0.1281 and 1.25, compared to the 0.1514-2.38 range of the predicted olivine compositions from the thermodynamic model.

The calculated LLD provides a good fit for the dominant Group I basalts, suggesting that low pressure fractionation dominated the differentiation of the Liuyuan Complex. This is consistent with observations and models of basalt fractionation at oceanic settings (e.g. White et al. 2014). Group II basalts have much higher TiO_2 values compared to the other lavas and the modelled LLD. A possible cause is ilmenite accumulation. The possibility of a distinct mantle source will be discussed in the next section.

2.6.4 Petrogenesis

The basalts and diabase of the Liuyuan Complex transition from tholeiite to transitional-calc-alkaline, forming a continuous trend across the distinct magma series, likely reflecting a variable degree of metasomatism in the source peridotite (e.g. Jaques and Green 1980, Gaetani and Grove 1988 Kinzler and Grove 1992, Grove et al. 2003). In the Th/Yb vs. Nb/Yb projection of Pearce (2008), the basalts from the Liuyuan Complex plot above the mantle array (Fig. 13a), between the N-MORB and E-MORB nodes. The data trend is offset from the mantle array at higher Th/Yb, suggesting pre-melt metasomatism of the mantle source by subduction derived fluids, implying the Liuyuan complex spreading ridge formed in a supra-subduction zone (SSZ) environment. Crustal contamination, as could be expected in a continental rift setting, on the other hand would produce a much steeper oblique trend on the Th/Yb vs. Nb/Yb projection (Pearce 2008). The SSZ interpretation is consistent with the $^{87}Sr/^{86}Sr$ values of 0.703662-0.704327 and highly positive $\varepsilon_{Nd(t)}$ between 6.6 and 9 reported by Mao et al. (2012) for these basalts.

The V vs. Ti plot (Fig. 2.13b) of Shervais (1982), modified by Pearce (2014), can be used to further characterize the SSZ signature. On this plot the Liuyuan Complex lavas and sheeted dykes plot in the field of MORB/slab-distal back-arc basin and/or fore-arc basin basalts, with the lavas trending both towards higher V and Ti concentrations (Fig. 2.13b). On this projection, lavas originated in a fore-arc setting generally show a trend evolving from the MORB field through the island arc tholeiite (IAT) field towards the boninite field (Pearce 2014). The presence of boninites in the volcanic sequence is a common fingerprint of fore-arc basin formation (e.g. Bédard 1999, Pearce 2014). None of the samples collected in the Liuyuan Complex plot in the IAT field. In fact, the samples from the Liuyuan Complex evolve away from the IAT and boninite field, a behavior inconsistent with their formation in a subduction initiation setting but consistent with their formation in a back-arc basin. No boninitic rocks have been identified in the Liuyuan Complex by us or other workers who have studied the volcanic sequence. A back-arc basin environment is also consistent with the low Cr_2O_3 and low mg# measured on the analyzed clinopyroxene (e.g. Hebert et al. 2003). In $(La/Nd)_N$ vs. $(La/Sm)_N$ diagram the lavas define an array with higher $(La/Nd)_N$ than MORB and boninites. The array stretches between primitive oceanic arc basalts and back-arc basins with variably metasomatized mantle sources, which further favors their formation in a back-arc environment.

In the TiO_2/Yb vs. Nb/Yb projection of Pearce (2008), the rocks from the Liuyuan Complex plot within the MORB array, indicating melting in the stability field of spinel peridotite (Fig. 2.13c). This interpretation is consistent with the shallow, LREE-depleted REE profiles observed in the basalts. Note the high Nb/Yb values for Group II samples compared to Group I samples is more easily distinguishable in this projection than in the Th/Yb vs. Nb/Yb, suggesting a slightly more enriched mantle source for Group II basalts. The Yb vs. TiO_2 projection of

Gribble et al. (1998) was used to estimate the degree of partial melting that produced the lavas of the Liuyuan Complex (Fig. 2.13d). To avoid the effects of differentiation within the suite, only lavas with mg# higher than 60 were plotted. The five samples that fit the criteria above are all Group I basalts and indicate a degree of partial melting between 10-17% in the stability field of spinel peridotite.

In addition to the large difference in TiO_2 concentrations, Group II lavas also show several trace element variations. When compared with Group I samples with similar degree of differentiation (MgO between 4.05-5.66 wt%), Group II basalts show similar LILE concentrations, higher Nb, lower Th, a lower average La/Sm (1.12 compared to 1.02 for Group I), and higher Sm/Yb (1.68 compared to 1.38 for Group I), with equally flat HREE profiles. The overlap of Group II and this subset of Group I samples in LILE and HFSE suggests they were formed by similar degrees of partial melting. Group II basalts lack a positive Ti anomaly that would be expected by ilmenite accumulation. In both the Th/Yb vs. Nb/Yb and TiO_2/Yb vs. Nb/Yb projections, the data from the Liuyuan Complex spans a wide array of Nb/Yb values suggesting a variably enriched source, with Group II lavas showing higher Nb/Yb and TiO_2/Yb. We suggest the distinct geochemical characteristics of Group II lavas are a result of partial melting from a slightly enriched, higher-Ti mantle source than Group I basalts.

Overall, the trace element signature of the basalts from the Liuyuan Complex indicates they formed from partial melting of a variably enriched previously metasomatized spinel peridotite in a SSZ setting, most likely in a back-arc basin. A back-arc basin setting is inconsistent with the tectonic model of Xiao et al. (2010) and Mao et al. (2012), who propose that the Liuyuan Complex was formed as a fore-arc ophiolite during the final subduction event responsible for closing the Paleo-Asian Ocean and collision of Composite Siberia with the Dunhuang terrane.

2. 7 Conclusion

Located at the southern edge of the CAOB, the Liuyuan Complex stratigraphy and tectonic setting has been controversial for decades and is of key importance for understanding the tectonic history of the CAOB. Our mapping has subdivided the Liuyuan Complex into troctolite, melatroctolite, layered gabbro, olivine gabbro, varitextured olivine gabbro, hornblende gabbro, plagiogranites, and sheeted dyke, in addition to the previously studied basalts and cherts. The lower gabbroic plutonic rocks in the Liuyuan Complex are separated from the volumetrically dominant upper basalts by a well-developed sheeted dyke complex. We demonstrate that the Liuyuan Complex preserves an almost complete oceanic crust stratigraphy, and formed as an ophiolite, not as a continental rift. The presence of a continuous sheeted dyke complex between the lower gabbroic rocks and the basalts suggests the magmatic supply kept up with oceanic spreading, a feature typical of fast-spreading ridges. The trace element signature of the lavas indicates they formed in a back-arc basin, from 10-17% melting of a variably enriched previously metasomatized spinel peridotite. Their liquid line of descent, constrained by whole rock chemistry, mineral chemistry and thermodynamic modelling indicated they fractionated olivine + plagioclase + clinopyroxene + ilmenite, in conditions consistent with an oceanic spreading ridge. Trace element fingerprinting of the basalt and diabase further indicates the Liuyuan Complex formed not as a continental rift or a fore-arc ophiolite, but as a back-arc basin.

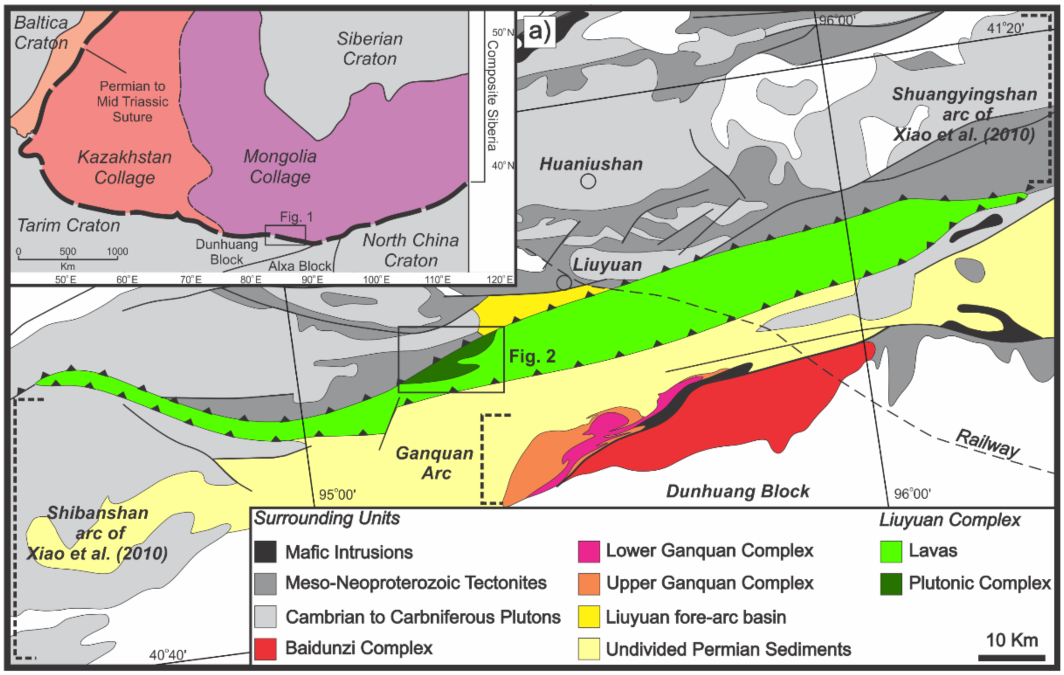

Figure 2.1: Tectonic context of the Liuyuan Complex within the southern Central Asia Orogenic Belt. Modified from Xiao et al. (2010).

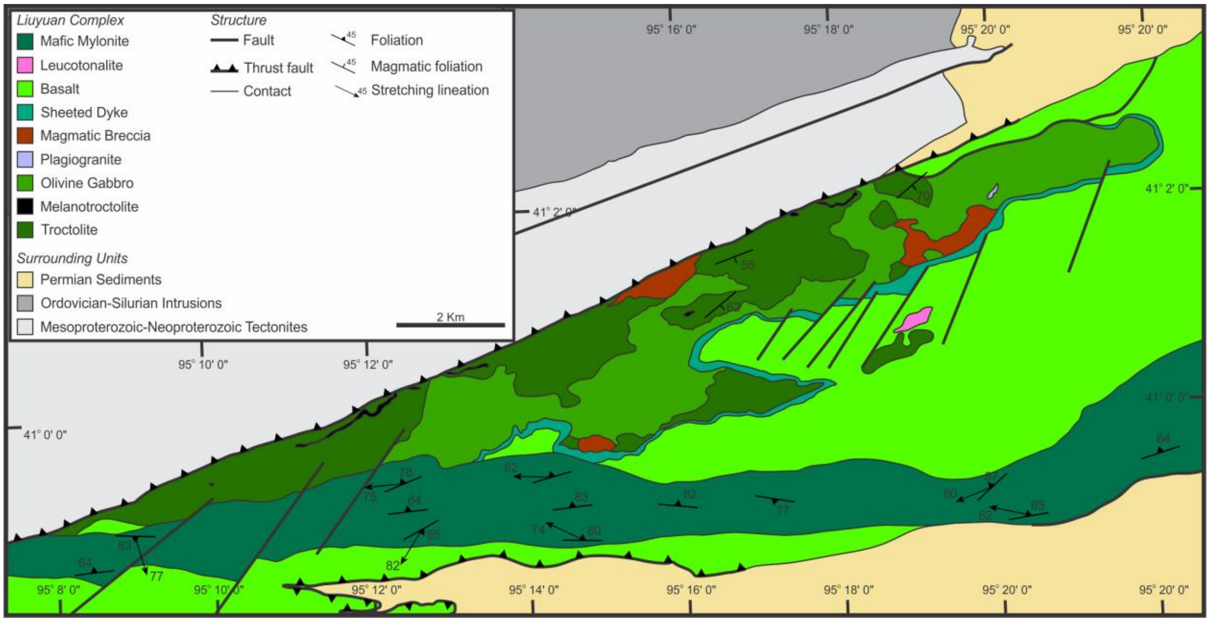

Figure 2.2: Geological map of the Liuyuan Complex and surrounding area, centered on the lower gabbroic rocks and sheeted dyke**.**

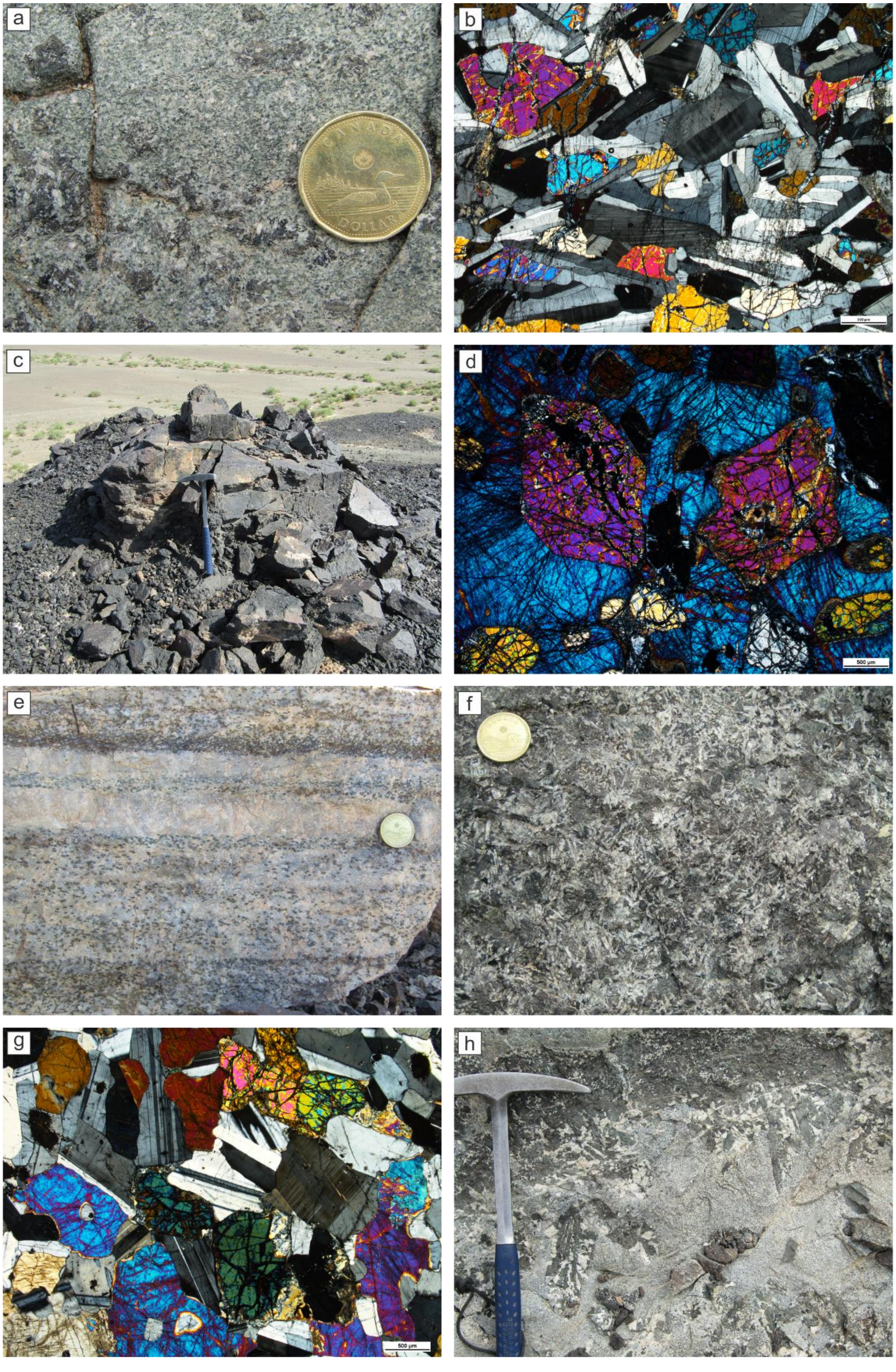
a
b
500 μm
c
d
500 μm
e
f
g
500 μm
h

Figure 2.3: Geology of the lower gabbroic rocks of the Liuyuan Complex. (a) Medium-grained troctolite, showing a typical poikilitic texture, with cm-scale clinopyroxene oikocrysts and predominantly olivine chadacrysts. (b) Troctolite in thin section. Note the alignment of euhedral plagioclase grains, defining a weak but noticeable magmatic foliation. Dihedral angles between plagioclase grains approximates 60^{o}, indicating some amount of solidus reequilibration has occurred. Scale bar is 500 µm. (c) Medium-grained melatroctolite. (d) Clinopyroxene oikocryst (second order blue interference color) and euhedral olivine chadacrysts in melatroctolite. Scale bar is 500 µm. (e) Layered intrusion in the Liuyuan Complex. The composition of individual layers ranges from melatroctolite to anorthosite, and layer thickness ranges between 0.5 and 5 cm. (f) Medium-grained subophitic gabbro. Part of the varitextured olivine gabbro overlying the lower troctolite cumulates in the Liuyuan Complex. (g) Olivine gabbro in thin section, showing approximately 20% interstitial clinopyroxene. Scale bar is 500 µm. (h) Gabbroic pegmatite showing mingled texture with an intruding plagiogranite. Clinopyroxene reaches up to 7 cm in length. Hammer is approximately 35 cm in length, and the coin diameter is 2.65 cm.

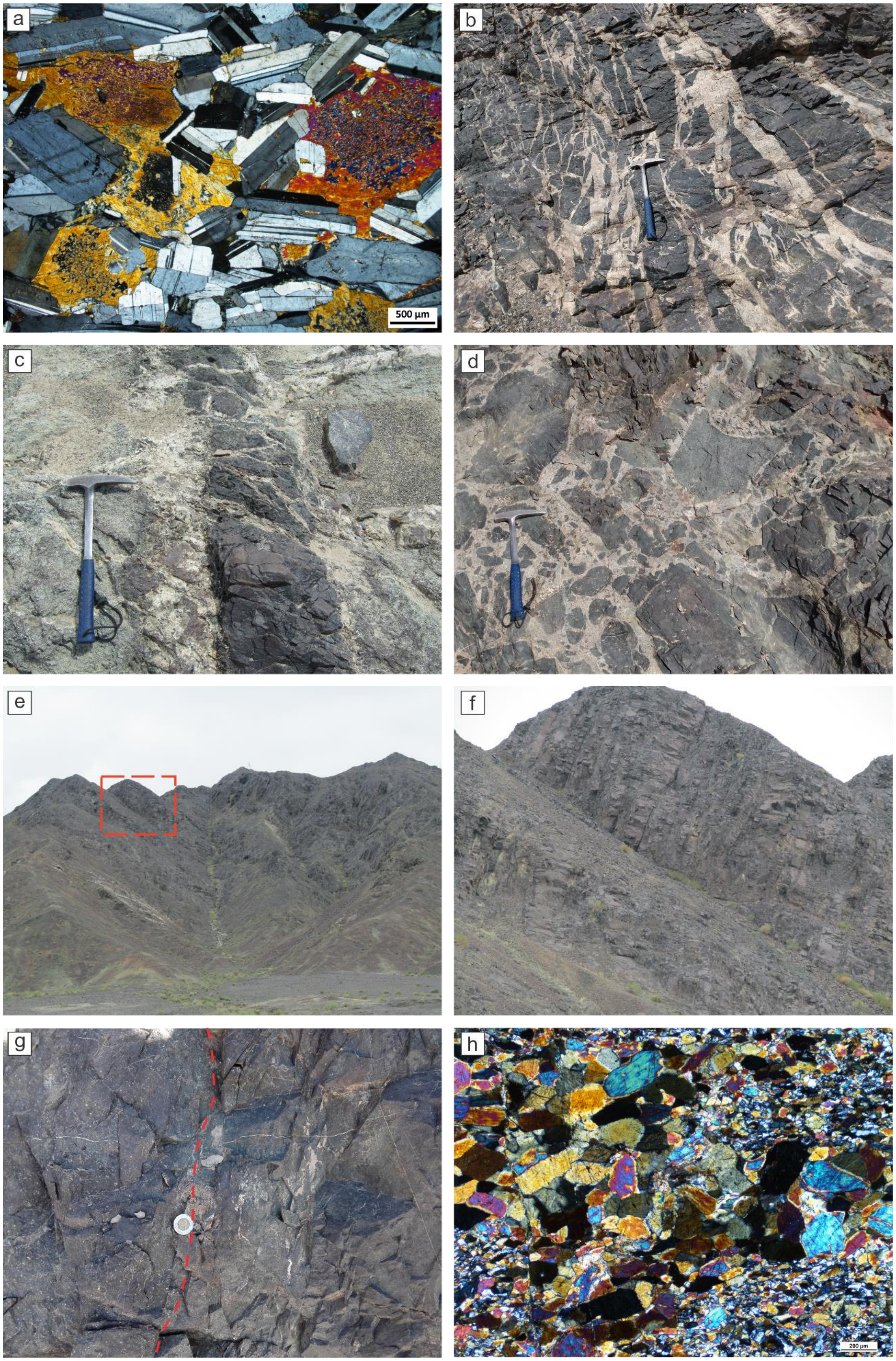
a
500 µm
b
c
d
e
f
g
h
200 µm

Figure 2.4: Intrusions in the lower gabbroic rocks and the sheeted dyke complex. (a) Medium-grained hornblende gabbro. Note the cumulate texture of the plagioclase and the reliquial interstitial clinopyroxene being replaced by hornblende. Scale bar is 500 µm. (b) Diabase-plagiogranite composite dyke at the base of the sheeted dyke complex, with plagiogranite locally forming net vein complexes in diabase clasts. (c) Diabase-plagiogranite composite dyke, intruding a medium-grained equigranular troctolite. Plagiogranite occurs on the edges of the dyke, and is mingled/brecciates the diabase at the center of the intrusion. (d) Magmatic breccia, located just below the base of the sheeted dyke complex. Fine-grained plagiogranite forms the groundmass, with diabase clasts. Diabase clasts are typically rounded, with a few angular occurrences. (e) An example of sheeted dyke from the Liuyuan Complex. The depicted mountain has approximately 100 meters from base to top, with the upper 70 meters comprising of sheeted dykes. (f) Close up view of the sheeted dyke complex, showing the red rectangle highlighted in (e). Individual dykes width range from 0.5 to 2 m. (g) Close up of the contact between a porphyritic diabase with approximately 15% plagioclase phenocrysts on the left and a micro gabbro on the right. Note the irregular nature of the contact. (h) Medium-grained amphibolite, located at the base of the sheeted dyke complex. Note the granoblastic texture, with hornblende and plagioclase dihedral angles approaching 60^o. Scale bar indicates 200 µm. Hammer is approximately 35 cm in length, and the coin diameter is 2.65 cm.

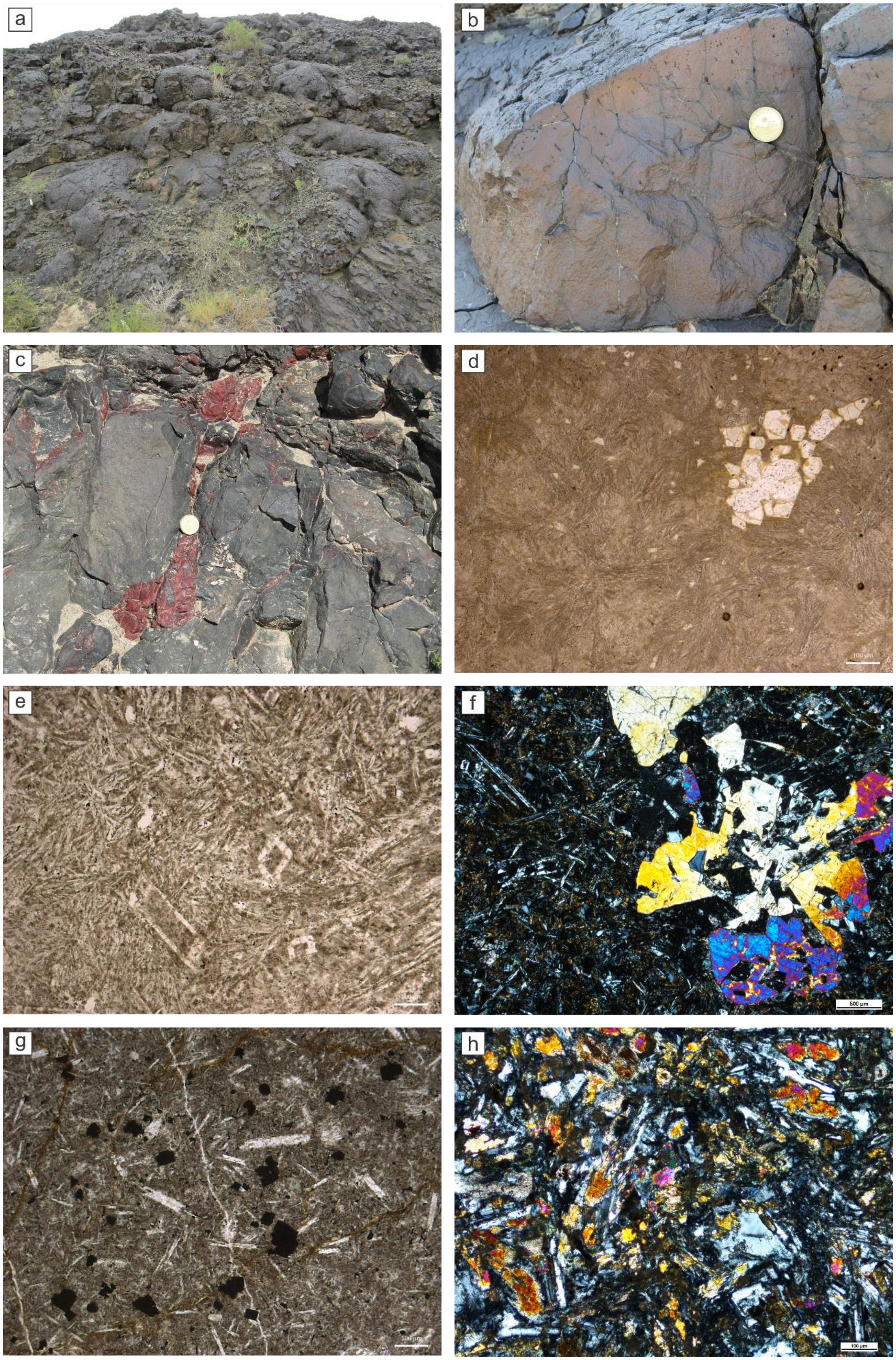
a
b
c
d
100 μm
e
f
500 μm
g
h
100 μm

Figure 2.5: Basalts of the Liuyuan Complex. (a) Pillow basalts. (b) Individual basaltic pillow showing abundant vesicles at its edge. (c) Jasper present as interpillow material. (d) Olivine phenocrysts, now replaced by chlorite in a spherulitic groundmass. Scale bar is 100 µm. (e) Plagioclase phenocrysts, showing both belt buckle and swallowtail morphologies. Scale bar is 100 µm. (f) Clinopyroxene glomerocrysts, with second order yellow-blue colors. Scale bar is 500 µm. (g) Plagioclase, with swallowtail morphology, and ilmenite phenocrysts in a basalt in the Liuyuan Complex. Scale bar is 100 µm. (g) Greenschist facies metamorphism in basalts of the Liuyuan Complex, comprising plagioclase, tremolite, chlorite and epidote. Scale bar is 500 µm. Hammer is approximately 35 cm in length, and the coin diameter is 2.65 cm.

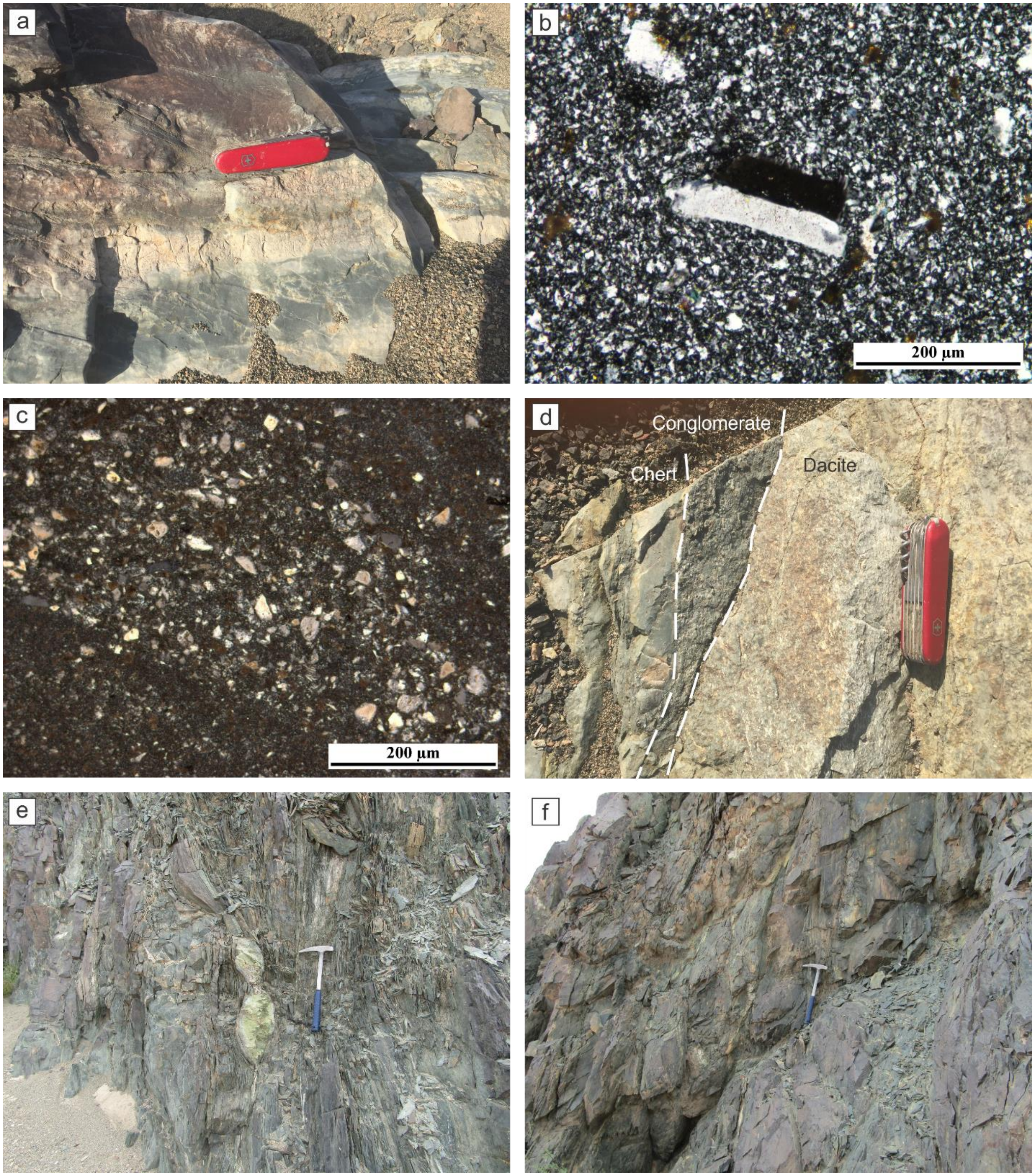

Figure 2.6: Upper lithologies and mafic mylonite. (a) Dark blue chert bed interlayered with basalts near the top of the Liuyuan Complex. This bed is approximately 25 centimeters thick. (b) Small angular plagioclase phenoclast a chert bed. Scale bar indicates 200 μm. (c) Dacitic crystal

tuff, with abundant quartz and subordinate plagioclase crystals. Scale bar is 200 µm. (d) Oligomictic pebble conglomerate, containing chert and basalt clasts at the contact between a lower chert and an upper dacite. (e) Mafic mylonite, a typical outcrop from the shear zone at the south of the Liuyuan Complex. (f) Note the intense strain partitioning between the intense shearing observed in the inter-pillow material and the relatively small strain in the pillows themselves.

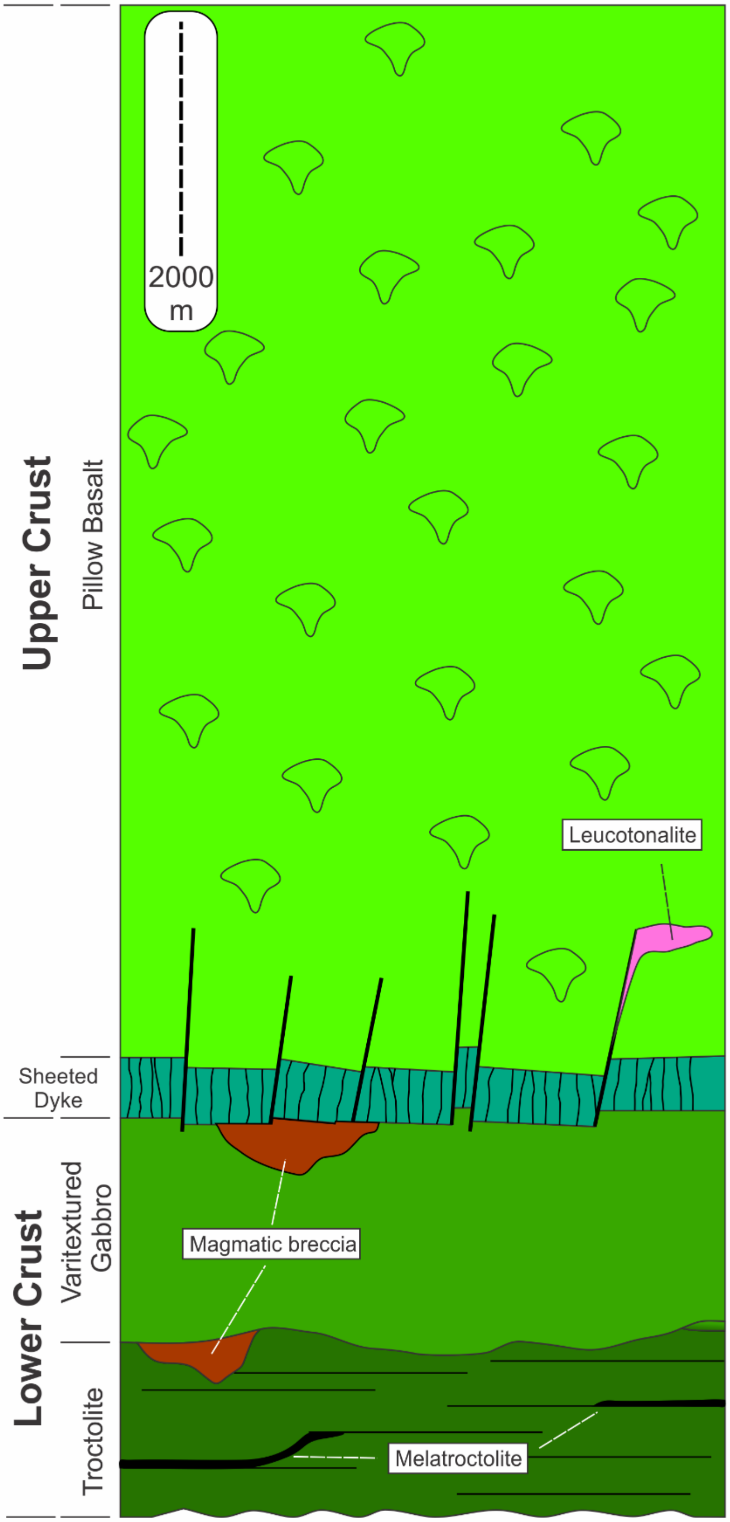

Figure 2.7: Measured stratigraphic section of the Liuyuan Complex. Colors for the major lithologies in the Liuyuan Complex are the same as Fig. 2.

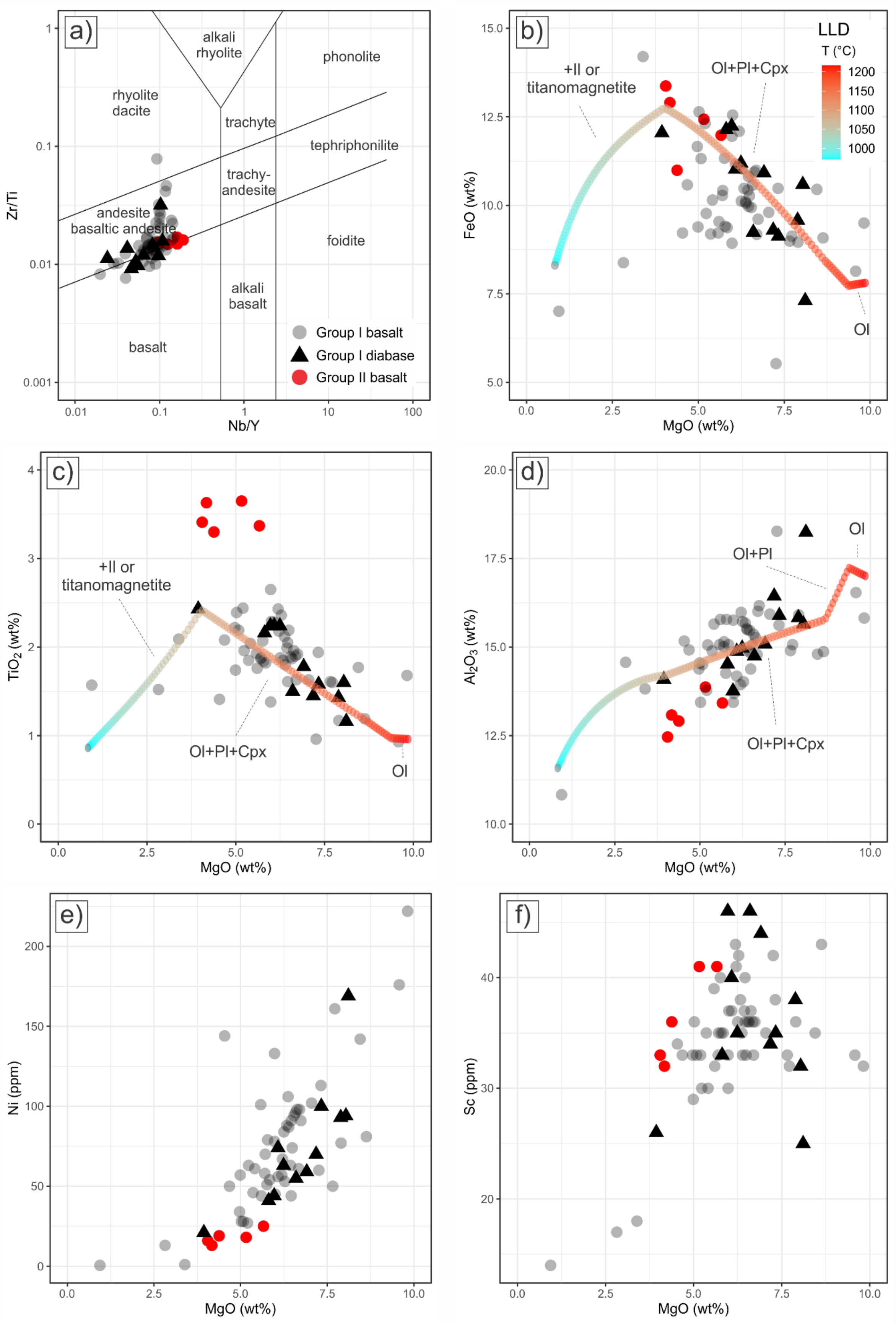
a)
Zr/Ti
Nb/Y
1
0.1
0.01
0.001
0.01
0.1
1
10
100
alkali rhyolite
phonolite
rhyolite dacite
trachyte
tephriphonilite
trachy-andesite
andesite
basaltic andesite
foidite
alkali basalt
basalt
Group I basalt
Group I diabase
Group II basalt
b)
FeO (wt%)
MgO (wt%)
15.0
12.5
10.0
7.5
5.0
0.0
2.5
5.0
7.5
10.0
LLD
T (°C)
1200
1150
1100
1050
1000
+Il or titanomagnetite
Ol+Pl+Cpx
Ol
c)
TiO2 (wt%)
MgO (wt%)
4
3
2
1
0
0.0
2.5
5.0
7.5
10.0
+Il or titanomagnetite
Ol+Pl+Cpx
Ol
d)
Al2O3 (wt%)
MgO (wt%)
20.0
17.5
15.0
12.5
10.0
0.0
2.5
5.0
7.5
10.0
Ol
Ol+Pl
Ol+Pl+Cpx
e)
Ni (ppm)
MgO (wt%)
200
150
100
50
0
0.0
2.5
5.0
7.5
10.0
f)
Sc (ppm)
MgO (wt%)
40
30
20
0.0
2.5
5.0
7.5
10.0

Figure 2.8: Geochemistry of the basalt and diabase of the Liuyuan Complex (a) Immobile element-based classification diagram (Pearce 1997) for the lavas of the Liuyuan Complex. Harker diagrams of MgO (wt%) vs. FeO (wt%) (b), TiO_2 (wt%) (c), Al_2O_3 (wt%) (d), Ni (ppm) (e), and Sc (ppm) (f). Details on the liquid line of descent plotted in (b-d) are discussed in the text.

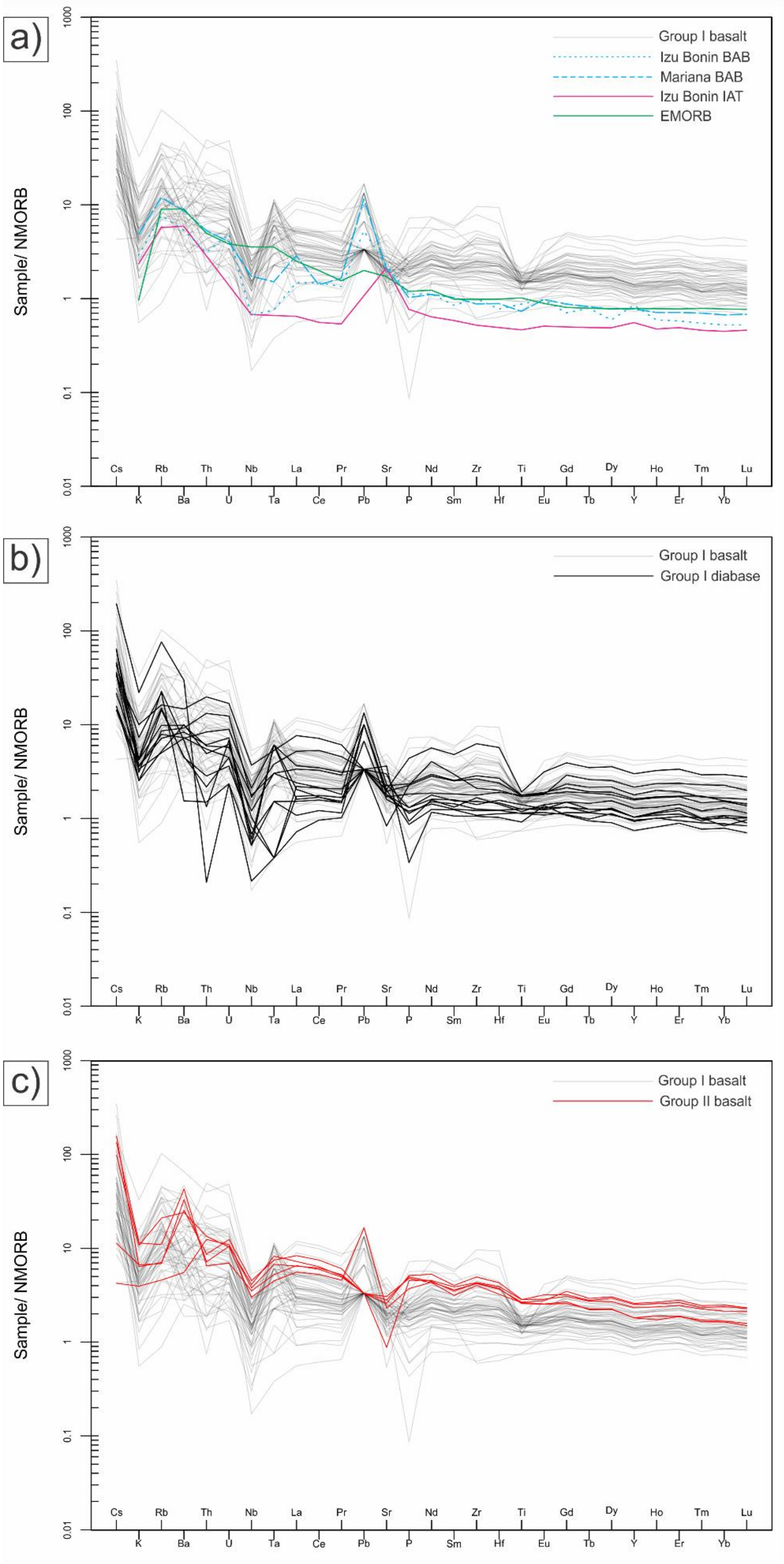
a)
Group I basalt
Izu Bonin BAB
Mariana BAB
Izu Bonin IAT
EMORB
b)
Group I basalt
Group I diabase
c)
Group I basalt
Group II basalt
Sample/ NMORB
1000
100
10
1
0.1
0.01
Cs
K
Rb
Ba
Th
U
Nb
Ta
La
Ce
Pr
Pb
Sr
P
Nd
Sm
Zr
Hf
Ti
Eu
Gd
Tb
Dy
Y
Ho
Er
Tm
Yb
Lu

Figure 2.9: Extended trace element patterns for Group I basalt (a), Group I diabase (b), and Group II basalt (c). Samples are normalized by the NMORB of McDonough and Sun (1989). EMORB data from McDonough and Sun (1989). Other reference compositions are from the compilation of Schmidt and Jagoutz (2017).

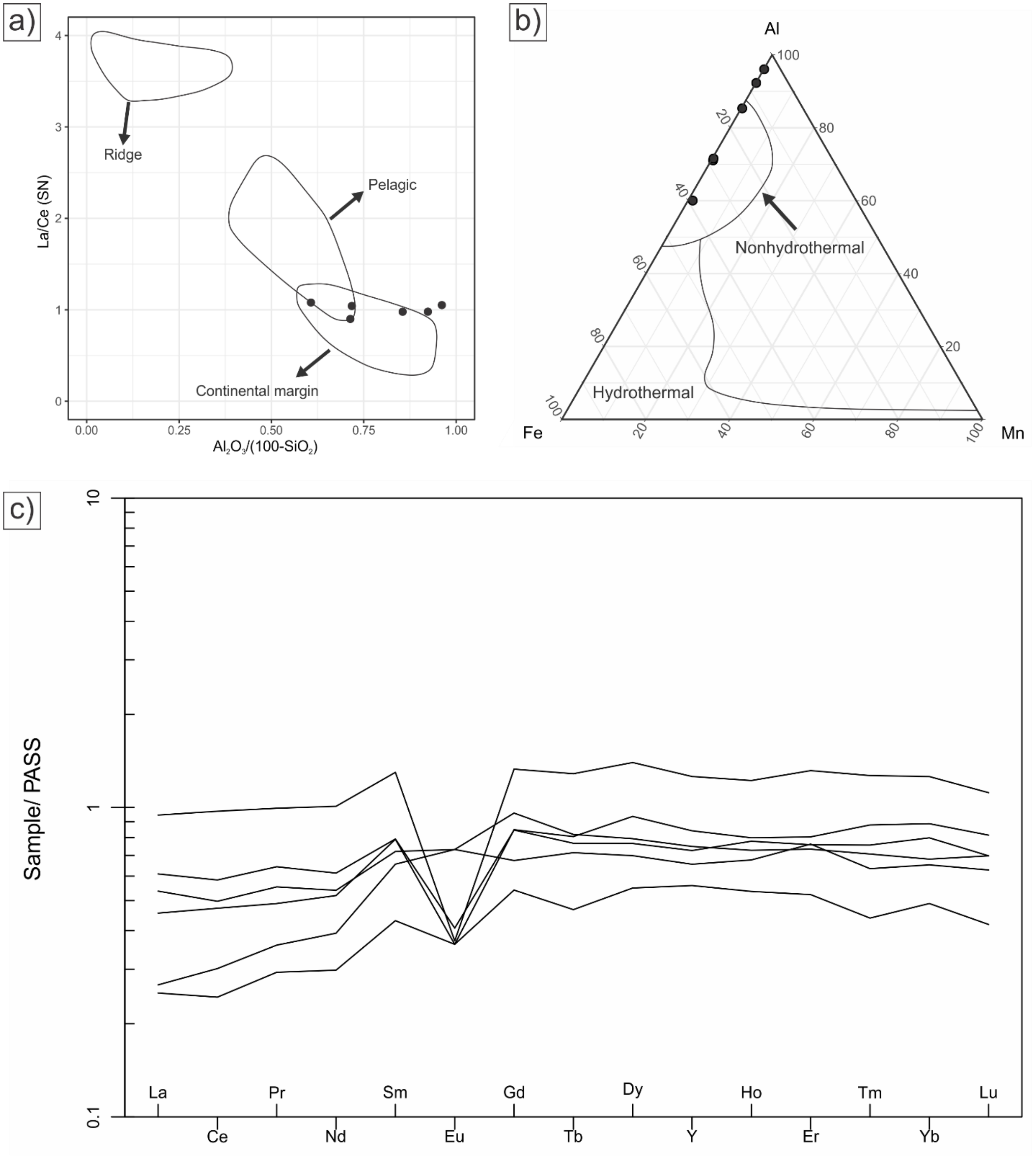

Figure 2.10: Geochemistry of the cherts of the Liuyuan Complex. (a) Depositional environment discrimination diagram of Murray (1991), where the cherts plot on the continental margin field.

(b) Ternary diagram of Adaki (1986), where the cherts plot on the field of nonhydrothermal chert. (c) Post Archean Australian Shale normalized spider diagram (McLennan 1989).

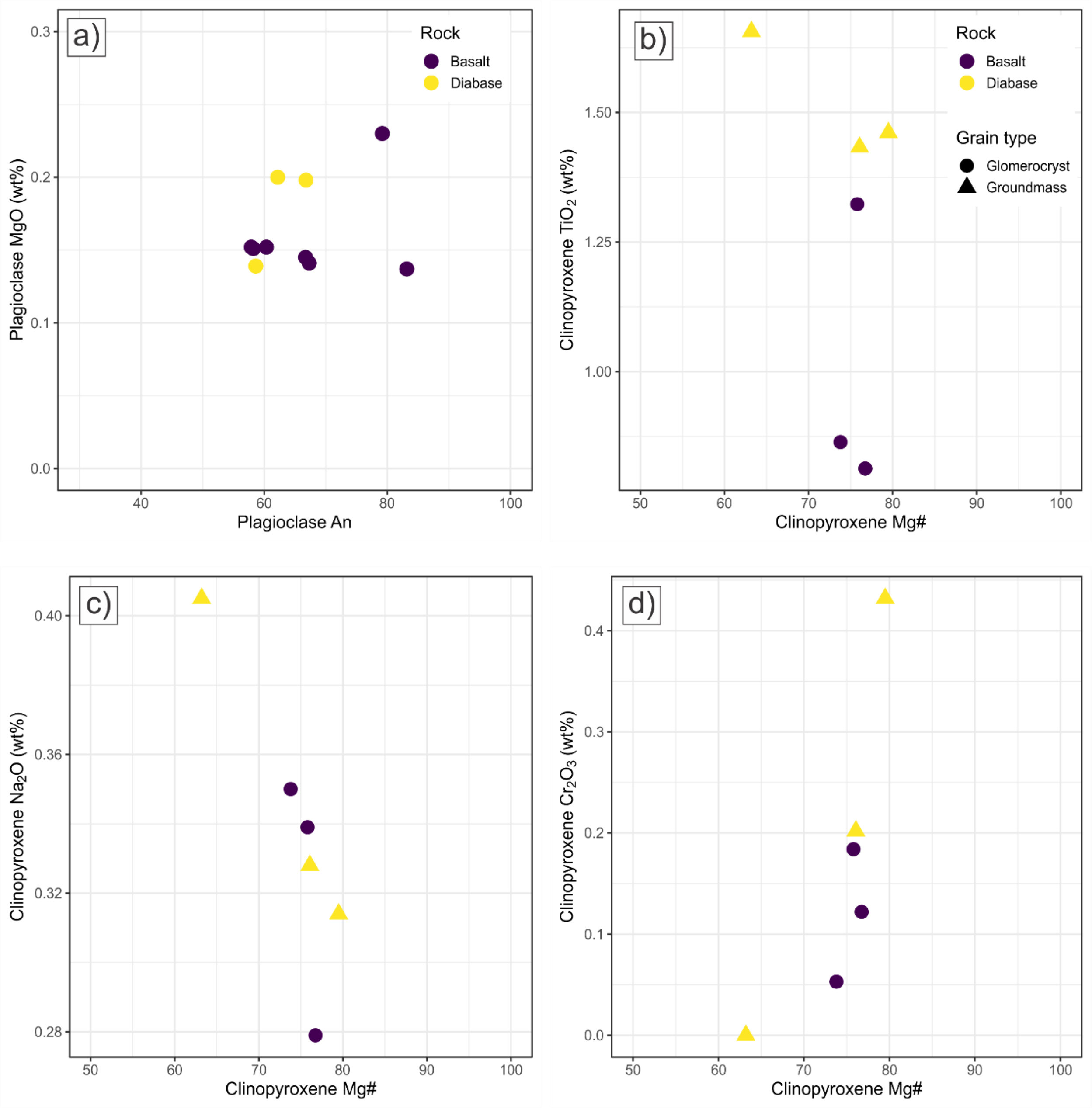

Figure 2.11: Chemistry of plagioclase and clinopyroxene of the Liuyuan Complex. (a) Plagioclase An vs. plagioclase MgO. Clinopyroxene TiO_2 (b), Na_2O (c), and Cr_2O_3 (d) vs Mg#.

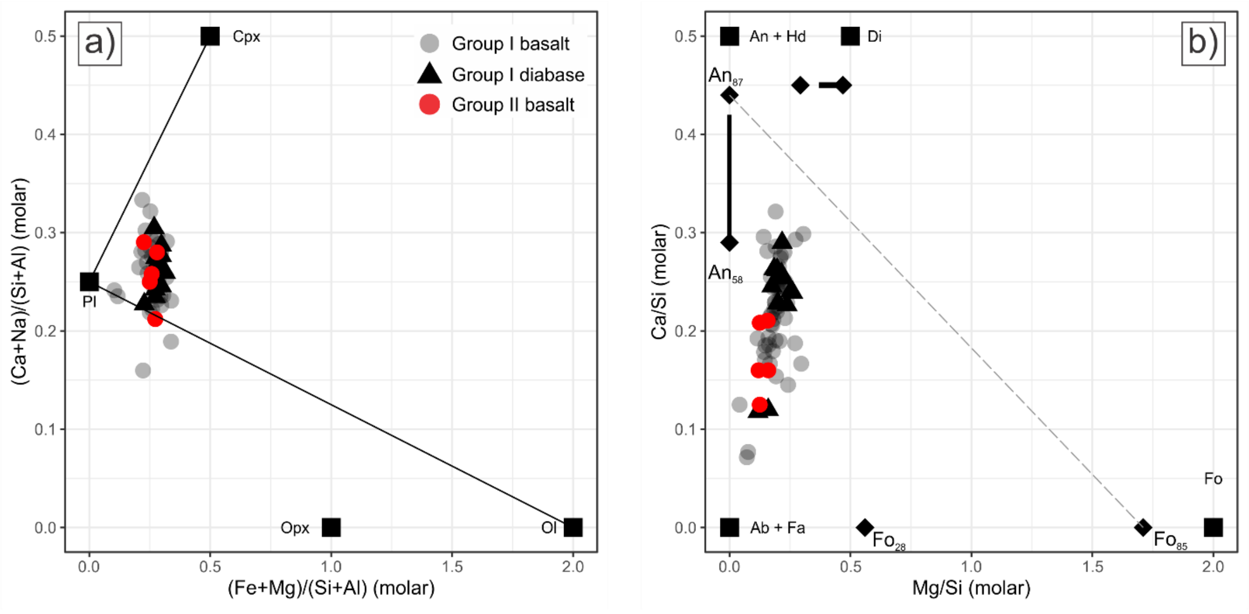

Figure 2.12: Molar element ratio diagrams. (a) (Ca+Na)/(Si+Al) vs. (Fe+Mg)/(Si+Al) diagram. (b) Ca/Si vs. Mg/Si diagram. Black diamonds indicate the mineral composition variation predicted by the thermodynamic model. Black bars indicate the range of measured mineral compositions measured on the basalt and diabase. Details on the text.

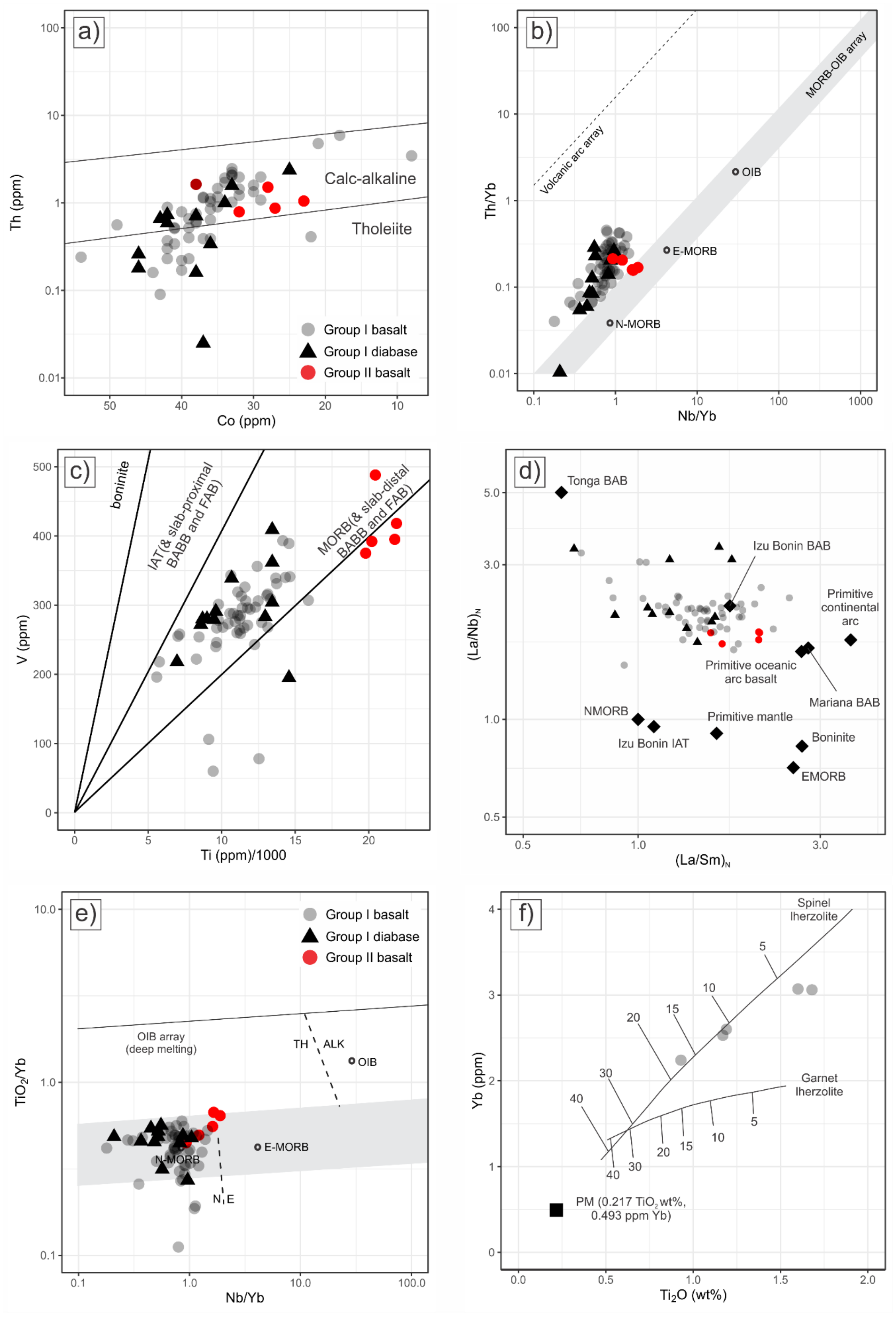a)
Th (ppm)
Co (ppm)
Calc-alkaline
Tholeiite
Group I basalt
Group I diabase
Group II basalt
b)
Th/Yb
Nb/Yb
Volcanic arc array
MORB-OIB array
OIB
E-MORB
N-MORB
c)
V (ppm)
Ti (ppm)/1000
boninite
IAT(& slab-proximal BABB and FAB)
MORB(& slab-distal BABB and FAB)
d)
(La/Nb)N
(La/Sm)N
Tonga BAB
Izu Bonin BAB
Primitive continental arc
Primitive oceanic arc basalt
Mariana BAB
NMORB
Primitive mantle
Izu Bonin IAT
Boninite
EMORB
e)
TiO2/Yb
Nb/Yb
Group I basalt
Group I diabase
Group II basalt
OIB array (deep melting)
TH
ALK
OIB
E-MORB
N-MORB
N
E
f)
Yb (ppm)
Ti2O (wt%)
Spinel lherzolite
Garnet lherzolite
PM (0.217 TiO2 wt%, 0.493 ppm Yb)

Figure 2.13: Tectonic discrimination diagrams. (a) Th vs. Co diagram (Hastie et al. 2007) for discrimination of magmatic series (b) Th/Yb vs. Nb/Yb projection of Pearce (2008). (c) V vs. Ti projection of Shervais (1982), modified by Pearce (2014). Samples from the Liuyuan Complex plot in the field of MORB (slab-distal BABB and FAB). BABB, back-arc basin basalt; FAB for fore-arc basin. (d) La/Nd vs. La/Sm diagram. Samples normalized to the NMORB of Sun and McDonough (1989). Reference points from Kelemen et al. (2003) and Schmidt and Jagoutz (2017). BAB, back-arc basin; IAT, island arc tholeiite. (e) TiO_2/Yb vs. Nd/Yb projection of Pearce (2008). (f) Yb vs. TiO_2 projection of Gribble et al. (1998). Only Group I lavas with mg# higher than 60 were plotted, avoiding the most fractionated.

Chapter 3: Petrology of gabbroic rocks from a back-arc basin ophiolite: the Liuyuan Complex, NW China

3.1 Introduction

Located at the southern edge of the Central Asian Orogenic Belt (CAOB), the 290-280 Ma Liuyuan Complex (Fig. 3.1a; Xiao et al. 2010, Mao et al. 2012, Wang et al 2017, Chapters 2 and 4) mainly comprises basalt, with subordinate gabbroic rocks, mafic to felsic dykes, plagiogranite, dacite, chert, and dark shales (Mao et al. 2012, Wang et al. 2017, Chapter 2). Some authors have argued that the Liuyuan Complex formed in a continental rift (Zuo et al. 1991, Qin et al. 2011, Su et al. 2011, Wang et al. 2017, He et al. 2018); while others favored an ophiolite setting (Xiao et al. 2010, Mao et al. 2012, Tian and Xiao 2020). Chapter 2 provided the first description of a laterally continuous sheeted dyke complex separating the lower gabbros from overlying basalts, supporting proposals that the Liuyuan Complex formed as an ophiolite. The presence of a well-developed sheeted dykes and the geochemical signatures of dykes and lavas were interpreted in terms of a fast-spreading back-arc basin environment (Chapter 2). Demonstrating a genetic relationship between the gabbroic rocks, the sheeted dykes, and the extrusive basalts would provide a key test of the ophiolite model for the formation of the Liuyuan Complex. Mao et al. (2012) suggested the basalts and gabbros were linked by fractionation of clinopyroxene, ilmenite, and plagioclase from a common parental melt; and therefore represents a comagmatic suite. In contrast, Wang et al. (2017) proposed that the gabbroic rocks and are intrusive into the overlying rift-related basalts. In this chapter we present the petrography, geochemistry and mineral chemistry of the plutonic facies of the Liuyuan Complex, and argue they are comagmatic with the basalts.

3.2 Local Geology

Located between the Shuangyingshan and Shibanshan arcs of Xiao et al. (2010), the 290-280 Ma Liuyuan Complex extends for approximately 90 km in an E-W direction (Fig. 3.1b). With a maximum preserved thickness of 9 Km, it is dominated by basaltic volcanic rocks (~90%), with subordinate mafic plutonic rocks, and minor plagiogranite (Mao et al. 2012, Chapter 2). The basalt in the Liuyuan Complex is dominated by a porphyritic facies with a hypohyaline groundmass, containing euhedral plagioclase laths (up to 15%) and granular olivine (up to 10%) as the dominant phenocrysts (Chapter 2). Clinopyroxene glomerocrysts were observed in two samples (Chapter 2). Pillow structures and lava tubes are widespread over the entire volcanic section of the Liuyuan Complex. The MgO and SiO_2 contents in the basalts, respectively, range between 2.82-9.82 wt% and 45.75-52.76 wt%, with mg# varying between 19.27-70.09. Trace element tectonic fingerprint presented in Chapter 2 indicates these basalts formed in a back-arc basin setting. The plutonic rocks identified by previous workers that are the focus of this chapter were mapped in detail and are described below. The coarser plutonic rocks are separated from the overlying basalts by a well-developed and laterally continuous sheeted dyke complex (Chapter 2) up to 500 m thick, composed of aphyric diabase (dominant) and minor porphyritic diabase containing ≤15% euhedral plagioclase phenocrysts (<1.5 mm) and rare olivine phenocrysts. The sheeted dyke complex is cut by several faults (10-100 m throws) that extend up into the volcanic rocks and which root into the underlying gabbro. These faults are commonly associated with epidote veins and likely guided hydrothermal systems that partly overprint the upper gabbroic rocks with greenschist facies minerals (Chapter 2). A measured stratigraphic column of the Liuyuan Complex is presented as Fig. 3.2a.

3.3 Field Relations and Petrography of the Plutonic Facies

The plutonic rocks exposed in the Liuyuan Complex have a maximum thickness of 2.5 km, but comprise only about 10% of its outcrop area (Chapter 2). The major lithologies in the plutonic complex are troctolite, melatroctolite, olivine gabbro, and hornblende gabbro. Both the olivine gabbro and the hornblende gabbro can be further subdivided into two groups. The olivine gabbro has been divided into olivine gabbro and podiform olivine gabbro, and the hornblende gabbro into podiform hornblende gabbro and intrusive hornblende gabbro. To facilitate descriptions and discussions, the gabbroic rocks of the Liuyuan Complex have been assigned to three zones. The lower zone (LZ) comprises the troctolite and melatroctolite. The middle zone (MZ) comprises the olivine gabbro, henceforth referred to as MZ olivine gabbro. The upper zone (UZ) comprises the upper section of the MZ olivine gabbro the podiform olivine gabbro, the podiform hornblende gabbro, and the intrusive hornblende gabbro. The host rock for the podiform olivine gabbro, the podiform hornblende gabbro, and the intrusive hornblende gabbro is the upper part of the MZ olivine gabbro. For brevity, the MZ olivine gabbro is described in the MZ section, and the UZ description is restricted to the podiform and intrusive lithologies.

3.3.1 Lower Zone (LZ)

The lowermost unit of the Liuyuan Complex is a fine- to medium-grained troctolite (Figs. 3.3a, 3.4a,b) with a maximum thickness of 1450 meters. This hypidiomorphic rock is typically medium grained, comprising euhedral prismatic plagioclase primocrysts (85-50%) and granular olivine primocrysts (15-45%), with subordinate anhedral interstitial clinopyroxene (<8%). Accumulations of plagioclase and olivine primocrysts define a weak magmatic foliation that strikes ENE, roughly parallel to the strike of lithological unit contacts within the Liuyuan Complex (Fig. 3.1b). Clinopyroxene locally forms oikocrysts up to 5 cm in diameter, with abundant plagioclase and subordinate olivine chadacrysts (Figs. 3.3b, 3.4c). Plagioclase chadacrysts are smaller and have more rounded grain boundaries that the larger primocrystic plagioclase grains (Fig. 3.4d). Chadacrysts typically fill ~25% of the oikocryst's volume, but concentrations of up to 80% have been observed. The dihedral angle of monomineralic plagioclase triple junctions approaches 120°. Hydrothermal alteration in this unit is limited, with minor saussuritization of plagioclase and serpentinization of primocryst olivine. Olivine and plagioclase chadacrysts in clinopyroxene typically remain fresh, however.

These troctolites contain isolated, isomodal, discontinuous layers of dark, medium-grained melatroctolite (Figs. 3.3c, 3.4e). Individual melatroctolite layers are approximately 5 m thick and have a maximum observed length of tens of meters. The contact between the melatroctolite and the surrounding troctolite is generally parallel to the magmatic foliation, although it is locally discordant, and is gradational over up to 5 centimeters. The melatroctolite consists of a framework of granular olivine primocrysts (60-80%) and subordinate lath-shaped plagioclase primocrysts (15-30%), with minor interstitial to poikilitic clinopyroxene (<10%). Olivine primocrysts are typically serpentinized, locally showing mesh textures (Fig. 3.4e), while plagioclase primocrysts displays intense saussurite alteration, particularly in their cores (Fig. 3.4f). Clinopyroxene oikocrysts reach up to 5 cm in diameter, containing euhedral olivine and rare plagioclase laths as chadacrysts (Fig. 3.4g). Large concentrically zoned crystals of subhedral brown pargasite (<5%) (Fig. 3.4h) were observed in two of the 11 melatroctolite samples petrographically examined, suggesting the pargasite crystallized in an open space from a hydrous trapped pore melt. In contrast igneous amphibole was not observed in the troctolite or in the overlying MZ olivine gabbro.

3.3.2 Middle Zone (MZ)

The contact between the lower troctolite-melatroctolite sequence (LZ) and the overlying MZ olivine gabbro is gradational over approximately 10 meters, and is marked by a progressive increase in modal clinopyroxene. At the eastern edge of the exposed plutonic complex, the gradual gradational contact between the LZ troctolite and MZ olivine gabbro is marked an approximately 100 m wide 50 m thick sequence of rhythmically layered cumulates. Individual layers are graded, and range between 2 and 10 cm in thickness. The composition of individual layers ranges from anorthosite to olivine melanogabbro, becoming more olivine-poor and clinopyroxene-rich towards the top of the layered sequence.

The LZ troctolite-melatroctolite sequence is overlain by the MZ olivine gabbro (Figs. 3.3e-g) that consists of euhedral plagioclase primocrysts (40-75%), euhedral olivine primocrysts (7-35%), and interstitial to poikilitic clinopyroxene (7-40%), with accessory orthopyroxene and ilmenite. This unit shows a gradual textural variation from base to top of the section, with little change in grain size. At the base of this unit, the texture of the MZ olivine gabbro is similar to the underlying troctolite, with a primocryst framework of prismatic plagioclase and granular olivine, with larger amounts of interstitial clinopyroxene (Fig. 3.5a). The clinopyroxene locally has a poikilitic habit, with oikocrysts up to 3 cm in length that contain both plagioclase and olivine chadacrysts (Fig. 3.5b). Upwards in the section, modal clinopyroxene proportions increase, and interstitial clinopyroxene characteristic in the lower MZ transitions to the sub-ophitic and ophitic intergrowths that are more typical in upper MZ and in the UZ section of the Liuyuan Complex. Greenschist metamorphism is present in the upper section of the MZ olivine gabbro, with chlorite forming olivine pseudomorphs, saussurite alteration in plagioclase, and minor actinolite and chlorite replacing clinopyroxene.

3.3.3 Upper Zone (UZ)

The UZ of the Liuyuan Complex comprises the stratigraphic level where the topmost MZ olivine gabbro hosts three other igneous units: the podiform olivine gabbro, the podiform hornblende gabbro, and the intrusive hornblende gabbro. Given the meter-scale distribution of these lithologies, they do not appear as mappable units in Fig. 3.1 but are schematically showed in Fig. 3.2a. The podiform olivine gabbro (Fig. 3.5c) occurs as meter-scale pods within the upper parts of the MZ olivine gabbro, typically clustered at the root of faults that disrupts the sheeted dyke complex and the lower parts of the basalt. These rocks are coarser grained than the MZ olivine gabbro, and typically show ophitic to poikilitic textures. Relatively intense hydrothermal alteration and greenschist metamorphism affects this unit (Fig. 3.5d), locally producing chlorite-actinolite metagabbros that have recognizable fossil ophitic and poikilitic textures. Olivine is completely replaced by chlorite pseudomorphs, with plagioclase showing intense saussurite alteration.

The podiform hornblende gabbro (3.5e) occurs as decimeter-scale discontinuous pods within the upper section of the MZ olivine gabbro. The podiform hornblende gabbro is predominantly medium grained, composed of euhedral prismatic plagioclase grains (55-65%), interstitial magnesio-hornblende (25-45%), and actinolite and chlorite pseudomorphs after clinopyroxene or olivine (<30%). A single fresh olivine grain was observed in the thin sections available from this unit. Rare interstitial clinopyroxene grains without amphibole rims are locally preserved. Plagioclase primocrysts show preferential orientation of their long axis, defining a week magmatic foliation (Fig. 6g). When present, the foliation within the podiform hornblende gabbro is continuous with the host MZ olivine gabbro. Actinolite locally epitaxially replaces the edges of magnesio-hornblende in this unit. The contact between the podiform hornblende gabbro and the host MZ olivine gabbro is gradational over a few centimeters, with modal proportions of clinopyroxene and magnesio-hornblende respectively decreasing and increasing towards the center of the podiform hornblende gabbro. The upper part MZ olivine gabbro is also intruded by medium- to fine-grained dykes up to 1 m thick of an isotropic hornblende gabbro. This intrusive hornblende gabbro (Fig. 3.3h, 3.5f) is composed of plagioclase (<55%), magnesio-hornblende (<40%), actinolite (<30%), and minor clinopyroxene relics in magnesio-hornblende. This intrusive hornblende gabbro shows greenschist facies metamorphism overprint, with widespread replacement of magnesio-hornblende by actinolite and of actinolite by chlorite.

The UZ and upper part of the MZ of the Liuyuan Complex are intruded by composite plagiogranite and diabase dykes, locally forming meter-scale composite dyke swarms and net-vein complexes, frequently with hornblende-rich selvedges. Locally, plagiogranite intrusions form the matrix of magmatic breccias that contain rounded diabase clasts up to half a meter in length, and a few angular medium-grained olivine gabbro and hornblende gabbro clasts. Diabase and plagiogranite commonly have serrated, lobate contacts suggestive of liquid-liquid interfaces (e.g. Wiebe 1987, Wiebe 1994, Wiebe et al. 2004), indicating plagiogranite intrusion took place while the mafic lithologies were not fully solidified. Alteration is more intense along spreading-related normal faults that displace the basalt/sheeted dyke contact (Chapter 2) with saussuritization of plagioclase, replacement of olivine by chlorite pseudomorphs, and of clinopyroxene by actinolite. Rare plagiogranite dykes were also observed in the LZ.

3.4 Analytical Methods

A total of 68 samples were analyzed, including 16 troctolites, 11 melatroctolites, 21 MZ olivine gabbros, 7 podiform olivine gabbros, 7 podiform hornblende gabbros, and 6 intrusive hornblende gabbros. Thin sections were fabricated at the Heibei Geology and Mineral Resources

Bureau's Langfang Laboratory. For analysis, about 1 kg of material was crushed until ≥ 70% would pass a 2 mm sieve. Then, 250 g of the crushed material was pulverized until ≥ 85% would pass a 75 µm sieve. Pulverized samples were analyzed for major and trace elements, including rare earth elements (REE), by inductively coupled plasma – atomic emission spectroscopy (ICP-AES) and inductively coupled plasma – mass spectrometry (ICP-MS) at ALS Chemex in Vancouver, Canada. The pulverized samples were mixed with a lithium borate flux and heated to 1000 ^{o}C in an inert crucible. The resulting homogeneous fusion product was digested in an *aqua regia* solution prior to ICP analysis. For quality assurance and control, several samples ran as pulp duplicates and international standards were analyzed. Blanks were also prepared. The blanks were good, and the largest variation in observed in the analyzed sample duplicates and in the measured standards was 5%. For data presentation and analysis, major element oxides were recalculated using FeO-total instead of Fe_2O_3. Mineral chemistry data was obtained via a JEOL JXA-830F electron microprobe at the Earth and Planetary Materials Analysis Laboratory at the University of Western Ontario, London, ON, Canada. A beam current of 20 nA at 15 kV was used during the analytical run. Counting times varied between 20 and 40 seconds on peak and background positions. Whole rock geochemistry is presented in Appendix 1, and mineral chemistry data in Appendix 2.

3.5 Geochemistry

3.5.1 LZ Troctolite

Troctolites in the Liuyuan Complex show a wide MgO range (4.75-20.11 wt%), high Al_2O_3 (16.08-27.44 wt%) (Fig. 3.6c), and moderately high CaO (8.37-14.82 wt%). Melanocratic-troctolites have high MgO with low Al_2O_3, whereas leuco-troctolites have low MgO with high Al_2O_3. MgO and Al_2O_3 values are inversely correlated, reflecting the olivine/plagioclase ratios observed in thin section. The troctolites have low FeO (2.48-7.90 wt%) (Fig. 3.6a), and a very narrow range in SiO_2 (43.50-48.04 wt%). The troctolite has the highest Sr (127.5-259 ppm) values in the Liuyuan Complex, while displaying variable Ni (132-712 ppm), Cr (20-1050 ppm) (Fig. 3.6d), and Sc (4-12 ppm) concentrations. Higher Ni and Cr concentrations are present in more melanocratic samples and lower Ni and Cr concentrations in more leucocratic samples, mirroring the variation in olivine/plagioclase ratio. The troctolites have low incompatible trace element concentrations and show flat REE profiles (La_N/Sm_N between 0.58-2.09 and Sm_N/Yb_N 0.89-2.06), with large positive Eu anomalies (Eu/Eu^* 1.31-4.09). The high Eu/Eu^* indicates significant plagioclase accumulation. On a NMORB-normalized (Sun and McDonough 1989) multi element diagram, the troctolite shows an overall depleted trace element signature, with positive Cs, Rb, U, Sr and Eu anomalies, but negative K, Th, Nb, and P anomalies (Fig. 7a).

3.5.2 LZ Melatroctolite

The discontinuous melatroctolite layers form a distinct cluster on Harker plots for major elements (Fig. 3.6). Among the Liuyuan cumulates, the melatroctolites have the highest MgO (24.00-33.25 wt%) and FeO (9.81-13.03 wt%) (Fig. 3.6a) and the lowest SiO_2 (36.95-42.15 wt%) and Al_2O_3 (4.55-10.02 wt%) (Fig. 3.6c) values. High LOI contents (3.97-10.41 wt%) reflect extensive serpentinization of olivine. The melatroctolite has high Cr (110-3240 ppm) (Fig. 3.6d) and Ni (644-1255 ppm) contents, with relatively low Sr (28.4-110.5 ppm) and Sc (6-21 ppm). The high Ni values correlate with the abundance of olivine observed in thin section, and rocks with high Sc have prominent clinopyroxene oikocrysts. On the NMORB normalized multi element diagram, the melatroctolite shows an overall depleted trace element signature similar to the troctolites, with positive Cs, Rb, Ta and Ti anomalies, and strong negative K, Nd, and P anomalies. The melatroctolites show flat REE profiles, with La_N/Sm_N (0.65-1.75) and Sm_N/Yb_N

(0.69-1.69) ratios similar to those of LZ troctolites. They also have weakly negative to strongly positive Eu anomalies (Eu/Eu^* 0.85-3.02) (Fig. 3.7b).

3.5.3 MZ Olivine Gabbro

The MZ olivine gabbro displays wide variations in MgO (4.93-13.63 wt%), FeO (3.35-7.99 wt%) (Fig. 3.6a), Al_2O_3 (16.12-23.23 wt%) (Fig. 3.6c), CaO (9.91-16.05 wt%) contents, with narrower ranges of TiO_2 (0.16-0.80 wt% (Fig. 3.6b) and SiO_2 (44.91-50.67 wt%). Their NMORB normalized REE patterns show variable enrichment in light REE (LREE) (La_N/Sm_N of 0.31-1.20), and flatter mid REE (MREE) to heavy REE (HREE) (Sm_N/Yb_N of 0.74-1.48) profiles, with Eu anomalies (Eu/Eu^* between 0.89-3.27) among the highest recorded in the Liuyuan Complex (Fig. 8c). This facies also displays large variations in Sr (79-206 ppm), Cr (140-1400 ppm), Ni (77-440 ppm), and Sc (8-42 ppm) concentrations. Normalized trace element profiles show positive Cs, Th, and Ti anomalies, negative K, Nb, Zr, anomalies, and variable contents of Rb, Ba, U, and P (Fig 3.7c).

3.5.4 UZ Podiform Olivine Gabbro

The podiform olivine gabbro show chemical compositions that completely overlap with those of the overlying sheeted dykes and lavas of the Liuyuan Complex (Chapter 2). Samples from this group show a relatively narrow variation in MgO (6.09-7.84 wt%), FeO (9.81-13.02 wt%) (Fig. 3.6a), TiO_2 (1.61-3.45 wt%) (Fig. 3.6b), Al_2O_3 (13.30-15.84 wt%) (Fig. 3.6c), CaO (8.29-11.22 wt%), and SiO_2 (46.98-50.53 wt%) contents. The podiform olivine gabbro shows enriched NMORB-normalized trace element patterns when compared with the MZ olivine gabbro, within the range defined by the overlying basalt and diabase, with similar profile shapes, positive Cs, Rb, and Th and Ta anomalies, and negative K and Nb anomalies. They have generally flat REE profiles (La_N/Sm_N of 0.77-1.22 and Sm_N/Yb_N of 1.21-1.69), with weakly negative Eu anomalies (Eu/Eu* 0.79-0.98) (Fig. 3.7c). Compared to the troctolite, melatroctolite, and MZ olivine gabbro, the podiform olivine gabbro displays a narrower variation of compatible elements like Sr (113-282 ppm), Cr (70-250 ppm) (Fig. 3.6d), Ni (28-119 ppm), and Sc (27-39 ppm) The narrow range of compatible elements and Al_2O_3/MgO variation implies the podiform olivine gabbro is not strongly cumulative, consistent with the textures observed in thin section. Their trace element profiles (Fig. 3.7c) suggests they represent quasi-liquid compositions that could have fed the sheeted dykes.

3.5.5 UZ Podiform Hornblende Gabbro

The podiform hornblende gabbro was sampled in 6 locations, all near the top of the MZ olivine gabbro. These hornblende gabbros show slightly higher SiO_2 (47.08-50.53 wt%) than the MZ olivine gabbros, with lower MgO (8.37-11.30 wt%), FeO (4.69-6.29 wt%) (Fig. 3.6a), Al_2O_3 (16.37-19.59 wt%) (Fig. 3.6c), CaO (12.96-15.02 wt%), and TiO_2 (0.29-0.96 wt%) (Fig. 3.6b). They also show higher Sr (139-199 ppm) concentrations when compared to the MZ olivine gabbro, but lower Cr (330-1470 ppm (Fig. 3.6d), Ni (113-263 ppm), and Sc (26-46 ppm). Their NMORB-normalized trace element signature contains positive Cs, Th, Sr, and Ti anomalies, with negative K, Nb, and P anomalies (Fig. 3.7d). Similar to the MZ olivine gabbro, the podiform hornblende gabbro shows variable enrichment in LREE (La_N/Sm_N of 0.44-1.27), but with a flatter MREE to HREE profile (Sm_N/Yb_N 1.11-1.32) (Fig 3.7d). These rocks show weakly negative to positive Eu anomalies (Eu/Eu* of 0.96-1.56). Overall, NMORB-normalized trace element signature of the podiform hornblende gabbro is similar to the MZ olivine gabbro.

3.5.6 UZ Intrusive Hornblende Gabbro

The intrusive hornblende gabbro was sampled in 6 locations in the Liuyuan Complex. Compared with the podiform hornblende gabbro, these samples display similar ranges in SiO_2

(47.27-52.02 wt%), but have lower MgO (5.70-7.76 wt%), Al_2O_3 (14.88-16.07 wt%) (Fig. 3.6c), CaO (6.29-11.40 wt%), and higher FeO (6.85-10.68 wt%) (Fig. 3.6a) and TiO_2 (0.63-1.74 wt%) (Fig. 3.6b) contents. The intrusive hornblende gabbro has similar Sr (102-192 ppm) concentrations as their podiform counterparts but show lower Cr (110-260 ppm) (Fig. 3.6d), Ni (49-73 ppm) and Sc (30-39 ppm) concentrations. On an NMORB-normalized extended trace element diagram, they also display positive Cs, Th, and Ti anomalies, with negative, K, Nb, P, and Zr anomalies. It also has flatter REE profiles (La_N/Sm_N of 0.61-1.51 and Sm_N/Yb_N of 1.13-1.39) compared to the podiform hornblende gabbro, with weakly negative Eu anomalies (Eu/Eu^* of 0.83-0.91) (Fig. 3.7d). Like the podiform olivine gabbro, the intrusive olivine gabbro has major and trace element compositions that completely overlap the basalt and diabase of the Liuyuan Complex, suggesting they also represent quasi-liquid compositions.

3.6 Mineral Chemistry

Mineral chemical data were obtained from all major lithologies in the Liuyuan Complex, except for the podiform olivine gabbro and the intrusive hornblende gabbro. Care was taken to analyze the least altered samples in each facies. The composition of plagioclase and clinopyroxene phenocrysts in the basalts of the Liuyuan Complex was discussed extensively in Chapter 2. For reference, their compositional ranges are displayed as fields in the appropriate mineral chemistry plates (Fig. 3.8).

3.6.1 Olivine

Olivine compositions are more primitive in the melatroctolite (Fo_{79-85}, NiO 0.174-0.242 wt%) and in the troctolite (Fo_{74-82}, NiO 0.105-0.186 wt%) than in the MZ olivine gabbro (Fo_{74-78}, NiO 0.098-0.132 wt%) (Figs. 3.8a). The single olivine grain observed in thin section in the podiform hornblende gabbro has a forsterite content of Fo_{74} and NiO of 0.121 wt%. Fig. 3.8a shows a model fractional crystallization trend calculated from the inferred parental melt of the Liuyuan Complex (basalt 19LYS-7182B, see Chapter 2 for details). The analyzed olivine grains in the plutonic rocks of the Liuyuan Complex follow this fractionation trend, with both olivine chadacrysts and primocrysts from the melatroctolite and troctolite as the most primitive in the dataset, plotting at a melt fraction higher than 0.85. Overall, chadacrysts in the troctolite and melatroctolite have higher Fo and Ni than surrounding equant primocrysts. Besides two chadacrysts in a troctolite, all other analyzed grains cluster at a model melt fraction between 0.85 and 0.82. Olivine Fo gradually decreases upwards in the stratigraphy of the Liuyuan Complex (Fig. 2b).

3.6.2 Clinopyroxene

Liuyuan Complex clinopyroxene is diopside and augite (Yavuz 2013, following IMA-88 nomenclature scheme). Clinopyroxene mg# shows little variation between the different lithologies, ranging between 78 and 88, with a formula varying between $Wo_{45} En_{43} Fs_{12}$ and $Wo_{45} En_{49} Fs_6$. Cr_2O_3 values range between 0.03-1.17 wt%, with the melatroctolite and troctolite having the highest values (0.51-1.17 wt%) (Fig. 3.8b). Overall, the variability of clinopyroxene mg# increases upwards in the stratigraphy of the Liuyuan Complex (Fig. 2d), with the podiform hornblende gabbro showing the largest variation. TiO_2 (Fig. 3.8c) is incompatible in clinopyroxene and show wide variation at constant mg#. The lithologies with the largest variations are the MZ olivine gabbro and the podiform hornblende gabbro, suggesting melt back-reaction played a role in the petrology of these rocks.

3.6.3 Plagioclase

Plagioclase composition in the troctolite is the most anorthitic (An_{77-83}), whereas plagioclase in melatroctolite (An_{57-76}), MZ olivine gabbro (An_{62-79}), and podiform hornblende gabbro (An_{62-77}) is more sodic and broadly overlapping compositions (Fig. 2c). There is no compositional difference between groundmass or chadacrysts plagioclase grains in the troctolite, melatroctolite, and MZ olivine gabbro. MgO content in plagioclase is low for all lithologies (Fig. 3.8d), much lower than the MgO content of plagioclase in the basaltic lavas and sheeted dykes (Chapter 2). K_2O (<0.12 wt%) and FeO (<0.52 wt%) concentrations are low, and are not correlated with An content. Plagioclase compositions becomes more sodic upwards in the stratigraphy of the Liuyuan Complex, with the exception of the melatroctolite, which shows a large variation in An content in the LZ, compared with tight compositional range in the troctolite (Fig. 3.2c)

3.6.4 Amphibole

Amphibole in the melatroctolite are pargasites, whereas the podiform hornblende gabbro contains magnesio-hornblende (Hawthorne et al. 2012, Locock 2013). Optical zoning was observed in pargasite, but not in magnesio-hornblende. Actinolite present in the podiform hornblende gabbro is interpreted to reflect greenschist facies metamorphism and is not further discussed. The pargasites in the melatroctolite have higher mg# (74-83) than the magnesio-hornblendes (68-76). The Al_2O_3 contents of pargasite (8.27-10.80 wt%) and magnesio-hornblende (7.66-10.68 wt%) are similar (Fig. 9f), but the melatroctolite pargasite grains have higher TiO_2, (up to 4.29 wt%). Cr contents are high, 0.12-0.44 wt% in pargasite, and 0.13-0.58 wt% in the magnesio-hornblendes. A pargasite grain in melatroctolite sample 18LYS-7275B is strongly zoned, with the dark brown core showing lower Al_2O_3 (9-15 vs. 10.80 wt%), MgO (17.11 vs. 17.20 wt%), CaO (11.44 vs. 11.66 wt%), higher Na_2O (30.5 vs. 2.90 wt%), K_2O (0.36-0.24 wt%) and FeO (6.65-6.59 wt%), and considerable higher TiO_2 (4.29 vs. 2.68 wt%) when compared with the light brown rim.

3.7 Geothermometry and Geohygrometry

The Putirka (2008) clinopyroxene thermometer (Eq. 32d) was applied using the WinPyrox software of Yavuz (2013). This thermometer is based on a new calibration of the clinopyroxene-only thermometer of Nimis and Taylor (2000), and is based on the activities of Ti, Fe, Al, Cr, Na, K, and the activity of the enstatite endmember. The lower temperature crystallization limit for this mineral was estimated with the Al_2O3 thermometer of France et al. (2010). According to the Putirka (2008) thermometer, clinopyroxene from the troctolites crystallized between 1211 ^oC and 1202 ^oC, with no systematic difference between interstitial grains and oikocrysts. The oikocrysts in the melatroctolite yielded temperatures between 1211 and 1196 ^oC. Clinopyroxene in the gabbros yielded the lowest crystallization temperatures, ranging between 1208-1072 ^oC for the MZ olivine gabbro and 1198-1168 ^oC for the podiform hornblende gabbro (Fig. 3.9a). The France et al. (2010) thermometer suggests lower crystallization temperatures: troctolite = 1057-1001 ^oC, melatroctolite = 1082-1050 ^oC, MZ olivine gabbro = 1055-942 ^oC, and podiform hornblende gabbro = 1101-877 ^oC (Fig. 3.9a).

Amphibole crystallization temperature was calculated using the hornblende-only thermometer of Putirka (2016) and the titanium–in-hornblende thermometer of Liao et al. (2021). The results presented here are the average temperature produced by both thermometers when applied to a single amphibole analysis. Samples in which the results of both thermometers differed by more than 50 ^oC were discarded. Temperature results from pargasite in the melatroctolite range between 1011-983 ^oC. In the podiform hornblende gabbro, magnesio-hornblende crystallization temperatures range between 884 ^oC and 818 ^oC. These amphibole crystallization temperatures provide our best estimates of the solidus of the melatroctolite and podiform hornblende gabbro.

Amphibole can also be used as geohygrometer (Merzbacher and Eggler 1984, Ridolfi et al. 2010, Krawczynski, et al. 2012). The geohygrometer of Ridolfi et al. (2010) was applied to the amphibole analyses in the Liuyuan Complex. Pargasite in the melatroctolite yielded H_2O melt contents between 2.3-5.0 wt% (Fig. 10b). Notably, a pargasite grain in melatroctolite sample 18LYS-7375B recorded a core to rim H_2O variation from 3.0 to 5 wt% in the coexisting melt. Melt H_2O calculated from magnesio-hornblende in the hornblende gabbro range from 4.5 to 5.9 wt% (Fig. 3.9b). The margin of error in the geohygrometer results ranges between 0.4-0.9 wt%.

3.8 Discussion

3.8.1 Magmatic Evolution

Molar element ratio diagrams (Stanley 2017) were used to investigate and clarify the cumulus processes in the Liuyuan Complex's lower crust. This provides a geochemical approach to identifying cumulus minerals and an evaluation of their proportions, which can be used to test the petrographic observations as well as the results of the MELTS modeling of magmatic evolution among the Liuyuan volcanic rocks presented in Chapter 2. Figs. 3.10a and 3.10b show Pearce element ratio (PER) diagrams evaluating the effect of olivine + plagioclase and olivine + plagioclase + clinopyroxene sorting. The olivine + plagioclase model provides a good fit for the troctolite and melatroctolite, with the MZ olivine gabbro and podiform hornblende gabbro showing more scatter. The olivine + plagioclase + clinopyroxene model provides a good fit for all of the facies, possibly indicating clinopyroxene is a heteradcumulate mineral. In a (Ca+Na)/(Si+Al) (molar) vs. (Fe+Mg)/(Si+Al) (molar) diagram (Fig. 3.10c), the rocks from the Liuyuan Complex plot in a polygon defined by the plagioclase, olivine and clinopyroxene nodes, in accordance with their petrography and the MELTS thermodynamic model presented in

Chapter 2. The troctolite and melatroctolite plot along a mixing line between the plagioclase and olivine nodes, with the melatroctolite closest to the olivine node. The MZ olivine gabbro and the podiform hornblende gabbro are offset to towards the clinopyroxene node from the more leucocratic troctolite, indicating the larger influence of cumulus clinopyroxene or a larger trapped melt fraction (TMF). When the whole rock and measured olivine and plagioclase compositions are plotted in a Ca/Si (molar) vs. Mg/Si (molar) diagram (Fig. 3.10d); the troctolite and melatroctolite plot in a straight line between the measured olivine and plagioclase compositions, indicating that their chemistry is dominated by these two phases and implying a low trapped melt fraction. The low overall incompatible trace element concentrations, and positive Eu-Sr anomalies are consistent with a strongly cumulate origin. The podiform olivine gabbro and the intrusive hornblende gabbro plot closer to the clinopyroxene node and overlap the composition of basalts and sheeted dykes in Fig. 3.10c and 3.10d. Given their major and trace element compositions completely overlap that of the overlying basalts in the Liuyuan Complex, we suggest thee two facies represents quasi-liquid compositions (e.g. Lissenberg et al. 2004). The outcrop location of the podiform olivine gabbro, typically near the root of faults close to the base of the sheeted dyke complex further supports this interpretation.

The gradation of mineral compositions up section in the troctolite, melatroctolite, and MZ olivine gabbro in the Liuyuan Complex (Fig. 3.2b-d) further suggests they formed from a common fractional crystallization trend, with minor influence of melt back-reaction in the MZ olivine gabbro and the podiform hornblende gabbro. NiO in both olivine primocrysts and chadacrysts in the Liuyuan Complex plot along the model fractional crystallization curve, with the melatroctolite as the most primitive facies, with troctolite, the MZ olivine gabbro, and the podiform hornblende gabbro having formed from progressively more fractionated melts (Fig.

3.8a). The high Cr_2O_3 measured in the oikocrysts in the melatroctolite, troctolite, and MZ olivine gabbro are consistent with their formation from a primitive melt (Pedersen et al. 1996, Leuthold et al. 2018). Conversely, the large variation in the incompatible TiO_2 (Fig. 3.8c), at constant mg# in clinopyroxene suggests the possibility of late refertilization of early formed clinopyroxene by reaction with trapped residual melt (Dick et al. 2002, Coogan et a. 2000a, Coogan 2014).

The composition of olivine, clinopyroxene, and amphibole can be used to invert the composition of the liquids they were in equilibrium with. This allows us to evaluate the progression in fractionation trends and to evaluate the composition of parental melts. To better constrain the nature of the melts from which the Liuyuan cumulates formed and compare them with the sheeted dyke and extrusive facies, we calculated the Fe/Mg values of the equilibrium melt from olivine and pyroxene using the Fe=Mg exchange reaction coefficient (K_D). We used 0.30 (Roeder and Emslie 1970) for the olivine K_D; and calculated clinopyroxene Kd using Eq. 11 from Bédard (2010). These results are summarized in Fig. 3.11a, where the calculated melt Fe/Mg ratios are compared with the Fe/Mg values recorded by the overlying basalts and sheeted dykes. Melt Fe/Mg values in equilibrium with analyzed olivine ranges between 0.69-1.19 in the troctolite, 0.54-0.64 in the melatroctolite, and 0.46-0.53 in the MZ olivine gabbro. The only olivine grain observed in a podiform hornblende gabbro yielded a very evolved melt Fe/Mg value of 0.46. Clinopyroxene Fe/Mg ranges between 0.81-0.85 in the troctolite, 0.66-0.95 in the melatroctolite, 0.68-1.35 in the MZ olivine gabbro, and 0.75-3.34 in the podiform hornblende gabbro. Overall, the Fe/Mg ratios of the melts from which olivine and clinopyroxene in the plutonic rocks formed vary between 0.69-1.19 in troctolite, 0.54-95 in melatroctolite, 0.46-1.35 in MZ olivine gabbro and 0.46-3.34 in the podiform hornblende gabbro, all within the range defined by the basalts of the Liuyuan Complex (Chapter 2).

The Fe/Mg value of the liquid in equilibrium with amphibole used a fixed K_D of 0.36 (estimated from Pichavant and Macdonald 2007; Pichavant et al. 2002). Calculated Fe/Mg ratios of liquids in equilibrium with amphibole range between 0.61-1.14 in melatroctolite and broadly overlap with values calculated for the podiform hornblende gabbro (0.88-1.32, Fig. 3.11b). In the melatroctolite, liquid Fe/Mg values calculated from olivine, clinopyroxene, and pargasite all overlap, indicating the Fe/Mg of the interstitial amphibole was in equilibrium with the surrounding primocryst minerals. The high pargasite Cr_2O_3 contents are also indicative of a primitive melt, consistent with the interstitial habit of pargasite in the melatroctolite. In contrast, the replacive habit of magnesio-hornblende in the hornblende gabbro suggests a different origin. In in the hornblende gabbro, melt Fe/Mg calculated from magnesio-hornblende falls in the lower end of the range defined by the melt Fe/Mg calculated from olivine and clinopyroxene. The presence of corroded relic clinopyroxene in magnesio-hornblende observed in the podiform hornblende gabbro suggests a reaction between higher temperature primocryst clinopyroxene and a lower temperature, more hydrous residual melt. The melt H_2O content calculated from the magnesio-hornblende in the hornblende gabbro is higher than in the pargasite from the melatroctolite (averages of 5.1 wt% in the hornblende gabbro and 3.2 wt% in the melatroctolite), indicating they formed from a more hydrous melt, as well as a more evolved one. The geohygrometer results discussed here imply significant H_2O wt% enrichment from the inferred initial H_2O content of 0.5% of the parental melt of the Liuyuan Complex magmatic suite, suggesting there was significant in-situ crystallization of trapped pore melt. The formation of amphibole in both the melatroctolite and hornblende gabbro from residual primitive melt crystallization and back-reaction with interstitial melts, respectively, is consistent with the observed their observed texture. Accumulation of amphibole would result in MREE inflections in these rocks. No such inflections are present (Fig. 8b,d).

3.8.2 Trace Element Inversions and the Comagmatic Hypothesis

An important question is whether the gabbroic rocks in the Liuyuan Complex all belong to a single liquid line of descent (LLD) originating from a common parental liquid, or whether they differentiated from a variety of parental melts. The major and trace element variations of basalts and diabase form the Liuyuan Complex investigated in Chapter 2 showed that the Liuyuan basalts formed by 10-17% partial melting of a dominantly N-MORB-like spinel peridotite source enriched by subduction derived fluids that resemble modern back-arc basin basalts. Chapter 2 further presented MELTS (Gualda et al. 2012 and Ghiorso and Gualda 2015) to model a LLD for the Liuyuan Complex volcanics. The model LLD assumed fractionation at 1 kbar, with the $_fO_2$ set at the QFM buffer, and an initial water content of 0.5 wt%. The MELTS models yielded a typical tholeiitic crystallization order, with olivine as the first mineral to saturate in the liquid 1206 ^oC, followed by plagioclase (1201 ^oC), clinopyroxene (1186 ^oC), and ilmenite (1090 ^oC). The cumulates resulting from the fractionation of the basalts provide a good match for the gabbroic rocks. However, the MELTS model is restricted to major element compositions.

The equilibrium distribution method of Bédard (1994, 2001) was used to invert the trace element composition of parental melts from representative samples of the different plutonic facies of the Liuyuan Complex. The major assumptions of this method are that all minerals in the sample crystallized from the same melt at the same temperature; melt was trapped at high temperatures; and that there was no superimposed post-cumulus melt- metasomatic processes. The application of the method requires an accurate whole rock trace element analysis, a realistic cumulus mode, a set of coherent partition coefficients appropriate to the conditions, an estimate of the trapped melt fraction and how this changes the cumulus mode.

The starting mineral modes used in the calculation are from point counting (50 spots per thins section). Partition coefficients (D) for olivine and clinopyroxene were calculated using the equations of Bédard (2005) and Bédard (2013, with some modifications). D values for plagioclase followed the equations of Bédard (2006, with unpublished revisions). To maintain mass balance, a proportion of minerals equivalent to the assumed TMF has to be removed from the rock mineral mode. Details on this backstripping procedure are presented in Bédard (2001). Olivine Fo content, clinopyroxene mg#, and Al^{iv}, and plagioclase An content were used as inputs for the D parameterizations. Minimal TMF values were constrained by the point at which a mineral disappears from the mode during the backstripping procedure. In all modelled samples, clinopyroxene was the first mineral out of the mode. This clinopyroxene-out TMF is a useful reference point but may not accurately reflect the actual TMF, e.g. the pore melt could have crystallized olivine and plagioclase before saturating in clinopyroxene. The implications of this clinopyroxene-out constrain for the petrology of these rocks will be discussed below. The resulting model liquid was then compared to target compositions.

The basalts of the Liuyuan Complex were used as a target composition. Highlighted in all plots are the trace element composition of samples 18LYS-7179 and 19LYS-7182B, the two most primitive samples from Chapter 2. Basalt 18LYS-7179 is variolitic, with approximately 10% plagioclase microlites, with SiO_2 of 47.86 wt%, MgO of 9.82 wt%, mg# of 64.81, Al_2O_3 of 15.82 wt%, 222 ppm of Ni, and 32 ppm of Sc. Sample 19LYS-8172B is a variolitic basalt with, approximately 15% of plagioclase microlites and no observed phenocrysts, with SiO_2 of 46.78 wt%, MgO of 9.58 wt%, mg# of 67.72, Al_2O_3 of 15.52 wt%, 176 ppm of Ni, and 33 ppm of Sc.

The textural and geochemical features of these primitive basalts suggest they represent liquid compositions minimally affected by fractionation or mineral accumulation after they were generated from a more primitive parental mantle melt. Five representative samples from the major plutonic facies of the Liuyuan Complex were chosen for the trace element inversion procedure (Fig. 3.12.

Four samples from the LZ were modelled (Fig. 3.12a). Sample 19LYS-8165 is the most feldspar-rich troctolite studied. A TMF of 4.5% exhausts clinopyroxene and results in a residual mode of 11% olivine and 84% plagioclase (Fig. 3.12b). Sample 18LYS-7008B is the most olivine-rich troctolite in the dataset, and has clinopyroxene oikocrysts. A TMF of 7% resulted in a residual mode of 45% olivine and 48% plagioclase in this sample (Fig. 3.12b). Sample 19LYS-7574 has a composition close to the average MgO and Al_2O_3 contents of the troctolites. The clinopyroxene-out TMF value for this sample is 15.5%, with a residual mode of 29% olivine and 55% plagioclase (Fig. 3.12b). Melatroctolite sample 18LYS-7365B is the freshest sample of this facies available, containing both clinopyroxene oikocrysts and interstitial pargasite. Pargasite is a minor phase (<1% modal) and was ignored during backstripping. For this sample a residual mode of 61% olivine and 24% plagioclase was reached at a TMF of 14% (Fig. 3.12b). The resulting modelled liquids are shown in Fig 3.12b. They have similar shapes and anomalies, overlapping the basalt and diabase compositional field.

For all the samples so far discussed, a slightly lower TMF (1-2 % lower than the values stated in the prior discussion) yields model melt trace element profiles plotting between the primitive lava samples 18LYS-7179 and 19LYS-7182B, but would leave small amounts of clinopyroxene in the residual mode. This implies some degree of clinopyroxene accumulation, likely as a heteradcumulate phase. The presence of small amounts of heteradcumulate clinopyroxene was previously hinted at by the behavior of the troctolite and melatroctolite in the molar element ratio plots shown in Fig. 3.10.

Sample 18LYS-7128A is a typical MZ olivine gabbro (Fig. 3.12a), with composition close to the average MgO and Al_2O_3 content of this unit. A very high TMF of 58% would be required to fully eliminate clinopyroxene from the cumulate assemblage of this olivine gabbro 18LYS-7128A, resulting in a residual mode of 6% olivine and 36% plagioclase. The resulting liquid from this very high TMF model has a composition slightly more primitive than the basalt (Fig. 3.12). A TMF of 58% is, however, unrealistically high. Fig. 3.12c also shows the results of four other models with TMF of 5%, 10%, 15%, and 20%, more in line with the clinopyroxene-out TMF values for the LZ troctolite and melatroctolite. These lower TMF models, leaving varying amounts of clinopyroxene in the mode, result in inverted liquids that are a good match for the primitive basalts of the Liuyuan Complex. The presence of clinopyroxene in the mode (23% modal clinopyroxene for a 5% TMF, 17% modal clinopyroxene for a 20% TMF) implies the accumulation of clinopyroxene in the MZ olivine gabbro.

Results from trace element inversions indicate the troctolite, melatroctolite, and MZ olivine gabbro formed from liquids with trace element compositions that are essentially identical to tholeiitic basaltic dykes and extrusives from the Liuyuan Complex, showing similar positive Cs, Rb, Pb, and Th anomalies and negative Nb anomalies, similar slopes and similar overall trace element abundances. Model trapped melt fractions vary from model to model depending on the proportions and textures of the minerals. Low model TMF (< 7 %) are in the Al_2O_3- and MgO-rich endmembers of the troctolitic suite that have only small amounts of interstitial clinopyroxene. Higher model TMF (< 15.5 %) in the melatroctolite and poikilitic troctolite are consistent with larger amounts of poikilitic clinopyroxene and interstitial pargasite. Trace element inversions also indicate the accumulation of clinopyroxene took place in the MZ olivine gabbro. This result is consistent with the thermodynamic model presented in Chapter 2.

The trace element inversions also suggest the Liuyuan Complex gabbroic rocks formed from a single parental melt, in contrast to several other recorded ophiolites (e.g. Bédard 1991, 1999, Dilek and Thy 2009, Ulrich et al. 2010, Rollinson 2019). The Liuyuan Complex troctolite and MZ olivine gabbro show a consistent upward cryptic mineral fractionation trend (Fig. 3.2c-d) with the troctolite recording more primitive olivine and plagioclase compositions than the olivine gabbro. Clinopyroxene shows a narrow mg# range in the LZ-MZ sequence. The narrow mg# range of clinopyroxene in these facies is consistent with a minor phase crystallizing mostly from trapped melt, with clinopyroxene saturation occurring during cooling at a common temperature/melt composition constrained by the position of the cotectic. This interpretation is consistent with thermometry results (Fig. 3.9), indicating a narrow range of fairly low clinopyroxene crystallization temperatures.

Trace element inversion on the melatroctolite, the facies with the most primitive olivine compositions in the dataset, generated an equilibrium melt very similar in shape to other model melts from more evolved troctolite and olivine gabbro samples (Fig. 14), and to the Liuyuan Complex extrusives. As they are embedded within more evolved troctolites, this suggests the melatroctolite did not form from a different type of magma, but from primitive replenishments to an already evolved crustal melt body crystallizing troctolite. Whether the replenishments are intra-cumulate sills emplaced into troctolitic hosts, or whether they represent successive chamber floor deposits, cannot be determined with certainty, but the presence of pargasite in the melatroctolite perhaps favors the sill hypothesis, as volatiles released during crystallization would have less chance to escape in this scenario.

3.8.3 Tectonic Setting

Chapter 2 presented an investigation of major and trace element variations of basalts and diabase from the Liuyuan Complex. Trace element fingerprinting of the basalt and diabase using Th/Yb, Nb/Yb, V(ppm)/Ti/1000(ppm), La_N/Sm_N, and La_N/Nb_N indicates they formed in a back-arc basin setting (Chapter 2). The composition of coexisting plagioclase and clinopyroxene of the gabbroic rocks can be used to further test the back-arc basin formation hypothesis. Plagioclase and clinopyroxene in oceanic gabbros crystalizing at mid-ocean ridges start at high anorthite content and clinopyroxene mg# defining a shallow slope toward more evolved compositions. Gabbroic rocks crystallized in back-arc basins have higher water contents and typically show a different trend, with an initially steeper gradient in plagioclase composition at near constant clinopyroxene mg#, that shallows at more evolved mineral compositions (Sanfillippo et al. 2013, 2016, Basch et al. 2019, 2020). Based on their compiled dataset from several back-arc basin megamullions, Basch et al. (2020) proposes this trend is a typical feature of back-arc basins.

The anorthite content in coexisting plagioclase vs. clinopyroxene mg# in the plutonic rocks of the Liuyuan Complex is shown in Fig. 3.12. Troctolites in the Liuyuan Complex contain the most primitive plagioclase compositions, with a narrow variation in clinopyroxene mg#. Two analyses on poikilitic troctolite deviate from this pattern, showing similar anorthite content but more evolved clinopyroxene oikocryst compositions. The compositional range recorded by the MZ olivine gabbro spans the largest variation in anorthite content, still with a comparatively narrow variation in clinopyroxene mg#. The MZ olivine gabbro trend is parallel to the subvertical back-arc basin trend defined by Basch et al. (2020), with slightly more evolved compositions. Despite the limited number of analysis available from the melatroctolite, in the plagioclase An vs. clinopyroxene mg# diagram this facies defines a trend parallel to the olivine gabbro, with similar range in plagioclase An content and clinopyroxene with higher mg#. The podiform hornblende gabbro shows a larger variation in clinopyroxene mg# for anorthite contents comparable to the other igneous facies. Overall, the gabbroic rocks of the Liuyuan Complex define fractionation trends consistent with a back-arc basin setting (Bash et al. 2020).

3.9 Summary and Conclusions

Located along the southern edge of the CAOB, the geology and tectonic setting of the Permian Liuyuan Complex is of critical importance in defining tectonic models for how the oceanic basins of the CAOB closed. In recent years, workers have debated whether the Liuyuan Complex formed as a forearc ophiolite (Xiao et al. 2010, Mao et al. 2012), or as a continental rift (Wang et al. 2017, He et al. 2018). Based on extensive mapping of the Liuyuan Complex and petrological studies of the dominant basalt facies, Chapter 2 documented the presence of a well-developed sheeted dyke complex at the contact between the lower gabbroic rocks and overlying basalts, indicating the Liuyuan Complex is an ophiolite, and proposed a back-arc setting. However, no detailed work on the lower crustal rocks of the Liuyuan Complex has been published.

In this chapter, we identify and provide petrographic data and whole rock and mineral chemistry data on the troctolite, melatroctolite, MZ olivine gabbro, podiform olivine gabbro, podiform hornblende gabbro, and intrusive hornblende gabbro facies that comprise the lowermost exposed part of the Liuyuan Complex. The troctolite and melatroctolite have low incompatible trace element concentrations, and major element data and petrography show they represent accumulations of olivine and plagioclase, with varying degrees of interstitial and poikilitic clinopyroxene forming from trapped melt fractions (TMF) ranging between 5 and 15%. Small amounts of heteradcumulate clinopyroxene may also be present in these facies. The melatroctolite is interpreted as formed via primitive replenishments of the magma chamber. The addition clinopyroxene as a trapped melt fraction and as a cumulate mineral to the accumulating assemblage of olivine and plagioclase is inferred for the MZ olivine gabbro facies. The podiform olivine gabbro and intrusive hornblende gabbro located immediately beneath the sheeted dyke complex differ the other facies in being less depleted in incompatible trace elements and have major element signatures indicating that they are quasi-liquid compositions that could have fed the overlying sheeted dykes and lavas.

Trace element inversions confirm that these diverse plutonic facies are consanguineous and are comagmatic with the overlying sheeted dykes and basalts. The covariation of plagioclase and clinopyroxene in the troctolite, melatroctolite, and MZ olivine gabbro is similar to what is observed in modern back-arc basins, with plagioclase moving to lower An-contents with little variation in clinopyroxene mg#. Amphibole formed as a late magmatic phase in the melatroctolite, indicating entrapment of hydrous melt. Amphibole formed as a reaction product between relic clinopyroxene and primitive melts in the podiform hornblende gabbro. The high water contents indicated by the presence of magmatic amphibole is consistent with the back-arc ophiolite model proposed by Chapters 2 and 4.

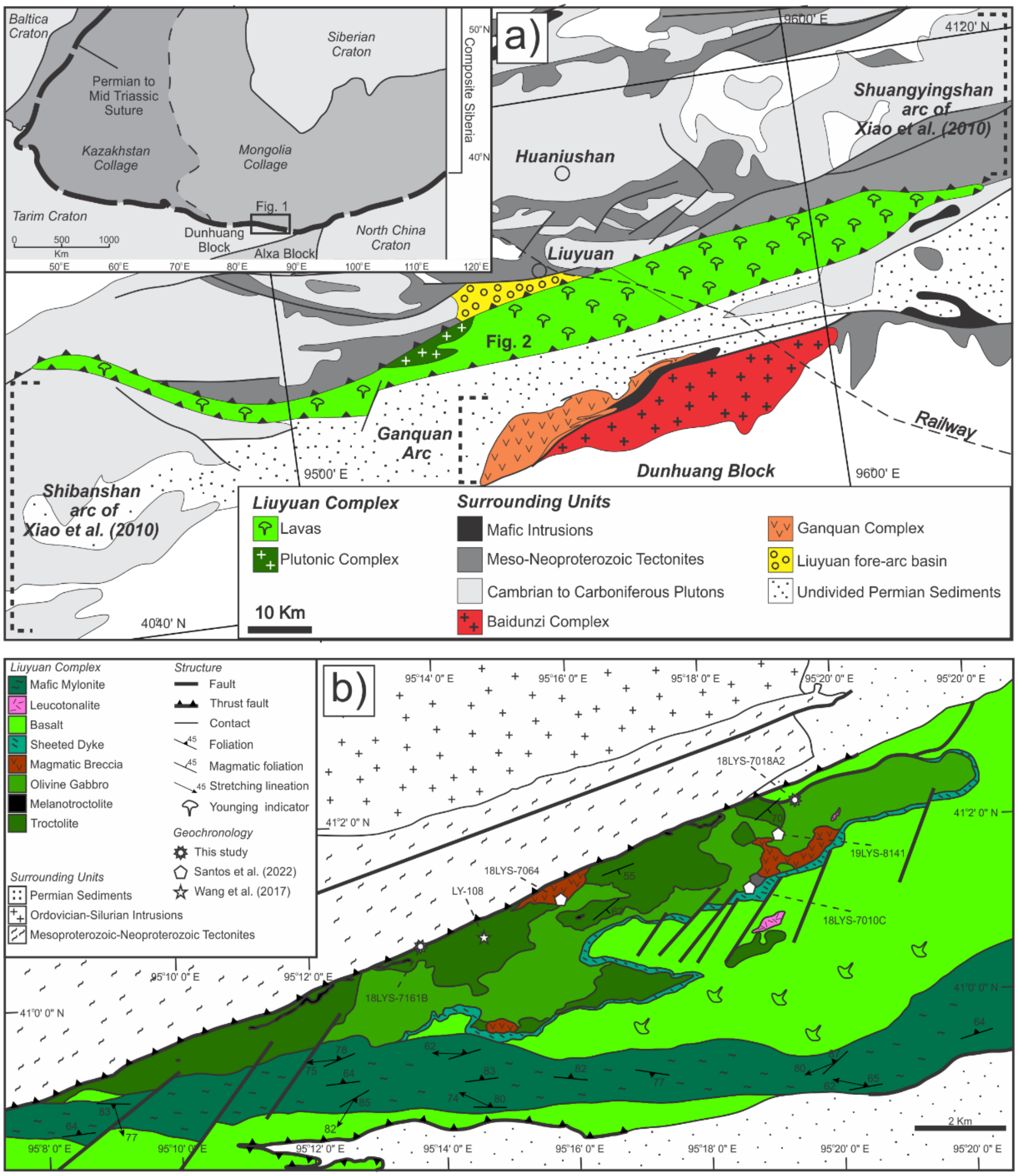

Figure 3.1: (a) Geological context of the Liuyuan Context in the southern Central Asian Orogenic Belt. (b) Geological map of the Liuyuan Complex, focused on the gabbroic rocks.

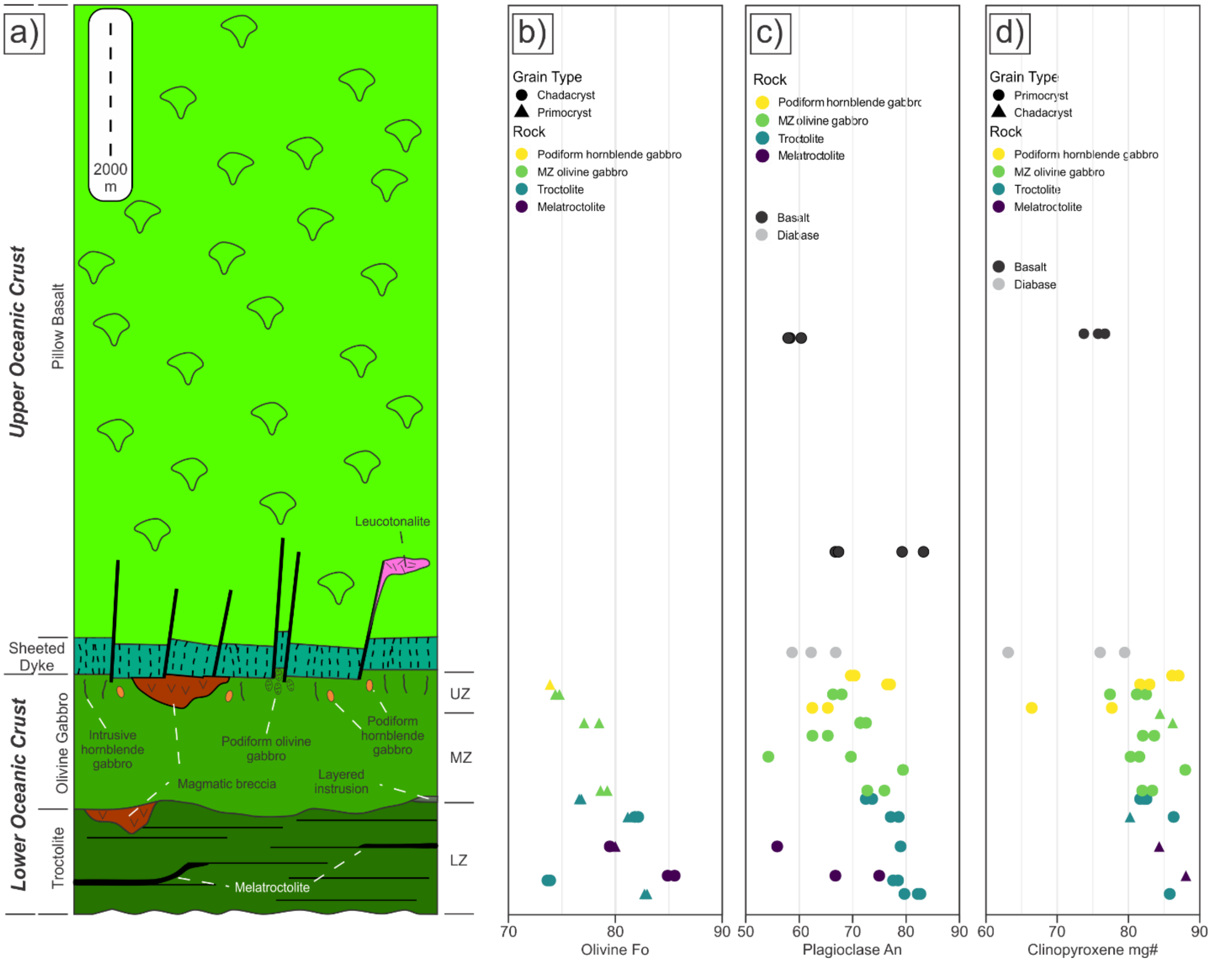

Figure 3.2: (a) Measured stratigraphic column of the Liuyuan Complex. Podiform olivine gabbro, podiform hornblende gabbro, intrusive hornblende gabbro not drawn to scale. (b) Variation of olivine Fo, (c) plagioclase An, and (d) clinopyroxene mg# along the stratigraphy of the Liuyuan Complex. LZ (lower zone), MZ (middle zone), and UZ (upper zone).

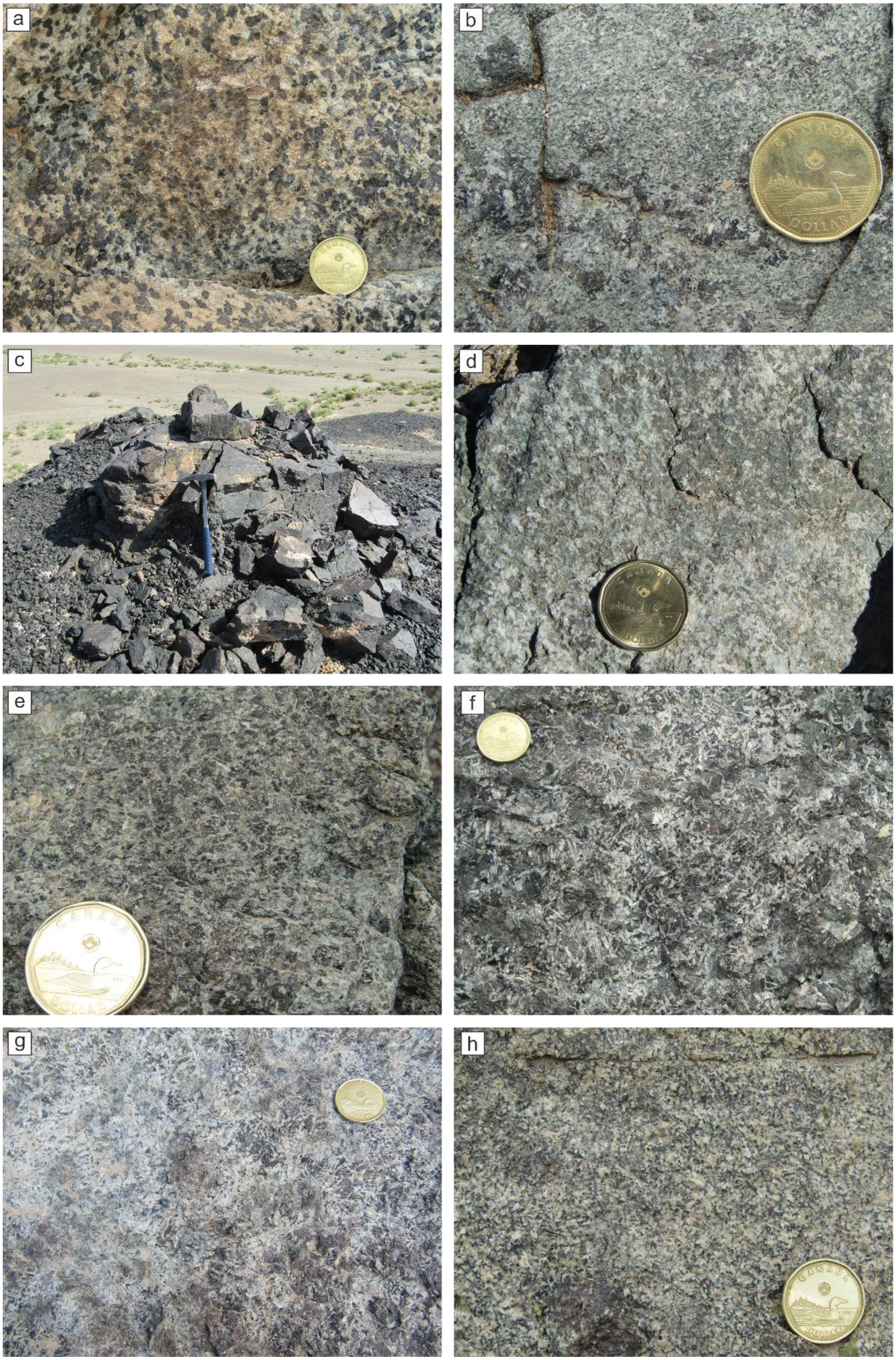
a
b
c
d
e
f
g
h

Figure 3.3: Outcrop images of the plutonic facies of the Liuyuan Complex. (a) Medium-grained troctolite. (b) Medium-grained troctolite showing clinopyroxene oikocrysts up to 2 cm in diameter. (c) Melatroctolite layer in the troctolite at the base of the Liuyuan Complex. (d) Equigranular medium-grained MZ olivine gabbro, with plagioclase laths and granular olivine forming a cumulate framework, with interstitial clinopyroxene. (e) MZ medium-grained olivine gabbro, with increasing modal clinopyroxene, forming interstitial and locally poikilitic grains. (f) Medium-grained ophitic MZ olivine gabbro, with coarser interstitial clinopyroxene partially enclosing plagioclase laths. (g) Coarse-grained poikilitic MZ olivine gabbro, with clinopyroxene oikocrysts of ~2.5 cm in diameter enclosing granular olivine grains and plagioclase laths. (h) Medium grained intrusive hornblende gabbro. Hammer is 35 cm in length and coin 2.65 cm is in diameter.

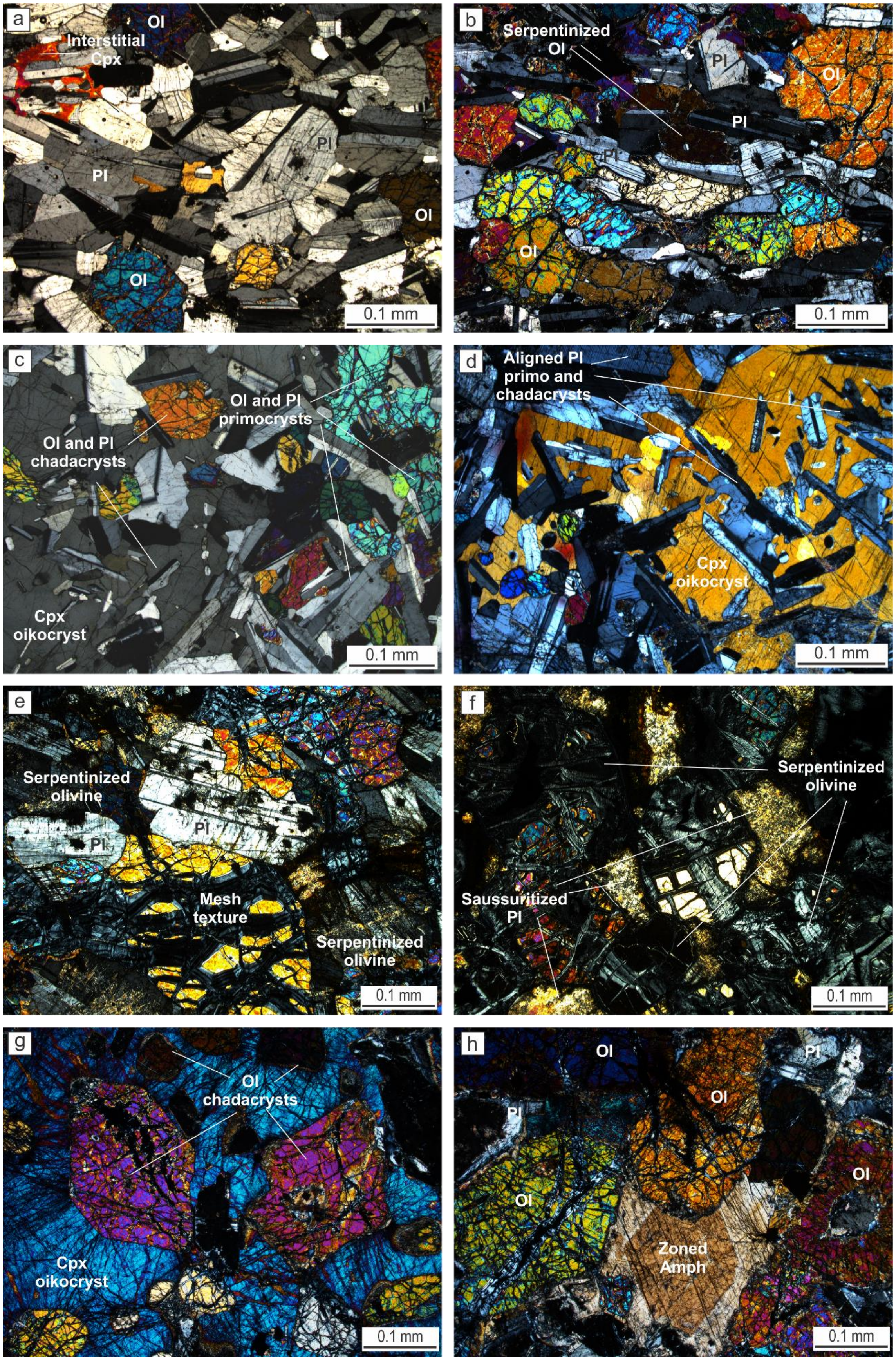
a
Ol
Interstitial Cpx
Pl
Pl
Ol
Ol
0.1 mm
b
Serpentinized Ol
Pl
Ol
Pl
Pl
Ol
0.1 mm
c
Ol and Pl primocrysts
Ol and Pl chadacrysts
Cpx oikocryst
0.1 mm
d
Aligned Pl primo and chadacrysts
Cpx oikocryst
0.1 mm
e
Serpentinized olivine
Pl
Pl
Mesh texture
Serpentinized olivine
0.1 mm
f
Serpentinized olivine
Saussuritized Pl
0.1 mm
g
Ol chadacrysts
Cpx oikocryst
0.1 mm
h
Ol
Pl
Ol
Pl
Ol
Ol
Zoned Amph
0.1 mm

Figure 3.4: Micrographs (crossed nicols) of the troctolite (a-d) and melatroctolite (d-h) units. (a) Leucocratic troctolite 19LYS-8165, with the highest Al_2O_3 of the troctolite facies in the Liuyuan Complex. Note the dihedral angles approaching 120^o in the plagioclase aggregates. A minor clinopyroxene (orange interference color in the upper left corner) has interstitial habit. (b) Melanocratic troctolite 18LYS-7008B, with the highest MgO of the troctolite facies in the Liuyuan Complex. Dihedral angles between olivine and plagioclase approaches 120^o. (c) Clinopyroxene oikocryst containing olivine and plagioclase chadacrysts. Chadacrysts show more rounded lath terminations and are finer grained than their primocryst counterparts. Troctolite sample 19LYS-8167B. (d) Clinopyroxene oikocryst with plagioclase chadacrysts that share the magmatic foliation of the surrounding coarser cumulus plagioclase in troctolite 19LYS8167B. (e) Fresh plagioclase and partially serpentinized olivine showing an incipient mesh texture in melatroctolite sample 19LYS-7311B. (f) Serpentinized olivine and sausuritized plagioclase grains in melatroctolite 19LYS-7662. (g) Fresh euhedral olivine chadacrysts in a clinopyroxene oikocryst in melatroctolite sample 18LYS-7375B. (h) Zoned interstitial brown amphibole surrounded by olivine and plagioclase primocrysts in melatroctolite sample 18LYS-7375B. Scale bar of 0.1mm in all pictures.

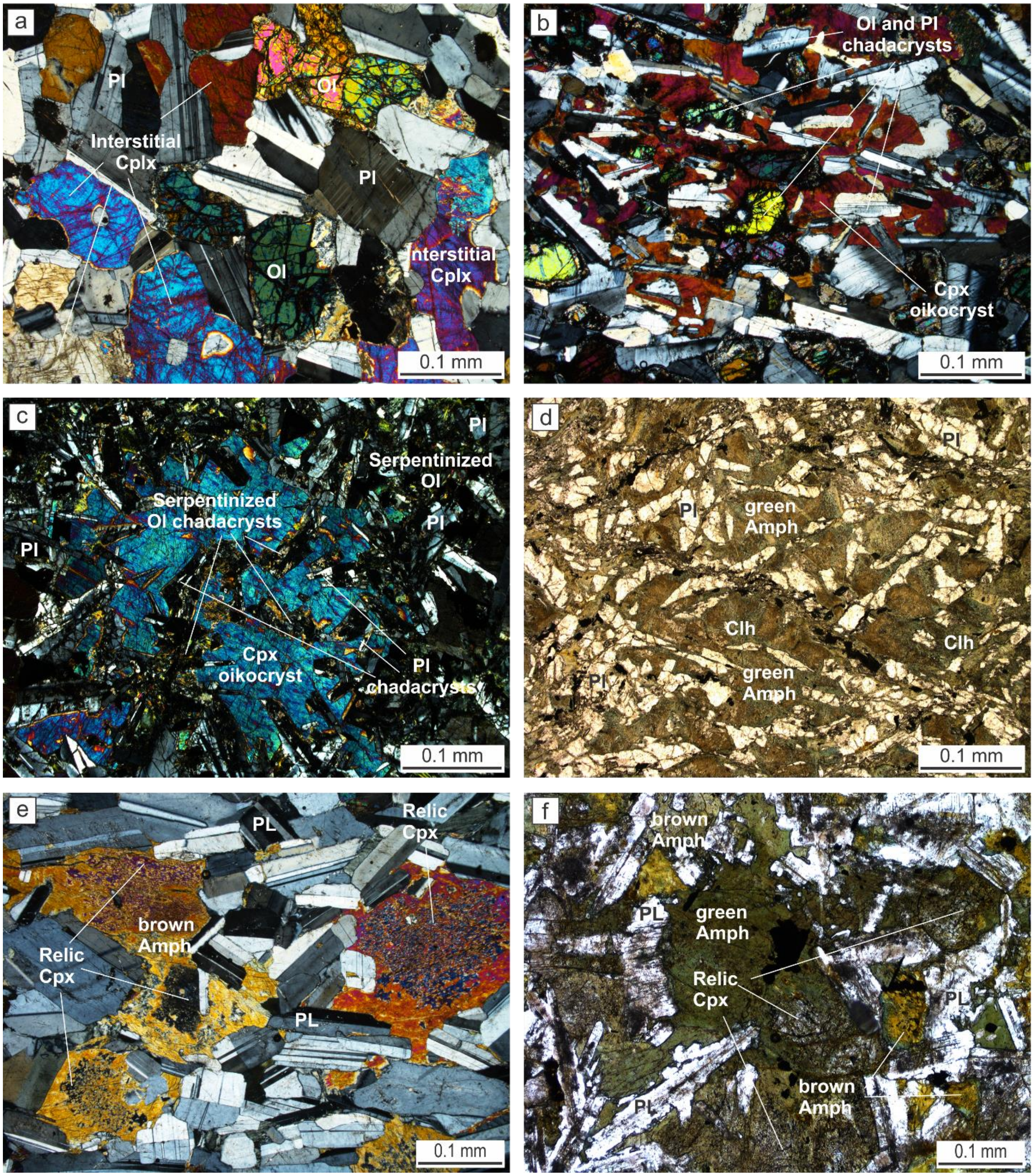

Figure 3.5: Micrographs (crossed nicols for a-c, and e; plane polarized light for d, and f) of the MZ olivine gabbro (a-b), podiform olivine gabbro (c-d) and podiform hornblende gabbro (e), and intrusive hornblende gabbro (f). (a) MZ olivine gabbro 18LYS-7002B with subequal amounts of

olivine and plagioclase and interstitial clinopyroxene (low relief and lower second order interference colors). (b) Clinopyroxene oikocryst (dark red) with abundant olivine and oriented plagioclase chadacrysts in MZ olivine gabbro 18LYS-7009C. Cumulus and chadacrysts plagioclase share the same magmatic foliation. (c) Metasomatized podiform olivine gabbro 18LYS-7318A, with serpentine forming pseudomorphs of olivine and intense saussurite alteration of plagioclase. An clinopyroxene oikocryst at the center of the figure remains fresh. (d) Greenschist facies podiform metagabbro 19LYS-8113, with clinopyroxene replaced by tremolite and minor chlorite, and albitized plagioclase. Ophitic to sub ophitic intergrowths are still discernible. (e) Medium-grained podiform hornblende gabbro 19LYS-8181, showing a cumulate framework of plagioclase, with clinopyroxene largely replaced by brown amphibole (yellow to orange second order birefringence). Spongy clinopyroxene relics within the amphibole have constant extinction angles, showing they were originally blocky cumulus clinopyroxene grains. Dihedral angles on plagioclase aggregates approaches 120^{o}. (f) Intrusive hornblende gabbro 18LYS-7118B1 retrogressed to greenschist facies, with green amphibole replacing brown amphibole. Relic clinopyroxene is still preserved. Scale bar of 500 µm in all pictures.. Relic clinopyroxene is still preserved. Scale bar of 500 µm in all pictures.

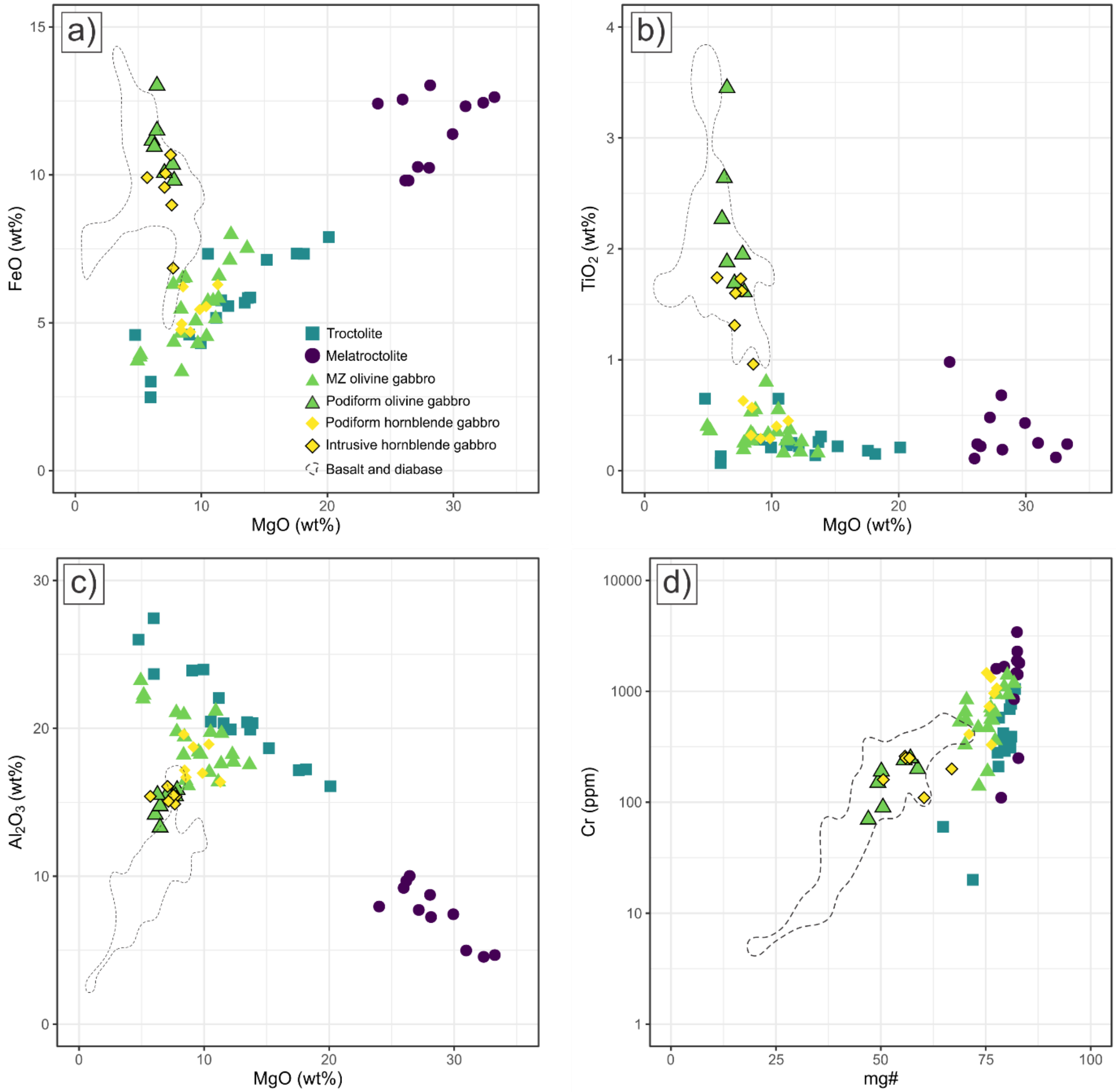

Figure 3.6: Major and trace element geochemistry. (a) FeO vs. MgO. (b) TiO_2 vs. MgO. (c) Al_2O_3 vs MgO. (d) Cr (ppm) vs mg#.

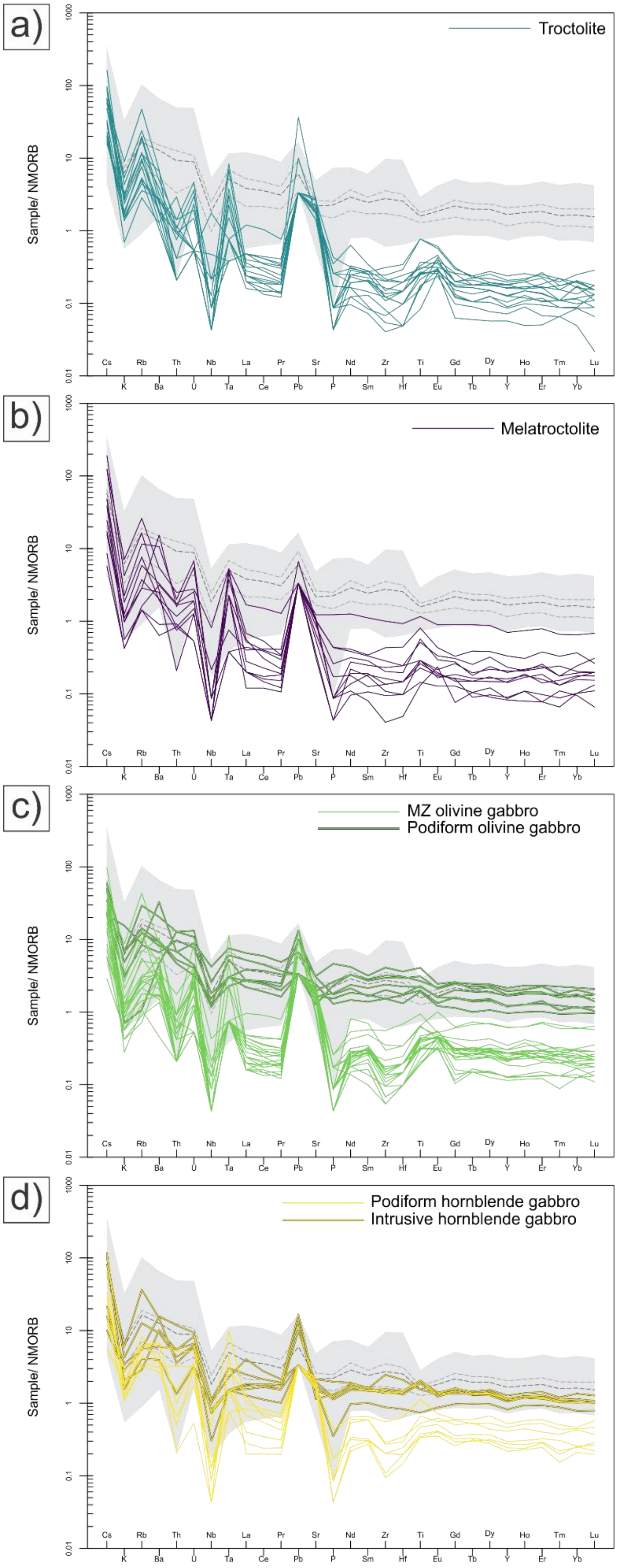
a)
Troctolite
b)
Melatroctolite
c)
MZ olivine gabbro
Podiform olivine gabbro
d)
Podiform hornblende gabbro
Intrusive hornblende gabbro
Sample/ NMORB
1000
100
10
1
0.1
0.01
Cs
K
Rb
Ba
Th
U
Nb
Ta
La
Ce
Pr
Pb
Sr
P
Nd
Sm
Zr
Hf
Ti
Eu
Gd
Tb
Dy
Y
Ho
Er
Tm
Yb
Lu

Figure 3.7: Extended trace element patterns. (a) Troctolite, Field in gray shows the range of compositions sampled in the basalts and dykes from Liuyuan complex. The basalt average composition (dark dashed line), and the interquartile range (light dashed lines) are shown. (b) Melatroctolite layers, (c) olivine gabbro, and (d) hornblende gabbro. Data normalized by the NMORB of Sun and McDonough (1989).

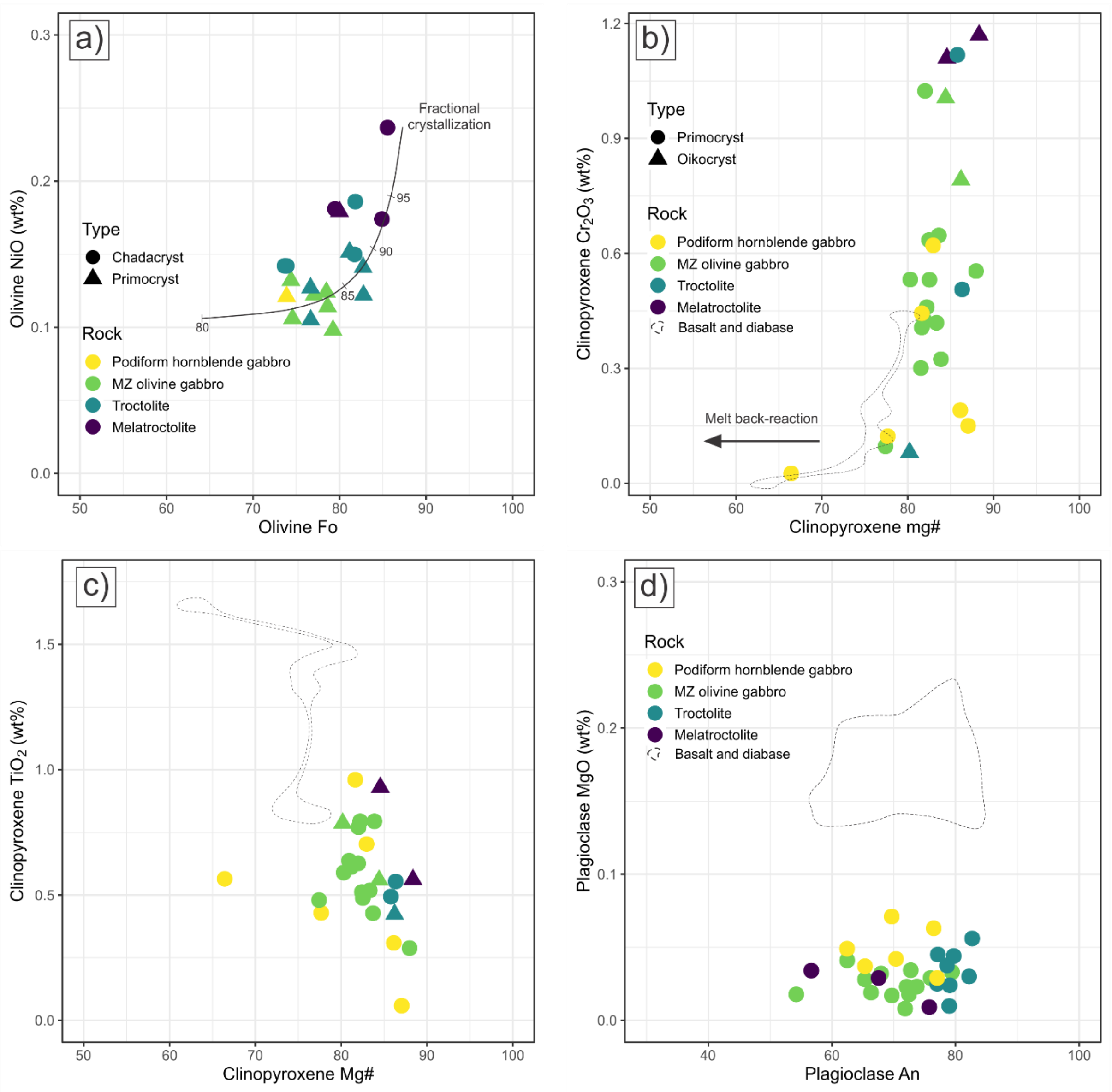

Figure 3.8: Mineral chemistry of the gabbroic rocks from the Liuyuan Complex. (a) Olivine NiO vs. olivine mg#. (b) Clinopyroxene Cr_2O_3 vs. clinopyroxene mg#. (c) Clinopyroxene TiO_2 vs. clinopyroxene mg#. (e) Plagioclase MgO vs. plagioclase An. Compositions of clinopyroxene and plagioclase phenocrysts in the sheeted dyke diabase and basalt of the Liuyuan Complex from Chapter 2.

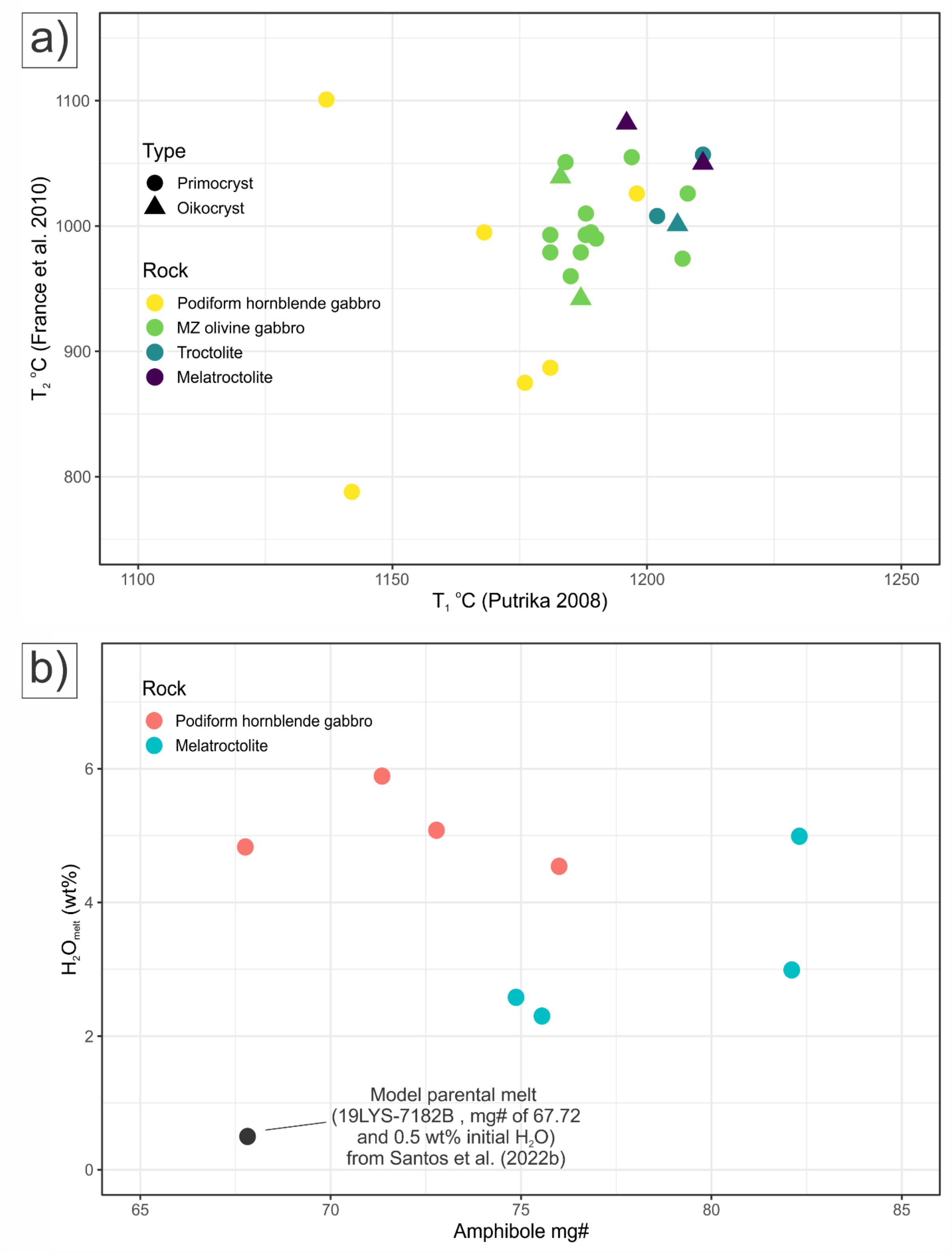
a)
Type
● Primocryst
▲ Oikocryst
Rock
● Podiform hornblende gabbro
● MZ olivine gabbro
● Troctolite
● Melatroctolite
T_2 °C (France et al. 2010)
800
900
1000
1100
1100
1150
1200
1250
T_1 °C (Putrika 2008)
b)
Rock
● Podiform hornblende gabbro
● Melatroctolite
H_2O_{melt} (wt%)
0
2
4
6
65
70
75
80
85
Amphibole mg#
Model parental melt
(19LYS-7182B , mg# of 67.72
and 0.5 wt% initial H_2O)
from Santos et al. (2022b)

Figure 3.9: (a) Results of France et al. (2010) vs. Putirka (2008) single-clinopyroxene thermometers (b) Geohygrometer results (Ridolfi et al. 2010) for amphibole vs. amphibole mg#.

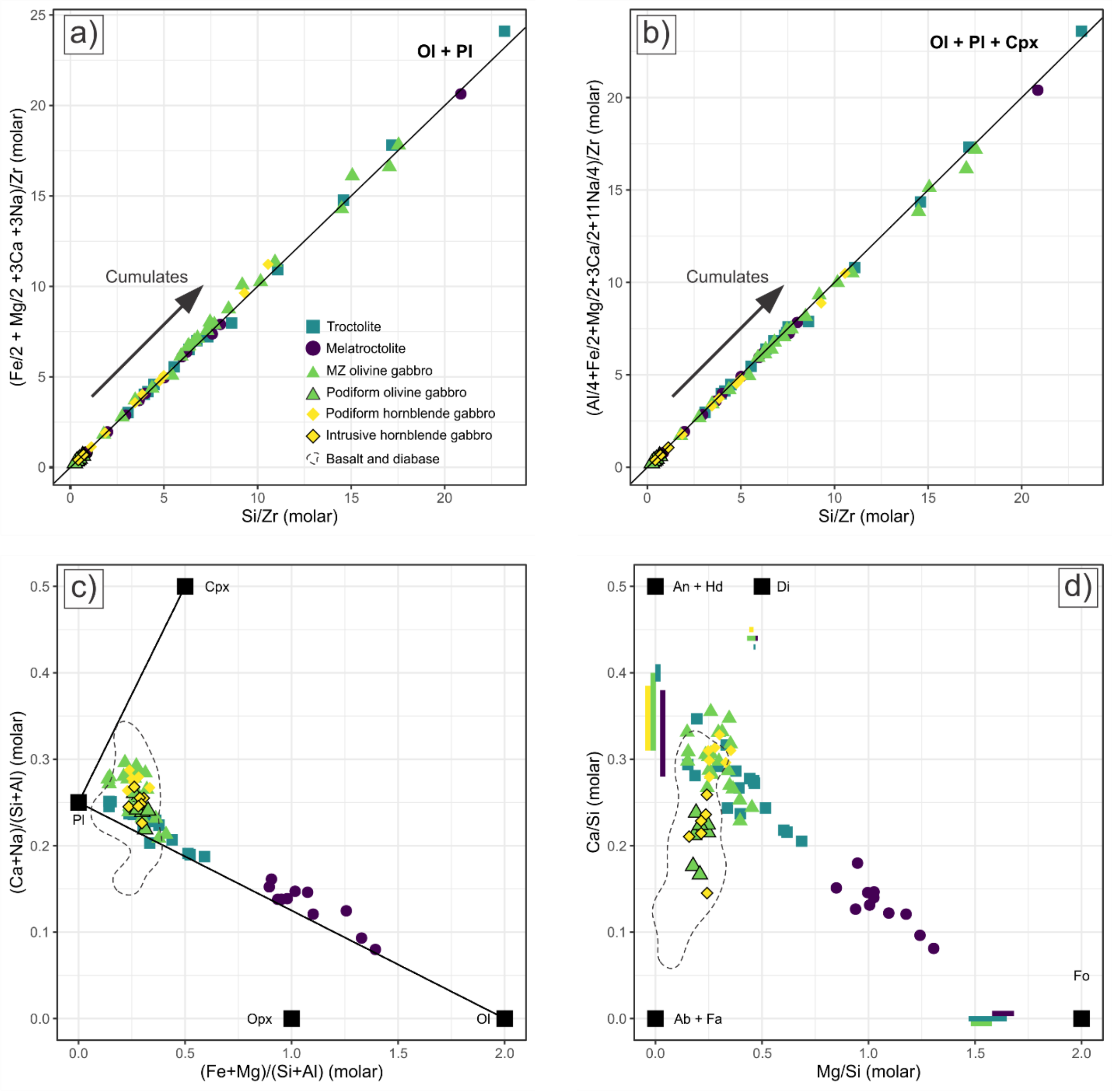

Figure 3.10: Molar element ratio diagrams (Pearce 1968, Stanley 2017) applied to plutonic rocks of the Liuyuan Complex showing the effects of olivine + plagioclase (a), and olivine + plagioclase + clinopyroxene (b) sorting. (c) (Ca+Na)/(Si+Al) vs. (Fe+Mg)/(Si+Al) diagram. The rocks of the Liuyuan complex plot in a field between the Pl – Ol – Cpx nodes. Note the distinct

troctolitic and gabbroic trends; with most troctolite and melatroctolite reflecting sorting of olivine and plagioclase primocrysts, whereas the MZ olivine gabbro shows presence of cumulus clinopyroxene. (d) Ca/Si vs. Mg/Si diagram. The colored bars (following the same color convention as rock types) at the abscissa and ordinate represent, respectively, the range in measured olivine and plagioclase compositions in the respective rock types. Clinopyroxene compositions are represented by averaging the wollastonite endmember of each unit.

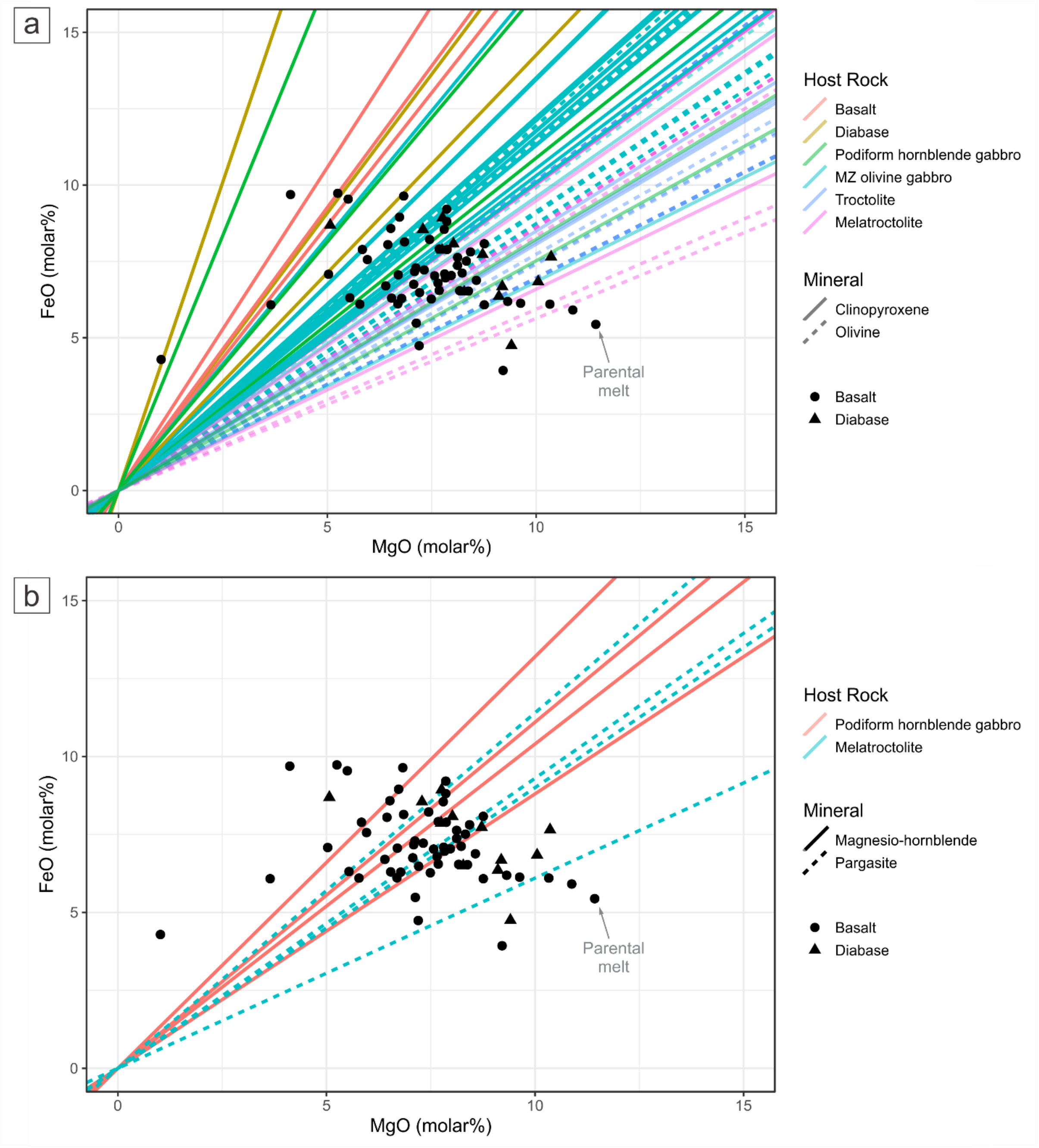

Figure 3.11: (a) FeO vs MgO (molar%) diagram showing melt FeO/MgO (molar) calculated from individual olivine and clinopyroxene mineral analysis are plotted as dashed and continuous lines (respectively). Olivine grains yield more primitive model melts than clinopyroxene. Olivine and clinopyroxene K_D values from Roeder and Emslie (1970) and Bédard (2010), respectively. (b) FeO vs MgO (molar%) of melt calculated from amphibole using the K_D value from Pichavant

and Macdonald (2007) and Pichavant et al. (2002). The melt FeO/MgO values calculated from the plutonic facies of the Liuyuan complex overlaps the FeO/MgO of coexisting lavas and dykes from the same complex. Basaltic lavas and diabase from the upper part of the Liuyuan Complex are plotted for reference (Santos et al. 2022). The sample marked by the gray arrow was used as a model parental melt of the suite by Santos et al (2022).

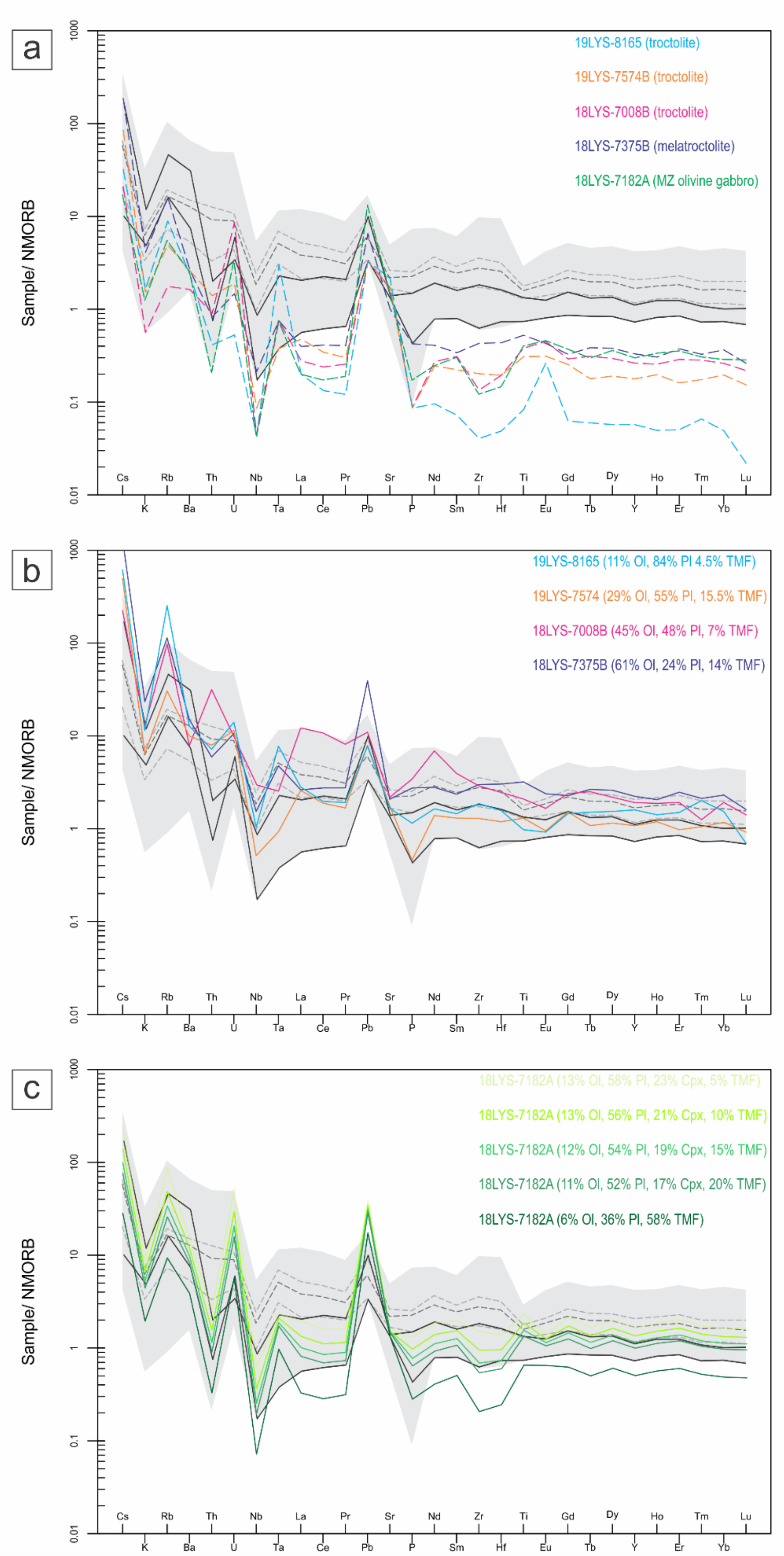
a
19LYS-8165 (troctolite)
19LYS-7574B (troctolite)
18LYS-7008B (troctolite)
18LYS-7375B (melatroctolite)
18LYS-7182A (MZ olivine gabbro)
b
19LYS-8165 (11% Ol, 84% Pl 4.5% TMF)
19LYS-7574 (29% Ol, 55% Pl, 15.5% TMF)
18LYS-7008B (45% Ol, 48% Pl, 7% TMF)
18LYS-7375B (61% Ol, 24% Pl, 14% TMF)
c
18LYS-7182A (13% Ol, 58% Pl, 23% Cpx, 5% TMF)
18LYS-7182A (13% Ol, 56% Pl, 21% Cpx, 10% TMF)
18LYS-7182A (12% Ol, 54% Pl, 19% Cpx, 15% TMF)
18LYS-7182A (11% Ol, 52% Pl, 17% Cpx, 20% TMF)
18LYS-7182A (6% Ol, 36% Pl, 58% TMF)
Sample/ NMORB
1000
100
10
1
0.1
0.01
Cs
K
Rb
Ba
Th
U
Nb
Ta
La
Ce
Pr
Pb
Sr
P
Nd
Sm
Zr
Hf
Ti
Eu
Gd
Tb
Dy
Y
Ho
Er
Tm
Yb
Lu

Figure 3.12: Trace element contents of model melts calculated from cumulate rocks using the method of Bedard et al (1994) displayed as NMOBRB-normalized (Sun and McDonough 1989) extended trace element patterns. Black solid lines show plausible candidates for the basaltic parental melt of the suite (Chapter 2). Gray field shows range of basaltic lava and dyke compositions from the Liuyuan Complex (Santos et al. 2022a,b). (a) Rock analyses used in modeling. (b) Inversion results for troctolites and melatroctolites. (c) Inversion results for MZ olivine gabbro.

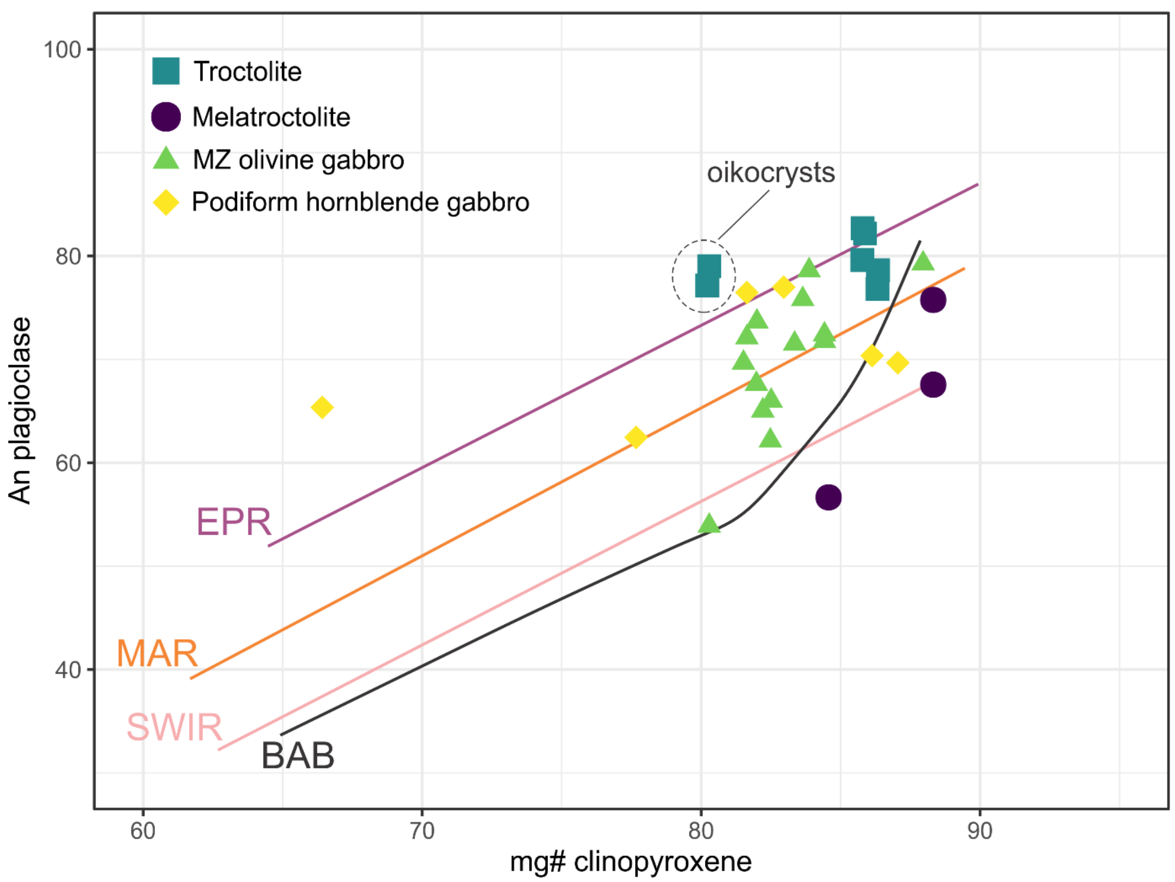

Figure 3.13: Anorthite in plagioclase vs. mg# in clinopyroxene diagram for the gabbroic rocks of the Liuyuan Complex EPR (East Pacific Rise), MAR (Mid Atlantic Ridge), SWIR (Southwest Indian Ridge), and BAB (Back-arc basin) reference lines from Bash et al. (2020).

Chapter 4: Permian back-arc basin formation and arc migration in the southern Central Asian Orogenic Belt, NW China

4.1 Introduction

The Central Asian Orogenic Belt (CAOB) is one of the largest and longest lived accretionary orogens in the world, with ages ranging between 100-250 Ma (Sengör 1996, Jahn et al. 2000, Windley et al. 2007, Xiao et al 2015, Xiao et al. 2018). A longstanding controversy regards the timing of final closure of the Paleo-Asian Ocean. Some authors argue that this took place before the Silurian (ca. 430 Ma, Wang et al. 2017, He et al. 2018), whereas others propose that the last vestige of the Paleo-Asian Ocean disappeared in the Permian (ca. 286 Ma, Xiao et al. 2010, Mao et al. 2012); a difference of ca. 140 My. These discrepancies arise at least in part from an absence of detailed geological information about the Permian geology of the CAOB, particularly along its southern edge, where the record of the final tectonic events might be preserved.

Located near the boundary between southern CAOB and the Dunhuang Block (part of Tarim Craton, e.g. Xiao et al. 2010, Zhang et al. 2013, Zong et al. 2013), the tectonic setting of the mafic Liuyuan Complex (Fig. 4.1a) is a critical part of this debate, as it is the southernmost extensive mafic unit in the CAOB, and has been dated at 290-280 (Mao et al. 2012, Wang et al. 2017, this work). Although there have been multiple studies (e.g. Qin et al. 2011, Su et al. 2011, Xiao et al. 2010, Mao et al. 2012, Cleven et al. 2013, Cleven et al. 2017, Wang et al. 2017, He et al. 2018), the internal stratigraphy and tectonic setting of the Liuyuan Complex remains poorly known. Xiao et al. (2010) proposed the Liuyuan Complex formed as a forearc ophiolite during the subduction of the final tract of the Paleo Asian Ocean. Alternatively, Wang et al. (2017) proposed the Liuyuan Complex is an intra-continental magmatic suite emplaced into the already amalgamated CAOB, with the lavas being the eruptive LIP facies, and the plutonic rocks representing a layered intrusion. Recently, Tian and Xiao (2020) suggested the Liuyuan Complex formed as a back-arc basin when slab roll-back on a south dipping subduction zone beneath the Shibanshan arc of Xiao et al. (2010) caused it to rift and drift away from its Dunhuang Block basement.

In previous contributions, we have documented the presence within the Liuyuan Complex of the characteristic ophiolitic crustal architecture, including a well-preserved and laterally continuous sheeted dyke complex that is consanguineous with the adjoining cumulates and lavas. Considered in tandem with geochemical fingerprinting of the basalts and results of new mapping and age-dating to the south in the Shinbanshan arc terrane, we propose a revised tectonic framework for the Permian evolution of this part of the southern CAOB. We conclude that the Liuyuan Complex formed as a 290-280 Ma back-arc basin to the newly identified Ganquan arc. Extension was caused by slab roll-back beneath the Ganquan arc. Magmatism in this arc ceases by ca. 281 Ma, and the Liuyuan Complex was part of the oceanic lithosphere consumed in a north dipping subduction zone beneath the leading edge of Composite Siberia.

4.2 Geologic Setting

The Liuyuan Complex (Fig. 4.1b) is located between the Silurian to Devonian Huaniushan-Dundunshan arc terrane and the Carboniferous to Permian Shibanshan arc terranes of Xiao et al. (2010), which represents the southernmost lithotectonic units of the CAOB (Fig. 1a). These poorly understood units have been the focus of recent field work by Xiao et al. (2010), who proposed a model whereby the Liuyuan Complex formed as a ca. 286 Ma forearc ophiolite to the Shibanshan arc (Fig. 4.2a), and is preserved as the final tract of the Paleo-Asian Ocean subducted beneath the Tarim Craton to the south and Composite Siberia (defined as the amalgamation of the Siberian Craton and the intra-oceanic arcs described by Xiao et al. 2010) to the north. In contrast to this oceanic interpretation, Wang et al. (2017) and He et al. (2018) proposed a model whereby the Liuyuan Complex formed in a continental rift within the Liuyuan Continental Terrane that was assembled by 420 Ma (Fig 4.2b, 4.2c). Recent investigations (Hong et al. 2022; van Staal et al., 2021) indicate a more complex tectonic history for the terranes surrounding the Liuyuan Complex, which we summarize below.

In the area Xiao et al. (2010) named the Shibanshan arc, van Staal et al. (2021) identified at least two different arc complexes: the Ganquan Complex and the Baidunzi Complex (Fig. 4.1a). New studies show that the Baidunzi Complex and Ganquan Complex are bounded by tectonic contacts and have distinct magmatic and tectonic histories before ca. 281 Ma (van Staal et al. 2021). The Shibanshan arc (Xiao et al. 2010, Tian and Xiao 2020) is described as an Andean-type arc built over the Dunhuang Block, containing a Neoproterozoic basement, Paleozoic metasedimentary rocks, and multi-stage arc plutonism (Orodovician-Silurian, Carboniferous-Permian, and Triassic). We argue that the Shibanshan arc terrane is composite and cannot be interpreted as a single continental arc terrane.

The Ganquan Complex of van Staal et al. (2021) is divided into two members. The lower volcanic member is mainly rhyolite and rhyodacite crystal and lithic tuff, locally intruded by porphyritic intrusions, which yielded SHRIMP U-Pb zircon ages between 295 and 283 Ma. This member is locally unconformably overlain by red sandstone, conglomerate, shale and light green tuff, belonging to the upper volcanosedimentary member of the Ganquan Complex, with the tuff yielding SHRIMP U-Pb zircon ages between 283 and 281 Ma. Based on field relations and Hf isotopic signatures, van Staal et al. (2021) and Hong et al. (2022) interpret the Ganquan Complex as an intra-oceanic island arc volcanic assemblage, indicating that oceanic arc magmatism (Ganquan arc) was coeval with the formation of the Liuyuan complex to its north.

The Baidunzi Complex, sandwiched between the Dunhuang block and the Ganquan Complex (Fig. 4.1a), was previously considered as part of the Shibanshan arc by Xiao et al. (2010); but van Staal et al. (2021) and Hong et al. (2022) argue the Baidunzi Complex is an exotic terrane relative to the Ganquan Complex, as there are marked differences in magmatic and structural history (Hong et al. 2022). The Baidunzi Complex predominantly consists of sheared and transposed Carboniferous-Permian meta-sedimentary rocks and syn-kinematic meta-diorite to granite plutonic suite (van Staal et al. 2021). A voluminous cogenetic ca. 281 Ma hornblende gabbro stiches the contact between the Ganquan Complex and the Baidunzi Complex (van Staal et al. 2021), implying terrane amalgamation was synchronous with arc magmatism.

To the North of the Liuyuan Complex, Wang et al. (2017) described a sedimentary unit composed of arenite, conglomerate, and shale, which they interpret to have been formed in a lacustrine environment. Recent reinvestigation of these sedimentary rocks shows them to be broken formations, occurring as fault-bounded chaotic sedimentary units (Li, 2019) (Fig. 1a). These units comprise graded, poorly sorted sandstone, conglomerate and shale, which are locally transformed into a ~200 m thick mélange with exotic clasts and knockers of basalt. The basalt knockers are interpreted to have been derived from the adjacent Liuyuan Complex. Turbiditic sedimentary rocks with porphyritic rhyolite and ash beds (SHRIMP U-Pb zircon ages between 282-279 Ma) cap this mélange, and were subsequently imbricated and folded. The sedimentary sequence is interpreted by Li (2019) to be a syn-tectonic deposit in a retro-foreland basin, located on the upper plate during the final accretion event of the CAOB. Our mapping and tectonic fingerprinting of the Liuyuan Complex presented in the following section is consistent with Li's (2019) interpretation. Henceforth, we will refer to this mélange as the Liuyuan fore-arc basin.

4.3 The Liuyuan Complex

With an exposed length of approximately 90 km, and a maximum exposed width of 9 km, the Permian Liuyuan Complex (Fig. 4.1b) is mainly composed of basalt, but mapping has identified large bodies of plutonic rocks: troctolite, mela-troctolite, olivine gabbro, varitextured olivine gabbro, plagiogranite and a hypabyssal sheeted dyke complex (Fig. 4.3a). The lowermost unit of the Liuyuan Complex is a fine- to medium-grained massive troctolite (Fig. 4.3b), consisting of euhedral cumulate plagioclase and olivine. Plagioclase grains define a weak magmatic foliation. Poikilitic (≤5 cm) clinopyroxene, containing mainly olivine chadacrysts, are locally present in the troctolite. In patches where oikocrysts are abundant, the troctolite locally grades into olivine gabbro. The layering in the troctolite is transected by meter-scale by tabular bodies of a dark, medium- to coarse-grained mela-troctolite, that may represent intra-cumulate sills.

A varitextured olivine gabbro occurs above the troctolite in the stratigraphy of the Liuyuan Complex (Fig. 4.3c). The contact between the lower troctolite and the varitextured olivine gabbro is typically gradational, but in one location, a 50m-thick layered cumulate sequence is observed at the contact between the lower troctolite and the overlying gabbro. At the base of the layered sequence, layers up to 5 cm in thickness show rhythmic alternations from anorthosite to foliated olivine mela-gabbro, with layers becoming progressively more olivine-poor and clinopyroxene-rich upward in the layered sequence.

The varitextured olivine gabbro is medium- to fine-grained, with equigranular to ophitic textures. This gabbro is intruded by plagiogranite and diabase dykes, locally forming meter-scale composite intrusions. Within individual composite dykes, the order of intrusion is variable, with diabase intruding plagiogranite and vice-versa, indicating they were coeval. The basaltic dyke chemistry is indistinguishable from that of the overlying basaltic lavas (Supplementary File S1).

The upper section of the Liuyuan Complex includes spectacular and extensive exposures of sheeted dykes (Fig. 4.3d) and basaltic extrusive rocks (Fig. 4.3e). The sheeted dyke complex ranges in thickness from a few meters to more than 100 meters thick, and contains dykes of diabase, fine-grained gabbro, and a distinctive porphyritic diabase. The sheeted dyke complex can be traced over the entire exposed contact between the lower gabbroic rocks and the overlying basalts (Fig. 4.1b). Basalt dominates the stratigraphy of the Liuyuan Complex above the sheeted dykes, and intact pillow structures and lava tubes are commonly preserved. Inter-pillow jasper and chert beds are locally present. Lavas may contain vesicles and may have up to 15% plagioclase and 10% olivine phenocrysts. Olivine phenocrysts are pseudomorphed by chlorite. Abundant epidote, fine-grained phyllosilicates, and locally tremolite/actinolite, indicate locally intense greenschist facies hydrothermal metamorphism that penetrated to the varitextured olivine gabbro along brittle structures. Near the top of the Liuyuan Complex, centimeter- to decimeter-scale beds of marine chert and dacite tuffs are interlayered with the basalt.

4.4 Analytical Methods

The collected samples were analyzed for major and trace elements by inductively coupled plasma – atomic emission (ICP-AES) and inductively coupled plasma – mass spectrometry (ICP-MS) at ALX Chemex in Vancouver, Canada. Sample duplicates, pulp duplicates, international standards and blanks were used in the analytical run for quality control and quality assurance. The blanks were good, and the largest variation in observed in the analyzed sample duplicates and in the measured standards was 5%. All whole rock chemical data and sample coordinates are provided in the Supplementary File S1.

U- Pb isotopic data of zircon grains were analyzed using the sensitive high-resolution ion microprobe-II (SHRIMP-II) at the Beijing SHRIMP Center at the Chinese Academy of Geological Sciences. Cathodoluminescence (CL) images were used to characterize zircon domains and to select analytical spots, avoiding complex internal structures. For spot selection, preference was given to euhedral zircon grains that were translucent and devoid of fractures in CL images, with the goal of avoiding radiation damage caused by high-U concentrations. Spots were preferentially positioned at the outer edge of the analyzed. All measurements with relative error larger than 5% (1σ) in ^{206}Pb/^{207}Pb and ^{206}Pb/^{238}U were excluded from the age calculations. Other exclusion criteria are discussed in individual samples. All collected isotopic data is presented in Appendix A3.

4.5 Geochronological Results

Mao et al. (2012) reported an age of 286 ± 2 Ma from a hornblende gabbro dyke and Wang et al. (2017) presented several ages in the area, with a gabbro from the Liuyuan Complex yielding an age of 280 ± 6 Ma. To further constrain the age of the Liuyuan Complex, two trondhjemite intrusions and one leucocratic varitextured gabbro were dated in this study. The results are presented below.

4.5.1 Trondhjemite, sample 18LYS-7010C

Sample 18LYS-7010C (4543599 mN, 694258 mE, UTM 46N) is part of magmatic breccia (Fig. 4a), with equigranular trondhjemite intruding the lower part of the diabase of the sheeted dyke complex. Zircon grains in this sample are typically dark in CL images and subhedral. A substantial portion of grains are anhedral, and irregular grain shapes. Grain sizes range between 20-110 µm. Selected zircon grains are clear in CL images and show either none to weak concentric zoning. A total of 12 grains from this sample were analyzed. Our best estimate of the crystallization age of the sample is based on a concordant group of 8 grains, yielding a Sakmarian-Artinskian age of 290.44 ± 1.41 Ma (MSWD = 0.1; Fig. 4.4a).

4.5.2 Trondhjemite, sample 18LYS-7064

Sample 18LYS-7064 (4542092 mN, 688582 mE, UTM 46N) is a medium-grained equigranular trondhjemite part of a trondhjemite-diabase composite dyke intruding a medium-grained, equigranular troctolite (Fig. 4.4b). Zircon grains in this sample are euhedral, and have subequal proportions of clean and dark grains in CL images, ranging in size between 40-100 µm. Concentric zoning is ubiquitous. A total of 15 zircon grains were analyzed in this trondhjemite. A zircon grain with a ^{206}Pb/^{235}U age of 576 Ma was excluded from further calculation as an age outlier. A remaining group of 12 concordant grains yielded an Artinskian age of 286.34 ± 1.05 Ma, with a MSWD of 0.46 (Fig. 4.4b), interpreted as the crystallization age of the sample.

4.5.3 Varitextured leucogabbro, sample 19LYS-8141

Sample 19LYS-8141 (4544666 mN, 694949 mE, UTM 46N) is a coarse-grained, locally pegmatitic, varitextured leucogabbro. Zircon grains in this sample are dark in CL images and euhedral, showing well-developed prismatic faces. These grains also have a low aspect ratio, and fractured grains are widespread. Grain size ranges between 100-200 µm. Given the higher degree of discordance observed in the 16 grains analyzed in this sample, samples with discordance higher than 20% were also excluded from the age calculation. If these highly discordant grains are included, the sample yields an age of 286.97 ± 0.99 Ma with a MSWD of 33. Excluding these grains, the resulting group of 7 zircon grains yields an age of 288.85 ± 1.37 Ma, with a MSWD of 6.1 (Fig. 4.4c). The latter is interpreted as the crystallization age of the sample.

4.5.4 Tonalite, sample 18LYS-7018A2

Sample 18LYS-7018A2 (4545468 mN, 695273mE, UTM 46N) is a fine-grained equigranular tonalite, part of a plagiogranite dyke intruding a coarse-grained varitextured gabbro. Zircon grains from this sample are euhedral and clear in CL, with grain size ranging between 50-100 µm. Concentric zoning is typical. A group of 13 concordant grains yielded a Kungurian age of 275.30 ± 1.24 Ma, with a MSWD of 2.8 (Fig. 4.5a), interpreted as the crystallization age of the sample.

4.5.5 Trondhjemite, sample 18LYS-7161B

Sample 18LYS-71761B (4542414 MN, 687261 mE, UTM 46N) is a trondhjemite intruding the fault between the troctolite of the Liuyuan Complex in the south and the Mesoproterozoic to Neoproterozoic rocks east of the town of Liuyuan attributed by Xiao et al. (2010) to the Shuanyingshan arc. The sample was collected approximately 100 meters north of the Liuyuan Complex. This rock is equigranular and coarse-grained. Zircon grains from this sample typically are dark in CL images, euhedral, and have low aspect ratios. Grain size ranges between approximately 80-150 µm. Concentric zoning is visible in a few grains, but zoning is not common. A concordia diagram for this sample is presented on Fig. 4.5b, showing considerable scatter in the analyzed grains. Fig. 4.5c shows a weighted mean plot for all 13 dated grains from this sample. Excluding three analysis yielding age outliers, zircon grains from this sample can be grouped in two coherent age groups. Group I comprise 5 grains, and yields an age of 286.81 ± 2.10 Ma, with a MSWD of 7.9 (Fig. 4.5d). Group II comprises 5 grains and yields a Roadian age of 269.77 ± 2.07 Ma, with an MSWD of 5.6 (Fig. 4.5e). There is no meaningful difference in zircon morphology between these two groups. The younger age calculated for Group II is interpreted as the crystallization age of this sample.

4.6 Tectonic Fingerprinting

The tectonic setting of basalts is commonly assigned on the basis of their trace element chemistry (e.g. Pearce and Cann 1973, Pearce 1996, Pearce 2008, Pearce 2014). In the Th/Yb vs. Nb/Yb projection of Pearce (2008), the basalts from the Liuyuan Complex plot as a tight group parallel to and slightly above the mantle array (Fig. 4.6a). The data scatter between Nb/Yb values characteristic of NMORB and E-MORB indicates derivation from a moderately depleted mantle source. The small elevation to higher Th/Yb values of the Liuyuan data could reflect minor contribution of subducted fluids and indicate a suprasubduction zone setting (SSZ). There is no clear cross-trend indicating extensive late crustal contamination (Fig. 4.6a), consistent with the low initial $^{87}Sr/^{86}Sr$ values of 0.703662-0.704327 and highly positive $\varepsilon_{Nd(t)}$ between +6.6 to +9 reported by Mao et al. (2012) for these basalts.

The lavas from the Liuyuan Complex plot in the slab-distal back-arc basin field in the V *vs* Ti projection (Shervais 1982, Pearce 2014) (Fig. 4.6b). On this projection, lavas that originated in a fore-arc setting show a trend evolving from the MORB field to the boninite field (Pearce 2014), with similar V but progressively decreasing Ti. This weakens the argument that the lavas from the Liuyuan Complex were formed in a forearc setting. No boninites have been identified in the Liuyuan Complex by us or any previous workers. Fig. 4.7 shows the Liuyuan Complex basalts on a $(La/Nb)_N$ vs. $(La/Sm)_N$ diagram, where they define a coherent array extending between a primitive oceanic arc and modern back-arc basins, further suggesting a back-arc setting for the Liuyuan Complex. The main compositional variation shown (Fig. 6) does not support an intra-continental basalt scenario, instead favoring a depleted oceanic mantle source affected by minor amounts of a subducted arc component.

4.7 Tectonic Implications

The identification of the Liuyuan Complex as an ophiolite, formed in a back-arc basin setting, provides critical constraints on tectonic evolution of the southern CAOB in the Permian. Our new data from the Liuyuan Complex, when combined with previous studies, and the new field studies on the rock units that bound the Liuyuan complex to the north (Li et al. 2019) and south (van Staal et al. 2021, Hong et al. 2022), allow us to propose a new model for the Permian evolution of the southern CAOB. The combined Ganquan arc and Baidunzi Complex were previous identified as the Shibanshan arc. We now interpret the Ganquan Complex to form part of an oceanic arc system, which was active between 295 and 282 Ma, and which we will call the Ganquan arc (Fig. 4.8a). The Ganquan arc likely developed above a north-dipping intra-oceanic subduction zone. The older Ganquan arc volcanic member breached sea level at least locally, since it was unconformably overlain by red beds and interlayered tuff. The arc was extensional, possibly due to slab roll-back. A slab roll-back environment could have had two additional direct effects. First, the active part of the Ganquan arc system could have migrated southwards and formed a new subaqueous arc, now mainly preserved as pyroclastic rocks interlayered with the marine strata of the upper member of the Ganquan Complex. Secondly, slab roll-back could have led to the opening of a back arc basin, a remnant of which we argue is represented by the 290-280 Ma Liuyuan Complex. The initiation of back-arc opening is constrained by the oldest U-Pb zircon magmatic age of ca. 290 Ma in a magmatic breccia at the base of the sheeted dykes of the Liuyuan Complex and coincides with the waning of volcanism in the lower volcanic member of the Ganquan Complex. The presence of a continuous sheeted dyke complex between the gabbroic crust and the overlying pillow basalts is consistent with a relatively fast-spreading oceanic ridge (e.g. Robinson et al. 2008). Magmatism in the Ganquan arc system (upper volcanic member) ceased by 281 Ma, possibly caused by the collision of this arc system with the exotic Baidunzi Complex (terrane) to the south (Fig. 4.8b).

After this collision, part of the back-arc oceanic lithosphere, of which the Liuyuan Complex is a remnant, started to be consumed at a north dipping subduction zone beneath the southern margin of Composite Siberia (Xiao et al. 2010, Li 2019). The formation of this active margin is recorded by the strata interpreted by Li (2019) as remnants of a fore-arc basin, accompanied by the felsic volcanism dated between 282 and 279 Ma (Li, 2019). The presence of the Ganquan arc south of the Liuyuan Complex and the 282-279 Ma arc on the leading edge of Composite Siberia is consistent with the proximal origin of turbidites in the Liuyuan area proposed by Guo et al. (2012). Arc magmatism associated with this north-dipping subduction zone beneath Composite Siberia migrated southwards over time, likely caused by slab-roll-back. The record of this southward migration is provided by the rhyolites and ash beds deposited in the Liuyuan forearc basin, on a piece of the back-arc basin lithosphere that became trapped in the forearc of the newly formed north-dipping subduction zone at ca. 282 Ma, and by the arc-related dacitic lavas and younger plagiogranite intrusions in the Liuyuan Complex. Hence, the preserved Liuyuan Complex locally became the basement to a new Kungurian-Roadian arc phase and transferred part of the previous Liuyuan forearc basin into a retro arc position (Fig. 4.8c). The 277-268 Ma ages reported by Wang et al. (2017) from gabbro intrusions and volcanic clasts in a conglomerate overlying the pillow basalts probably formed during this arc phase. The zircon population observed in the ca. 270 Ma trondhjemite sample 18LYS-7161B also may provide evidence of recycling of the Liuyuan Complex, since an older zircon population in this sample has an age of 286 Ma, typical of the underlying Liuyuan Complex. It’s intrusion on the north bounding fault of the Liuyuan Complex suggests this plagiogranite was emplaced during or after the exhumation of the ophiolite. The presence of the Ganquan arc south of the Liuyuan Complex and the 282-279 Ma arc on the leading edge of Composite Siberia is consistent with the proximal origin of turbidites in the Liuyuan area proposed by Guo et al. (2012).

This northward subduction polarity is consistent with the southward thrusting of the Liuyuan Complex over Permian sediments along its southern boundary and the southwards thrusting of the fore-arc-basin sediments over the Liuyuan Complex observed along its northern boundary (Li 2019, van Staal et al., 2021). The overall low metamorphic grade and absence of regional penetrative deformation in the Liuyuan Complex are consistent with it being on the upper plate during this collision (Fig. 4.8c). The field and geochronological constrains presented here are inconsistent with the double verging subduction zone proposed by Guo et al. (2012) for the closure of the Liuyuan oceanic basin. The change in the composition of the volcanic rocks from rhyolitic to dacitic possibly reflects a transition in the arc basement due to arc-trench migration from the continental crust of Composite Siberia to the oceanic crust of the Liuyuan Complex. The 270 Ma trondhjemite age and the presence of the 268 Ma dacitic crystal tuff dated by van Staal et al. (2021) suggests arc magmatism was long lived, consuming not only the oceanic lithosphere produced during back-arc spreading, but also any previously existing oceanic lithosphere of what remained of the Paleo-Asian Ocean. The 268 Ma dacitic crystal tuff that overlies the Liuyuan Complex provides a minimum exhumation age (Fig. 4.8d) and provides a minimum age for the existence of active arc systems in the Paleo Asian Ocean.

Our model differs from the proposed forearc ophiolite formation (Xiao et al. 2010, Mao et al. 2012) and continental rift hypothesis (Wang et al. 2017, He et al. 2018) for the origin of the Liuyuan Complex. Tectonic fingerprinting of the basalts is inconsistent with a forearc origin, and the ophiolite stratigraphy of the Liuyuan Complex casts aside a continental rift setting. Our mapping has identified distinct arcs (e.g. Ganquan arc) and exotic terranes (e.g. Baidunzi Complex) in the area defined by Xiao et al. (2010) as the Shibanshan arc. The presence of these distinct arcs is inconsistent with the model of Tang and Xiao (2020), where the Liuyuan Complex formed as the Shibanshan arc rifted from its Dunhuang block basement.

4.8 Conclusions

The 290-280 Ma Liuyuan Complex at the southern edge of the Central Asian Orogenic Belt preserves an almost complete and coherent section of oceanic crust. The stratigraphy of the Liuyuan Complex and the whole rock and isotopic geochemistry of the lavas indicate it originally formed in a fast-spreading intra-oceanic back-arc basin. Back-arc basin spreading would have taken place behind a southward-migrating Ganquan oceanic arc system. Both arc migration and back-arc spreading were probably due to slab roll-back. The Liuyuan Complex was preserved and incorporated in a Permian orogenic wedge along the southern edge of the CAOB, because it was transferred into a forearc setting following a subduction step-back into the back-arc basin, which closed the remainder of the back-arc basin. The tectonic setting for the Liuyuan Complex and the surrounding terranes advocated here is different from previous models for the Permian tectonics of the CAOB. Instead of a single-stage final collision between Composite Siberia and the Dunhuang Block; or the rifting of previously accreted continental crust, we argue the Paleo-Asian Ocean in the Permian during its closure was a complex system of short-lived intra-oceanic and arcs and back-arc basins, analogous to the evolution of parts of the present-day southern-Pacific Ocean or Mediterranean systems.

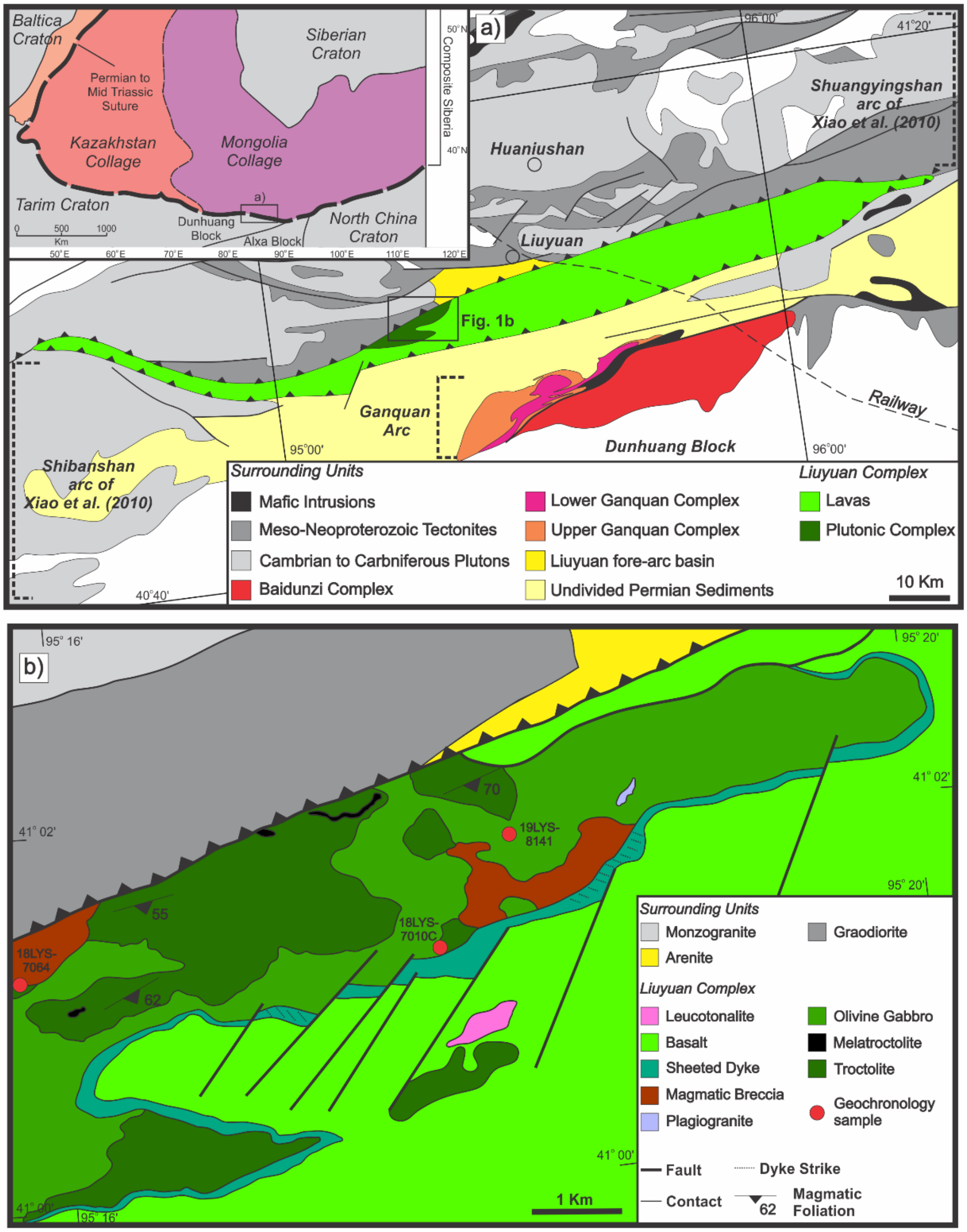

Figure 4.1: (a) Tectonic context of the Liuyuan Complex and surrounding units. Modified from Xiao et al. (2010). (b) Geology of the Liuyuan Complex.

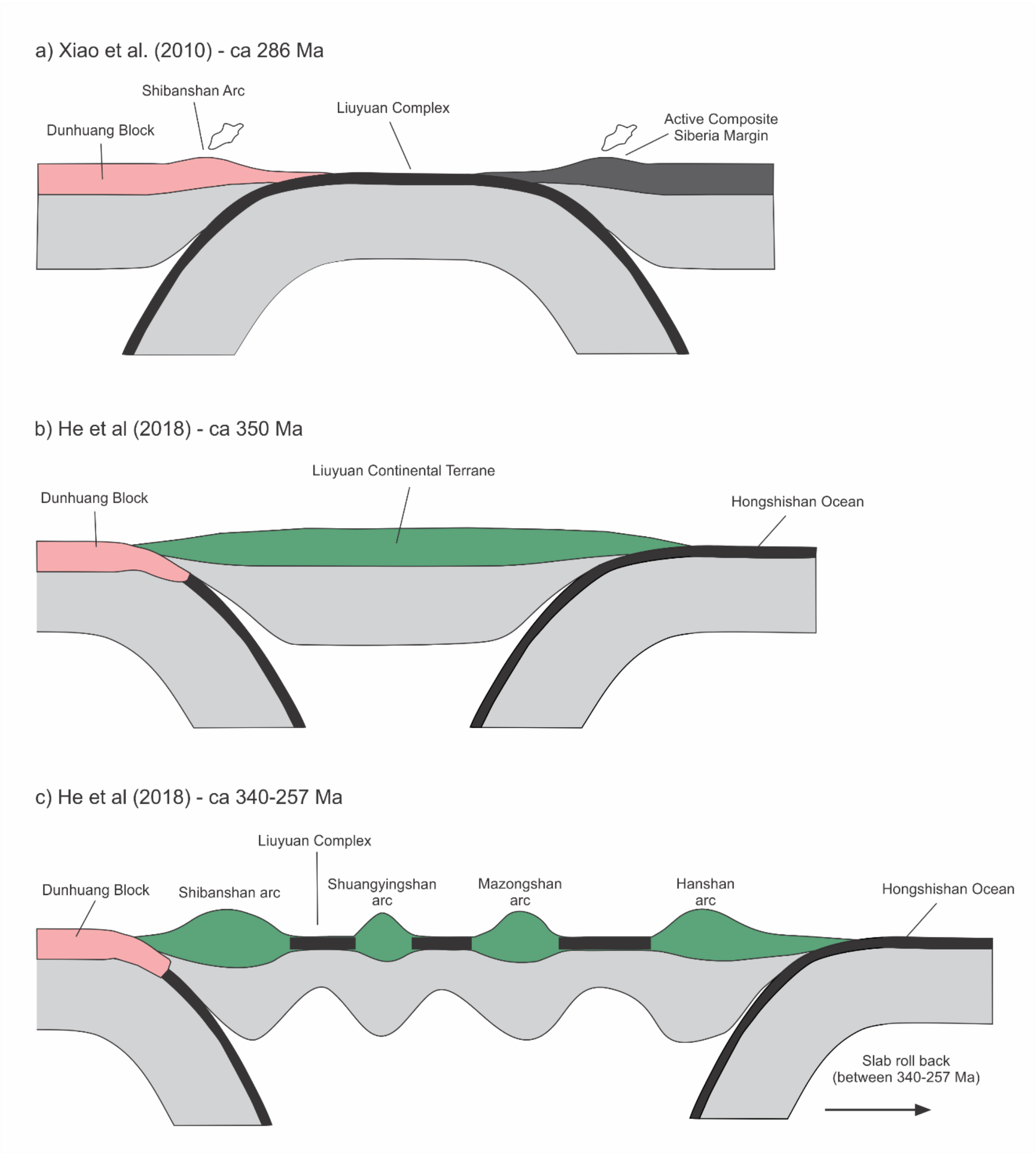

a) Xiao et al. (2010) - ca 286 Ma

b) He et al (2018) - ca 350 Ma

c) He et al (2018) - ca 340-257 Ma

Figure 4.2: Previous tectonic models for the Liuyuan Complex. (a) Model of Xiao et al. (2010), where the Liuyuan Complex formed in the forearc of the Shibanshan arc, during the last subduction event in the CAOB. (b) and (c) Model of He et al. (2018), where all terranes of Xiao et al. (2010) of the southern CAOB were once part of single continental terrane (the Liuyuan Continental Terrane) and the Liuyuan Complex formed as a rift in the Liuyuan Continental Terrane, consistent with the work of Wang et al. (2017) on the Liuyuan Complex. (a) modified from Xiao et al. (2010) and (b) and (c) from He et al. (2018).

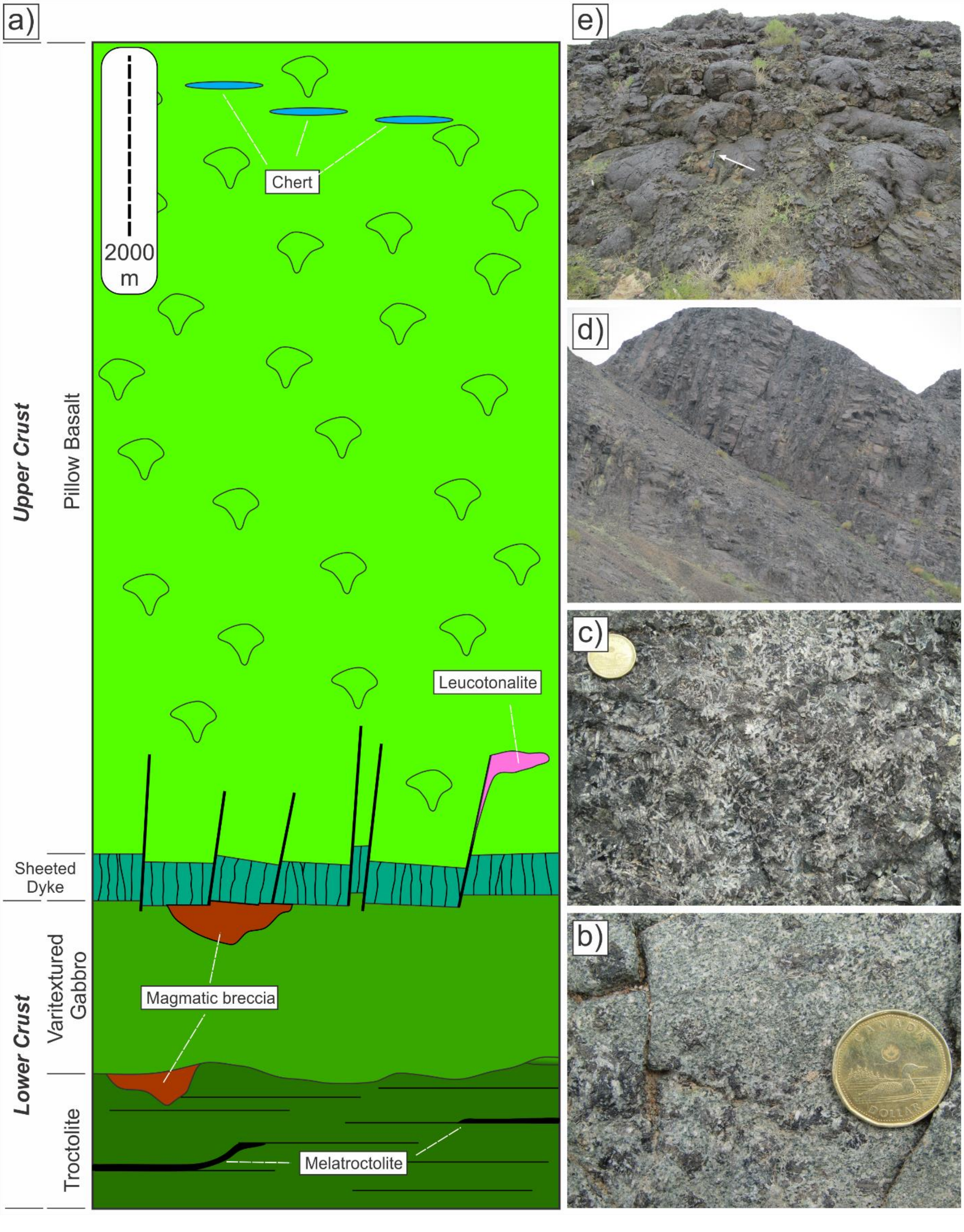
a)
e)
d)
c)
b)
Upper Crust
Pillow Basalt
2000 m
Chert
Leucotonalite
Sheeted Dyke
Lower Crust
Varitextured Gabbro
Magmatic breccia
Troctolite
Melatroctolite

Figure 4.3: (a) Measured stratigraphic column of the Liuyuan Complex. (b) Medium-grained troctolite, showing poikilitic clinopyroxene. (c) Medium-grained subophitic olivine gabbro. (d) Close up view of the sheeted dyke complex. Individual dyke width ranges from 0.5 to 2 m. Field of view is approximately 20x20 meters. (e) Pillow basalts. Hammer in (e) is approximately 35 cm in length, and the coin diameter is 2.65 cm.

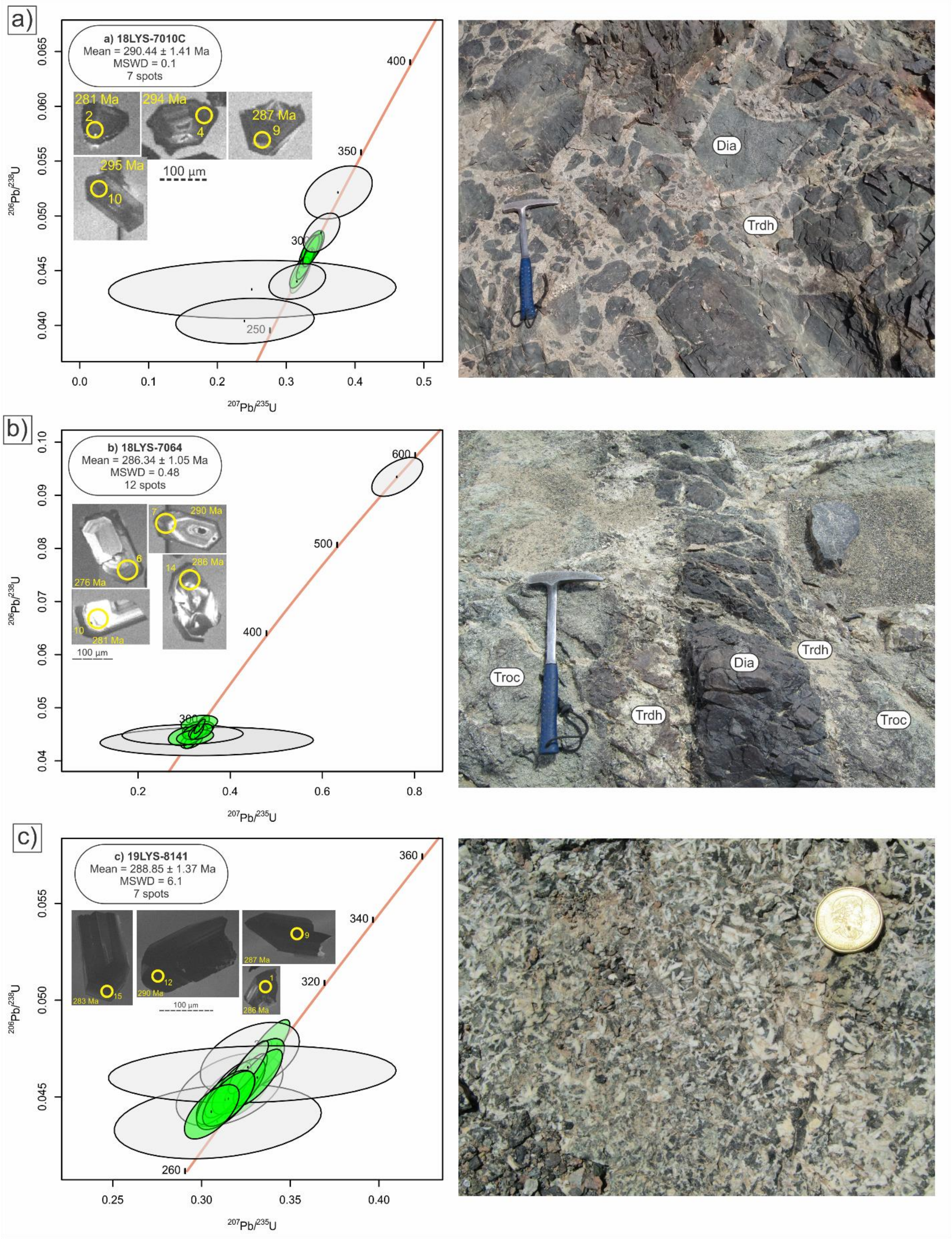a)
a) 18LYS-7010C
Mean = 290.44 ± 1.41 Ma
MSWD = 0.1
7 spots
281 Ma
2
294 Ma
4
287 Ma
9
295 Ma
10
100 µm
400
350
300
250
0.065
0.060
0.055
0.050
0.045
0.040
^{206}Pb/^{238}U
0.0
0.1
0.2
0.3
0.4
0.5
^{207}Pb/^{235}U
Dia
Trdh
b)
b) 18LYS-7064
Mean = 286.34 ± 1.05 Ma
MSWD = 0.48
12 spots
7
290 Ma
6
276 Ma
14
286 Ma
10
281 Ma
100 µm
600
500
400
300
0.10
0.09
0.08
0.07
0.06
0.05
0.04
^{206}Pb/^{238}U
0.2
0.4
0.6
0.8
^{207}Pb/^{235}U
Trdh
Dia
Troc
Trdh
Troc
c)
c) 19LYS-8141
Mean = 288.85 ± 1.37 Ma
MSWD = 6.1
7 spots
15
283 Ma
12
290 Ma
9
287 Ma
1
286 Ma
100 µm
360
340
320
260
0.055
0.050
0.045
^{206}Pb/^{238}U
0.25
0.30
0.35
0.40
^{207}Pb/^{235}U

Figure 4.4: Geochronology of the Artinskian-Kungurain magmatism in the Liuyuan Complex. Concordia diagram for samples (a) 18LYS-7010C, (b) 18LYS-7064, and (c) 19LYS-8141. Insets in each diagram shows a typical range of zircon grain morphology in the samples. Error ellipses are displayed at the 2σ confidence interval. The diagrams show every analyzed grain in each of the dated samples, but only grains highlighted in green or blue were used in the calculation of the reported ages. The corresponding field photos for the dated samples are given to the right of each Concordia diagram.

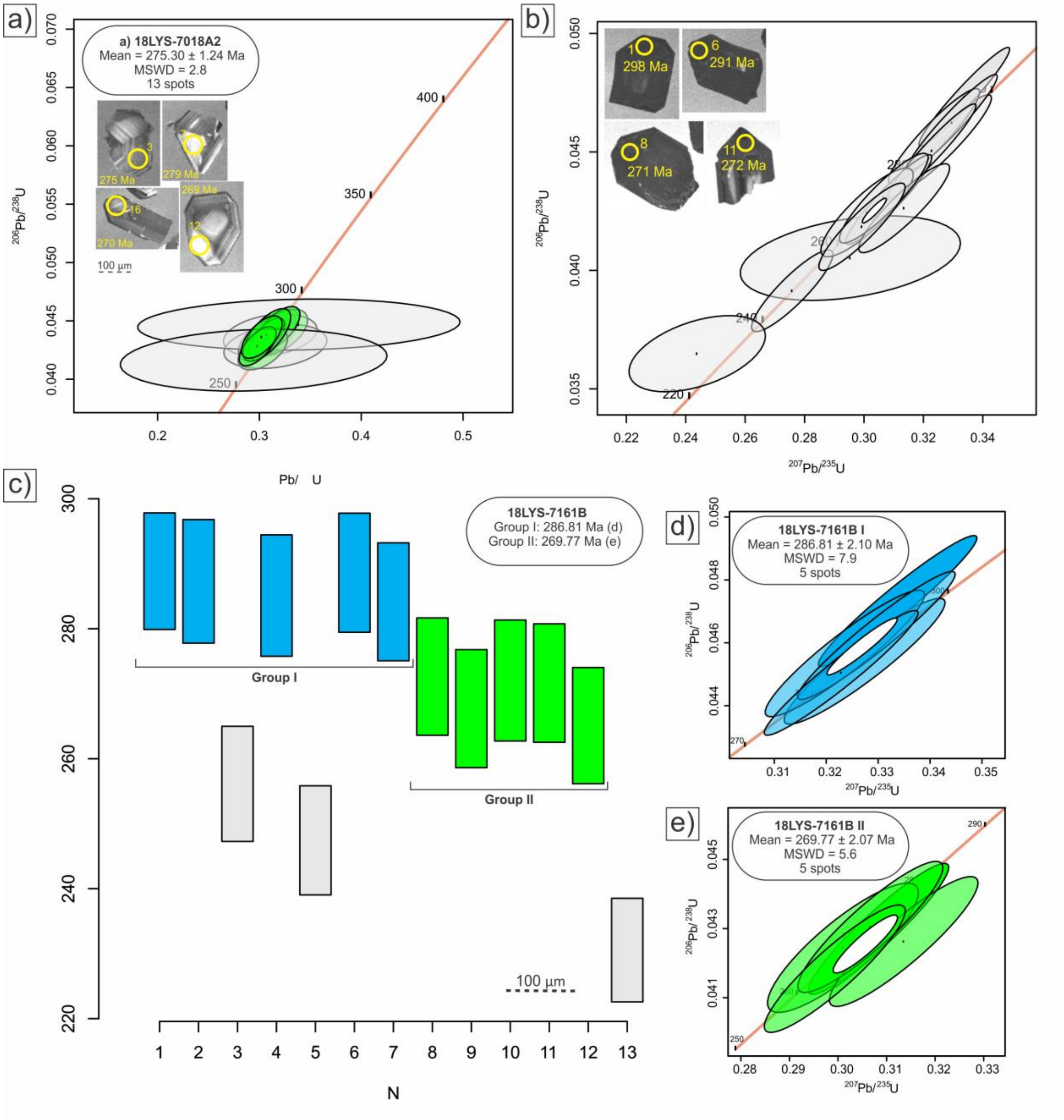

Figure 4.5: Concordia plots for the Kungurian-Roadian magmatism in the Liuyuan Complex. Concordia diagram for samples (a) 18LYS-7018A2, (b) 18LYS-7161B, (c) shows a weighted mean diagram for sample 18LYS-7161B. Concordia diagrams for the highlighted distinct zircon populations are shows in (d) and (e). Insets in each diagram shows a typical range of zircon grain morphology in the samples. Error ellipses are displayed at the 2σ confidence interval. The

diagrams show every analyzed grain in each of the dated samples, but only grains highlighted in green or blue were used in the calculation of the reported ages.

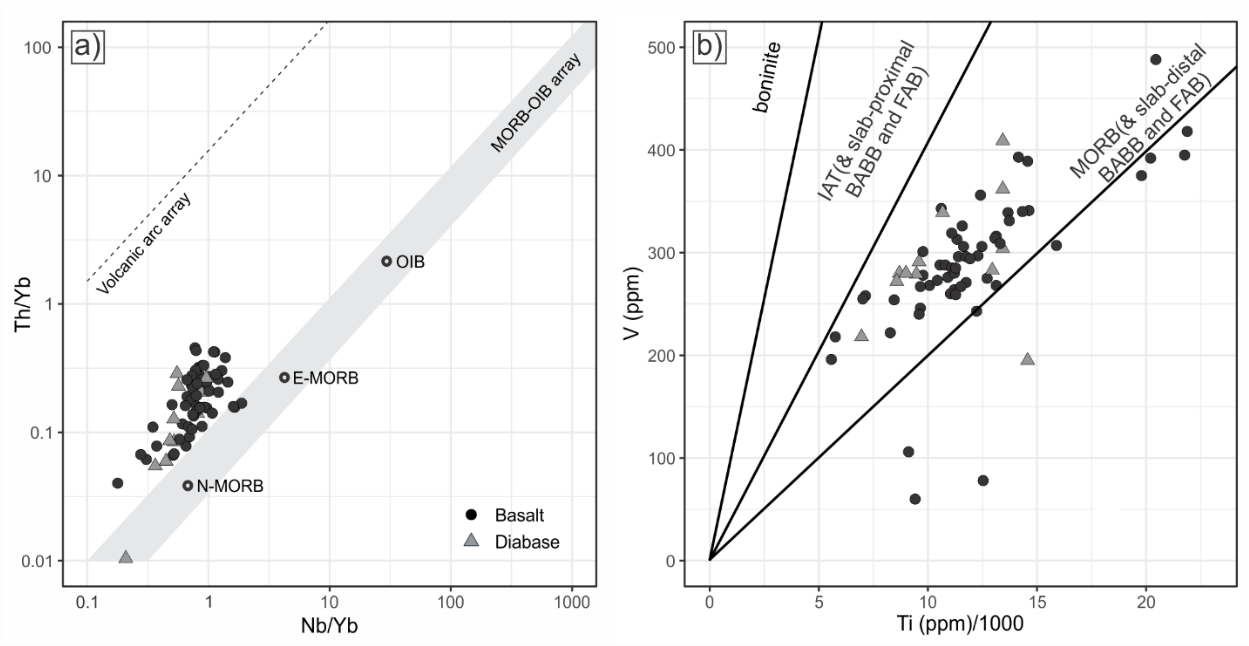

Figure 4.6: (a) Th/Yb vs. Nb/Yb projection of Pearce (2008). (b) V vs. Ti projection of Shervais (1982), modified by Pearce (2014).

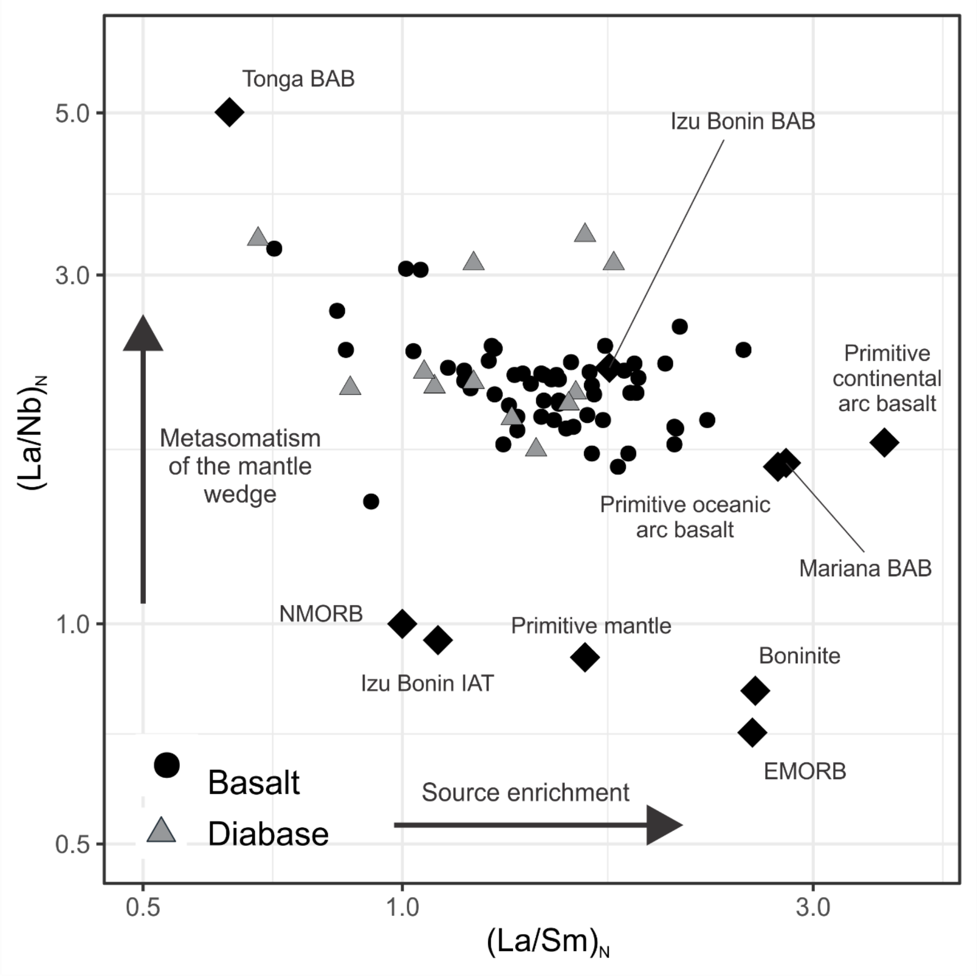

Figure 4.7: La/Nb vs. La/Sm normalized to the NMORB of Sun and McDonough (1989). Reference compositions were taken from Kelemen et al. (2003) and Schmidt and Jagoutz (2017). BAB, back-arc basin; IAT, island arc tholeiite.

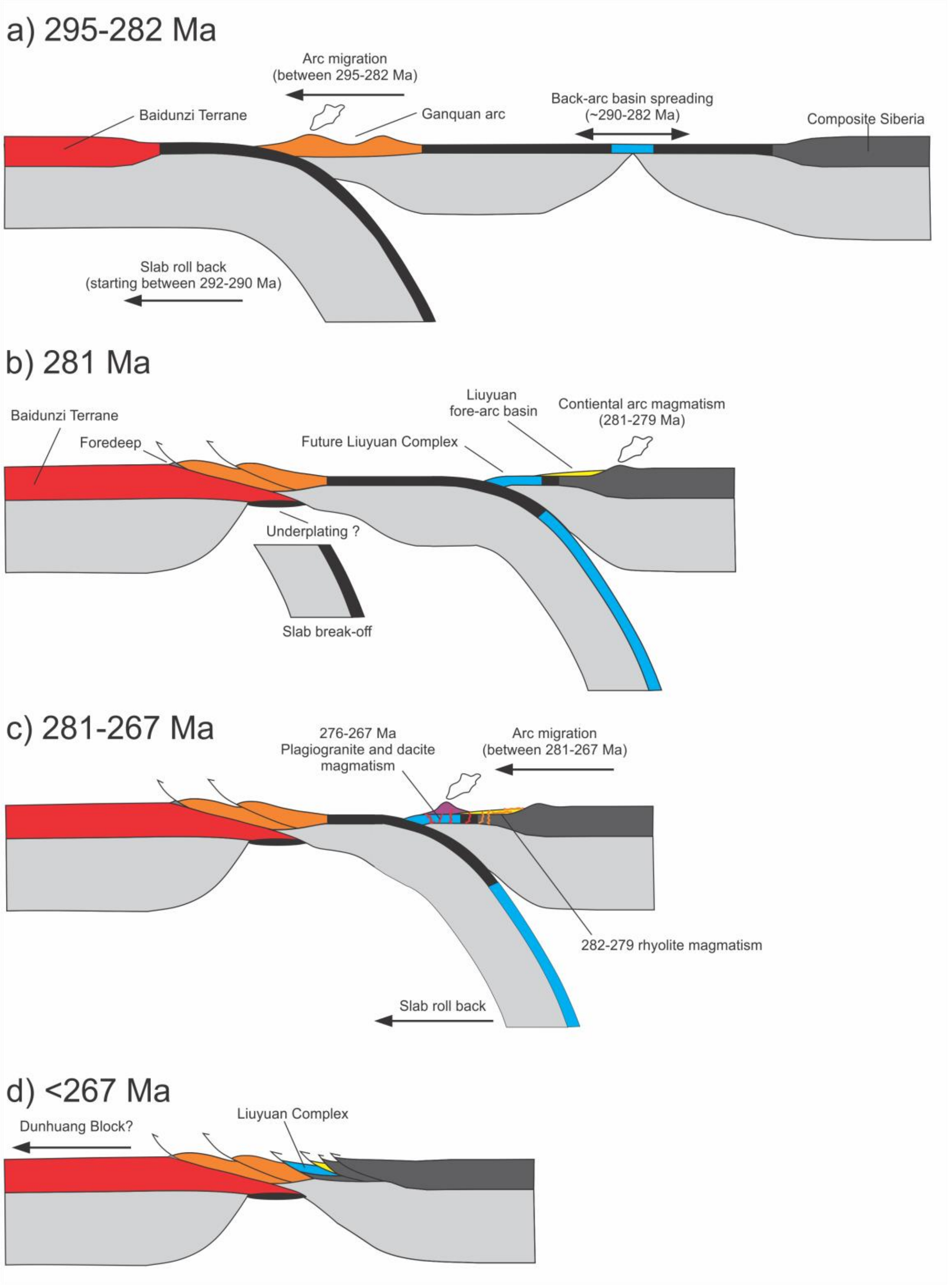

Figure 4.8: The proposed model for the Tectonic evolution of the southern CAOB in the Liuyuan area. (a) Initial Ganquan arc migration and back-arc spreading. (b) Initiation of

subduction underneath Composite Siberia. (c) The Liuyuan Complex as basement of a nascent arc. (d) Present configuration of the Liuyuan Complex and surrounding units.

Chapter 5: Summary and Conclusions

5.1 Main Conclusions

5.1.1 Geology of the Liuyuan Complex

- The Liuyuan Complex comprises dominant basalt, interlayered with minor chert, dacite, and dark shales (Chapter 2). The subordinate gabbroic rocks were grouped into a lower zone (LZ), middle zone (MZ), and upper zone (UZ). Troctolite and melatroctolite, comprises the LZ; olivine gabbro comprises the MZ; podiform olivine gabbro, podiform hornblende gabbro, intrusive hornblende gabbro, and minor plagiogranite intrusions comprise the UZ (Chapter 3).The gabbroic rocks are separated from the dominant overlying basalt by a well-developed and laterally continuous sheeted dyke complex (Chapter 2).
- Metamorphic grade in the Liuyuan Complex can be broadly characterized as greenschist facies, peaking at amphibolite facies at the base of the sheeted dyke complex. The upper gabbroic rocks are overprinted by a fault controlled hydrothermal system (Chapter 2).
- The stratigraphy of the Liuyuan Complex is consistent with its formation in a fast-spreading oceanic ridge, and not in a continental rift (Chapter 2 and 4).

5.1.2 Magmatism in the Liuyuan Complex

- The basalts in the Liuyuan Complex formed by 10-17% partial melt of two slightly distinct mantle sources in a back-arc basin tectonic environment (Chapter 2).
- Thermodynamic modelling suggests fractionation of these basalts followed the typical tholeiitic sequence at conditions observed in modern spreading centers, with saturation of

olivine + plagioclase + clinopyroxene + ilmenite, with a liquidus temperature of 1206 ^{o}C, pressure of 1 kbar, and $_{f}O_2$ at the QFM buffer (Chapter 2).

- Thermodynamic modelling, mineral chemistry, and trace element inversions indicate the gabbroic rocks of the Liuyuan Complex formed as cumulates from a parental melt of composition similar to the overlying basalt. The podiform olivine gabbro and intrusive hornblende gabbro population records quasi-liquid compositions (Chapter 3).
- The differentiation of troctolite, melatroctolite, and MZ olivine gabbro took place by the fractionation of variable proportions of olivine and plagioclase, with clinopyroxene as an interstitial and possible heteradcumulate phase. Trapped melt fraction tends to be lower in the non-poikilitic troctolite (<7%) intermediate in poikilitic troctolite and in the melatroctolite (~15%), and likely up to 20% in the MZ olivine gabbro (Chapter 3).
- The melatroctolite likely represents intra-cumulate sill formed from primitive replenishments a crustal magma chamber crystallizing troctolite (Chapter 3)
- Amphibole in the melatroctolite and podiform hornblende gabbro records primitive compositions, comparable with clinopyroxene and olivine in these rocks. However, they preserve the record of water concentrations in the interstitial melt of up to 6 wt%, considerable higher than the modelled 0.5 wt% initial parental melt of the suite (Chapter 2, 3).
- The large variation in An contents at almost constant clinopyroxene mg# in gabbroic rocks is consistent with their formation in a back-arc basin (Chapter 3).
- Ages obtained in plagiogranite intrusions at several stratigraphic levels and in leucocratic olivine gabbro samples indicate magmatism in the Liuyuan Complex took place in two phases. The older Artinksian-Kungurian phase lasted between 290-280 Ma

and represents the time of back-arc spreading. A younger Kungurian-Roadian phase lasted between 275-267 Ma. Thie younger magmatic phase occurred as the Liuyuan Complex became the basement for a migrating arc (Chapter 4).

5.1.3 Tectonic Implications

- The fast spreading back-arc basin in setting for the Liuyuan Complex and recent findings in the local geology are incompatible with existing tectonic models. I propose the Liuyuan Complex formed between 290-280 in a back-arc basin as slab roll-back led to extension in the recently discovered Ganquan arc (Chapter 4).
- Magmatism in the Ganquan arc ceased circa 281 Ma, likely caused by the collision of the exotic Baudunzi Complex with the southern margin of the Ganquan arc. Subduction then jumped north, onto the leading edge of Composite Siberia (Chapter 4).
- As the back-arc basin was consumed by northward subduction beneath Composite Siberia, the Liuyuan Complex becomes the basement of a Kungurian-Roadian phase of arc magmatism. Final exhumation of the ophiolite took place before 267 Ma, as recorded by an unconformably overlying dacite (Chapter 4).

5.2 Future Directions

- A lot of the work presented in this PhD thesis is the result of detailed field work and mapping. The current mapping effort should be further expanded, as it has proven key for understanding the geological history of the region.
- The provenance of the dark shales interlayered with the Liuyuan Complex remains poorly understood. Focused geochemical and isotopic studies on these sedimentary rocks would have important implications for the paleohydrology of the Liuyuan back-arc basin.

- The plagiogranites of the Liuyuan Complex are the only major igneous rocks not investigated petrologically in this dissertation. Several key questions remain unanswered, such as the relationship, if any, between the plagiogranite and the overlying dacites; the relationships between the distinct plagiogranite intrusions, and the depth of intrusion. All of these questions could have important implications for the tectonic model proposed here for the Liuyuan Complex.

References

Anonymous, 1972. Penrose field conference on ophiolites. Geotimes 17: 24-25.

Basch, V., Sanfilipo, A, Sani, C., Ohara, Y., Snow, J., Ishzuka, O., Harigane, Y., Michibayashi, K., Sen, A., Akiwaza, N., Okino, K., Fuji, M., and Yamashita, H., 2020. Crustal accretion in a slow spreading back-arc basin: Insights from the Mado Mgamullion Oceanic Core Complex in the Shikoky Basin. Geochemistry, Geophysics, Geosystems 21-11: doi.org/10.1029/2020GC009199.

Bazhenov, M.L., Levashova, N.M., Degtyarev, K.E., Van der Voo, R., Abrajevitch, A.V., and McCausland, P.J.A., 2012. Unraveling the early–middle Paleozoic paleogeography of Kazakhstan on the basis of Ordovician and Devonian paleomagnetic results. Gondwana Research 22: 974–991.

Bédard, J.H., 1991. Cumulate recycling and crustal evolution in the Bay of Islands Ophiolite. Journal of Geology 99: 225-249.

Bédard, J.H., 1999. Petrogenesis of boninites form the Betts Cove ophiolite, Newfoundland, Canada: Identification of subducted source components. Journal of Petrology 40-12: 1853-1889.

Bédard, J.H., 2001. Parental magmas of the Nain Plutonic Suite anorthosites and mafic cumulates: a trace element modelling approach. Contributions to Mineralogy and Petrology 141: 747-771.

Bédard, J.H., 2005. Partitioning coefficients between olivine and silicate melts. Lithos 83: 394–419.

Bédard, J.H., 2006. Trace element partitioning in plagioclase feldspar. Geochimica et Cosmochimica Acta 70: 3717–3742.

Bédard, J.H., 2006. Parametrization of the F = Mg exchange coefficient (Kd) between clinopyroxene and silicate melts. Chemical Geology 274(3): 169-176.

Bédard, J.H., 2010. Parametrization of the Fe=Mg exchange coefficient (Kd) between clinopyroxene and silicate melts. Chemical Geology 274: 169-176.

Bazhenov, M.L., Levashova, N.M., Degtyarev, K.E., Van der Voo, R., Abrajevitch, A.V., and McCausland, P.J.A., 2012. Unraveling the early–middle Paleozoic paleogeography of Kazakhstan on the basis of Ordovician and Devonian paleomagnetic results. Gondwana Research 22: 974–991.

Black, L. P., Kamo, S. L., Allen, C. M., Aleinikoff, J. N., Davis, D. W., Korsch, R. J., & Foudoulis, C., 2003. TEMORA 1: a new zircon standard for Phanerozoic U–Pb geochronology. Chemical Geology 200(1–2): 155–170.

Bolhar R., Kamber, B.S., Moorbath. S., Fedo, C.M., and Whitehouse, M.J. 2004. Characterisation of early Archaean chemical sediments by trace element signatures. Earth and Planetary Science Letters 222: 43– 60.

Byrne, R. and Sholkovitz, E. 1996. Marine chemistry and geochemistry of the lanthanides. In: Handbook on the Physics and Chemistry of Rare Earths (eds. KA Gschneider Jr and L Eyring) 158-23: 497–593.

Claoué-Long, J. C., Compston, W., Roberts, J., & Fanning, C. M., 1995. Two Carboniferous Ages: A Comparison of Shrimp Zircon Dating with Conventional Zircon Ages and 40Ar/39Ar Analysis. Geochronology, Time Scales and Global Stratigraphic Correlation, 3–21.

Cleven, N.R., Lin, S., and Xiao, W., 2013. The Hongliuhe fold-and-thrust belt: Evidence of terminal collision and suture-reacivation after the Early Permian in the Beishan orogenic collage, Northwest China. Gondwana Reserarch 27-2: 796-810.

Cleven, N., Lin, S., Davis, D.W., Xiao, W., Guilmette, C., 2016. Elucidating tectonic events and processes from variably tectonized conglomerate clast detrital geochronology: examples from the Permian Hongliuhe Formation in the southern Central Asian Orogenic Belt, NW, China. Tectonics, 37(7): 1626-1641.

Cleven, N.R., Lin, S., Xiao, W., Davis, D.W., and Davis, B., 2017. Successive arc accretion in the southern Central Asian orogenic belt. NW China: Evidence from two Paleozoic arcs with offset magmatic period. GSA Bulletin 130: 537-557.

Compston, W., Williams I. S., Kirschvink, J.L., Zichao, Z., and Guogan, M.A., (1992). Zircon U-Pb ages for the Early Cambrian time-scale. Journal of the Geological Society, 149-2: 171–184.

Coogan, L.A., Gillis, K.M., MacLeod, C.J., Thompson, G., and Hekinian, R., 2002 Petrology and geochemistry of the lower ocean crust formed at the East Pacific Rise and exposed at Hess Deep: A synthesis and new results. Geochemistry, Geophysics, Geosystems 3(11): 8604.

Coogan, L.A., 2014. The lower oceanic crust. Treatise on Geochemistry, Volume 4, Chapter 13. Edited by Holland, D., and Turekian, H.

Cumming, G. L., and Richards, J. R., 1975. Ore lead isotope ratios in a continuously changing earth. Earth and Planetary Science Letters 28-2: 155–171.

de Vries, J., Lin., S., van Staal, C.R., Yakymchuck, 2022. A structural–metamorphic study of the Gubaoquan eclogites and enveloping rock units in the Beishan Orogenic Collage, NW China, with emphasis on the structural evolution, nature of juxtaposition and exhumation. International Journal of Earth Science, https://doi.org/10.1007/s00531-022-02192-3.

Deuser, W.G., 1975. Reducing environments. In Chemical Oceanography, vol 3. Edited by Riley, J.P, and Skirrow, G.

Dick, H.B., Ozawa, K., Meyer, P.S., Niu, Y., Robinson, P.T., Constantin, M., Hebert, R., Maeda, J., Natland, J.H., Hirth, J.G., and Mackie, S.M., 2002. Primary silicate mineral chemistry of a 1.5 km section of very slow spreading lower oceanic crust: ODP Hole 735B, Southwest Indian Ridge. Proceeding in the Ocean Drilling Program, Scientific Results, 176: 1-13.

Dilek, Y. 2003. Ophiolite concept and its evolution. Ophiolite Concept and the Evolution of Geological Thought: Geological Society of America Special Paper 373: 1-16. Edited by Dilek, Y. and Newcomb, S.

Dilek, Y., and Thy, P., 2009. Island arc tholeiite to boninitic melt evolution of the Cretaceous Kizildag (Turkey) ophiolite: Model for multi-stage early arc-forearc magmatism in Tethyan subduction factories. Lithos 113: 68-87.

Feig, S.T., Koepke, J., and Snow, J.E., 2006. Effect of water on tholeiitic basalt phase equilibria: An experimental study under oxidizing conditions. Contributions to Mineralogy and Petrology 152: 611–638.

France, L., Koepke, J., Ildefonse, B., Cichy, S.B., and Deschamps, F., 2010. Hydrous partial melting in the sheeted dyke complex at fast spreading ridges: experimental and natural observations. Contributions to Mineralogy and Petrology 160: 683-704.

Gan, B., Diwu,C., Lai, S., Wang, S., and Wu, L., 2019. Petrogenesis of early Paleozoic granitoids in the Dunhuang Block, NW China: Insights into magma evolution and crustal thickening. Lithos 402-403.

Garcia-Solsona E., Jeandel, C., Labatut, M., Lacan, F., Vance, D., Chavagnac, V, and Pradoux, C., 2014. Rare earth elements and Nd isotopes tracing water mass mixing and particle-seawater interactions in the SE Atlantic. Geochimica et Cosmochimica Acta 125: 351–372.

Garvine, R.W., 1971. A simple model of coastal upwelling dynamics. Journal of Physical Oceanography 1-3: 169-179.

Gaetani, G. A., and Grove, T. L., 1998. The influence of water on melting of mantle peridotite. Contributions to Mineralogy and Petrology 131(4): 323– 346.

Germn, C.R., and Elderfield, H., 1990. Application of the Ce-anomaly as a paleoredox indicator: the ground rules. Paleoceanography 5: 823-833.

German, C.R., Holliday, B.P., and Elderfield, H. 1991. Redox cycling of rare earth elements in the suboxic zone of the Black Sea. Geochimica et Cosmochimica Acta 55: 3535–3558.

Ghiorso M.S., Gualda, G.A.R., 2015. An H2O-CO2 mixed fluid saturation model compatible with rhyolite-MELTS. Contributions to Mineralogy and Petrology 165-53, https://doi.org/10.1007/s00410-015-1141-8.

Gribble, R.F., Stern, R., Newman, S., Bloomer, S.H., and O’Hearn, 1998. Chemical and isotopic composition of lavas from the Northern Mariana Through: implications for magmagenesis in back-arc basins. Journal of Petrology 39-1: 125-154.

Grove, T. L., Elkins-Tanton, L. T., Parman, S. W., Chatterjee, N., Meuntener, O., and Gaetani, G. A., 2003. Fractional crystallization and mantle melting controls on calc-alkaline differentiation trends. Contributions to Mineralogy and Petrology 45(5): 515– 533.

Gualda G.A.R., Ghiorso M.S., Lemons R.V., Carley T.L., 2012. Rhyolite-MELTS: A modified calibration of MELTS optimized for silica-rich, fluid-bearing magmatic systems. Journal of Petrology 53: 875-890.

Guo, Q., Xiao, W., Windely, B.F., Mao, Q., Han., C., Qu, J., Ao, S., Li, J., Song, D., Yong., 2012. Provenance and tectonic settings of Permian turbidites from the Beishan Mountains, NW China: Implications for the Late Paleozoic accretionary tectonics of the southern Altaids." Journal of Asian Earth Sciences 49: 54-68.

Hammarstrom, E.Z., and Zen, J., 1986. Aluminum in hornblende: an empirical igneous geobarometer. American Mineralogist 71(11-12): 1297-1313.

Han, C., Xiao, W., Zhao, G., Mao, J., Li, S., Yan, Z., and Mao, Q., 2006. Major types, characteristics and geodynamic mechanism of Late Paleozoic copper deposits in Northern Xinjiang, Northwestern China. Ore Geology Review 28-3: 308–328.

Hastie, A.R., Kerr, A.C., Pearce, J.A., and Mitchell, S.F., 2007. Classification of altered volcanic island arc rocks using immobile trace elements: development of the Th Co discrimination diagram. Journal of Petrology 48: 2341-2357.

Hawthorne, F.C., Oberti, R., Harlow, G.E., Maresch, W.V., Martin, R.F., Schumacher, J.C., and Welch, M.D., 2012. IMA report, nomenclature of the amphibole supergroup. American Mineralogist 97: 2013-2220.

He, Z.Y., Klend, R., Yan, L.L., and Zhang, Z.M., 2018. The origin and crustal evolution of microcontinents in the Beishan orogen of the southern Central Asian Orogenic Belt. Earth-Science Reviews 185: 1-14.

Hébert, R., Huot, F., Wang, C., Liu, Z., 2003. Yarlung Zangbo ophiolites (Southern Tibet) revisited: geodynamic implications from the mineral record. Geological Society of London, Special Publications 218(1): 165-190.

Hong. T., dos Santos, G., van Staal, C.R., Ji, W., and Lin, S., 2022. Detailed geological mapping uncovered a complex Pemian arc/back-arc system in the southern Beishan Orogen, Central Asian Orogenic Belt. National Science Review, in press.

Jahn, B.-M., Wu, F.-Y., Chen, B., 2000. Granitoids of the Central Asian Orogenic Belt and continental growth in the Phanerozoic. Transactions of the Royal Society of Edinburgh Earth Sciences 91: 181–193.

Jahn, B.-M., Windley, B., Natal'in, B., and Dobretsov, N., 2004. Phanerozoic continental growth in Central Asia. Journal of Asian Earth Sciences 23: 599–603.

Jaques, A. L., and Green, D. H., 1980. Anhydrous melting of peridotite at 0–15 Kb pressure and the genesis of tholeiitic basalts. Contributions to Mineralogy and Petrology 73(3): 287– 310.

Kelemen, P.B., Hanghøj, K., and Greene, A.R., 2003. One view of the geochemistry of subduction-related magmatic arcs, with an emphasis on primitive andesite and lower crust. Treatise on Geochemistry 3: 593–659.

Kheraskova, T.N., Didenko, A.N., Bush, V.A. and Volozh, Y.A., 2003. The Vendian–Early Paleozoic history of the continental margin of eastern Paleogondwana, Paleoasian ocean, and Central Asian fold belt. Russian Journal of Earth Sciences 5: 165–184.

Kinny, P. D., 1986. 3820 Ma zircons from a tonalitic Armîsoq gneiss in the Godthåb district of Southern West Greenland. Earth and Planetary Science Letters, 79-3: 337–347.

Kinzler, R. J., & Grove, T. L., 1992. Primary magmas of mid-ocean ridge basalts: 1. Experiments and methods. Journal of Geophysical Research 97(B5): 6885– 6906.

Krawczynski, M.J., Groove, T.L., and Behrens, H., 2012. Amphibole stability in primitive arc magmas: effects of temperature, H2O content, and oxygen fugacity. Contributions to Mineralogy and Petrology 164: 317-339.

Leuthold J., Lissenberg, C.J., O’Driscoll, B., Karakas, O., Falloon, T., Klimentyeva, D.N., and Ulmer, P., 2018. Partial melting of lower oceanic crust gabbro: Contrains from poikilitic clinopyroxene primocrysts. Frontiers in Earth Science **6(15): h**ttps://doi.org/10.3389/feart.2018.00015.

Li, J., 2019. A structural and stratigraphic study in Liuyuan area, southern Beishan Orogenic Collage, Northwest China. MSc thesis defended at the University of Waterloo, Canada.

Liao, Y., Wei, C., and Ur R.H., 2021. Titanium in calcium amphibole: behavior and thermometry. American Mineralogist 106(2): 180-191.

Locock, A.J., 2013. An Excel spreadsheet to classify chemical analysis of amphiboles following the IMA 2012 recommendations. Computers & Geosciences 62: 1-11.

MacLeod, C.J., Searle, R.C., Murton, B.J., Casey, J.F., Mallows, C., Unsworth, S.C., Achenbach, K.L., and Harris, M., 2009. Life cycle of oceanic core complexes. Earth and Planetary Science Letters 287: 333-344.

Manatscha, G., Sauter, D., Karpoff, A.M., Masini, E., Mohn, G. and Lagabrielle, Y., 2011. The Chenalliet Ophiolite in the French/Italian Alps: An ancient analogue for an oceanic core complex? Lithos 124: 169-184.

Mao, Q. G., Xiao, W. J., Han, C. M., Sun, M., Yuan, C., Zhang, J. E., Ao, S. J., and Li, J. L., 2010. Discovery of Middle Silurian adakite granite and its tectonic significance in the Liuyuan area, Beishan Mountains, NW China. Acta Petrologica Sinica 26-2: 584–596.

Mao, Q., Xiao, W., Windley, B.F., Han, C., Qu, J., Ao, S., Zhang, J., and Guo, Q., 2012. The Liuyuan Complex in Beishan, NW China: a Carboniferous-Permian ophiolitic fore-arc silver in the southern Altaids. Geological Magazine 149(2): 483-506.

Masago, H., Omori, S., and Maruyama, S., 2010. Significance of retrograde hydration in collisional metamorphism: a case study of water infiltration in the Kokchetav ultrahigh-pressure metamorphic rocks, northern Kazakhstan. Gondwana Research 18: 205–212.

McLennan, S.M. 1989. Rare earth elements in sedimentary rocks: influence of provenance and sedimentary processes. Geochemistry and Mineralogy of Rare Earth Elements. In Reviews in

Mineralogy, vol. 21 (eds. BR Lipin e GH Mckay). Mineralogical Society of America, Washington, D.C: 170–200.

McDonough, W.F., Sun, S.S., 1995. The composition of the Earth. Chemical Geology 67-5: 1050-1056.

Merzbacher, C., and Eggler, D.H. 1984. A magmatic geohygrometer: Application to mount St. Helens and other dacitic magmas. Geology 12(10): 587-590.

Nasdala, L., Hofmeister, W., Norberg, N., Martinson, J.M., Corfu, F., Dörr, W., Kamo, S. L., Kennedy, A.K., Kronz, A., Reiners, P.W., Frei, D., Kosler, J., Wan, Y., Götze, J., Häger, T., Kröner, A., and Valley, J.W., 2008. Zircon M257 – a Homogeneous Natural Reference Material for the Ion Microprobe U-Pb Analysis of Zircon. Geostandards and Geoanalytical Research 32(3): 247–265.

Nelson, D. R. 1998. Compilation of SHRIMP U-Pb zircon geochronology data, 1997. Geological Survey of Western Australia, 242 p.

Nimis, P., and Taylor, W.R., 200. Single clinopyroxene thermobarometry for garnet peridotites. Part 1 Calibration and testing of a Cr-in-cpx barometer and an enstatite-in-cpx thermometer. Contributions to Mineralogy and Petrology 139: 122-135.

Pearce, J.A., 1996. A user's guide to basalt discrimination diagram. Trace Element Geochemistry of Volcanic Rocks: Application for Massive Sulphide Exploration: Geological Association of Canada, Short Course Notes 12, p. 79-113.

Pearce, J.A., 2008. Geochemical fingerprinting of oceanic basalts with applications to ophiolite classification and the search for Archean oceanic crust. Lithos v. 100, p. 14-48.

Pearce, J.A., 2014. Immobile element fingerprinting of ophiolites. Elements v. 10, p. 101-108.

Pearce, J.A., and Cann, J.R., 1973. Tectonic setting of basic volcanic rocks determined using trace element analysis. Earth and Planetary Science Letter v. 19, 290-300.

Pedersen, R.B., Malpas., J., and Falloon, T., 1996. Petrology and geochemistry of gabbroic and related rocks from Site 894, Hess Deep. Proceedings from the Ocean Drilling Program, Scientific Results 147: 3-19.

Pichavant, M. and Macdonald, R., 2007. Crystallization of primitive basaltic magmas at crustal pressures and genesis of the calc-alkaline igneous suite: experimental evidence from St Vincent, Lesser Antilles arc. Contributions to Mineralogy and Petrology 154(5): 535-558.

Pichavant, M., Mysen, B., and Macdonald, R., 2002. Source and H2O content of high-MgO magmas in island arc settings: an experimental study of a primitive calc-alkaline basalt from St. Vincent, Lesser Antilles arc. Geochimica et Cosmochimica Acta 66(12): 2193-2209.

Pisarevsky, S.A., Wingate, M.T.D., Powell, C., MA., Johnson, S., and Evans, D.A.D., 2003. Models of Rodinia assembly and fragmentation. In: Yoshida, M., Windley, B.F. and Dasgupta, S.(eds), Proterozoic East Gondwana: Supercontinent Assembly and Breakup. Geological Society, London, Special Publications 206: 35–55.

Planavsky, N.J., Bekker, A., Rouxel, O.J., Knudsen, A., and Lyons, T.W. 2010. Rare earth element and yttrium compositions of Archean and Paleoproterozoic iron formations revisited: New perspectives on the significance and mechanisms of deposition. Geochimica et Cosmochimica Acta 74: 6387–6405.

Pufhal, P.K., and Hiatt, E.E., 2012. Oxygenation of the Earth’s atmorphere-ocean system: A review of physical and chemical sedimentologic responses. Marine and Petroleum Geolgy 32: 1-20.

Putrika, K., 2008. Thermometers and barometer for volcanic system. In K.D. Putirka and F.J. Tepley III, Eds., Minerals, Inclusions and Volcanic Processes, 69, p. 61–142. Reviews in Mineralogy and Geochemistry, Mineralogical Society of America, Chantilly, Virginia.

Putrika, K., 2016. Amphibole thermometers and barometer for igneous systems and some implications for eruptions mechanisms of felsic magmas at arc volcanoes. American Mineralogist 101: 841-858.

Qin, K.Z., Su, B.X., Li, X.H., Tang, D.M., Sakyi, P.A., Sun, H., Xiao, Q.H., and Liu, P.P., 2011. SIMS zircon U–Pb geochronology and Sr–Nd isotopes of mafic–ultramafic intrusions in Eastern Tianshan and Beishan in correlation with flood basalts in Tarim Basin (NW China): constraints on a ca. 280 Mantle plume. American Journal of Sciences v. 311, p. 237–60.

Ridolfi, F., Renzulli, A., and Puerini, M., 2010. Stability and chemical equilibrium of amphibole in calc-alkaline magmas: an overview, new thermobarometric formulations and application to subduction-related volcanoes. Contributions to Mineralogy and Petrology 160: 45-66.

Robinson, P.T., Malpas, J., Dilek, Y., and Zhou, M., 2008. The significance of sheeted dike complexes in ophiolites. GSA Today v. 18-11, p. 4-10.

Roeder, P.L, and Emslie, R.F., 1970. Olivine-liquid equilibrium. Contributions to Mineralogy and Petrology 29: 275-289.

Rollinson, H., 2019. Dunites in the mantle section of the Oman ophiolite - The boninite connection. Lithos 334-335: 1-7.

Sanfilippo, A., Dick, H. J. B., and Ohara, Y., 2013. Melt-rock reaction in the mantle: Mantle troctolites from the Parece Vela Ancient Back-Arc Spreading Center. Journal of Petrology 54-5: 861– 885

Sanfilippo, A., Dick, H. J. B., Ohara, Y., and Tiepolo, M., 2016. New insights on the origin of troctolites from the breakaway area of the Godzilla Megamullion (Parece Vela back-arc basin): The role of melt mantle interaction on the composition of the lower crust. Island Arc 25-3: 220– 234.

Şengör, A.M.C., Natal'in, B.A., and Burtman, U.S., 1993. Evolution of the Altaid tectonic collage and Paleozoic crustal growth in Eurasia. Nature 364: 209–304.

Şengör, A.M.C., Natal'in, B.A., 1996. Paleotectonics of Asia: fragments of a synthesis. In: Yin, A., Harrison, M. (Eds.), The Tectonic Evolution of Asia. Cambridge University Press, Cambridge, pp. 486–640.

Schmidt, M.W., and Jagoutz, O., 2017. The global systematic of primitive arc melts. Geochemistry, Geophysics, Geosystems v. 18, p. 2817-2854.

Shannon, R.D. 1976. Revised effective ionic radii and systematic studies of interatomic distances in halides and chalcogenides. Acta Crystallographica v. A32, p. 751– 767.

Shervais, J.W., 1982. Ti-V plots and the petrogenesis of modern and ophiolitic lavas. Earth and Planetary Science Letters v. 59, p. 101-118.

Shi, M., Hou, Q., Wu, C., Yan, Q., Cheng, N., Zhang, Q., Wang, H., 2021. Origins of the meta-mafic rocks in the southern Dunhuan Block (NW China): Implication for tectonic framework of the southernmost Central Orogenic Belt. Geological Journal 56-8: 3959-3973.

Song, D., Xiao, W., Han, C., Li, J., Qu, J., Guo, Q., Lin, L., and Wang, Z., 2013. Progressive accretionary tectonics of the Beishan orogenic collage, southern Altaids: insights from zircon U–Pb and Hf isotopic data of high-grade complexes. Precambrian Research 227: 368–388.

Stanley, C., 2017. Molar element ratio analysis of lithogeochemical data: a toolbox for use in mineral exploration and mining. Proceedings of Exploration 17: Sixth Decennial International Conference on Mineral Exploration, edited by V. Tschirhart and M.D. Thomas: 471–494.

Su, B.X., Qin, K.Z., Sakyi, P.A., Li, X.H., Yang, Y.H., Sun, H., Tang, D.M., Liu, P.P., Xiao, Q. H., and Malaviarachichi, S.P.K., 2011. U–Pb ages and Hf–O isotopes of zircons from Late Paleozoic mafic–ultramafic units in the southern Central Asian Orogenic Belt: Tectonic implications and evidence for an Early-Permian mantle plume. Gondwana Research v. 20, p. 516–31.

Sun, S.S., and McDonough, W.F., 1989. Chemical and isotopic systematics of oceanic basalts: Implication for mantle compositions and processes. Magmatism in the Ocean Basins, Geological Society of London Special Publications 42: 313-345.

Tian, Z., and Xiao, W., 2020. An Andean-type arc transferred into a Japanese-type arc at final closure stage of the Paleo-Asian Ocean in the southernmost Altaids. Geological Journal v. 55-3, p. 2023-2043.

Todd, S.E., Pufahl, P.K., Murphy, J.B., Taylor, K.G., 2019. Sedimentology and oceanography of Early Ordovician ironstone, Bell Island, Newfoundland: Ferruginous seawater and upwelling in the Rheic Ocean. Sedimentary Geology 279: 1-15.

Tremblay, A., Meshi, A., and Bédard, J.H., 2009. Oceanic core complexes and ancient oceanic lithosphere: Insights from Iapetan and Tethyan ophiolites (Canada and Albania). Tectonophysics 473: 36-52.

Tucholke, B.E., Behn, M.D., Buck, W.R., and Lin, J., 2008. Role of melt supply in oceanic detachment faulting and formation of megamullions. Geology 36-6: 455-458.

Ulrich, M., Picard, C., Stéphane, G., Chauvel, C., Cluzel, D. and Meffre, S., 2010. Multiple melting stages and refertilization as indicators for ridge to subduction formation: The New Caledonia ophiolite. Lithos 115: 223-236.

van Staal, C., Zagorevski, A., 2020. Accretion, soft and hard collision: Similarities, differences and an application from the Newfoundland Appalachian Orogen. Geoscience Canada 47-3: 103-118.

van Staal, C.R., Hong, T., Lin, S., Ji, W.H., 2021. Bedrock Geological Map of the Baidunzi Area, Guazhou, Gansu, China, scale 1:25,000: China Geological Survey, DOI: 10.35080/data.C.2021.P01.

Varfalvy, V., Hébert, R., Bédard, J.H., and Lafleche, M.R., 1997. Petrology and geochemistry of pyroxenite dykes in upper mantle peridotites of the North Arm Mountain Massif, Bay of Islands ophiolite, Newfoundland: Implications for the genesis of boninitic and related magmas. The Canadian Mineralogist 35(2): 543-570.

Villiger, E.B., Wark, D.A., and Ulmer, P., 2007. Crystallization pressures of mid-ocean ridge from major element variations of glasses from and fractional crystallization elements. Journal of Geophysical Research 112: B01202.

Wang, Y., Luo, Z., Santoshi, M., Wang, S., and Wang, N., 2017. The Liuyuan Volcanic Belt in NW China revisited: evidence for Permian rifting associated with the assembly of continental blocks in the Central Asian Orogenic Belt. Geological Magazine 154-2: 265-285.

White, W.M., and Klein, E.M., 2014. Composition of the oceanic crust. Treatise on Geochemistry, Volume 4, Chapter 13. Edited by Holland, D., and Turekian, H.

Wiebe, R.A., 1987. Evidence for stratification of basic, silicic, and hybrid magmas in the Newark Island layered intrusion, Main, Labrador. Geology 15-4: 349-352.

Wiebe R.A., 1994. Silicic magma chambers as traps for basaltic magmas: the Cadillac Mountain Intrusive Complex, Mount Desert Island, Maine. Journal of Geology 102: 423-437.

Wiebe R.A., Manon, M.R., Hawkins, D.P., and McDonough W.F., 2004. Late-stage mafic injection and thermal rejuvenation of the Vinalhaven Granite, Coastal Maine. Journal of Petrology 45-11: 2133-2153.

Wilhem, C., Windley, B.F., and Stampfli, G.M., 2012. The Altaids of Central Asia: a tectonic and evolutionary innovative review. Earth-Science Reviews 113: 303–341.

Williams, I.S., 1997. U-Th-Pb Geochronology by Ion Microprobe. Applications of Microanalytical Techniques to Understanding Mineralizing Processes, 1–35. https://doi.org/10.5382/REV.07.01.

Windley, B.F., Alexeiev, D., Xiao, W., Kröner, A., and Badarch, G., 2007. Tectonic models for accretion of the Central Asian Orogenic belt. Journal of the Geological Society of London v. 164, p. 31–47.

Xiao, W.J., Windley, B.F., Huang, B.C., Han, C.M., Yuan, C., Chen, H.L., Sun, M., Sun, S., and Li, J.L., 2009. End-Permian to mid-Triassic termination of the accretionary processes of the Southern Altaids: implications for the geodynamic evolution, Phanerozoic continental growth, and metallogeny of Central Asia. International Journal of Earth Science 98: 1189–1287.

Xiao, W.J., Mao, Q.G., Windley, B.F., Han, C.M., Qu, J.F., Zhang, J.E., Ao, S.J., Guo, Q.Q., Cleven, N.R., Lin, S.F., Shan, Y.H., and Li, J.L, 2010. Paleozoic multiple accretionary and collisional processes of the Beishan Orogenic Collage. American Journal of Science v. 310, p. 1553-1594.

Xiao, W.J., Windley, B.F., Sun, S., Li, J.L., Huang, B.C., Han, C.M., Yuan, C., Sun, M., and Chen, H.L., 2015. A tale of amalgamation of three collage systems in the Permian-Middle Triassic in Central Asia: oroclines, sutures and terminal accretion. Annual. Review of Earth and Planetary Science v. 43, p. 477–507.

Xiao, W., Windley, B.F., Han, C., Liu, W., Wan, B., Zhang, J.Z., Ao, S., Zhang, Z., and Song, D., 2018. Late Paleozoic to early Triassic multiple roll-back and oroclinal bending of the Mongolia collage in Central Asia. Earth-Science Reviews v. 186: 94-128.

Xue, S., Li, C., Qin, K., Yao, Z., and Ripley, E.M., 2018. Sub-arc mantle heterogeneity in oxygen isotopes: evidence from Permian mafic-ultramafic intrusions in the Central Asian Orogenic Belt. Contributions to Mineralogy and Petrology 173: /doi.org/10.1007/s00410-018-1521-y.

Yakubchuk, A., 2004. Architecture and mineral deposit settings of the Altaid orogenic collage: a revised model. Journal of Asian Earth Sciences 23: 761–779.

Yavuz, F., 2013. WinPyrox: a Windows program for pyroxene calculation, classification and thermobarometry. American Mineralogist **98(7)**: 1338-1359.

Zagorevski, A., and van Staal, C., 2011. The record of Ordovician arc-arc and arc-continent collisions in the Canadian Appalachians during closure of Iapetus. In Browm, D., and Ryan, P.D., Arc-Continent Collision: Frontiers in Earth Sciences: 341-371.

Zhang, J., Yu, S., Gong, J., Li, H., and Hou, K., 2013. The latest Neoarchean-Paleoproterozoic evolution of the Dunhuang bloc, eastern Tarim craton, northwestern China: Evidence from zircon U-Pb dating and Hf isotopic analyses. Precambrian Research v. **226, p.** 21-42.

Zhao, Y., Sun, Y., Diwu, C., Guo, A., Ao, W., and Zhu, T., 2016. The Dunhuang block is a Paleozoic orogenic belt and part of the Central Asian Orognic Belt (CAOB), NW China. Gondwana Research **30**: 207-223.

Zhao, Y., Ao, W., Yan, J., Zhai, M., Zhang, M., Wang, Q., and Sun, Y., 2019. Paleozoic tectonothermal event in Mt. Dongbatu, Dunhuang terrane, southernmost Central Asian Orogenic Belt (CAOB): Implications for the petrogenesis and geological evolution. Lithos **326-327**: 491-512.

Zhu, W., Charvet, J., Xiao, W., and Jahn, B.M., 2011. Continental accretion and intra-continental deformation of the Central Asian Orogenic Belt. Journal of Asian Earth Sciences **42**: 769–773.

Zonenshain, L.P., Kuzmin, M.I., and Natapov, L.M., 1990. Geology of the USSR: a Plate Tectonic Synthesis. Geodynamic Series Vol. 21. American Geophysical Union, Washington, D.C (242 pp).

Zong, K., Liu, Y., Zhang, Z., He., Z., Hu, Z., Gao, J., and Chen, K., 2013. The generation and evolution of Archean continental crust in the Dunhuang block, northeastern Tarim craton, northwestern China. Precambrian Research v. **235** p. 251-263.

Zuo, G.C., Zhang, S.L.,He, G.Q., and Zhang, Y., 1991. Plate tectonic characteristics during the early Paleozoic in Beishan near the Sino-Mongolian border region, China. Tectonophysics **188:** 385–392.

Appendices

Appendix A1: Whole Rock Geochemistry

Table A1 – I: Basalt and diabase whole rock geochemistry

Sample	*18LYS-7018B2*	*18LYS-7018D1*	*18LYS-7030*	*18LYS-7035*	*18LYS-7043*	*18LYS-7045*	*18LYS-7067*	*18LYS-7071A*	*18LYS-7071B*	*18LYS-7137A*	*18LYS-7179*	*18LYS-7186*	*18LYS-7262*	*18LYS-7278*	*18LYS-7299*	*18LYS-7318B*	*18LYS-7324*
Coordinates (UTM 46N)																	
mN	4545468	4545468	4541779	4540690	4538641	4538853	4548560	4547695	4547695	4539192	4537769	4538319	4547143	4541777	4545027	4542283	4542979
mE	695273	695273	695401	695090	688614	688664	702689	702967	702967	685688	685666	685307	705019	700253	699567	697665	697591
Major elements (wt%)																	
SiO_2	48.6	47.4	51.3	49.8	45	46.5	50.2	61	51.7	49.9	46.9	47.3	49.5	48.4	48.5	49.1	50.8
Al_2O_3	16.3	15.35	14.65	14	14.4	14.7	12.2	10.85	13.75	14.2	15.5	15.7	15.4	14.7	15.65	14.65	14.35
Fe_2O_3	10.25	11.55	11.55	12.25	11.3	9.86	14.55	7.8	15.7	12.55	10.35	10	10.35	12.1	9.99	12.7	12.45
CaO	11.55	10.8	8.71	9.83	7.9	6.21	7.95	7.25	5.08	10.95	6.95	7.98	8.91	11.25	11.35	11.15	8.6
MgO	7.12	7.89	4.6	6	8.22	7.56	3.96	0.94	3.37	5.74	9.62	6.57	5.47	6.01	7.22	6.44	5.03
Na_2O	2.71	2.71	3.63	3.07	3	3.96	4.03	4.86	2.75	3.15	2.28	3.59	4.2	2.64	2.37	2.36	3.78
K_2O	0.31	0.22	0.49	0.22	0.18	0.12	0.77	0.29	2.35	0.28	0.84	0.37	0.87	0.3	0.26	0.35	0.48
TiO_2	1.44	1.57	2.04	2.25	1.72	1.59	3.34	1.57	2.08	2.06	1.65	1.6	1.72	2.21	1.56	1.87	2.17
MnO	0.17	0.18	0.16	0.18	0.19	0.18	0.21	0.17	0.21	0.19	0.15	0.15	0.15	0.17	0.14	0.21	0.18
P_2O_5	0.1	0.13	0.33	0.28	0.25	0.15	0.43	0.66	0.84	0.24	0.17	0.17	0.28	0.26	0.15	0.21	0.36
LOI	1.61	1.47	1.89	2.08	6.26	8.83	1.7	5.56	3.24	1.61	4.63	5.63	1.81	1.95	2.28	1.65	1.97
Total	100.16	99.27	99.35	99.96	98.42	99.66	99.34	100.95	101.07	100.87	99.04	99.06	98.66	99.99	99.47	100.69	100.17
Trace elements (µg/g)																	
Cd	0.7	0.6	0.8	0.7	0.5	0.6	0.6	<0.5	0.5	1.1	<0.5	<0.5	0.6	0.7	<0.5	0.5	0.7
Co	38	46	33	37	49	40	38	8	21	42	54	39	32	38	43	36	34
Cu	78	81	46	57	54	47	36	11	15	65	51	57	70	64	66	59	37
Li	<10	<10	10	10	30	30	10	<10	10	<10	50	20	10	10	10	10	10
Mo	1	1	<1	1	<1	<1	1	1	5	1	<1	1	<1	1	1	1	1
Ni	70	94	50	56	142	50	16	<1	1	51	222	98	44	74	100	87	28
Pb	3	3	4	2	<2	4	5	4	5	4	3	<2	3	3	4	4	5
Sc	34	32	33	37	35	33	33	14	18	40	32	33	32	40	35	33	33
Tl	<10	<10	<10	<10	<10	<10	<10	<10	10	<10	<10	<10	<10	<10	<10	<10	10
Zn	74	90	103	91	97	88	123	117	153	106	92	79	90	95	76	91	112
Ba	42.7	28.8	129	39.4	82.9	23.7	153.5	55.1	414	50.3	194.5	25.2	222	62	45.6	77.6	54
Ce	9.1	11.8	39.4	26.3	21.8	13.3	40	59.3	74	22.5	16.8	15.7	33.7	24.4	16	22.1	38.5
Cr	300	250	130	140	360	110	10	5	10	160	550	280	150	210	280	240	80
Cs	0.25	0.44	0.35	0.17	1.84	0.81	0.69	0.24	1.06	0.09	1.18	2.43	0.6	0.45	0.32	0.16	0.26
Dy	5.11	5.87	13	10.55	7.09	5.87	14	14.85	19.1	8.93	6.1	6.27	6.88	9.83	5.63	8.92	12.45
Er	2.8	3.61	7.57	6.42	4.23	3.59	8.41	8.42	11.8	5.49	3.68	3.76	3.87	5.72	3.3	5.65	7.91
Eu	1.18	1.26	2.32	2.1	1.59	1.25	2.85	2.89	4.21	1.77	1.27	1.46	1.85	1.9	1.33	1.75	2.33
Ga	17.4	17.7	22.2	19.7	17.5	14.5	21.8	16	26.7	20.6	14.6	15.3	18.7	19.3	17.4	19.6	22
Gd	4.05	4.87	11.3	9.06	6.89	5.43	12.95	13.55	17.95	8.08	5.6	5.77	6.87	8.61	4.84	7.87	11.1
Hf	2.3	2.5	8	5.8	3.7	2.9	7.6	9.1	13	4.6	3.3	3	4.5	4.9	3	4.8	7.4
Ho	1.02	1.15	2.6	2.15	1.42	1.19	2.72	2.98	4.01	2	1.25	1.27	1.34	2.02	1.1	1.82	2.66
La	2.7	3.8	14.6	9.4	8.3	4.3	14.1	22.4	27.6	7.7	5.1	5	13.2	8.4	6	7.5	13.9
Lu	0.38	0.46	1.01	0.92	0.51	0.45	1.07	1.16	1.64	0.71	0.46	0.49	0.51	0.73	0.41	0.7	1
Nb	1.2	1.6	6.6	4	3.5	1.7	7.1	9.2	12.4	3.6	2	2.1	5.2	4.1	2.8	3.4	6.7
Nd	9.1	11	29.4	22.6	17.3	12.5	32.1	41.8	54.2	19.3	13.9	14.2	23.2	20.7	13	19.4	29.9
Pr	1.51	1.94	5.9	4.27	3.27	2.27	6.11	8.55	10.85	3.53	2.75	2.58	4.79	3.83	2.38	3.4	5.58
Rb	12.7	8	6.6	4.7	5.1	2.6	11.9	3.9	57.5	4.5	25.8	10.7	17.1	5.5	4.4	5	15
Sm	3.25	3.77	9.19	7.34	5.3	4.41	9.6	11.65	15.75	6.11	4.18	4.45	5.57	6.6	4.05	6.17	8.9
Sn	1	1	3	2	1	1	3	4	6	2	1	1	1	2	1	2	3
Sr	181.5	161	155.5	108	439	102.5	209	159.5	188.5	156.5	125	177	333	174.5	208	139.5	172.5
Ta	0.2	0.2	0.6	0.4	0.4	0.3	0.6	0.7	0.9	0.3	0.3	0.3	0.5	0.4	0.4	0.3	0.5
Tb	0.66	0.78	1.89	1.56	1.07	0.83	1.98	2.22	2.88	1.3	0.88	0.93	1.08	1.44	0.84	1.3	1.91
Th	0.16	0.26	2.08	1.14	0.56	0.22	1.63	3.45	4.77	0.89	0.24	0.4	1.44	0.71	0.66	0.85	1.92
Tm	0.41	0.45	1.06	0.96	0.53	0.46	1.13	1.26	1.66	0.74	0.49	0.48	0.54	0.77	0.43	0.8	1.05
U	0.32	0.21	0.56	0.33	0.11	0.24	0.49	1	2.27	0.26	0.16	0.2	0.41	0.27	0.21	0.26	0.48
V	280	291	306	339	343	246	488	60	78	356	268	278	288	362	279	288	316
W	<1	1	1	<1	<1	3	1	<1	<1	<1	<1	<1	<1	<1	<1	<1	<1
Y	26	28.9	66.1	57.4	37	29	73.2	78.4	103.5	47.6	31	32	35.1	49.8	28.9	48.2	67
Yb	2.68	3.07	7.63	6	3.61	3.32	7.65	8.17	11.25	5	3.06	3.44	3.77	5.03	3.22	5.27	7.43
Zr	80	93	309	225	146	116	314	391	581	170	135	126	179	195	112	182	285

Table A1 – I: (continued)

Sample	*18LYS-7391*	*18LYS-7394*	*18LYS-7395*	*18LYS-7396*	*18LYS-7397*	*18LYS-7399*	*18LYS-7400*	*18LYS-7401A*	*18LYS-7402*	*18LYS-7403*	*18LYS-7404*	*18LYS-7405*	*18LYS-7444*	*18LYS-7450*	*19LYS-7010*	*19LYS-7012*	*19LYS-7016*
Coordinates (UTM 46N)																	
mN	4547287	4548149	4548648	4549092	4549674	4550125	4550371	4550956	4551266	4551548	4552042	4552632	4542378	4543118	4538760	4538289	4537708
mE	727988	728003	728221	728250	728205	727828	727765	727992	727694	727515	727562	727785	720348	721771	681186	681354	682436
Major elements (wt%)																	
SiO_2	49.9	50.3	51.7	48.3	50	49.7	47.8	47.1	49.1	48.2	47	50.9	47.4	48	48.6	47.9	50.5
Al_2O_3	15.15	14.85	15.05	14.15	15.6	14.65	15.85	15	15.5	15.45	15.85	15.2	14.8	13.85	15.3	15.75	15.15
Fe_2O_3	10.3	11.3	10.85	10.15	11.25	10.05	10.5	11	11.2	12	12.25	10.5	10.05	12.1	11.7	9.91	10.2
CaO	12.35	8.67	8.87	11.85	9.12	10.3	12.35	11.9	10.15	11.45	11.05	10.5	12.8	9.97	11.25	14.5	9.87
MgO	5.61	5.64	5.23	4.85	5.39	5.27	5.81	6.51	6.36	6.45	6.16	5.89	8.59	6.2	6.55	5.98	7.76
Na_2O	2.79	3.59	3.78	2.92	3.67	4.27	2.9	3.04	3.32	2.54	3.19	4.18	2.37	3.28	2.8	3.05	2.76
K_2O	0.24	1.12	0.48	0.09	0.95	0.39	0.12	0.3	0.23	0.41	0.41	0.12	0.14	0.06	0.37	0.04	0.54
TiO_2	1.94	1.85	1.96	1.69	2.03	1.82	1.85	1.88	2.12	2.05	2.16	1.84	1.18	2.33	1.86	1.38	1.61
MnO	0.16	0.16	0.16	0.15	0.16	0.15	0.16	0.18	0.17	0.16	0.18	0.15	0.17	0.17	0.17	0.14	0.15
P_2O_5	0.22	0.29	0.26	0.25	0.29	0.28	0.21	0.2	0.27	0.2	0.24	0.25	0.07	0.27	0.2	0.13	0.17
LOI	2.92	2.27	2.67	3.88	2.37	2.53	3.97	3.55	2.54	2.17	1.93	2.38	2.99	3.75	1.97	2.13	2.87
Total	101.58	100.04	101.01	98.28	100.83	99.41	101.52	100.66	100.96	101.08	100.42	101.91	100.56	99.98	100.77	100.91	101.58
Trace elements (μg/g)																	
Cd	1	<0.5	<0.5	<0.5	<0.5	0.5	<0.5	0.5	<0.5	<0.5	<0.5	<0.5	0.6	0.8	<0.5	<0.5	<0.5
Co	42	33	32	30	33	35	36	38	38	42	39	32	44	40	33	39	41
Cu	65	56	49	47	49	55	59	57	55	61	59	50	93	58	65	62	60
Li	20	10	10	10	10	10	10	10	10	10	10	10	20	10	10	10	30
Mo	1	<1	<1	<1	<1	1	<1	1	<1	<1	<1	<1	1	1	1	<1	<1
Ni	101	58	63	57	61	46	79	94	106	91	67	54	81	53	96	133	161
Pb	<2	<2	5	2	<2	2	<2	2	<2	<2	<2	<2	<2	4	<2	<2	<2
Sc	39	33	30	29	30	35	35	36	35	40	41	35	43	42	36	33	32
Tl	10	<10	<10	<10	<10	<10	<10	<10	<10	<10	<10	<10	<10	<10	<10	<10	<10
Zn	83	106	82	76	91	89	80	82	96	86	90	83	67	99	86	62	70
Ba	27.3	103.5	109.5	22.5	294	58.3	17.6	47.6	33	52.6	42.2	70	46.2	36.7	94	16	37.7
Ce	19.1	37.9	34.8	30	35.9	33.4	20.9	20.1	24.6	16.7	21.4	26.4	7.7	26	19.9	10.6	15.2
Cr	260	180	180	180	160	150	220	280	250	250	210	180	360	180	240	340	380
Cs	0.36	0.17	0.14	0.1	0.34	0.17	0.21	0.13	0.1	0.09	0.39	0.21	0.19	0.39	0.3	0.27	0.75
Dy	7.61	11.15	10.05	7.7	10.45	9.41	6.85	7.12	7.74	6.93	8.15	7.59	4.44	9.5	7.59	4.8	5.97
Er	4.32	7.25	6.72	4.96	6.53	5.57	4.1	4.16	4.49	4.4	5.24	4.69	2.86	5.55	4.83	2.91	3.37
Eu	1.88	2.23	2.08	1.91	2.1	2.05	1.61	1.69	1.63	1.65	1.76	1.65	1.06	2.06	1.58	1.24	1.37
Ga	18.9	22.6	19.9	22.1	22.1	21.6	19.1	19.6	19.3	20.1	21.8	19.4	16.2	20.7	18.3	18.5	18.2
Gd	6.81	10.65	8.9	6.82	9.65	8.41	6.36	6.52	7.17	6.62	7.39	7.26	4.03	8.55	6.76	4.3	5.02
Hf	4	8.7	7.9	5.6	8.2	6.4	4.1	3.8	4.8	3.8	4.8	4.8	2	5	4	2.5	3.1
Ho	1.54	2.26	2.21	1.64	2.13	1.82	1.34	1.39	1.57	1.49	1.54	1.51	0.97	1.96	1.39	0.95	1.08
La	6.3	13.8	12.9	11.6	13.3	12.5	7.3	6.8	9	5.3	7.4	10	2.3	9.3	7.4	3.6	5.4
Lu	0.59	0.89	0.95	0.67	0.89	0.78	0.49	0.55	0.6	0.57	0.64	0.61	0.37	0.77	0.53	0.38	0.4
Nb	2.8	5.8	5.3	5.7	5.7	6.8	3.2	3.6	4.5	2.3	3.6	4.5	0.8	4.3	3.2	1.5	2.1
Nd	17.1	27.8	25.7	21.3	27.9	24.2	16.2	16.4	20.7	15.6	19.1	20.3	7.8	21.3	16.7	10.6	13.7
Pr	3.09	5.63	5.27	4.21	5.39	4.87	3.25	3.12	3.82	2.82	3.49	3.78	1.38	4.04	3.11	1.66	2.63
Rb	6.6	22.6	5.8	2.5	8.9	5.6	1.7	4.2	3.3	8.7	5.9	1.2	3.1	1.1	8.4	0.5	10.9
Sm	5.53	8.02	7.29	5.4	7.44	7.19	5.46	5.48	6.01	4.73	5.73	5.62	2.89	6.72	5.22	3.34	4.46
Sn	1	4	3	2	3	2	1	2	2	1	1	2	1	2	1	1	1
Sr	252	298	284	143.5	376	129.5	252	327	277	229	182	226	224	218	189.5	175	147.5
Ta	0.3	0.9	0.8	1.4	0.8	0.5	1.1	0.4	0.8	0.8	0.6	0.7	0.2	0.3	0.8	0.9	1.5
Tb	1.13	1.74	1.5	1.11	1.6	1.38	1.05	1.03	1.1	1.17	1.29	1.14	0.64	1.39	1.13	0.73	0.81
Th	0.37	2.24	1.97	1.34	2.06	1.46	0.64	0.61	0.59	0.3	0.66	1.22	0.16	0.79	1.02	0.23	0.34
Tm	0.54	0.94	0.92	0.63	0.88	0.75	0.54	0.57	0.64	0.59	0.64	0.6	0.42	0.85	0.55	0.36	0.43
U	0.16	0.67	0.63	0.43	0.71	0.5	0.22	0.2	0.23	0.1	0.22	0.4	0.16	0.33	0.44	0.11	0.09
V	326	264	271	273	243	285	260	313	275	297	314	276	258	393	280	222	240
W	1	1	1	1	1	1	1	<1	1	1	1	1	<1	<1	1	1	1
Y	38.8	59.4	53.7	40	55.9	49.4	35	36.5	40	37.7	43.2	39.4	24.7	50.9	39	23.7	28.5
Yb	4.01	6.97	5.93	4.42	6.21	5.64	4.01	3.89	4.18	4.41	4.5	4.48	2.6	5.06	4.4	2.6	3.07
Zr	161	360	332	232	328	262	172	153	184	148	186	182	73	188	140	87	126

Table A1 – I: (continued)

Sample	*19LYS-7103*	*19LYS-7182A*	*19LYS-7182B*	*19LYS-7245*	*19LYS-7263C*	*19LYS-7286*	*19LYS-7287*	*19LYS-7288*	*19LYS-7289*	*19LYS-7290*	*19LYS-7397*	*19LYS-7403*	*19LYS-7536*	*19LYS-7628*	*19LYS-7635B*	*19LYS-8065*	*19LYS-8068*
Coordinates (UTM 46N)																	
mN	4546568	4536858	4536858	4542299	4544817	4548255	4549139	4549840	4550271	4550864	4541959	4541334	4540754	4545033	4544647	4543312	4543026
mE	688334	673372	673372	694833	695297	717511	717604	717374	717203	716810	692984	692216	690754	707612	695961	694544	694852
Major elements (wt%)																	
SiO_2	48.8	50.3	46.4	50	49.8	48.7	48.7	49.8	48.6	52.6	50.9	50.4	51.5	47.9	50.4	50.2	50.6
Al_2O_3	13.6	13.5	16.4	14.65	15.9	16.2	14.8	15.05	15.8	14.05	13.25	18.25	14.15	15.25	14.25	13.45	14.75
Fe_2O_3	13.45	13.4	8.97	12.1	10.7	10.7	12.3	11.5	11.3	13.35	13.85	6.13	12.75	12.15	13.25	13.7	11
CaO	11.25	8.72	12.85	10.25	10.7	9.87	10.3	10.15	11.75	6.38	9.73	12	8.07	12.3	6.04	8.44	10.65
MgO	5.9	5.09	9.5	6.62	7.93	6.75	6.17	5.67	6.28	3.93	4.95	7.25	4.89	6.62	5.7	5.9	6.42
Na_2O	2.79	3.44	1.47	2.72	2.82	3.18	3.29	3.34	3.12	5.24	3.45	3.7	3.53	2.41	5.04	3.13	3.09
K_2O	0.18	0.32	0.35	0.3	0.26	0.72	0.24	0.44	0.3	0.72	0.26	0.24	0.8	0.2	0.18	0.73	0.18
TiO_2	2.21	2.39	0.92	1.88	1.44	1.92	2.22	1.87	1.89	2.42	2.36	0.96	2.18	1.96	2.12	2.25	1.6
MnO	0.24	0.19	0.14	0.2	0.14	0.17	0.19	0.18	0.17	0.22	0.21	0.1	0.21	0.17	0.27	0.23	0.17
P_2O_5	0.21	0.33	0.05	0.24	0.14	0.25	0.27	0.23	0.2	0.51	0.32	0.01	0.27	0.19	0.26	0.23	0.17
LOI	1.57	1.62	3.03	1.3	1.71	2.78	1.64	2.26	2.22	1.62	0.71	1.46	1.33	1.95	1.97	1.39	1.8
Total	100.2	99.3	100.08	100.26	101.54	101.24	100.12	100.49	101.63	101.04	99.99	100.5	99.68	101.1	99.48	99.65	100.43
Trace elements (μg/g)																	
Cd	0.5	<0.5	<0.5	<0.5	<0.5	<0.5	<0.5	<0.5	<0.5	<0.5	<0.5	<0.5	<0.5	<0.5	<0.5	<0.5	<0.5
Co	42	29	43	36	42	35	34	35	38	25	30	22	33	41	33	29	36
Cu	66	26	57	56	28	51	54	58	67	26	14	5	35	65	17	11	54
Li	20	10	10	10	<10	20	10	20	10	10	10	<10	10	10	10	10	10
Mo	<1	1	<1	<1	<1	<1	<1	<1	<1	1	<1	<1	1	<1	<1	<1	<1
Ni	44	27	176	61	93	91	63	70	84	21	28	60	34	98	41	45	44
Pb	<2	<2	<2	<2	2	<2	<2	<2	<2	<2	<2	<2	<2	<2	<2	<2	<2
Sc	46	33	33	36	38	36	35	35	36	26	36	42	33	37	33	37	36
Tl	<10	<10	<10	<10	<10	<10	<10	<10	<10	<10	<10	<10	<10	<10	<10	<10	<10
Zn	116	106	68	92	47	89	94	87	84	128	120	38	94	93	132	92	88
Ba	63	51.7	46.5	41.5	52.5	50.2	45.1	31.4	29	92.5	100.5	42.9	233	20.4	58	180	38.3
Ce	15.8	34.5	4.6	20.6	12.7	24.9	26	27	20.1	53.5	27.5	11.9	28.3	16.3	39.8	23.4	18.6
Cr	80	30	440	180	240	210	190	200	240	60	60	420	70	230	120	140	90
Cs	0.24	0.17	0.07	0.96	0.11	0.5	0.1	0.17	0.27	0.23	0.35	0.06	0.32	0.29	0.11	0.22	0.08
Dy	8.14	11.85	3.78	7.93	4.96	7.55	8.66	8.69	7.29	16.2	10.05	6.1	9.07	6.26	11.55	11.3	7.55
Er	5.07	7.94	2.5	4.74	3.12	4.52	5.14	5.68	4.29	9.96	6.81	3.87	5.96	3.77	7.02	6.87	4.52
Eu	1.85	2.43	0.82	1.58	1.11	1.66	1.93	1.76	1.58	3.2	2.11	1.07	1.85	1.54	1.83	2.01	1.34
Ga	20.7	24.3	15.5	19.6	18.2	19.9	21	20.9	20.5	25.4	22.2	17.5	21.7	19.9	18.8	19.6	19.7
Gd	7.07	10.85	3.16	6.55	4.25	7.05	7.84	7.72	6.23	14.4	9.41	5.33	8.41	5.42	10.65	8.97	6.02
Hf	3.9	7.7	1.5	4.5	2.5	5.1	5.5	6	4.5	11.7	5.7	1.3	5.3	3.2	4.1	5.5	3.8
Ho	1.68	2.43	0.82	1.51	1.01	1.44	1.72	1.7	1.34	3.28	2.15	1.29	1.93	1.19	2.37	2.22	1.36
La	5.5	12.5	1.4	7.6	5.1	9.3	9.1	9.4	7.3	19.1	9.9	3.3	10.8	6	13	8.1	6.8
Lu	0.62	0.98	0.31	0.64	0.44	0.58	0.65	0.64	0.56	1.26	0.89	0.55	0.86	0.5	0.91	0.95	0.59
Nb	2.4	5.1	0.4	3.5	1.4	5.3	4.9	4.6	3.1	8.6	4.2	1.3	4.2	2.8	3.9	3.3	2.9
Nd	13.6	26.6	5.7	16.7	10.4	19.2	21.6	20.4	17.3	41.2	23.1	11.2	21.6	13.6	29.5	21.4	15.4
Pr	2.72	5.16	0.86	3.24	1.93	3.79	4.11	4.17	3.29	8.04	4.27	2.04	4.02	2.58	6.01	3.74	2.81
Rb	2.9	8	9	9.6	4	17.6	2.8	10.5	5	9.1	4.4	4.1	24.7	1.8	4.8	19.1	3.9
Sm	4.79	8.4	2.08	5.26	3.3	5.51	6.69	6.58	5.1	12.6	7.53	4.06	6.61	4.14	7.77	6.78	4.89
Sn	1	3	1	2	1	1	2	2	2	4	3	2	2	1	4	2	2
Sr	153	155.5	117.5	135.5	143.5	253	201	186	235	182.5	152.5	189.5	147	182	74.8	105	134
Ta	<0.1	1.2	<0.1	0.7	0.8	0.9	0.8	1	1.3	0.7	0.6	0.1	1.5	0.6	0.5	1.4	1.4
Tb	1.25	1.81	0.56	1.14	0.77	1.09	1.29	1.27	1.09	2.33	1.55	0.92	1.39	0.92	1.74	1.62	1.08
Th	0.59	1.98	0.09	1.03	0.73	0.9	1	1.17	0.75	2.37	1.59	0.41	2.46	0.51	1.58	1.08	1.12
Tm	0.67	1.11	0.33	0.71	0.46	0.54	0.79	0.68	0.59	1.33	0.9	0.55	0.78	0.51	1.04	0.89	0.66
U	0.29	0.67	0.28	0.34	0.34	0.32	0.42	0.5	0.34	0.79	0.53	0.2	1.1	0.16	0.58	0.46	0.38
V	409	341	196	296	272	267	304	259	285	195	340	218	309	296	283	331	267
W	1	1	1	1	1	1	1	1	2	1	1	1	1	1	1	1	1
Y	44	64.9	20.3	42.1	26.9	37.8	45.4	45.1	37	83.8	57.9	32.9	51.6	31.3	60.5	58.2	38.8
Yb	4.63	6.52	2.24	4.69	2.54	3.66	4.71	4.75	3.89	8.96	5.75	3.73	5.41	3.29	6.89	6.57	4.36
Zr	131	280	46	160	90	186	211	228	174	463	206	44	193	118	155	198	142

Table A1 – I: (continued)

Sample	*19LYS-8069*	*19LYS-8070*	*19LYS-8071*	*19LYS-8079*	*19LYS-8080*	*19LYS-8082*	*19LYS-8083*	*19LYS-8117*	*19LYS-8141*	*19LYS-8145*	*19LYS-8149*	*19LYS-8154A*	*19LYS-8168*	*19LYS-8169*	*19LYS-8172*	*19LYS-8173*	*19LYS-8176*
Coordinates (UTM 46N)																	
mN	4541928	4541467	4540987	4548730	4547715	4546080	4544313	4539503	4544666	4538054	4538300	4542651	4551070	4547410	4542119	4542277	4545490
mE	695040	695194	695143	707720	707821	707452	707537	688664	694949	720962	725723	724589	716562	718025	720243	720318	719214
Major elements (wt%)																	
SiO_2	48.9	46.8	50.4	50.3	48.8	46.8	51.6	59.7	48.4	49.7	45.2	45.9	47.4	49.6	47.5	49.4	48.2
Al_2O_3	14.7	14.85	14.25	13.3	14	15.95	13.15	14.45	13.05	13	13.7	15.3	15.75	14.85	18.4	16.05	14.95
Fe_2O_3	11.45	11.95	11.3	13.15	13.5	10.9	14.4	9.24	12.95	12.3	13.65	11.4	11.7	10.35	8.19	10.05	10.1
CaO	10.95	12.45	7.39	8.78	10.7	12.2	6.9	3.32	7.64	9.17	9.12	11.2	11.25	12.4	10.4	10.7	13.45
MgO	6.36	6.8	6.43	5.92	6.22	7.06	4.19	2.8	5.5	4.41	5.1	7.17	6.36	6.65	8.18	7.97	4.48
Na_2O	2.73	2.37	3.56	4.26	3.13	2.75	5.93	6.54	3.17	4.51	3.99	1.84	3.02	3.59	2.5	3.42	3.98
K_2O	0.33	0.3	0.8	0.32	0.4	0.35	0.29	0.78	0.81	0.49	0.46	0.27	0.67	0.53	1.6	0.35	0.14
TiO_2	1.96	1.75	2.17	2.62	2.44	1.63	3.65	1.51	3.28	3.32	3.61	1.9	1.86	1.51	1.17	1.18	1.39
MnO	0.17	0.19	0.18	0.17	0.2	0.16	0.18	0.11	0.17	0.19	0.22	0.19	0.21	0.16	0.12	0.16	0.15
P_2O_5	0.25	0.15	0.29	0.32	0.24	0.16	0.54	0.41	0.55	0.59	0.6	0.21	0.2	0.11	0.04	0.07	0.1
LOI	2.09	2.05	3.43	1.17	2.18	3.26	1.11	1.23	3.03	4.24	4.52	3.69	3.2	2	3.59	2.51	2.64
Total	99.89	99.66	100.2	100.31	101.81	101.22	101.94	100.09	98.55	101.92	100.17	99.07	101.62	101.75	101.69	101.86	99.58
Trace elements (µg/g)																	
Cd	<0.5	<0.5	<0.5	<0.5	<0.5	<0.5	<0.5	<0.5	<0.5	<0.5	<0.5	<0.5	<0.5	0.5	<0.5	<0.5	<0.5
Co	37	36	34	38	39	37	28	18	32	27	23	36	41	46	37	40	42
Cu	45	45	47	12	60	52	1	27	30	60	23	57	66	76	79	83	67
Li	10	10	20	10	10	10	10	10	30	20	30	20	30	10	30	10	10
Mo	<1	<1	<1	<1	1	<1	1	1	<1	<1	<1	<1	<1	<1	<1	<1	<1
Ni	63	59	74	78	57	102	13	13	25	19	18	113	88	55	169	77	144
Pb	<2	<2	<2	<2	<2	<2	<2	3	<2	<2	<2	<2	<2	<2	<2	<2	<2
Sc	37	44	33	30	43	35	32	17	41	36	41	38	38	46	25	36	34
Tl	<10	<10	<10	<10	<10	<10	<10	<10	<10	<10	<10	<10	<10	<10	<10	<10	<10
Zn	93	86	107	41	112	76	92	89	115	97	113	84	91	77	49	65	72
Ba	77.8	28.1	112.5	54.4	17.1	19.6	35.3	81.8	273	210	162.5	81.6	48.1	9.7	187	24.5	11.8
Ce	25	13.2	36.1	38.7	20.1	13.8	46.7	80.1	45.2	48.2	56.8	18.4	18.3	12.6	7.2	7.3	11.5
Cr	190	250	190	110	180	320	10	30	50	50	60	360	260	320	460	340	330
Cs	0.12	0.15	0.26	0.03	0.14	0.56	0.03	0.4	0.95	0.08	1.11	0.25	0.77	0.3	1.36	0.55	0.14
Dy	7.78	7.02	11.7	16.8	8.51	5.68	13.55	21.3	10.25	10.35	12.4	6.58	6.56	5.7	4.1	5.26	5.16
Er	4.63	4.21	7.2	9.81	5.33	3.44	7.91	13.95	5.72	5.61	7.39	3.91	4.26	3.83	2.64	2.91	3.31
Eu	1.52	1.29	2.21	3.17	1.84	1.26	3.29	3.04	2.63	2.62	2.95	1.49	1.75	1.43	1.4	0.99	1.3
Ga	19.8	20.1	22.2	21.9	21.9	19.2	23.6	27.7	20.5	20.8	22.3	19.4	21	17.1	18.1	16.2	18.5
Gd	6.64	5.52	10.6	17.1	7.62	4.89	11.95	18.75	10	9.57	11.45	5.91	6.4	5.5	3.96	3.91	4.74
Hf	4.7	3.2	7.9	6.4	4.6	2.6	8.1	19.2	6.7	7.7	8.9	3.6	3.8	2.9	2.1	2	2.8
Ho	1.53	1.33	2.41	3.23	1.72	1.07	2.62	4.27	1.93	1.77	2.42	1.29	1.32	1.18	0.82	1.07	1.14
La	9.6	4.3	13.2	12.5	7.1	5.1	16.3	29.6	16.5	18.3	21.1	6.4	6.6	4	1.8	2.3	3.6
Lu	0.57	0.52	0.96	1.04	0.67	0.45	1.05	1.9	0.69	0.73	0.98	0.5	0.5	0.47	0.32	0.42	0.4
Nb	4.7	1.9	5.8	7.9	3.6	2.2	8.9	10.8	8.3	9.7	10.6	3.1	2.8	1.2	0.5	0.7	1.1
Nd	19.4	11.7	26.8	39.8	16.7	10.9	33.5	52.9	31.7	32.7	39	14.4	15.5	11.5	8.5	7.3	10.5
Pr	3.65	2.2	5.48	6.95	3.33	2.2	6.99	11.55	6.6	6.79	8.1	2.96	2.84	2.01	1.34	1.21	1.85
Rb	5.1	8.4	19.8	6.5	7.2	8.3	2.6	14.3	6.2	3.9	4	5.7	19.6	12.3	42.7	9.1	3.3
Sm	5.9	4.16	8.38	14.25	5.48	3.54	10.3	14.85	8.36	9.31	10.7	4.64	4.8	3.47	2.79	2.39	3.6
Sn	2	1	2	2	2	1	2	12	2	2	3	2	1	1	1	1	1
Sr	170	161	113.5	176.5	197	216	80	48.7	279	256	236	227	184.5	268	326	170.5	267
Ta	1.4	<0.1	0.7	0.9	0.1	0.4	0.9	1	0.7	1.1	1	0.8	0.5	0.8	<0.1	0.6	0.5
Tb	1.21	0.97	1.74	2.62	1.32	0.76	1.88	3.02	1.5	1.53	1.85	0.95	1.04	0.84	0.63	0.7	0.78
Th	1.16	0.34	1.72	1.63	0.52	0.39	1.51	5.92	0.79	0.87	1.05	0.39	0.52	0.18	<0.05	0.17	0.23
Tm	0.61	0.55	1.01	1.23	0.73	0.4	1.08	1.92	0.76	0.79	1.04	0.53	0.54	0.46	0.35	0.4	0.45
U	0.41	0.17	0.62	0.77	0.26	0.24	0.52	1.76	0.33	0.5	0.59	0.15	0.25	0.11	0.11	0.08	0.13
V	294	339	268	307	389	301	395	106	392	375	418	306	319	280	218	255	254
W	1	1	1	1	1	1	1	1	1	2	1	1	1	1	<1	1	<1
Y	39.6	35.9	64.1	83.8	45.1	29.1	71.2	116.5	51.5	51.3	65.8	34.2	33	29	20.8	24.5	28.1
Yb	4.08	3.95	7.18	7.78	4.91	2.91	7.35	13.65	5.04	5.16	6.59	3.5	3.77	3.29	2.4	2.53	2.94
Zr	158	104	295	250	163	94	322	713	301	318	371	138	146	123	78	71	104

Table A1 – II: Chert whole rock geochemistry

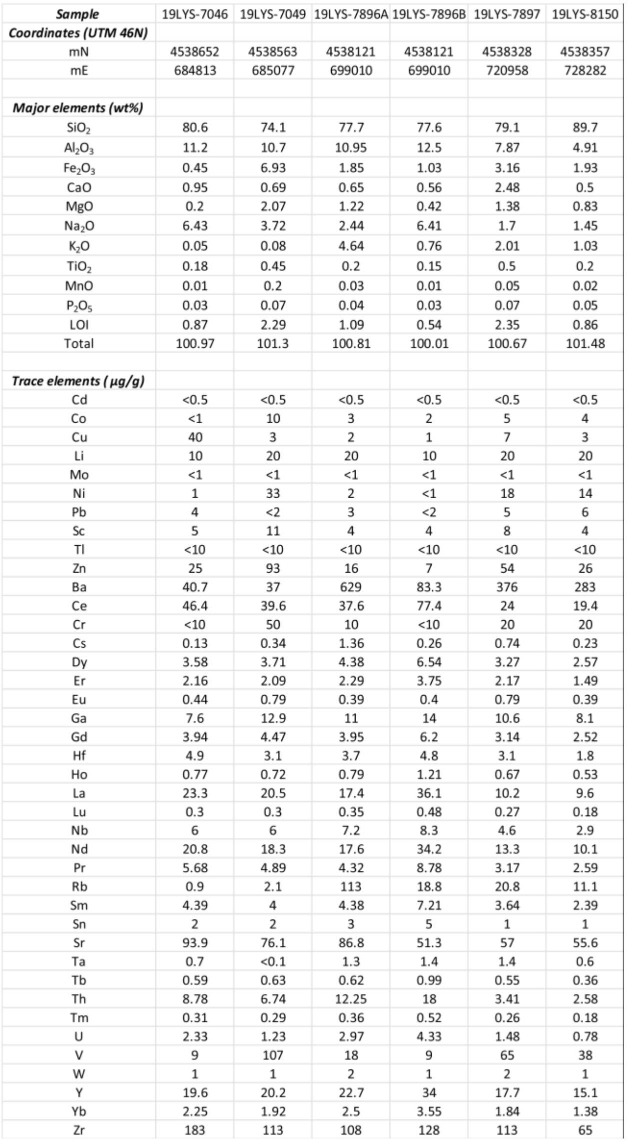

Sample	19LYS-7046	19LYS-7049	19LYS-7896A	19LYS-7896B	19LYS-7897	19LYS-8150
Coordinates (UTM 46N)						
mN	4538652	4538563	4538121	4538121	4538328	4538357
mE	684813	685077	699010	699010	720958	728282
Major elements (wt%)						
SiO_2	80.6	74.1	77.7	77.6	79.1	89.7
Al_2O_3	11.2	10.7	10.95	12.5	7.87	4.91
Fe_2O_3	0.45	6.93	1.85	1.03	3.16	1.93
CaO	0.95	0.69	0.65	0.56	2.48	0.5
MgO	0.2	2.07	1.22	0.42	1.38	0.83
Na_2O	6.43	3.72	2.44	6.41	1.7	1.45
K_2O	0.05	0.08	4.64	0.76	2.01	1.03
TiO_2	0.18	0.45	0.2	0.15	0.5	0.2
MnO	0.01	0.2	0.03	0.01	0.05	0.02
P_2O_5	0.03	0.07	0.04	0.03	0.07	0.05
LOI	0.87	2.29	1.09	0.54	2.35	0.86
Total	100.97	101.3	100.81	100.01	100.67	101.48
Trace elements (μg/g)						
Cd	<0.5	<0.5	<0.5	<0.5	<0.5	<0.5
Co	<1	10	3	2	5	4
Cu	40	3	2	1	7	3
Li	10	20	20	10	20	20
Mo	<1	<1	<1	<1	<1	<1
Ni	1	33	2	<1	18	14
Pb	4	<2	3	<2	5	6
Sc	5	11	4	4	8	4
Tl	<10	<10	<10	<10	<10	<10
Zn	25	93	16	7	54	26
Ba	40.7	37	629	83.3	376	283
Ce	46.4	39.6	37.6	77.4	24	19.4
Cr	<10	50	10	<10	20	20
Cs	0.13	0.34	1.36	0.26	0.74	0.23
Dy	3.58	3.71	4.38	6.54	3.27	2.57
Er	2.16	2.09	2.29	3.75	2.17	1.49
Eu	0.44	0.79	0.39	0.4	0.79	0.39
Ga	7.6	12.9	11	14	10.6	8.1
Gd	3.94	4.47	3.95	6.2	3.14	2.52
Hf	4.9	3.1	3.7	4.8	3.1	1.8
Ho	0.77	0.72	0.79	1.21	0.67	0.53
La	23.3	20.5	17.4	36.1	10.2	9.6
Lu	0.3	0.3	0.35	0.48	0.27	0.18
Nb	6	6	7.2	8.3	4.6	2.9
Nd	20.8	18.3	17.6	34.2	13.3	10.1
Pr	5.68	4.89	4.32	8.78	3.17	2.59
Rb	0.9	2.1	113	18.8	20.8	11.1
Sm	4.39	4	4.38	7.21	3.64	2.39
Sn	2	2	3	5	1	1
Sr	93.9	76.1	86.8	51.3	57	55.6
Ta	0.7	<0.1	1.3	1.4	1.4	0.6
Tb	0.59	0.63	0.62	0.99	0.55	0.36
Th	8.78	6.74	12.25	18	3.41	2.58
Tm	0.31	0.29	0.36	0.52	0.26	0.18
U	2.33	1.23	2.97	4.33	1.48	0.78
V	9	107	18	9	65	38
W	1	1	2	1	2	1
Y	19.6	20.2	22.7	34	17.7	15.1
Yb	2.25	1.92	2.5	3.55	1.84	1.38
Zr	183	113	108	128	113	65

Table A1 – III: Gabbroic rocks whole rock geochemistry

Sample	18LYS-7000A	18LYS-7002A	18LYS-7002B	18LYS-7005A	18LYS-7005B	18LYS-7008A	18LYS-7008B	18LYS-7008C	18LYS-7009A	18LYS-7009C	18LYS-7009D	18LYS-7010A
Rock Type	Olivine gabbro	Olivine gabbro	Olivine gabbro	Olivine gabbro	Olivine gabbro	Troctolite	Troctolite	Troctolite	Troctolite	Olivine gabbro	Olivine gabbro	Hornblende gabbro
Coordinates (UTM 46N)												
mN	4545261	4545261	4545261	4544674	4544674	4544305	4544305	4544305	4543880	4543880	4543880	4543599
mE	694198	694198	694198	694089	694089	694403	694403	694403	694451	694451	694451	694258
Major elements (wt%)												
SiO_2	49.1	46.8	40.8	47.1	48.9	46.1	47.1	49.6	49.1	39.3	44	44
Al_2O_3	14.65	20.7	8.56	15	19.5	19.8	16.15	22.1	18.9	4.59	20.3	20.1
Fe_2O_3	12.7	6.01	11.15	11	4.76	6.39	6.9	4.33	5.26	13.8	6.39	6.44
CaO	11.15	12.3	5.04	11.9	13.95	12.3	13.65	14.3	14.35	3.55	10.95	11.2
MgO	6.44	8.29	27.5	6.51	7.71	10.55	11.15	5.13	9.21	32.7	11.55	13.7
Na_2O	2.36	2.06	0.81	3.04	2.56	1.63	1.5	2.88	2.16	0.19	1.85	1.53
K_2O	0.35	0.15	0.3	0.3	0.04	0.07	0.08	0.08	0.09	0.13	0.39	0.11
TiO_2	2.26	0.35	0.32	0.36	0.39	0.18	0.21	0.15	0.65	0.26	0.55	1.73
MnO	0.18	0.08	0.08	0.07	0.07	0.1	0.12	0.1	0.12	0.12	0.1	0.16
P_2O_5	0.27	<0.01	0.01	0.01	0.01	0.02	0.04	0.01	0.03	0.01	0.01	0.14
LOI	2.07	0.9	0.92	0.94	0.76	3.62	1.96	2.95	1.5	3.53	1.05	1.04
Total	100.78	99.43	98.49	100.48	98.98	100.12	99.09	100.61	100.55	100.51	100.26	100.48
Trace elements (μg/g)												
Cd	0.6	<0.5	<0.5	<0.5	<0.5	<0.5	0.5	<0.5	0.5	<0.5	<0.5	1.3
Co	35	36	34	25	19	69	81	72	50	60	30	40
Cu	55	116	116	70	17	56	29	46	62	90	4	45
Li	10	<10	<10	<10	<10	<10	<10	<10	<10	<10	<10	<10
Mo	<1	<1	<1	1	<1	<1	<1	<1	<1	<1	<1	1
Ni	52	178	194	103	77	583	712	649	310	280	131	52
Pb	<2	<2	<2	<2	<2	<2	<2	<2	3	<2	<2	5
Sc	35	42	39	18	20	6	6	4	10	8	41	37
Tl	<10	<10	<10	<10	10	<10	<10	<10	<10	<10	10	<10
Zn	87	28	26	26	22	49	58	52	62	64	32	95
Ba	41.6	2.9	10.4	24.7	20.2	16.1	8.2	10.9	16.3	10.8	22.2	64
Ce	27.8	1.5	1.8	2.3	2.7	1.5	7.8	1.1	2.7	2	6.8	16
Cr	150	930	1400	550	540	770	1050	990	20	140	840	160
Cs	0.16	0.18	0.15	0.09	0.06	0.67	0.14	0.66	0.47	0.37	0.09	0.15
Dy	10.95	1.41	1.35	1.32	1.37	0.56	0.83	0.35	1.25	1.08	3.1	6.92
Er	6.88	0.79	0.86	0.72	0.89	0.31	0.49	0.2	0.69	0.6	2.07	4.22
Eu	2.21	0.44	0.46	0.56	0.55	0.31	0.38	0.24	0.58	0.44	1.03	1.43
Ga	20.7	11.7	12.1	17.6	17.6	11.1	10.7	11	14.8	12.5	15.6	17.9
Gd	9.38	1.17	1.08	1	1.07	0.44	0.74	0.36	1.09	0.81	2.29	5.74
Hf	6.3	0.4	0.4	0.3	0.4	0.2	0.4	<0.2	0.7	0.4	0.7	3
Ho	2.34	0.27	0.26	0.29	0.28	0.13	0.16	0.09	0.26	0.18	0.63	1.39
La	9.7	0.4	0.7	1	1.1	0.6	3	0.4	1	0.8	2.4	6.2
Lu	0.95	0.11	0.1	0.11	0.1	0.05	0.06	0.03	0.13	0.08	0.29	0.58
Nb	4.2	<0.2	<0.2	<0.2	<0.2	<0.2	4.1	<0.2	0.5	0.2	1	2.6
Nd	23.9	1.9	2	2.1	2.3	1.2	4.6	0.9	2.2	1.8	5.9	13.4
Pr	4.36	0.29	0.34	0.39	0.42	0.24	1.01	0.19	0.43	0.32	1.05	2.52
Rb	4.7	0.6	1	1.8	1.4	10.4	4.3	5.5	2.5	0.8	1.2	1.6
Sm	7.43	0.82	0.82	0.77	0.91	0.38	0.9	0.34	0.71	0.7	1.84	4.29
Sn	2	<1	<1	<1	<1	<1	<1	<1	<1	<1	1	1
Sr	113	127.5	154.5	189	191.5	171	158	162	150	135	150	136.5
Ta	0.4	0.1	0.1	0.1	0.1	0.1	0.1	0.1	0.2	0.1	0.1	0.4
Tb	1.64	0.21	0.21	0.18	0.22	0.07	0.14	0.06	0.16	0.15	0.49	0.97
Th	1.17	<0.05	0.11	0.07	0.11	<0.05	0.35	<0.05	0.14	0.11	0.21	0.65
Tm	1.02	0.11	0.13	0.12	0.11	0.05	0.05	0.03	0.09	0.09	0.27	0.55
U	0.36	<0.05	0.41	0.13	0.15	<0.05	<0.05	<0.05	<0.05	0.1	0.19	0.39
V	367	142	133	121	128	43	51	41	103	66	220	296
W	<1	<1	<1	<1	<1	<1	<1	<1	<1	<1	1	<1
Y	60.2	7.4	7.4	6.7	7.4	2.9	4.5	2	6.7	5.2	17.1	35.8
Yb	6.59	0.76	0.8	0.76	0.71	0.3	0.53	0.26	0.76	0.51	1.8	4.12
Zr	236	12	10	10	11	9	16	6	23	13	22	104

Table A1 – III: (continued)

Sample	18LYS-7018B1	18LYS-7018C	18LYS-7018D2	18LYS-7020 B	18LYS-7062A	18LYS-7062B	18LYS-7063	18LYS-7119A	18LYS-7122	18LYS-7128A	18LYS-7128B	18LYS-7154A
Rock Type	Hornblende gabbro	Hornblende gabbro	Hornblende gabbro	Hornblende gabbro	Olivine gabbro	Olivine gabbro	Olivine gabbro	Olivine gabbro	Olivine gabbro	Olivine gabbro	Olivine gabbro	Olivine gabbro
Coordinates (UTM 46N)												
mN	4545468	4545468	4545468	4545262	4541662	4541662	4541876	4541697	4541228	4540322	4540322	4541967
mE	695273	695273	695273	695427	688319	688319	688304	686127	686148	686513	686513	687463
Major elements (wt%)												
SiO_2	44.6	39.4	40.4	44.2	43.6	46.7	36.2	47.7	38.4	47.3	40.4	39.3
Al_2O_3	24	9.97	9.51	22.1	19.65	15	4.46	23.5	4.87	19	7.15	7.67
Fe_2O_3	4.79	10.85	10.7	5.76	6.4	7.41	13.55	3.32	13.4	3.65	14.3	11.35
CaO	13.2	5.35	6.74	11.8	11.2	11.1	2.74	12.5	4.35	15.7	5.5	5.11
MgO	9.96	26.3	25.7	11.2	13.5	7.56	31.7	5.95	30.3	8.24	27.8	27
Na_2O	1.46	0.63	0.52	1.42	1.42	2.54	0.18	2.71	0.42	1.85	0.61	0.81
K_2O	0.19	0.08	0.16	0.21	0.11	0.3	0.03	0.23	0.03	0.07	0.07	0.07
TiO_2	1.57	1.71	0.29	1.58	0.27	0.28	0.16	0.19	0.32	0.34	0.17	0.16
MnO	0.17	0.18	0.1	0.17	0.09	0.1	0.13	0.09	0.13	0.11	0.11	0.09
P_2O_5	0.15	0.13	<0.01	0.14	<0.01	<0.01	0.02	0.01	<0.01	0.02	<0.01	0.01
LOI	8.59	1.88	1.65	1.36	2.22	1.02	4.2	2.54	1.65	1.66	2.77	1.23
Total	98.08	100.11	100.47	99.61	99.44	99.21	100.6	99.41	99.54	99.96	99.5	100.32
Trace elements (μg/g)												
Cd	0.5	0.6	<0.5	0.7	<0.5	<0.5	0.6	<0.5	0.6	<0.5	<0.5	<0.5
Co	38	47	42	41	37	43	59	36	36	30	55	46
Cu	48	82	51	69	80	87	122	29	89	1575	86	88
Li	30	<10	<10	<10	<10	<10	<10	<10	<10	<10	<10	<10
Mo	<1	1	<1	<1	1	<1	<1	<1	<1	<1	<1	<1
Ni	49	73	113	62	210	250	440	193	98	137	253	247
Pb	4	3	<2	<2	3	3	2	<2	<2	4	3	2
Sc	32	36	41	39	39	30	12	9	40	38	11	10
Tl	<10	<10	<10	10	10	<10	<10	<10	<10	<10	<10	10
Zn	88	82	31	69	34	40	66	43	38	45	46	31
Ba	25	93	22.4	38	36.2	8.5	28.9	29.3	19.7	16.1	14.3	10.9
Ce	13.8	12.5	1.8	13.5	1.4	1.5	1.1	1.8	1.1	1.3	1	1.6
Cr	110	260	330	250	1100	940	650	530	330	710	190	360
Cs	0.82	0.57	0.23	0.07	0.05	0.1	0.35	0.17	0.04	0.12	0.68	0.21
Dy	5.83	6.07	1.43	6.55	1.38	1.24	0.57	0.66	1.45	1.64	0.67	0.7
Er	3.53	3.42	0.87	3.62	0.89	0.71	0.36	0.45	0.89	1.06	0.39	0.4
Eu	1.25	1.34	0.41	1.34	0.32	0.41	0.39	0.45	0.47	0.47	0.32	0.34
Ga	14.8	18.2	12.7	18.8	10.9	12.2	12.5	15.2	14.3	13.7	12.8	13.7
Gd	5.39	5.04	1.08	5.44	1.14	0.85	0.51	0.59	1.16	1.37	0.42	0.38
Hf	3	2.9	0.4	2.7	0.4	0.3	0.2	0.2	0.3	0.3	0.2	0.2
Ho	1.21	1.2	0.27	1.27	0.29	0.25	0.12	0.14	0.38	0.34	0.13	0.13
La	4.3	3.9	0.7	4.6	0.5	0.6	0.5	0.9	0.4	0.5	0.4	0.6
Lu	0.47	0.46	0.13	0.49	0.11	0.12	0.06	0.06	0.13	0.13	0.07	0.05
Nb	1.9	1.8	<0.2	1.7	<0.2	<0.2	<0.2	<0.2	<0.2	<0.2	<0.2	0.3
Nd	12.5	11.1	1.8	12.1	1.7	1.6	1	1.3	1.5	1.8	1.1	1.3
Pr	2.33	2.02	0.32	2.06	0.26	0.24	0.16	0.25	0.2	0.25	0.18	0.22
Rb	2.3	20.5	4.6	3.1	1.6	0.5	5.9	2.8	0.4	3.1	7.6	1
Sm	3.96	3.99	0.8	3.88	0.86	0.73	0.26	0.52	0.68	0.8	0.43	0.36
Sn	1	1	<1	1	<1	<1	<1	<1	<1	<1	<1	<1
Sr	102.5	159.5	153	178.5	79.2	91.8	206	162.5	137	136.5	159.5	175
Ta	0.2	0.2	0.1	0.2	0.1	0.1	0.1	0.1	0.1	0.1	0.1	0.1
Tb	0.87	0.91	0.2	0.87	0.19	0.18	0.1	0.1	0.2	0.2	0.11	0.1
Th	0.16	0.43	0.06	0.67	<0.05	<0.05	<0.05	0.05	<0.05	<0.05	0.06	0.09
Tm	0.47	0.48	0.1	0.49	0.15	0.09	0.04	0.06	0.12	0.14	0.06	0.06
U	0.15	0.28	0.14	0.31	0.05	0.05	0.18	0.11	0.18	0.16	0.08	<0.05
V	250	308	142	307	151	123	51	68	144	145	59	46
W	3	<1	<1	<1	<1	<1	<1	<1	<1	<1	<1	<1
Y	29.4	31	7.7	32.4	7.8	6.4	3.2	3.6	8.5	8.4	3.6	3.5
Yb	3.1	3.19	0.75	3.47	0.89	0.7	0.38	0.51	0.92	0.88	0.38	0.42
Zr	116	102	8	109	11	10	4	5	7	9	4	7

Table A1 – III: (continued)

Sample	18LYS-7177A	18LYS-7177C	18LYS-7249B	18LYS-7251A	18LYS-7251B	18LYS-7292	18LYS-7318A	18LYS-7375A	18LYS-7375B	18LYS-7401B	19LYS-7132	19LYS-7218
Rock Type	Hornblende gabbro	Hornblende gabbro	Melatroctolite	Troctolite	Olivine gabbro	Olivine gabbro	Olivine gabbro	Olivine gabbro	Melatroctolite	Olivine gabbro	Olivine gabbro	Olivine gabbro
Coordinates (UTM 46N)												
mN	4542364	4542364	4544675	4544521	4544521	4544385	4542283	4541722	4541722	4550956	4541548	4542328
mE	689104	689104	692963	692282	692282	700082	697665	693128	693128	727992	686188	689086
Major elements (wt%)												
SiO_2	49.7	40.3	41.1	47.7	46.7	45.9	49.5	46.1	42.7	49.6	46.1	45.6
Al_2O_3	16	7.35	7.75	15.3	25.9	23.9	15.5	13.05	18.2	16.5	19.4	27.3
Fe_2O_3	10.6	12.5	13.45	12	5.08	5.11	11.15	14.2	7.72	6.83	7.21	2.74
CaO	10.35	4.66	5.69	8.18	12.8	12.5	10.6	8.2	9.69	13	11.4	14.75
MgO	7.05	29.6	23.4	6.18	4.73	9.04	7.04	6.36	14.8	8.45	11.25	5.94
Na_2O	3.36	0.46	0.75	4.43	2.56	2	2.61	2.63	1.4	2.48	2.14	1.77
K_2O	0.25	0.09	0.5	0.05	0.1	0.1	0.48	1.1	0.19	0.19	0.07	0.12
TiO_2	0.4	0.57	0.11	0.22	0.8	1.6	1.87	0.52	0.67	1.88	0.25	0.55
MnO	0.09	0.08	0.18	0.08	0.09	0.17	0.21	0.14	0.16	0.18	0.08	0.1
P_2O_5	0.02	0.01	0.01	0.01	0.03	0.15	0.21	0.03	0.05	0.2	0.01	0.01
LOI	2.98	1.12	4.8	4.37	2.27	3.16	1.65	2.54	4.06	3.55	1.32	3.46
Total	101.3	101.3	100.36	99.51	100.81	100.2	100.69	99.54	99.1	100.66	99.08	100.96
Trace elements (μg/g)												
Cd	<0.5	0.5	0.8	<0.5	<0.5	0.7	0.8	0.5	<0.5	0.5	<0.5	<0.5
Co	43	30	110	48	32	42	45	36	98	38	27	40
Cu	106	8	39	40	3	62	58	102	42	57	95	58
Li	<10	<10	<10	10	<10	10	10	10	<10	10	10	10
Mo	<1	1	<1	<1	<1	1	<1	<1	<1	1	<1	<1
Ni	263	148	644	326	199	119	87	152	948	94	97	251
Pb	<2	<2	<2	<2	2	<2	4	<2	2	2	<2	<2
Sc	26	46	9	8	32	27	37	16	10	36	31	15
Tl	<10	10	<10	<10	<10	<10	<10	<10	<10	<10	<10	<10
Zn	36	30	68	39	20	82	106	80	82	82	24	39
Ba	16.9	23.4	5.7	43.1	54.3	59.8	51	66	16.8	47.6	18.8	20.3
Ce	2.6	5.5	1.1	1.6	3.2	14.3	20	3.4	3.1	20.1	1.3	2.2
Cr	960	1470	110	290	650	200	190	470	1800	280	560	550
Cs	0.1	0.04	0.27	0.43	0.26	0.35	0.24	0.34	1.34	0.13	0.02	0.09
Dy	1.67	2.42	0.41	0.82	3.18	4.85	8.49	1.95	1.74	7.12	1.15	1.29
Er	0.96	1.56	0.23	0.55	2.15	3.01	5.26	1.1	1.12	4.16	0.62	0.74
Eu	0.52	0.57	0.24	0.28	0.53	1.23	1.66	0.49	0.44	1.69	0.44	0.44
Ga	13.8	13.9	7.4	12.4	12.8	17.7	19.7	15.3	8.6	19.6	15.6	13.7
Gd	1.3	2.15	0.28	0.66	2.21	4.2	7.41	1.58	1.21	6.52	0.97	0.98
Hf	0.5	0.6	<0.2	0.3	1.4	2.7	4.6	0.7	0.9	3.8	0.2	0.5
Ho	0.31	0.52	0.08	0.16	0.63	1.01	1.8	0.42	0.31	1.39	0.25	0.23
La	1	2.1	0.5	0.6	1.2	5.5	6.9	1.2	1	6.8	0.6	0.9
Lu	0.12	0.21	0.03	0.07	0.26	0.44	0.79	0.16	0.12	0.55	0.09	0.09
Nb	0.3	0.3	<0.2	<0.2	0.5	2.7	3	0.4	0.5	3.6	<0.2	0.3
Nd	2.3	4.4	0.8	1.7	3.9	10.7	17.3	3.1	3	16.4	1.3	2
Pr	0.41	0.83	0.16	0.25	0.57	2.15	3.28	0.55	0.54	3.12	0.25	0.34
Rb	1.8	2.4	0.8	26.5	24.2	8	7.1	3.8	9.2	4.2	0.7	1.7
Sm	0.8	1.55	0.21	0.52	1.5	3.64	5.62	1.29	0.9	5.48	0.59	0.72
Sn	1	1	<1	<1	<1	1	2	<1	<1	2	<1	<1
Sr	139.5	148.5	99.8	128	182.5	217	148	174.5	90.9	327	157	134.5
Ta	0.2	0.1	<0.1	0.1	0.1	0.4	0.3	0.1	0.1	0.4	0.1	1.5
Tb	0.25	0.35	0.07	0.12	0.45	0.67	1.28	0.27	0.26	1.03	0.18	0.17
Th	0.08	0.18	0.11	<0.05	0.11	0.63	0.82	0.07	0.1	0.61	<0.05	0.06
Tm	0.14	0.2	0.05	0.1	0.3	0.43	0.78	0.13	0.15	0.57	0.12	0.1
U	0.08	0.17	<0.05	<0.05	0.11	0.19	0.21	0.06	0.07	0.2	0.06	0.08
V	114	185	33	57	199	272	314	124	147	313	112	85
W	1	<1	<1	<1	<1	<1	<1	<1	<1	<1	1	1
Y	8.3	13	2.3	5	17.3	27	46.9	9.7	9.3	36.5	6	6.1
Yb	0.78	1.35	0.29	0.5	1.84	2.91	5.06	0.96	1.12	3.89	0.59	0.55
Zr	15	20	3	8	41	113	177	26	32	153	5	16

Table A1 – III: (continued)

Sample	19LYS-7225	19LYS-7227	19LYS-7248	19LYS-7249	19LYS-7262	19LYS-7308	19LYS-7311A	19LYS-7311B	19LYS-7399	19LYS-7530	19LYS-7574	19LYS-7636
Rock Type	Hornblende gabbro	Olivine gabbro	Hornblende gabbro	Melatroctolite	Troctolite	Troctolite	Troctolite	Melatroctolite	Melatroctolite	Troctolite	Troctolite	Hornblende gabbro
Coordinates (UTM 46N)												
mN	4544878	4544683	4545678	4545715	4544986	4541445	4541047	4541047	4541552	4541649	4536326	4545006
mE	694120	694092	695769	695701	695267	689543	689426	689426	692620	690903	666647	696034
Major elements (wt%)												
SiO_2	45	49.6	49.1	39.3	44	44	44.6	39.4	40.4	44.2	43.6	46.7
Al_2O_3	20.3	19.7	18.9	4.59	20.3	20.1	24	9.97	9.51	22.1	19.65	15
Fe_2O_3	6.28	5.32	5.26	13.8	6.39	6.44	4.79	10.85	10.7	5.76	6.4	7.41
CaO	11.65	13.85	14.35	3.55	10.95	11.2	13.2	5.35	6.74	11.8	11.2	11.1
MgO	13.35	8.42	9.21	32.7	11.55	13.7	9.96	26.3	25.7	11.2	13.5	7.56
Na_2O	1.61	2.14	2.16	0.19	1.85	1.53	1.46	0.63	0.52	1.42	1.42	2.54
K_2O	0.05	0.14	0.09	0.13	0.39	0.11	0.19	0.08	0.16	0.21	0.11	0.3
TiO_2	0.44	0.36	0.29	0.24	0.25	0.31	0.21	0.22	0.24	0.23	0.26	0.61
MnO	0.11	0.07	0.09	0.21	0.1	0.09	0.07	0.14	0.17	0.09	0.09	0.12
P_2O_5	0.01	0.02	<0.01	<0.01	0.01	0.01	<0.01	0.01	0.01	<0.01	0.01	0.04
LOI	2.27	0.87	1.94	5.02	4.65	1.92	2.08	7.62	5.12	3.8	3.08	6.74
Total	99.36	99.74	101.39	99.73	100.44	99.41	100.56	100.57	99.27	100.81	99.32	98.12
Trace elements (μg/g)												
Cd	<0.5	<0.5	<0.5	<0.5	<0.5	<0.5	<0.5	<0.5	<0.5	<0.5	<0.5	<0.5
Co	45	25	30	117	52	50	38	105	96	45	52	34
Cu	69	84	20	26	62	39	24	70	66	108	31	7
Li	10	10	10	10	10	<10	<10	10	10	10	10	10
Mo	<1	<1	<1	<1	5	<1	<1	<1	1	<1	<1	<1
Ni	212	135	168	1255	369	442	278	751	878	276	382	88
Pb	<2	<2	<2	<2	11	<2	<2	<2	<2	<2	<2	<2
Sc	39	22	30	14	8	8	6	6	11	6	9	40
Tl	<10	<10	<10	<10	<10	<10	<10	<10	<10	<10	<10	<10
Zn	41	23	27	109	59	36	33	53	85	56	38	40
Ba	19.6	22.1	30.9	12.3	30.8	6.6	11.7	15.8	67	19.9	16.5	58.1
Ce	5	2.6	1.5	1.7	3.1	1.4	3.1	1.2	4	1.8	2.6	8.4
Cr	1330	650	1070	3420	580	310	390	250	1420	340	690	200
Cs	0.12	0.04	0.45	0.34	0.4	0.12	0.34	0.17	0.87	0.11	0.61	0.71
Dy	1.99	1.28	1.26	0.67	0.88	0.8	0.69	0.44	0.99	0.68	0.87	4.43
Er	1.19	0.86	0.73	0.42	0.66	0.5	0.32	0.29	0.67	0.41	0.48	2.77
Eu	0.64	0.55	0.36	0.2	0.4	0.36	0.29	0.19	0.22	0.26	0.32	0.89
Ga	13.7	18.1	14	5.2	13.7	12.8	13.4	7	7.2	13.7	12.6	15.7
Gd	1.85	1.13	0.95	0.55	0.96	0.73	0.63	0.59	0.96	0.56	0.94	3.57
Hf	0.7	0.4	0.3	0.2	0.5	0.3	0.2	0.3	0.5	0.3	0.4	1.7
Ho	0.45	0.3	0.23	0.19	0.2	0.17	0.12	0.11	0.21	0.15	0.2	0.95
La	3.1	1.1	0.5	0.7	1.2	0.5	1.2	0.5	1.7	0.7	1.2	3.2
Lu	0.17	0.1	0.09	0.08	0.07	0.08	0.04	0.05	0.09	0.06	0.07	0.36
Nb	0.2	<0.2	<0.2	<0.2	0.2	<0.2	1.1	<0.2	0.2	0.2	0.2	0.7
Nd	3.9	2.3	1.6	1.6	2.4	1.4	2.1	1	2	1.4	1.8	7.1
Pr	0.7	0.42	0.26	0.25	0.44	0.24	0.47	0.2	0.45	0.26	0.4	1.33
Rb	2	1.5	3.2	4.3	13.4	2.8	6.7	1.6	6.5	11.2	2.8	7.1
Sm	1.56	0.91	0.72	0.46	0.74	0.54	0.66	0.48	0.65	0.54	0.59	2.65
Sn	<1	<1	<1	<1	<1	<1	<1	<1	2	<1	<1	1
Sr	155.5	192.5	199.5	28.4	231	127.5	242	92.1	91.3	158	157.5	142
Ta	0.4	0.3	0.6	0.7	<0.1	0.3	<0.1	0.3	0.6	0.1	<0.1	0.2
Tb	0.36	0.2	0.21	0.1	0.16	0.12	0.11	0.06	0.13	0.09	0.12	0.66
Th	0.39	0.09	<0.05	0.09	0.17	<0.05	0.11	<0.05	0.24	0.11	0.17	0.52
Tm	0.17	0.11	0.07	0.07	0.07	0.07	0.05	0.04	0.11	0.05	0.08	0.4
U	0.15	0.12	<0.05	0.06	0.22	<0.05	<0.05	0.06	0.32	0.07	0.09	0.29
V	204	125	102	105	47	66	42	35	59	47	78	181
W	1	1	1	1	1	1	1	1	1	1	1	1
Y	11.5	7.4	6.1	4.1	5.1	4.6	3.5	2.5	5.8	3.6	5	23
Yb	1.31	0.71	0.64	0.54	0.63	0.41	0.35	0.31	0.62	0.36	0.6	2.39
Zr	21	12	7	8	15	10	9	12	17	9	15	65

Appendix A2: Mineral Chemistry

Table A2 – I: Olivine chemistry

Sample	*18LYS-7002B-1*	*18LYS-7002B-2*	*18LYS-7009A-1*	*18LYS-7009A-2*	*18LYS-7375B-3*	*18LYS-7375B-6*	*18LYS-7375B-7*	*19LYS-7039A-1*	*19LYS-7039A-4*	*19LYS-7147-1*	*19LYS-7147-3*
Rock	*Olivine gabbro*	*Olivine gabbro*	*Troctolite*	*Troctolite*	*Melatroctolite*	*Melatroctolite*	*Melatroctolite*	*Olivine gabbro*	*Olivine gabbro*	*Olivine gabbro*	*Olivine gabbro*
Type	*Groundmass*	*Groundmass*	*Chadacryst*	*Chadacryst*	*Groundmass*	*Chadacryst*	*Chadacryst*	*Groundmass*	*Groundmass*	*Groundmass*	*Groundmass*
SiO_2	39.42	39.25	38.53	38.31	39.67	40.21	40.42	38.19	38.37	38.93	38.81
Al_2O_3	0.02	0.00	0.01	0.01	0.01	0.01	0.02	0.00	0.00	0.00	0.01
Na_2O	0.00	0.00	0.00	0.00	0.01	0.00	0.01	0.00	0.00	0.02	0.00
MgO	40.13	40.95	37.50	37.08	44.38	45.25	45.58	37.53	37.51	39.66	40.10
TiO_2	0.00	0.02	0.04	0.01	0.02	0.01	0.01	0.00	0.00	0.02	0.01
CaO	0.02	0.03	0.08	0.06	0.12	0.10	0.15	0.06	0.03	0.05	0.04
NiO	0.11	0.10	0.14	0.14	0.24	0.17	0.24	0.11	0.13	0.12	0.12
Cr_2O_3	0.00	0.02	0.00	0.00	0.01	0.01	0.02	0.00	0.00	0.01	0.00
FeO	19.47	19.13	23.63	23.69	15.13	14.35	13.73	22.82	23.04	21.04	19.59
MnO	0.29	0.29	0.39	0.41	0.27	0.28	0.22	0.36	0.38	0.37	0.35
Total	99.47	99.79	100.32	99.71	99.85	100.39	100.40	99.07	99.46	100.23	99.05
Sample	*19LYS-7225-6*	*19LYS-7238-4*	*19LYS-7238-5*	*19LYS-8100-1*	*19LYS-8100-2*	*19LYS-8165-1*	*19LYS-8165-2*	*19LYS-8167B-1*	*19LYS-8167B-2*	*19LYS-8167B-6*	
Rock	*Hornblende gabbro*	*Melatroctolite*	*Melatroctolite*	*Troctolite*	*Troctolite*	*Troctolite*	*Troctolite*	*Troctolite*	*Troctolite*	*Troctolite*	
Type	*Groundmass*	*Groundmass*	*Chadacryst*	*Groundmass*	*Groundmass*	*Groundmass*	*Groundmass*	*Chadacryst*	*Chadacryst*	*Groundmass*	
SiO_2	38.43	39.64	38.94	38.36	38.78	39.57	39.64	39.96	39.84	39.96	
Al_2O_3	0.00	0.00	0.01	0.02	0.01	0.00	0.01	0.01	0.00	0.01	
Na_2O	0.01	0.01	0.00	0.00	0.00	0.01	0.00	0.00	0.00	0.00	
MgO	37.50	41.87	40.95	38.88	39.09	43.38	43.42	42.85	42.60	42.29	
TiO_2	0.03	0.01	0.02	0.00	0.00	0.01	0.01	0.02	0.01	0.03	
CaO	0.04	0.03	0.13	0.04	0.03	0.05	0.06	0.05	0.04	0.07	
NiO	0.12	0.18	0.18	0.11	0.13	0.14	0.12	0.19	0.15	0.15	
Cr_2O_3	0.01	0.00	0.01	0.00	0.01	0.00	0.00	0.00	0.02	0.02	
FeO	23.63	18.66	18.85	21.10	21.21	16.15	16.12	16.97	16.96	17.49	
MnO	0.34	0.33	0.33	0.33	0.33	0.27	0.27	0.26	0.25	0.29	
Total	100.12	100.73	99.41	98.83	99.58	99.58	99.65	100.30	99.86	100.31	

Table A2 – II: Clinopyroxene chemistry

Sample	*18LYS-7002B-3*	*18LYS-7002B-5*	*18LYS-7009A-3*	*18LYS-7009D-1*	*18LYS-7009D-4*	*18LYS-7062A-1*	*18LYS-7299-1*	*18LYS-7299-2*	*18LYS-7299-3*	*18LYS-7318B-1*
Rock	*Olivine gabbro*	*Olivine gabbro*	*Olivine gabbro*	*Olivine gabbro*	*Olivine gabbro*	*Olivine gabbro*	*Diabase*	*Diabase*	*Diabase*	*Basalt*
Type	*Groundmass*	*Groundmass*	*Oikocryst*	*Groundmass*	*Groundmass*	*Groundmass*	*Groundmass*	*Groundmass*	*Groundmass*	*Glomerocryst*
SiO_2	53.25	52.07	53.02	52.14	53.31	54.05	50.76	50.72	50.02	52.04
Al_2O_3	3.05	3.36	2.15	2.69	2.54	2.49	4.90	4.16	3.47	2.27
Na_2O	0.31	0.35	0.37	0.28	0.31	0.27	0.31	0.33	0.41	0.35
MgO	16.88	16.09	15.95	15.29	15.30	16.84	14.84	14.57	12.07	14.92
TiO_2	0.43	0.77	0.79	0.59	0.63	0.29	1.46	1.43	1.66	0.86
CaO	20.34	20.24	20.99	21.98	22.23	21.47	21.16	20.56	19.95	19.29
K_2O	0.00	0.01	0.00	0.00	0.00	0.00	0.00	0.00	0.00	0.00
NiO	0.00	0.00	0.06	0.03	0.05	0.02	0.05	0.01	0.00	0.04
Cr_2O_3	0.65	1.02	0.08	0.53	0.30	0.55	0.43	0.20	0.00	0.05
V_2O_3	0.04	0.06	0.07	0.06	0.06	0.02	0.10	0.10	0.11	0.08
FeO	5.90	6.29	7.01	6.69	6.18	4.11	6.82	8.17	12.53	9.45
MnO	0.15	0.18	0.22	0.20	0.18	0.10	0.15	0.22	0.34	0.33
Sc2O3	0.01	0.01	0.00	0.00	0.03	0.01	0.01	0.01	0.02	0.03
Total	101.01	100.43	100.69	100.48	101.10	100.21	101.01	100.47	100.57	99.72

Sample	*18LYS-7318B-2*	*18LYS-7318B-3*	*18LYS-7375B-8*	*19LYS-7039A-2*	*19LYS-7039A-5*	*19LYS-7039A-6*	*19LYS-7132-1*	*19LYS-7132-2*	*19LYS-7147-4*	*19LYS-7225-1*
Rock	*Basalt*	*Basalt*	*Wehrlite*	*Olivine gabbro*	*Olivine gabbro*	*Olivine gabbro*	*Olivine gabbro*	*Olivine gabbro*	*Olivine gabbro*	*Hornblende gabbro*
Type	*Glomerocryst*	*Glomerocryst*	*Oikocryst*	*Groundmass*	*Groundmass*	*Groundmass*	*Groundmass*	*Groundmass*	*Oikocryst*	*Groundmass*
SiO_2	52.47	50.90	52.64	52.35	52.09	54.50	52.71	52.01	51.64	52.67
Al_2O_3	2.12	3.78	3.31	2.71	3.32	1.48	2.66	2.88	3.19	3.04
Na_2O	0.28	0.34	0.31	0.41	0.49	0.03	0.40	0.35	0.45	0.33
MgO	16.23	15.04	16.85	15.46	15.20	27.35	15.45	15.19	15.08	16.29
TiO_2	0.81	1.32	0.56	0.63	0.79	0.48	0.49	0.51	0.56	0.70
CaO	19.05	19.72	21.49	21.68	21.88	1.28	21.97	22.10	22.57	20.96
K_2O	0.00	0.00	0.01	0.01	0.01	0.00	0.00	0.01	0.02	0.00
NiO	0.04	0.00	0.02	0.01	0.00	0.03	0.02	0.05	0.01	0.00
Cr_2O_3	0.12	0.18	1.17	0.42	0.46	0.10	0.53	0.64	1.01	0.62
V_2O_3	0.07	0.06	0.04	0.05	0.05	0.02	0.04	0.06	0.04	0.05
FeO	8.77	8.57	3.97	6.06	5.87	14.22	5.84	5.75	4.96	5.96
MnO	0.26	0.22	0.11	0.20	0.20	0.36	0.18	0.19	0.17	0.16
Sc_2O_3	0.01	0.00	0.01	0.00	0.00	0.00	0.00	0.01	0.00	0.00
Total	100.23	100.15	100.49	99.97	100.36	99.83	100.29	99.74	99.70	100.80

Table A2 – II: (continued)

Sample	*19LYS-7225-3*	*19LYS-7238-6*	*19LYS-8100-3*	*19LYS-8100-5*	*19LYS-8100-6*	*19LYS-8160-1*	*19LYS-8160-2*	*19LYS-8165-3*	*19LYS-8167B-3*	*19LYS-8167B-4*
Rock	*Hornblende gabbro*	*Melatroctolite*	*Olivine gabbro*	*Olivine gabbro*	*Olivine gabbro*	*Hornblende gabbro*	*Hornblende gabbro*	*Troctolite*	*Troctolite*	*Troctolite*
Type	*Groundmass*	*Oikocryst*	*Groundmass*	*Groundmass*	*Groundmass*	*Groundmass*	*Groundmass*	*Groundmass*	*Oikocryst*	*Groundmass*
SiO_2	52.21	51.91	52.22	51.80	52.62	52.89	53.78	52.38	53.43	53.69
Al_2O_3	2.72	3.64	2.34	2.70	2.54	3.85	1.43	3.38	2.78	2.85
Na_2O	0.35	0.34	0.34	0.35	0.31	0.64	0.30	0.29	0.29	0.27
MgO	14.86	16.15	15.78	14.93	15.48	14.96	15.03	16.60	16.68	16.73
TiO_2	0.96	0.94	0.79	0.62	0.52	0.56	0.43	0.49	0.43	0.56
CaO	22.47	21.21	22.36	21.96	22.28	12.05	22.07	21.32	21.45	21.90
K_2O	0.00	0.00	0.01	0.00	0.01	0.14	0.00	0.00	0.00	0.01
NiO	0.01	0.03	0.05	0.01	0.00	0.04	0.00	0.02	0.02	0.03
Cr_2O_3	0.44	1.11	0.32	0.41	0.42	0.03	0.12	1.12	0.79	0.51
V_2O_3	0.07	0.05	0.07	0.06	0.06	0.04	0.05	0.06	0.05	0.06
FeO	5.95	5.25	5.41	5.99	5.51	13.49	7.70	4.90	4.75	4.72
MnO	0.21	0.12	0.16	0.18	0.19	0.20	0.18	0.13	0.12	0.13
Sc_2O_3	0.00	0.01	0.02	0.01	0.02	0.00	0.00	0.00	0.01	0.00
Total	100.25	100.76	99.86	99.00	99.96	98.88	101.09	100.70	100.80	101.45

Sample	*19LYS-8181-7*	*19LYS-8181-8*
Rock	*Hornblende gabbro*	*Hornblende gabbro*
Type	*Groundmass*	*Groundmass*
SiO_2	55.23	53.77
Al_2O_3	0.50	1.55
Na_2O	0.05	0.31
MgO	16.39	16.04
TiO_2	0.06	0.31
CaO	24.13	23.30
K_2O	0.00	0.01
NiO	0.00	0.02
Cr_2O_3	0.15	0.19
V_2O_3	0.03	0.01
FeO	4.35	4.60
MnO	0.20	0.17
Sc_2O_3	0.02	0.01
Total	101.09	100.29

Table A2 – III: Plagioclase chemistry

Sample	*18LYS-7002B-4*	*18LYS-7002B-6*	*18LYS-7009A-4*	*18LYS-7009A-5*	*18LYS-7009D-2*	*18LYS-7009D-5*	*18LYS-7062A-2*	*18LYS-7299-4*	*18LYS-7299-5*	*18LYS-7299-6*
Rock	*Olivine gabbro*	*Olivine gabbro*	*Troctolite*	*Troctolite*	*Olivine gabbro*	*Olivine gabbro*	*Olivine gabbro*	*Diabase*	*Diabase*	*Diabase*
Type	*Groundmass*	*Groundmass*	*Chadacryst*	*Chadacryst*	*Groundmass*	*Groundmass*	*Groundmass*	*Groundmass*	*Groundmass*	*Groundmass*
SiO_2	49.82	50.21	49.46	48.70	50.95	55.61	49.07	54.44	53.59	52.36
Al_2O_3	32.34	31.68	32.53	32.61	31.03	28.78	32.78	28.72	29.25	30.13
Na_2O	2.71	2.93	2.55	2.32	3.44	5.18	2.31	4.65	4.21	3.72
MgO	0.03	0.02	0.03	0.02	0.02	0.02	0.03	0.14	0.20	0.20
TiO_2	0.05	0.07	0.05	0.01	0.07	0.04	0.04	0.09	0.09	0.07
CaO	15.53	14.99	15.80	15.98	14.39	11.23	16.34	12.07	12.69	13.69
K_2O	0.02	0.02	0.05	0.03	0.02	0.08	0.04	0.09	0.09	0.07
Cr_2O_3	0.00	0.00	0.00	0.00	0.00	0.00	0.00	0.01	0.02	0.00
FeO	0.28	0.32	0.48	0.45	0.36	0.31	0.31	0.69	0.66	0.67
MnO	0.01	0.02	0.00	0.01	0.00	nd	0.00	0.00	0.00	0.00
Total	100.78	100.27	100.95	100.14	100.27	101.27	100.92	100.89	100.79	100.90

Sample	*18LYS-7318B-4*	*18LYS-7318B-5*	*18LYS-7318B-6*	*18LYS-7375B-4*	*18LYS-7375B-5*	*19LYS-7039A-3*	*19LYS-7039A-7*	*19LYS-7132-3*	*19LYS-7132-4*	*19LYS-7147-2*
Rock	*Basalt*	*Basalt*	*Basalt*	*Melatroctolite*	*Melatroctolite*	*Olivine gabbro*	*Olivine gabbro*	*Olivine gabbro*	*Olivine gabbro*	*Olivine gabbro*
Type	*Phenocryst*	*Phenocryst*	*Phenocryst*	*Groundmass*	*Groundmass*	*Groundmass*	*Groundmass*	*Groundmass*	*Groundmass*	*Groundmass*
SiO_2	53.62	54.16	54.16	51.72	49.58	51.51	52.13	51.95	52.68	50.35
Al_2O_3	28.74	28.53	28.47	30.82	32.39	30.83	30.25	30.44	29.62	31.42
Na_2O	4.45	4.70	4.72	3.68	2.72	3.59	3.90	3.78	4.22	3.04
MgO	0.15	0.15	0.15	0.03	0.01	0.03	0.03	0.02	0.04	0.03
TiO_2	0.10	0.09	0.08	0.05	0.04	0.03	0.08	0.06	0.07	0.07
CaO	12.38	11.96	11.89	13.94	15.44	13.95	13.46	13.55	12.84	14.81
K_2O	0.07	0.07	0.08	0.04	0.02	0.07	0.06	0.04	0.06	0.05
Cr_2O_3	0.00	0.00	0.00	0.00	0.00	0.01	0.00	0.01	0.00	0.02
FeO	0.68	0.72	0.70	0.33	0.42	0.30	0.30	0.29	0.30	0.43
MnO	0.01	0.02	0.00	0.01	0.00	0.01	0.01	0.00	0.01	0.00
Total	100.20	100.40	100.26	100.61	100.62	100.33	100.21	100.12	99.85	100.20

Table A2 – III: (continued)

Sample	*19LYS-7147-5*	*19LYS-7225-2*	*19LYS-7225-4*	*19LYS-7238-3*	*19LYS-7263C-1*	*19LYS-7263C-2*	*19LYS-7263C-3*	*19LYS-7263C-4*	*19LYS-8100-4*	*19LYS-8100-7*
Rock	*Olivine gabbro*	*Hornblende gabbro*	*Hornblende gabbro*	*Melatroctolite*	*Basalt*	*Basalt*	*Basalt*	*Basalt*	*Troctolite*	*Olivine gabbro*
Type	*Groundmass*	*Groundmass*	*Groundmass*	*Groundmass*	*Glomerocyrst*	*Glomerocryst*	*Phenocryst*	*Phenocryst*	*Groundmass*	*Groundmass*
SiO_2	50.31	49.28	49.55	54.35	49.06	48.15	52.10	52.05	48.48	49.96
Al_2O_3	31.50	32.19	32.26	29.01	32.42	33.20	30.25	30.35	32.80	31.37
Na_2O	3.12	2.55	2.61	4.91	2.33	1.88	3.74	3.66	2.36	3.06
MgO	0.02	0.03	0.06	0.03	0.23	0.14	0.15	0.14	0.01	0.02
TiO_2	0.04	0.08	0.03	0.10	0.01	0.03	0.04	0.06	0.04	0.05
CaO	14.76	15.69	15.45	11.72	16.03	16.88	13.73	13.86	16.13	14.75
K_2O	0.05	0.07	0.03	0.07	0.01	0.01	0.08	0.09	0.03	0.06
Cr_2O_3	0.01	0.00	0.01	0.00	0.00	0.01	0.00	0.00	0.01	0.00
FeO	0.28	0.34	0.45	0.52	0.39	0.39	0.44	0.52	0.14	0.18
MnO	0.01	0.01	0.01	0.01	0.01	0.01	0.00	0.01	0.00	0.00
Total	100.10	100.24	100.47	100.73	100.47	100.69	100.53	100.72	99.98	99.45
Sample	*19LYS-8100-8*	*19LYS-8160-3*	*19LYS-8160-6*	*19LYS-8165-4*	*19LYS-8165-5*	*19LYS-8165-6*	*19LYS-8167B-4*	*19LYS-8167B-5*	*19LYS-8167B-8*	*19LYS-8181-1*
Rock	*Olivine gabbro*	*Hornblende gabbro*	*Hornblende gabbro*	*Troctolite*	*Troctolite*	*Troctolite*	*Troctolite*	*Troctolite*	*Troctolite*	*Hornblende gabbro*
Type	*Groundmass*	*Groundmass*	*Groundmass*	*Groundmass*	*Groundmass*	*Groundmass*	*Chadacryst*	*Chadacryst*	*Groundmass*	*Groundmass*
SiO_2	50.21	52.17	53.47	48.28	48.96	47.98	48.63	49.24	49.42	51.13
Al_2O_3	31.39	30.33	29.81	33.36	32.72	33.16	31.92	32.68	31.93	30.73
Na_2O	3.13	3.82	4.17	2.00	2.27	1.94	2.35	2.38	2.51	3.36
MgO	0.01	0.04	0.05	0.03	0.04	0.06	0.87	0.04	0.05	0.07
TiO_2	0.07	0.08	0.06	0.03	0.05	0.06	0.04	0.05	0.06	0.03
CaO	14.59	13.31	12.78	16.84	16.30	16.96	15.38	16.02	15.50	14.20
K_2O	0.05	0.12	0.11	0.03	0.04	0.03	0.04	0.04	0.05	0.09
Cr_2O_3	0.00	0.00	0.00	0.00	0.00	0.00	0.01	0.00	0.00	0.00
FeO	0.23	0.41	0.45	0.36	0.40	0.41	0.42	0.40	0.38	0.46
MnO	0.00	0.00	0.02	0.00	0.02	0.01	0.02	0.00	0.00	0.00
Total	99.67	100.28	100.92	100.93	100.79	100.60	99.66	100.85	99.89	100.08

Table A2 – III: (continued)

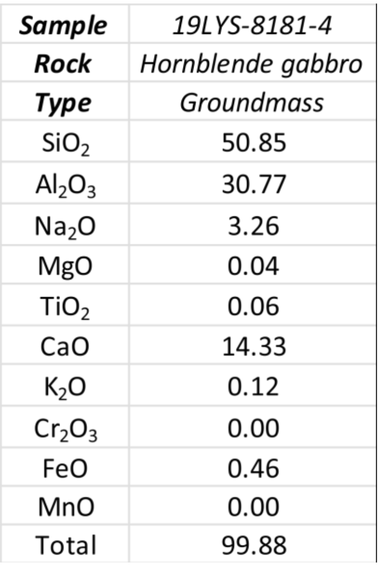

Sample	*19LYS-8181-4*
Rock	*Hornblende gabbro*
Type	*Groundmass*
SiO_2	50.85
Al_2O_3	30.77
Na_2O	3.26
MgO	0.04
TiO_2	0.06
CaO	14.33
K_2O	0.12
Cr_2O_3	0.00
FeO	0.46
MnO	0.00
Total	99.88

Table A2 – IV: Amphibole chemistry

Sample	*18LYS-7009D-6*	*18LYS-7375B-1*	*18LYS-7375B-2*	*19LYS-7225-5*	*19LYS-7238-1*	*19LYS-7238-2*	*19LYS-8160-4*	*19LYS-8160-5*	*19LYS-8181-2*	*19LYS-8181-3*	*19LYS-8181-5*	*19LYS-8181-6*
Rock	*Hornblende gabbro*	*Melatroctolite*	*Melatroctolite*	*Hornblende gabbro*	*Melatroctolite*	*Melatroctolite*	*Hornblende gabbro*	*Hornblende gabbro*	*Hornblende gabbro*	*Hornblende gabbro*	*Hornblende gabbro*	*Hornblende gabbro*
SiO_2	48.699	45.397	45.157	44.102	45.509	45.242	47.552	52.835	48.615	46.462	51.69	49.241
Al_2O_3	7.157	9.151	10.796	10.682	8.268	8.395	7.661	3.508	6.58	9.129	5.515	6.721
Na_2O	1.549	3.051	2.896	1.653	2.971	2.905	1.41	0.609	1.158	1.815	1.008	1.349
MgO	13.102	17.109	17.201	14.183	15.902	15.875	14.616	14.731	14.064	15.098	15.714	16.843
TiO_2	0.7	4.288	2.679	3.857	4.274	4.013	1.884	0.402	0.515	2.54	0.224	1.157
CaO	11.819	11.436	11.66	11.575	10.472	10.544	11.029	12.224	11.94	11.478	12.089	11.722
K_2O	0.304	0.357	0.241	0.57	0.608	0.587	0.542	0.128	0.269	0.579	0.161	0.35
Cr_2O_3	0	0.428	0.437	0.579	0.122	0.296	0.524	0.065	0.095	0.302	0.155	0.127
FeO	15.203	6.646	6.589	10.148	9.175	9.498	12.397	13.882	12.737	10.067	10.943	9.479
MnO	0.189	0.11	0.098	0.147	0.11	0.107	0.146	0.182	0.25	0.146	0.185	0.154
Total	98.722	97.973	97.754	97.496	97.411	97.462	97.761	98.566	96.223	97.616	97.684	97.143

Appendix A3: Geochronology

Table A3 – I: Isotopic data

								Isotopic Ratios					**Isotopic age (Ma)**		
	(ppm)	(ppm)	(ppm)	(ppm)											
Sample	**Pb(c)**	**Pb(*)**	**U**	**Th**	**Th/U**	**^{207}Pb/^{206}Pb**	**1σ (%)**	**^{207}Pb/^{235}U**	**1σ (%)**	**^{206}Pb/^{238}U**	**1σ (%)**	**^{207}Pb/^{206}Pb**	**2σ**	**^{206}Pb/^{238}U**	**2σ**
18LYS-7010C-1	-18	31	770	813	1.09	0.0520	1.5	0.3388	2	0.0472	1.3	290	± 34	297	±3.8
18LYS-7010C-2	44	52	1346	1379	1.06	0.0526	1.1	0.3209	1.9	0.0446	1.5	294	± 26	281	±4.2
18LYS-7010C-3	5212	2	62	23	0.38	0.0839	4	0.2480	34	0.0433	2.5	-254	±860	273	±6.8
18LYS-7010C-4	14	92	2296	2699	1.21	0.0523	0.85	0.3362	1.5	0.0467	1.3	294	± 20	294	±3.6
18LYS-7010C-5	357	6	136	70	0.53	0.0552	3.3	0.3760	5.3	0.0521	1.9	298	±110	328	±5.9
18LYS-7010C-6	-2	50	1240	978	0.82	0.0517	1.2	0.3333	1.7	0.0468	1.3	271	± 27	295	±3.7
18LYS-7010C-7	-102	52	1361	976	0.74	0.0509	1	0.3194	1.8	0.0448	1.3	272	± 29	283	±3.7
18LYS-7010C-8	1797	3	83	52	0.65	0.0576	5.3	0.2400	17	0.0404	2.1	-162	±410	255	±5.3
18LYS-7010C-9	2	85	2178	2111	1.00	0.0521	0.88	0.3277	1.6	0.0456	1.3	289	± 22	288	±3.5
18LYS-7010C-10	118	86	2140	2091	1.01	0.0533	0.86	0.3383	1.7	0.0469	1.3	301	± 25	295	±3.6
18LYS-7010C-11	0	9	207	90	0.45	0.0526	2.7	0.3520	3	0.0485	1.5	313	± 60	305	±4.3
18LYS-7010C-12	100	8	224	207	0.95	0.0529	2.7	0.3160	5.3	0.0440	1.5	288	±120	278	±4.0
18LYD-7018A2-1	483	20	523	307	0.61	0.0514	3.1	0.3090	3.5	0.0436	1.6	259	± 72	275	±4.4
18LYD-7018A2-2	1818	22	565	483	0.88	0.0515	5.8	0.3110	6	0.0438	1.7	265	±130	276	±4.5
18LYD-7018A2-3	0	18	488	328	0.69	0.0520	1.8	0.3125	2.4	0.0436	1.6	286	± 41	275	±4.4
18LYD-7018A2-4	32	46	1199	1115	0.96	0.0513	1.2	0.3132	2	0.0443	1.6	253	± 27	280	±4.4
18LYD-7018A2-5	151	23	604	639	1.09	0.0514	2.7	0.3122	3.1	0.0440	1.6	259	± 61	278	±4.5
18LYD-7018A2-6	1854	17	462	492	1.10	0.0535	6.3	0.3160	6.5	0.0428	1.8	350	±140	270	±4.8
18LYD-7018A2-7	239	23	611	660	1.12	0.0519	2.4	0.3164	2.9	0.0443	1.6	279	± 54	279	±4.5
18LYD-7018A2-8	-178	7	194	117	0.62	0.0528	2.9	0.3210	3.4	0.0441	1.8	321	± 66	278	±4.8
18LYD-7018A2-9	108	11	299	190	0.66	0.0507	2.7	0.3030	3.2	0.0434	1.7	225	± 62	274	±4.6
18LYD-7018A2-10	18521	79	1666	2230	1.38	0.0550	19	0.3390	19	0.0447	2	416	±420	282	±5.5
18LYD-7018A2-11	-177	27	713	728	1.05	0.0521	2.1	0.3188	2.7	0.0444	1.7	290	± 47	280	±4.7

Table A3 – I: (continued)

								Isotopic Ratios					**Isotopic age (Ma)**		
	(ppm)	(ppm)	(ppm)	(ppm)											
Sample	**Pb(c)**	**Pb(*)**	**U**	**Th**	**Th/U**	**^{207}Pb/^{206}Pb**	**1σ (%)**	**^{207}Pb/^{235}U**	**1σ (%)**	**^{206}Pb/^{238}U**	**1σ (%)**	**^{207}Pb/^{206}Pb**	**2σ**	**^{206}Pb/^{238}U**	**2σ**
18LYD-7018A2-12	200	11	308	209	0.70	0.0517	2.8	0.3033	3.3	0.0426	1.7	271	± 64	269	±4.5
18LYD-7018A2-13	73	30	813	1066	1.35	0.0511	1.7	0.3071	2.3	0.0436	1.6	247	± 38	275	±4.4
18LYD-7018A2-14	3729	5	140	81	0.60	0.0513	18	0.2940	18	0.0416	2.6	253	±420	263	±6.6
18LYD-7018A2-15	231	16	412	260	0.65	0.0509	2.3	0.3074	3.1	0.0438	2.1	237	± 54	276	±5.7
18LYD-7018A2-16	133	30	815	914	1.16	0.0505	1.9	0.2984	2.5	0.0428	1.6	219	± 44	270	±4.3
18LYD-7018A2-17	159	22	575	625	1.12	0.0503	2.1	0.3024	2.7	0.0436	1.7	208	± 49	275	±4.4
18LYS-7064-1	10546	5	116	78	0.70	0.0580	27	0.3480	27	0.0436	2.5	523	±590	275	±6.7
18LYS-7064-2	6500	11	260	156	0.62	0.0479	18	0.2970	18	0.0450	1.7	95	±430	283	±4.7
18LYS-7064-3	62	97	2464	2957	1.24	0.0523	0.87	0.3298	1.5	0.0458	1.2	297	± 20	289	±3.5
18LYS-7064-4	47	68	1699	454	0.28	0.0524	1.4	0.3387	2	0.0469	1.4	303	± 32	295	±3.9
18LYS-7064-5	734	47	1241	38	0.03	0.0524	2.8	0.3162	3.1	0.0437	1.3	305	± 64	276	±3.5
18LYS-7064-6	185	25	667	540	0.84	0.0524	1.6	0.3160	2.1	0.0437	1.3	303	± 36	276	±3.5
18LYS-7064-7	1180	28	689	412	0.62	0.0521	4	0.3310	4.2	0.0460	1.3	291	± 90	290	±3.8
18LYS-7064-8	99	20	245	256	1.08	0.0592	2.5	0.7630	3	0.0934	1.6	574	± 55	576	±8.7
18LYS-7064-9	925	152	3725	3474	0.96	0.0513	4.7	0.3330	4.9	0.0471	1.3	254	±110	297	±3.7
18LYS-7064-10	305	5	141	58	0.43	0.0493	4.8	0.3030	5	0.0446	1.6	163	±110	281	±4.4
18LYS-7064-11	283	32	827	875	1.09	0.0517	3.1	0.3240	3.3	0.0455	1.3	273	± 70	287	±3.7
18LYS-7064-12	1952	28	717	620	0.89	0.0528	4.9	0.3240	5.1	0.0445	1.3	318	±110	281	±3.7
18LYS-7064-13	1154	59	1489	1432	0.99	0.0535	2.9	0.3360	3.2	0.0455	1.3	350	± 66	287	±3.6
18LYS-7064-14	56	49	1246	1334	1.11	0.0523	1.3	0.3276	1.8	0.0454	1.3	298	± 30	286	±3.6
18LYS-7064-15	57	154	3842	5837	1.57	0.0520	0.82	0.3338	1.5	0.0465	1.2	287	± 19	293	±3.6
18LYS-7161B-1	14	303	7445	6523	0.91	0.0512	0.51	0.3339	1.9	0.0473	1.8	249	± 12	298	±5.2
18LYS-7161B-2	182	281	7202	3950	0.57	0.0523	0.71	0.3274	1.9	0.0454	1.8	299	± 16	286	±5.0

Table A3 – I: (continued)

								Isotopic Ratios					Isotopic age (Ma)		
	(ppm)	(ppm)	(ppm)	(ppm)											
Sample	**Pb(c)**	**Pb(*)**	**U**	**Th**	**Th/U**	**^{207}Pb/^{206}Pb**	**1σ (%)**	**^{207}Pb/^{235}U**	**1σ (%)**	**^{206}Pb/^{238}U**	**1σ (%)**	**^{207}Pb/^{206}Pb**	**2σ**	**^{206}Pb/^{238}U**	**2σ**
18LYS-7161B-3	1741	90	2526	4371	1.79	0.0529	4.8	0.2950	5.1	0.0405	1.8	324	±110	256	±4.6
18LYS-7161B-4	-1	146	3731	2253	0.62	0.0514	0.72	0.3237	1.9	0.0457	1.8	260	± 17	288	±5.1
18LYS-7161B-5	392	279	8250	6864	0.86	0.0511	0.93	0.2760	2	0.0391	1.8	247	± 21	248	±4.4
18LYS-7161B-6	-9	246	6199	4498	0.75	0.0517	0.55	0.3298	1.9	0.0462	1.8	274	± 13	291	±5.1
18LYS-7161B-7	10	253	6535	4617	0.73	0.0520	0.53	0.3229	1.9	0.0450	1.8	286	± 12	284	±5.0
18LYS-7161B-8	14	196	5318	3559	0.69	0.0520	0.66	0.3084	1.9	0.0430	1.8	287	± 15	271	±4.8
18LYS-7161B-9	373	169	4608	5445	1.22	0.0515	1.1	0.3012	2.1	0.0424	1.8	262	± 26	268	±4.7
18LYS-7161B-10	169	183	4989	3768	0.78	0.0534	0.86	0.3137	2	0.0426	1.8	344	± 20	269	±4.7
18LYS-7161B-11	213	220	5937	5862	1.02	0.0517	0.85	0.3068	2	0.0431	1.8	272	± 19	272	±4.9
18LYS-7161B-12	106	134	3714	2819	0.78	0.0519	0.83	0.2994	2	0.0418	1.8	282	± 19	264	±4.7
18LYS-7161B-13	1720	84	2624	8215	3.24	0.0485	3.4	0.2440	3.9	0.0365	1.8	124	± 81	232	±4.1
19LYS-8141-1	30	48	1228	1066	0.90	0.0518	1.5	0.3240	2	0.0453	1.3	278	± 35	286	±3.6
19LYS-8141-2	44	12	294	272	0.95	0.0505	3.5	0.3160	3.9	0.0454	1.7	219	± 82	286	±4.6
19LYS-8141-3	573	5	135	321	2.46	0.0513	7.5	0.3100	7.7	0.0437	1.8	256	±170	276	±5.0
19LYS-8141-4	65	118	2892	291	0.10	0.0515	0.9	0.3370	1.5	0.0475	1.3	261	± 21	299	±3.7
19LYS-8141-5	146	80	2058	1048	0.53	0.0501	1.3	0.3111	1.8	0.0450	1.3	201	± 30	284	±3.5
19LYS-8141-6	144	17	427	224	0.54	0.0505	3.1	0.3280	3.5	0.0470	1.6	219	± 73	296	±4.6
19LYS-8141-7	32	49	1220	1088	0.92	0.0517	1.4	0.3314	1.9	0.0465	1.3	270	± 32	293	±3.8
19LYS-8141-8	84	108	2713	1746	0.66	0.0516	10	0.3286	1.6	0.0462	1.3	269	± 23	291	±3.6
19LYS-8141-9	60	128	3250	2056	0.65	0.0515	0.86	0.3249	1.5	0.0458	1.3	262	± 20	289	±3.5
19LYS-8141-10	57	76	1949	1933	1.02	0.0504	1.1	0.3151	1.7	0.0454	1.3	213	± 25	286	±3.6
19LYS-8141-11	124	79	2004	1540	0.79	0.0511	1.4	0.3211	1.9	0.0455	1.3	247	± 32	287	±3.6
19LYS-8141-12	24	99	2512	2832	1.16	0.0523	1.1	0.3319	1.6	0.0460	1.3	300	± 24	290	±3.6

Table A3 – I: (continued)

								Isotopic Ratios					Isotopic age (Ma)		
	(ppm)	(ppm)	(ppm)	(ppm)											
Sample	**Pb(c)**	**Pb(*)**	**U**	**Th**	**Th/U**	**^{207}Pb/^{206}Pb**	**1σ (%)**	**^{207}Pb/^{235}U**	**1σ (%)**	**^{206}Pb/^{238}U**	**1σ (%)**	**^{207}Pb/^{206}Pb**	**2σ**	**^{206}Pb/^{238}U**	**2σ**
19LYS-8141-13	49	181	4524	9884	2.26	0.0509	0.74	0.3266	1.5	0.0465	1.2	236	± 17	293	±3.6
19LYS-8141-14	147	51	1320	3253	2.55	0.0507	1.6	0.3137	2.1	0.0449	1.4	229	± 36	283	±3.9
19LYS-8141-15	119	58	1502	738	0.51	0.0510	1.4	0.3155	1.9	0.0449	1.3	239	± 32	283	±3.5
19LYS-8141-16	172	37	982	235	0.25	0.0502	1.6	0.3059	2	0.0442	1.3	203	± 37	279	±3.6